Development of Pharmaceutical 3D Printing Filament for Fused Deposition Modelling: Material Considerations and Process Limitations

by

Moulham Alsuleman

Supervised by

Professor Gavin Halbert

A thesis in fulfilment of the requirements for the degree of Doctor of Philosophy

Strathclyde Institute of Pharmacy and Biomedical Sciences

Glasgow, United Kingdom

2024

Declaration of Authenticity and Author's Rights

This is the result of the author's original research. It has been composed by the author and has not been previously submitted for examination which has led to the award of a degree.

Date: 22/04/2024

Signed:

Moulham Alsuleman

Acknowledgments

To my Academic family:

I would like to express my sincere gratefulness to the people who have supported me throughout my academic journey. First and foremost, I want to thank to my supervisor, Professor Gavin Halbert, for his invaluable his tremendous assistance, support and guidance throughout my PhD. His expertise, encouragement, and constructive feedback were crucial in enlightening my PhD path and helping me to develop as a scholar.

I would also like to thank all the members of CMAC for the insightful conversations with them and the technical support they provided, my thanks are especially to Elke Prasad, Ecaterina Bordos, Alice Turner, John Robertson, Blair Johnston, Daniel Markl, Russell Miller, Alastair Florence, Thomas McGlone, Musab Osman, Peter Hou, Keir Murphy, Deborah Bowering, Monika Warzecha, Laura Pereira Diaz, Julia Gasol Cardona, Aleksandar Josifovic, Christoph Busche, Jenna Johnston, Martin Prostredny, Michael Devlin, Patrycja Bartkowiak, Pattavet Vivattanaseth, Sara Ottoboni, Mark McGowan, Vishal Raval, Michael Chrubasik, Aruna Prakash, Andrew Cashmore, Iyke Onyemelukwe, Tariq Islam, Carlota Mendez-Torrecillas, Ali Anwar, David McKechnie, Antony Vassileiou, Murray Robertson and everyone in how supported directly and indirectly my project. I want to thank Silke Henry from Ghent University, with whom I shared a passion for 3D printing and engaged in many interesting discussions our research area.

I would like to thank my industry mentors particularly Susanna Abrahmsén-Alami, Jonathan Booth, Pratik Pankaj Upadhyay and Helen Wheatcroft from AstraZeneca for their helpful advice, ideas and discussion we exchanged during my industrial placement (Chapter 5). I do appreciate their positive attitude and their sincere interest in applying advanced science to improve drugs and patients' life.

I would like to acknowledge the role of the University of Strathclyde in providing support and healthy environment for researcher to perform their best and improve our world. I want to thank the Cancer Research UK and their formulation unit for the generous funding and supporting for this work (Grant number C149/A20496).

To my real family and friends:

I would also like to thank my friends and family for their unwavering support, unfailing love, and constant encouragement over the last four year and before. Their support has been a constant source of inspiration and motivation.

My warmest feeling and thank words to my soulmate, Mai Alhussain, I will always be grateful for your love and presence in my life, you gave me the strength and motivation to overcome every obstacle and keep going during the hardest times. My full respect and deepest thanks go to my father Mohamad Alsuleman, who scarified all his life to provide an ideal life for me and my siblings in a part of the world where the ideal is impossible. My love and gratitude to my mother; Seham Alokdah, for her endless care and love and my siblings; Ola, Ayham, Deaa and Alaa for their unlimited support and encouragement. They were with me regardless the distance that forced on us due to Covid pandemic and travel difficulties. I would like to thank my mother-, my sisters- and brothers- in-low; Wafaa, Yolla, Walaa, Alaa, Omama, Huzaifa, Ali, Batoul, Afraa, Lumai and Alghaith. I would like to thank the people in CMAC and my supervisor but this time as friends.

I want to thank all Syrians who have shown remarkable resilience and strength in the face of adversity. Your courage and determination have been always inspired and taught me to be strong and encounter all kind difficulties.

Moulham Alsuleman

Published Conference Papers and Presentations:

CMAC Open Day, 2022:

"A story of a 3D printing filament" – 2nd place poster award

ExciPerience, March 2022: Online attendance.

AstraZeneca internal symposium 13 January 2022:

"AZD0837 formulation on FDM 3D printing technology" _ presentation.

AAPS PharmaSci360, 2020:

"Comparison between phase diagrams of Solid dispersion system using different analytical techniques" _ poster.

CMAC mini symposium, 2020:

"Can we 3D Print Any Drug Using Fused Deposition Modelling (FDM) 3D printer?" poster and presentation.

Controlled Release Society Annual Meeting & Exposition, May 2020: Online attendance.

AstraZeneca Meeting 27 Oct 2020:

"Material based decision for formulating a 3D printing filament" _ presentation

CMAC internal research day, 2020:

"Systematic pharmaceutical formulation on 3D-printing technology" _ poster

Chemlink HME Seminar, February 2020, Chester, UK: Attendance.

CMAC Summer school, June 2019:

"3D printing of mefenamic acid tablet" _ poster and presentation.

APS Additive Manufacturing Symposium, March 2019, London: Attendance.

SIPBS Conference, October 2019, Glasgow, UK:

"Systematic pharmaceutical formulation on 3D-printing technology" _ poster.

Making Pharmaceuticals, April 2018, Coventry, UK: Attendance.

In preparation:

"3D printing filament: printability prediction using Design of Experiment approach", to be submitted before mid-2025, The Pharmaceuticals journal by MDPI.

"A systematic approach for polymer blends for Fused Filament Fabrication (FFF) 3D printing", to be submitted before end-2025 submitted before mid-2025, The Pharmaceuticals journal by MDPI.

Abstract

With the current improvements in the health sector and technology, such as collecting patient data from wearables and using human body simulations and advanced models, and due to the diversity in the human body's interaction with medicine, a strong need to improve pharmacotherapy has emerged. 3D printing showed high potential to be a solution to produce customised, complex structure or polydrug medicines offering flexibility to change the number of drugs, their dose and/or their release. This study focusses on the fused deposition modelling 3D printing technology to systematically study formula development by identifying quality attributes and exploring formulation space, thereby defining the technology's potential and limitations and accelerating the formulation process.

Three main combinations were explored mefenamic acid with Eudragit EPO, AZD0837 (AstraZeneca's model drug) with hypromellose succinate acetate and AZD0837 with polyethylene oxide. The filaments physical state, molecular interactions and their performance were studied using various techniques like differential scanning calorimetry, Raman spectroscopy, X-ray diffraction, mechanical and rheological tests, thermal degradation and dissolution tests. Hansen Solubility Parameters (HSPs) and Design of Experiment (DoE) were utilised for prediction during filament development.

The study analyses 3D printing limitations and associates them with critical filament attributes. The minimum limit of elastic modulus on viscosity ratio at printing temperature was 0.8×10^{-3} MPa/%Pas for effective material extrusion from the 3D printer nozzle. The minimum limit of strain at break was 35% to allow the material to coil and bend in the feeder tube during printing. The minimum limit of maximum stress was 22.9 MPa to tolerate the pressure applied by the feeder gears and transfer the gear rotation into linear downforce. The study also investigates prediction tools to speed up formula development, reducing material and time requirements to produce new 3DP filament. HSPs were used to plasticise the polymer without reducing drug solubility in the polymer. Two printable filaments were developed using both single polymer (mefenamic acid with Eudragit EPO-based formula) and polymer mixture (AZD0837 with both hypromellose succinate acetate and polyethylene oxide) approaches. A balance between ratios was required to achieve the correct mechanical and rheological properties for a specific 3D printer. The first formula consisted of 5.1% stearic acid, 13.2% mefenamic acid (wt% of Eudragit EPO), and 14.5% fumed silica (of the total

weight). The second formula consisted of 30% (wt% of total weight) AZD0837 drug, 25% polyethylene oxide (wt% of polymer mix), and 75% hypromellose (wt% of polymer mix).

This study offers insights into the materials requirements for effective printing and investigates innovative solutions to the formulation process's challenges with the ultimate goal of developing pharmaceutical printable filaments. The results will permit improved formulations to increase the printable drug portfolio and accelerate reaching drug customisation to increase pharmacotherapeutic efficacy.

Table of Contents

Declaration of Authenticity and Author's Rights **2**

Acknowledgments **3**

Published Conference Papers and Presentations: **5**

Abstract **7**

Table of Contents **9**

Units, Symbols, Abbreviations and Synonyms: **13**

List of Figures **20**

Chapter 1: Introduction in Fused Deposition Modelling: principle, advantages and pharmaceutical applications ***34***

1.1. A need for innovation: 34

1.2. Advantages of 3D printing in different scenarios: 35

1.2.1. Alter the drug dose: 35

1.2.2. Multiple drug therapy: 37

1.2.3. Complex structure: 38

1.2.4. Patient acceptability: 39

1.2.5. Prototyping technique: 39

1.3. 3D printing a family of many techniques: 40

1.4. Building quality: 45

1.5. FFF 3D printer ink/filament: 47

1.5.1. FFF 3D printing machine in details: 47

1.5.2. From process parameters to material properties: 49

1.5.3. Filament production 53

1.5.3.1. Printable formula: 53

1.5.3.1. Formula other consideration: 64

1.5.4. Engineering the problem 64

1.6. Some material and analytical method background: 65

1.6.1. Materials: 65

1.6.1.1. Mefenamic acid (MFA): 65

1.6.1.2. Methacrylate-Copolymer Eudragit EPO (EPO): 65

1.6.1.3. AstraZeneca model drug, AZD0837 (AZ): 66

1.6.1.4. hydroxypropyl methylcellulose (hypromellose) acetate succinate (HPMC-AS): 66

1.6.1.5. Polyethylene glycol/oxide (PEG/PEO): 67

1.6.2. Analytical techniques: 67

1.6.2.1. X-ray diffraction techniques: 68

1.6.2.2. Thermal behaviour analytical techniques: 68

1.6.2.3. Texture analyser: 69
1.6.2.4. Rotary rheometer: 70
1.6.2.5. Optical coherence tomography (OCT): 71
1.6.2.6. Raman spectroscopy: 71
Aims and objectives: 73
The study aims are: 73
The study objectives are: 73
Chapter 2: Mefenamic acid filament, single polymer approach: Binary system Drug-Polymer, mefenamic acid Eudragit EPO 76
2.1. Introduction 76
2.2. Materials and Methods 77
2.2.1. Materials 77
2.2.2. Methods 78
2.2.2.1. Filament and extrudate preparation: 78
2.2.2.2. Solid state study and molecular interaction 79
2.2.2.3. Thermal analysis 80
2.2.2.5. Formulae performance 82
2.2.2.6. Statistical studies 85
2.3. Results and Discussion 85
2.3.1. Material selection and extrudates production 85
2.3.2. Solid state study and Phase diagram 90
2.3.3. Molecular interaction 96
2.3.4. Thermal study 100
2.3.5. Formulae performance 104
2.4. Conclusion 119
Chapter 3: Multicomponent systems (Drug-Polymer-Plasticizer), mefenamic acid-Eudragit formula development: 122
3.1. Introduction 122
3.2. Materials and Methods 122
3.2.1. Materials 122
3.2.2. Methods 122
3.2.2.1. Plasticizer screening 123
3.2.2.2. TGA, Pure component thermal degradation 124
3.2.2.3. Production of the filaments (Hot melt extrusion): 124
3.2.2.4. Phase separation: 126
3.2.2.5. Performance and mechanical properties 127
3.3. Results and discussion 128
3.3.1. Binary system Polymer – plasticizer 128
3.3.1.1. Plasticizers compatibility study 128

3.3.1.2. Pure components degradation 136
3.3.1.3. Production and EPO:plasticizer performance 139
3.3.2. Binary to Ternary system: drug - polymer – plasticizer 145
3.3.3. MFA:EPO:StA systems potential for 3D printing 157
3.4. Conclusion 160

Chapter 4: Quaternary systems ratio optimisation, mefenamic acid-Eudragit EPO- Stearic acid and Fumed silica formula development: 163

4.1. Introduction 163
4.2. Materials and Methods 163
4.2.1. Materials 163
4.2.2. Methods 164
4.2.2.1. Thermal analysis 164
4.2.2.2. Extrudate preparation 164
4.2.2.3. Design of Experiment (DoE) 166
4.2.2.4. Formulae performance 169
4.3. Results and discussion 173
4.3.1. Filler screening 173
4.3.2. Quality attributes for 3D printing filament 178
4.3.2.1. Evaluation of mechanical properties from 3PB and TS 178
4.3.2.2. Rheological properties 184
4.3.2.3. Stickiness 194
4.3.3. Define quality attributes limits 196
4.3.4. DoE results 200
4.3.4.1. Comparing mechanical properties using MODDE 200
4.3.4.2. DoE model for 3D printability 203
4.3.4.3. Prediction of DoE responses 205
4.3.4.4. Best formula printability test 208
4.4. Conclusion 210

Chapter 5: AZD0837 3D printing filament using polymer blend approach: 213

5.1. Introduction 213
5.2. Materials and Methods 213
5.2.1. Materials 213
5.2.2. Methods 214
5.2.2.1. HME extrusion 214
5.2.2.2. Solid state 215
5.2.2.3. Physical properties 215
5.2.2.3. Caplets production 216
5.2.2.4. Caplets characterisation 218
5.2.2.6. Filament stability 218

5.3. Results and Discussion 219
5.3.1. Binary mixtures 219
5.3.1.1. Filament production: 220
5.3.1.2. Solid state 224
5.3.1.3. Physical properties 233
5.3.1.4. 3D printing 239
5.3.2. Ternary mixtures 246
5.3.2.1. Ternary systems extrusion 246
5.3.2.2. Ternary systems' solid state 249
5.3.2.3. Ternary systems mechanical properties 252
5.3.2.4. Ternary systems optimal formula 254
5.3.3. Caplets production 255
5.3.3.1. Printing temperature and printing test 255
5.3.3.2. Accuracy and precision evaluation 256
5.3.3.3. Injection moulding equivalent caplets 258
5.3.4. Dissolution test 261
5.3.5. Filament stability 266
5.4. Conclusion 270

Chapter 6: Conclusions, Challenges and Future Work 274

6.1. Thesis achievements: 274
6.1.1. Essential ingredients (drug and carrier): 274
6.1.2. Single polymer approach: 275
6.1.3. Polymer blend approach: 275
6.2 Beyond findings and future work: 276
6.2.1. Polymer screening: 276
6.2.2. Plasticizer screening: 278
6.2.3. Define printer limitation and filament quality attributes: 278

Reference 281

Appendix 1: Chapter 2 supporting information 308

Appendix 2: Chapter 3 supporting information 316

Appendix 3: Chapter 4 supporting information 318

Units, Symbols, Abbreviations and Synonyms:

List of units:

Unit symbol	Unit name/meaning
Å	Angstrom
a.u.	Arbitrary Unit (Given unit after normalisation)
cm	centimetre
°	degree
°C	degree Celsius
°C/min	degree Celsius per minute
g/mm²	gram per millimetre square
g/mol	gram per mole
K	Kelvin
kg	kilogram
kg/hr	kilogram per hour
kV	kilovolt
MPa	Mega Pascal
MPa/%	Mega Pascal for each 1% deformation
µg/mL	microgram per millilitre
µg.mm^{-2}.sec^{-1}	microgram per millimetre square per second
µm	micrometre
mA	milliampere
mg	milligram

Unit symbol	Unit name/meaning
mL	millilitre
mm	millimetre
mm/min	millimetre per minute
mm/sec or mm/s	millimetre per second
mW/mg	milliwatt per milligram
min	minute
M	molarity = mol/l
nm	nanometre
N	Newton
Nm	Newton-meter unit of Unit of torque
Pa	Pascal
%	percentage
R.I.	relative intensity (Dimensionless unit from normalisation)
rpm	revolutions per minute
s or sec	second
M6	Thread size
2θ	Two-theta, diffraction angle
wt:wt	Weight ratio
wt%	Weight ratio (fraction of total)

List of symbols:

Symbol	Meaning	Symbol	Meaning
ΔP_c	stress needed for 3D printing extrusion	**Δq**	difference in the heat flow
L	distance between the rollers and the liquefier	E_f	flexural Modulus
R	filament diameter	**σ**	stress
E	elastic modulus	**ε**	strain
r	nozzle diameter	**l**	length of the liquefier
η	viscosity	$\dot{\gamma}$	shear rate
σ_c	buckling force	c_p	heat capacity
E_γ	Young's modulus	**P**	the vapour pressure
π	Pi (≈ 3.14)	**Log**	logarithm
K [in $\eta = K(\dot{\gamma})^{n-1}$**]**	power-law fit parameters	**dm (in eq 2.1)**	change in the mass
η_a	apparent viscosity	**dt (in eq 2.1)**	change in the mass
Q	volumetric flow rate	**N (in eq 2.1)**	sample size
s	significant (based on confidence level usually 95%)	**Ns**	non-significant (based on confidence level usually 95%)
Ra MFA	interaction radius with mefenamic acid	**Ra** EPO	interaction radius with Eudragit EPO
δ_D	the energy from dispersion forces between molecules	f_D	normalised energy from dispersion forces between molecules (eq 2.2).
δ_H	the energy from hydrogen bonds between molecules	f_H	normalised energy from hydrogen forces between molecules (eq 2.4).
δ_P	the energy from dipolar intermolecular forces between	f_P	normalised energy from dipolar forces between molecules (eq 2.3).

	molecules		
Δδ	difference in the overall solubility	**R^2**	coefficient of determination
P > 0.05	refer to non-significant statistical difference	**P < 0.05**	refer to significant statistical difference

Abbreviation list:

Abb	Definition	Abb	Definition
^{18}F- FDG	Radiolabelled Fluorodeoxyglucose	**mLLDP**	Metallocene low-density polyethylenes
1D	One dimension	**MT-S**	Feeder model
2D	Two dimensions	**MVol**	Molecular volume
3D	Three dimension	**MW**	Molecular weight
3DP	3D printing	**NA**	Not applicable
AM	Additive manufacturing	**NHS**	National Health Service
API	Active pharmaceutical ingredient	**NME**	New molecular entity
ASA	Aminosalicylic acid	**NPJ**	Nano-Particle Jetting
ASA	Aminosalicylic acids	**OCT**	Optical coherence tomography
ASTM	American Society for Testing and Materials	**PC**	Product code
AZ	AstraZeneca model drug AZD0837	**PCL**	Poly(ε-caprolactone)
BCS	Biopharmaceutical classification system	**PCL**	Polycaprolactone
BCS Class IIa	Class II means high permeable but low soluble drug. IIa is subclass with relatively better solubility.	**PED**	Precision Extruding Deposition
BJ	Binder Jetting	**PEG**	Polyethylene glycol
CAD	Computer-aided design	**PEG4h**	Polyethylene glycol (4000 molecular weight)

Cc	Critical concentration
CCDC	Cambridge Structural Database
CMAC	The Continuous Manufacturing and Advanced Crystallisation Hub
CMC	Aqualon carboxy methyl cellulose
CMC E / N14	Aqualon carboxy methyl cellulose different grads
CQA	Critical Quality Attributes
Cu	Copper
DMF	Dimethylformamide
DMLS	Direct Metal Laser Sintering
DMT	Direct Metal Tooling
DOD	Drop on Demand
DoE	Design of Experiment
DSC	Differential scanning calorimetry
EBAM	Electron-beam Additive Manufacturing
EC	Ethyl cellulose
EPO	Eudragit EPO (Methacrylate-Copolymer)
EtOH	Ethanol
EVA	Ethylene-vinyl acetate
Evonik ®	A company name, manufacturer of Eudragit
ext in Figure (2-8)	extrudate

PEG4k	Polyethylene glycol (400 molecular weight)
PEO	Polyethylene oxide
PEO WSR N10	Polyethylene oxide of 100,000 g/mol molecular weight
pH	Solution acidity
phyMx	Physical mixtures
PI	Photoinitiator
pKa	Acidic strength
PLLA	Poly-L-lactic acid
PM	Physical mixtures
PMMA	Poly(methyl methacrylate)
PTFE	Polytetrafluoroethylene
PTFE	Polytetrafluoroethylene
PVA	Polyvinyl alcohol
PVA	Polyvinyl alcohol
PVC	polyvinyl chloride
PVP K12	Polyvinylpyrrolidone grade K12
QbD	Quality by Design
QTPP	Quality Target Product Profile
RP	Rapid Prototyping
RS:RL	Eudragit RS / Eudragit RL ratio

FabRx	Start up in 3D printing for pharmaceitcal application	**SA/V**	Surface area to volume ratio
FDA	Food and Drug Administration	**SAX**	Small-angle X-ray scattering
FDM	Fused deposition modeling	**SEM**	Scanning electric microscope
FFF	Fused Filament Fabrication	**SFF**	Solid Free Form technology
FM (table 2-8)	Flexural modulus	**SLA**	Stereolithography
FT-IR	Fourier-transform infrared spectroscopy	**SLM**	Selective Laser Melting
GI	Gastrointestinal	**SLS**	Selective Laser Sintering
Gr-mm	Grain size of the filter material	**SLS**	selective laser sintering
GSK	GlaxoSmithKline, pharmaceutical company	**SSE**	Semi-Solid Extrusion
HME	Hot melt extrusion	**SSE**	Semi-Solid Extrusion
HPC	Hydroxypropyl cellulose	**StA**	Stearic acid
HPC	Hydroxylpropyl cellulose, E/L/S viscosity grades	**T die**	Set temperature of the die in the HME
HPC EF / LF / SSL	Grades of Hydroxypropyl cellulose	**T°C$_{(HME/3DP)}$**	Process temperature of Hot melt extrusion and 3D printer in degree Celsius
HPMC	Hypermellose also called Hydroxypropyl methylcellulose	**TA**	Texture analyser
HPMCAS-LG/MG/HG	Different grades of Hydroxypropyl Methylcellulose Acetate Succinate	**TCP**	Tricresyl phosphate
HSM	Hot stage microscopy	**TEC**	Triethyl citrate
HSPiP	Software version to calculate Hansen	**Tg**	Glass transition temperature

	Solubility Parameters		
HSPs	Hansen Solubility Parameters	**TGA**	Thermogravimetric Analysis
IBC	Intermediate Bulk Container	**THz-Raman**	Terahertz Raman
ICH	International Council for Harmonization	**T_k**	Temperature in Kelvin
IDR	Intrinsic dissolution rate	**T_p**	Process temperature
IR	Infrared spectroscopy	**TWN**	Tween 80
LIW	Loss In Weight	**T_{Zone8}**	Set temperature of the zone 8 in the HME
LOM	Laminated Object Manufacturing	**UAM**	Ultrasonic Additive Manufacturing
MED®	Melt-Extrusion Deposition	**USP**	United States Pharmacopeia
MeOH	Methanol	**UV-Vis**	Ultraviolet–visible light
MFA	Mefenamic acid	**WAX**	Wide-angle X-ray
MHRA	Medicines and Healthcare products Regulatory Agency	**XRPD**	X-ray powder diffraction
MJ	Material Jetting	**Y-MB**	Yamamoto-Molecular Break method to calculate Hansen solubility parameter
MJT	Material jetting		
MK8	type of 3D printing extruder		

Synonym list:

Name	Synonyms
Kollidon CL-F / 12PF	Commercial name of crosspovidone. CL-F and 12PF different grades.
HPMC-AS	Hydroxypropyl Methylcellulose Acetate Succinate
Tecoflex EG-72D / EG-80A	Commercial name of polyurethanes (TPUs). EG-72D and EG-80A are the grade.
Tecophilic SP-93A-100 / TG-2000	Commercial name of polyurethanes (TPUs). SP-93A-100 and TG-2000 are the grade.
Plasdone™ S-630	Commercial name of copovidone
Ac-Di-Sol	Croscarmellose sodium
Polyplasdone-XL	Commercial name of crospovidone. XL is a grade.
XYANAC	Mefenamic acid crystalline form I
XYANAC02	Mefenamic acid crystalline form II
BenecelTM	E grade of Hydroxypropyl methylcellulose (HPMC)
Affinisol 15cP	Commercial name of a grade of hypromellose (HPMC)
Klucel LF / EF	Commercial name of Hydroxypropylcellulose. LF and EF different grades.
Aqualon N7	Commercial name of Ethyl Cellulose
Soluplus	Commercial name of Polyvinyl caprolactam–polyvinyl acetate–polyethylene glycol
Eudragit RL / L / E / RL PO / RL100 / RS100	Different grades of Methacrylate-Copolymers
Kollicoat IR	Polyvinyl alcohol-polyethylene glycol graft copolymer
Kollidon VA64	Commercial name of Polyvinylpyrrolidone-vinyl acetate copolymer
AQUOT-LG (HPMCAS-LG)	Commercial name of Hydroxypropyl Methylcellulose Acetate Succinate LG grade.

List of Figures

Figure 1-1. Different morphology, size, colour and complexity of printed tablets (all the photos are taken from the original papers). a) tablets with different sizes but similar surface area to volume ratio (SA/V) using stereolithography (SLA) 3D printing (3DP) [24]. b) Pollypill of five drugs loaded in four compartments, the tablet has dots for distinguishing [25]. c) Caplets of two drugs, paracetamol and caffeine, printed by Fused Filament Fabrication (FFF) 3DP in two patterns, the left release both drugs simultaneously and the right delays the one in the core [26]. d) tablet with a gyroid shape for improving solubility printed using the selective laser sintering (SLS) 3DP [18]. e) Caplets that have channels with different alignments using the FFF-3DP. f) Multi-compartment capsular devices that can contains different drugs or different drug release, the body printed using FFF-3DP [27] . g) Placebo tablets with different colours and shapes printed using Hydroxypropylcellulose on FFF-3DP [28]. h) Pollypill tablets of four drugs isinopril, indapamide, rosuvastatin and amlodipine printed using FFF-3DP [29]. i) Tablets as gummi candies for improving paediatric compliance [30].....37

Figure 1-2. Ishikawa diagram material critical attributes and critical process parameters that affect tablet disintegration and dissolution (Figure taken from literature [61]). 47

Figure 1-3. FFF head extrusion mechanism. a) The head elements. b) cross section during the extrusion process in both cases success and fail. c) Temperature and stress across the filament where ΔP is the pressure applied through the gears, L is the length between the gear and the liquefier, R is the filament radius, E is the elasticity of the filament at specific temperature and feed rate, r is the nozzle radius and η is the viscosity of the liquified filament at specific temperature. 49

Figure 1-4. Hot melt extruder schematic showing the screw elements and the thermal change in the barrel. The material is passed and mixed through the barrel and extruded to produce filament. 54

Figure 1-5. Chemical structure of mefenamic acid. 65

Figure 1-6. Chemical structure of Eudragit EPO. 66

Figure 1-7. Chemical structure of HPMCAS. 67

Figure 1-8. Chemical structure of PEO. 67

Figure 1-9. Schematic of Differential Scanning Calorimetry showing the principle of the measurement (copied from the literature [116]). 69

Figure 1-10. Schematic of texture analyser components (copied from the literature [119]). 70
Figure 1-11. Schematic of rotary rheometer. 71
Figure 1-12. Schematic of optical coherence tomography (reproduced [122]). 71
Figure 1-13. Schematic representation of energy transitions in Raman spectroscopy (reproduced [123], [124]). 72
Figure 2-1. Diagram for the extrudate, filament, formula and physical mixture terms used in this thesis. 77
Figure 2-2. Schematic of the 3D point bend test experiment (A), and the mechanical test graph and points (B), picture of the setup (C [130]). 83
Figure 2-3. Torque against the process temperature for different EPO:MFA drug loads from 0 to 40% (wt%), shaded area represents the range (A). Torque values against the drug load from the HME experiments at 140 and 150°C (B). Mann-Whitney test conducted on the overlapped values, n = 60 (measurement every 5 sec for 5 min), bar and shaded areas are ranges (max-min), s indicated significant difference between the samples (ns = non-significant, P > 0.05). 87
Figure 2-4. Pressure values from the HME die versus the process temperature. Bar represents the range (max-min), n=60 (measurement every 5 sec for 5 min)..... 88
Figure 2-5. low-frequency THz-Raman spectroscopy reference, (Black) MFA form I, (Blue) MFA form II and (Red) EPO. Peaks indicated with stars are the characteristic ones. 91
Figure 2-6. Inline-THz Raman Spectra and XRPD examples of EPO:MFA extrudates (A, C) and the corresponding phase diagram from each technique (B, D). In Figures B and D, the borders of the regions are the middle point of the neighbour measurements (accuracy ±10°C, ±5% wt%). 93
Figure 2-7. Offline THz-Raman of extrudates after two months of the extrusion. First group (top) all spectra that showed no presence of MFA crystalline peaks. Second group spectra with form I MFA peaks indicating crystalline solid dispersion. Third group (bottom graph) shows repetition of MFA:EPO 40:60 extruded at 170°C. ... 95
Figure 2-8 . Raman of N-H stretch peak of MFA:EPO 30:70 (wt%) samples processed at 140°C and 150°C showing presence of MFA form I. 96
Figure 2-9 . Raman peaks of [Ar] C-C-C in phase bending in the aromatic ring and N-H bending out of plane in the mefenamic acid at 578.1 and 622.9 cm-1 (top) and CN

stretching vibration in the Eudragit EPO at 601.6 cm-1 (bottom). Blueshift of the Eudragit peak in the extrudates samples between 10 and 40% (wt%) drug load ...98
Figure 2-10. DSC first heating cycle of MFA and MFA:EPO physical mixtures (PM) and Eudragit EPO.....101
Figure 2-11. DSC first heating cycle of MFA:EPO and Eudragit EPO extrudates processed at different temperature on the HME (Tp). 102
Figure 2-12. Mass loss between 130-230°C from extrudates using TGA (Average value, n=2, bar = SD and max fluctuation of an empty pan below 0.14%).....103
Figure 2-13. Mechanical properties of MFA:EPO extrudates at different drug loadings (0%, 10%, 20%, 30% and 40%, wt%) using the three point bend test. The graphs show examples of 3-point bend test (A) flexural modulus (B), Maximum stress (C) and Strain at break in these systems it was also = Strain at maximum stress (D). Amorphous samples coloured green (≤Cc) and crystalline coloured blue (>Cc). Average value (n=5, error bar = Standard deviation, ANOVA test s = $P < 0.05$ significant difference and ns = $P > 0.05$ no significant difference). ANOVA study for the temperature impact are not added to the graph but can be found in table 2-8. 106
Figure 2-14. Cross section images from the SEM of the net polymer EPO extrudate (A) the MFA:EPO extrudates at different drug load (B - D). Red arrows (stress direction), dashed line (separate the compression and tension areas) and stars (toward the tension area). * samples broken using three point bend test.....114
Figure 2-15. Cross section images from the SEM of the MFA:EPO 30:70 (wt:wt) extrudates at different process temperature 120-150°C (A – D, respectively). Red arrows (stress direction), dashed line (separate the compression and tension areas) and stars (toward the tension area).....115
Figure 2-16. The Amount of MFA (A) and the calculated intrinsic dissolution rate of MFA (B) from the 6 mm compressed tablets of the MFA powder and MFA:EPO physical mixtures, and extrudates loaded with drug at different concentration or processed at different temperatures. IDR values calculated according to eq 2-1. Average (n = number of data points in graph A, 200), Mann-Whitney test (s = $P <$ 0.05 significant difference). 118
Figure 3-1. Schematics from two sides of the direct extruder of the 3D printer used in this study, main elements defined (left), and main dimensions indicated (right). 128

Figure 3-2. Teas Plot of chosen plasticizers (green), MFA (blue) and EPO (red) showing the relative distances between the pure components' solubility parameters. 131
Figure 3-3. DSC traces of EPO:Plasticizer formulae (mixtures not extrudates) and the pure component from thermal profile of two cycle. Cooling graphs from melt of the first cycle (A), Heating graphs of the second cycle (B). 132
Figure 3-4. Microscopic images from the film casting of EPO:Plasticizers at 85:15 (wt%) ratios. 135
Figure 3-5. Mass loss of the pure components by two thermogravimetric analysis methods. One step heating to 240°C (Top) and Two phases namely heating then holding at high temperature (Bottom). 138
Figure 3-6. Schematic of MFA and StA interaction with EPO, MFA:EPO system (A), EPO:StA system (B) and MFA:EPO:StA system (C), and plasticization effect associated with both molecules, transmission plasticization effect (D) and separation plasticization effect (F). Strong bonds like hydrogen bond (red), while Van der Waals bonds (green). 144
Figure 3-7. Mechanical properties from 3 point bend test for pure EPO, EPO:Plasticizers 95:5 and 85:15 (wt%). Stress-strain curves (A), flexural modulus (B), maximum stress (C) and strain at break (D). Average value (n=5, error bar = SD), ANOVA test only non-significant difference (ns, P>0.05) added to the graph i.e. all the rest are significant. 145
Figure 3-8. Optical microscopic images of EPO:plasticizers 95:5, 85:15 and MFA:EPO:plasticizers 20:76:4 (all in wt%), red colours indicated phase separation blue colour indicated homogenous system. 147
Figure 3-9. DSC traces of EPO-plasticizer at two ratios 5% and 15% and EPO-MFA-plasticizer system during the first cooling cycle, glass transition (star). 150
Figure 3-10. Xray diffraction pattern of ternary systems at two plasticizers ratio MFA:EPO:plasticizer 20:76:4 (L) and 20:65:15 (H). 151
Figure 3-11. Mechanical properties of EPO and EPO:plasticizer 95:5 (wt%) versus the corresponded formulae loaded with 20% (wt%) MFA. Stress-strain curves, flexural modulus, maximum stress and strain at break. Average value (n=5, error bar = SD), ANOVA test only non-significant difference (ns, P>0.05) added to the graph i.e. all the rest are significant. 153
Figure 3-12. Schematic of MFA-EPO formula development. 154

Figure 3-13. Cross section images from the SEM of MFA:EPO:plasticizer 20:76:4 (wt%) extrudate. * samples broken using three point bend test. 155
Figure 3-14. SAX (left) and WAX (right) data of the EPO extrudate, EPO:StA at ratio of 95:5, 90:10 and 85:15. 157
Figure 3-15. 3-point bend test of six different EPO formulations using StA as plasticizer and MFA as a drug. StA ratios were 0, 5 and 10% (wt%) while MFA ratios were 0 and 20% (wt%). Stress-strain curve (A) and extracted mechnical property values (B). 159
Figure 4-1. Schematic and photo of filament collection and diameter adjustment. 165
Figure 4-2. Schematic of formulation development (completion of Figure 3-12) and 3D scatter plot of the DoE experiments. 168
Figure 4-3. Schematic of the tensile strength test experiment (A) and picture of the setup (B). 170
Figure 4-4. Mass loss (%wt) of the fillers from the thermogravimetric analysis at heating rate of 20°C/min. 174
Figure 4-5. EPO:StA:filler (72:8:20) filaments, fillers (silk, talc < 45 µm, talc <75 µm and Silica), scale (1 mm increment). 175
Figure 4-6. Mechanical properties from 3-point bend test for filler containing and filler free extrudates. Stress-strain curves (A), flexural modulus (B), maximum stress (C) and strain at break (D). Average value (n=5, error bar = SD), ANOVA test only non-significant difference (ns, P<0.05) added to the graph i.e. all the remainder are significant. 177
Figure 4-7. Elastic modulus and stress values of DoE filaments from both three-point bend (3PB) tensile strength (TS) tests. 183
Figure 4-8. Strain values of DoE filaments from both three-point bend (3PB) tensile strength (TS) tests. 183
Figure 4-9. Storage (G') and loss (G") moduli of DoE central points (1 and 5) from the amplitude sweep test showing complex behaviour and linear viscoelastic region limit (arrows), data from other samples are shown in Figure appendix 3-5. 184
Figure 4-10. Viscosity of all DoE formulae at different temperature plotted together, zoom in box (right side). Central points (DoE1 and 5) were overlapping. 186
Figure 4-11. Storage modulus (A), loss modulus (B) and tan(δ) with the crossover points and peaks (C) of the DoE filaments. 188

Figure 4-12. Complex viscosity from frequency sweep test of DoE formulae 1, 2, 4, 5, 6 and 8 at different temperatures, if G' was dominant curves coloured with grey (1>tan(δ)). 190
Figure 4-13. Complex viscosity from frequency sweep test of DoE formulae 3, 7, 9 and 10 at different temperatures, in theses formulae G' was always dominant (1>tan(δ)). 190
Figure 4-14. E/η in MPa/%Pas of all DoE formulae at 150°C and different frequencies. 191
Figure 4-15. Logarithm the shift factor (aT) against the inverse temperature (1/T in Kelvin), the Arrhenius fit was performed at 150°C. 192
Figure 4-16. Viscosity difference between high shear rate (428.1 rad/s) and low shear rate (0.92 rad/s). 194
Figure 4-17. Glass transition measured from cooling cycles from both DSC (using onset value) and temperature sweep test (using peaks of tan(δ)) and stickiness evaluation of the DoEs filaments. 196
Figure 4-18. Cooling cycle of the DoE filaments DSC traces. 196
Figure 4-19. Effect of the viscosity on the Gears pressure limit. 200
Figure 4-20. Coefficients plots (coefficients scaled and centred) of elastic modulus (left), maximum stress (middle) and yield stress (right) from both 3PB test (top) and TS test (bottom). Non-significant coefficients were removed and confidence level was 0.95, for numerical values see table Appendix 3-1. 201
Figure 4-21. Coefficients plots (coefficients scaled and centred) of strain at maximum stress (left), strain at break from TS test. Non-significant coefficients were removed , For numerical values see table Appendix 3-1. 202
Figure 4-22. Tan(δ) summary fit, coefficients and contour plot, N is the number of the samples (10), DF = degree of freedom. 203
Figure 4-23. Summary of fit plot for the five responses (from left to right; $E/\eta_{150°C}$, maximum stress, strain at break, MFA ratio and stickiness), N is the number of the samples (10), DF = degree of freedom. 204
Figure 4-24. Coefficients plots (coefficients scaled and centred) of DoE responses, non-significant coefficients were removed. For numerical values see table Appendix 3-1. 205
Figure 4-25. Contour plots of the DoE responses, maximum stress from 3PB test (green), strain at break from TS test (red), E/η at 150°C (blue) and Tg_{Rhe} (gray). 206

Figure 4-26. Sweet spots (responses above the defined limits/criteria) at low, high and medium silica content and different MFA and StA ratios. 207
Figure 4-27. Sweet spot plot (left) and design space plot (right) at 14.5% (wt of total) silica showing the space where all criteria were satisfied and failure probability. 208
Figure 4-28. Optimum formula printed on Ender 3 3D printer at 160°C. 210
Figure 5-1. Thermogravimetry temperature profile. 216
Figure 5-2. tablet and caplets design with their dimensions printed using 3D printing. 217
Figure 5-3. First stage workflow for exploring the 3D printing formulation space of AZ-PEO and AZ-HPMCAS formulae. 219
Figure 5-4. 50A50P/S100/T180 immediately after extrusion (left and middle) and after a few hours (right) showing rubber-like behaviour after extrusion that disappeared over time.....224
Figure 5-5. DSC traces of AZ, HPMCAS and AZ-MPMCAS physical mixtures (A), glass transitions and melting values (B) and linear fitting of the melting enthalpy to estimate the drug solubility level in HPMCAS (C). 226
Figure 5-6. DSC traces of AZ, PEO and AZ-PEO physical mixtures (A), glass transitions and melting values (B) and linea fitting of the melting enthalpy to estimate the drug solubility level in PEO (C). 227
Figure 5-7. DSC traces during heating (A) and cooling (B) of the AZ-HPMCAS and AZ-PEO formulae, both Tm and Tg assigned (C) and PEO crystallinity calculated from the enthalpy (D). 228
Figure 5-8. X-ray diffraction patterns of the drug and HPMCAS-based formulae. 229
Figure 5-9. X-ray diffraction patterns of the drug (top), PEO-based formulae on the same day of the extrusion and after 10 days of the extrusion (middle), and PEO samples (bottom) as received and from the melt. 230
Figure 5-10. Regional phase diagram of AZ-PEO and AZ-HPMCAS formulae on 11 HME, Circles with no fill indicate process settings that were not tested, but outcomes can be inferred based on surrounding data. 230
Figure 5-11. Inline low-frequency Raman spectra from the HME die for both AZ-HPMCAS based formulae (top) and AZ-PEO formulae (bottom).....232
Figure 5-12. Low-frequency Raman spectra during cooling of PEO and AZ-PEO formulae filaments immediately after HME extrusion at 180°C, arrows indicated

peaks presented only in PEO (black), only in solid dispersion systems (pink), only in 50A50P (blue) or in both PEO cooling and solid dispersion systems but not in 50A50P (red). 233
Figure 5-13. Mechanical properties of AZ-HPMCAS formulae (line plot) and extracted values (bar charts), namely elastic modulus, maximum stress and strain at break, average values recorded (n=5, error bar = SD), t-test only significant difference (s, P<0.05) added to the graph i.e. all the rest are non-significant. 235
Figure 5-14. Mechanical properties of AZ-PEO formulae (line plot) and extracted values (bar charts), namely elastic modulus, maximum stress and strain at break, average values recorded (n=5, error bar = SD), t-test only non-significant difference (ns, P>0.05) added to the graph i.e. all the rest are significant. 236
Figure 5-15. Storage (G', solid line) and loss (G", dashed line) moduli of AZ-HPMCAS and AZ-PEO filaments from the amplitude sweep test showing linear viscoelastic region. 237
Figure 5-16. Viscosity (top) and tan(δ) (bottom) of AZ-HPMCAS (left) and AZ-PEO (right) based formulae. 239
Figure 5-17. E/η ratios across a range of temperatures for AZ-HPMCAS formulae (solid lines) and AZ-PEO formulae (dashed lines, close to the x-axis). The black dotted line represents the E/η threshold (0.8×10^{-3} MPa/%Pas) found in the previous chapter. 240
Figure 5-18. Buckling of 50A50P/15S/T180 in the 3D printer extruder head from the 3DP-extrudability test at 180°C and 0.5 mm/s. 242
Figure 5-19. 3D printing failure of 30A70P/S15/T180 filament at 180°C nozzle temperature and 0.25 mm/s due to the lack of structural support of the prints, poor solidification and material dragging with nozzle movement (A) Skipped steps on both of the print sides and the histogram of the mini-steps that form the curves per layer (B) An attempt to reduce the mini-steps in the g-code by reducing the number of walls and increasing the number of long lines (C) An attempt to improve layer solidification by printing two caplets and increasing the time between consequential layers (D) best attempt – no walls (E). 246
Figure 5-20. Second stage workflow for exploring the 3D printing formulation space of AZ-PEO and AZ-HPMCAS formulae. 247
Figure 5-21. Die pressure of the 30% (wt%) AZ with 70% (wt%) polymer mixture in the HME at different HME process temperatures. 248

Figure 5-22. In-line low-frequency Raman spectroscopy of different AZ-PEO-HPMCAS ternary formulae compared with AZ drug spectra. 249
Figure 5-23. Off-line XRPD patterns of the different AZ-PEO-HPMCAS ternary formulae. 250
Figure 5-24. DSC traces of AZ-PEO-HPMCAS based formulae during the first heating cycle. 251
Figure 5-25. Stress-strain curve from the three-point bend test of the AZ-PEO-HPMCAS based filaments where solid lines represent the average and the shaded areas are the intervals (n=5), extracted values are shown in Figure 5-25. 253
Figure 5-26. Extracted values namely elastic modulus, maximum stress and strain at break from the three-point bend test (Figure 5-24) of the AZ-PEO-HPMCAS based filaments. Values were averaged (n=5, error bar = SD), ANOVA test only non-significant difference (ns, P>0.05) added to the graph i.e. all the rest are significant. 254
Figure 5-27. 30A(25P75H)/S100/T110 filament fresh extruded and coiled with a diameter of 1.71 ± 0.02 mm. 255
Figure 5-28. Example of HPMCAS mass loss trace from the thermogravimetric analysis at 170°C (graph) and results for pure materials degradation. 256
Figure 5-29. IM-caplets (IM, left) and 3D printing ones (middle and right) with the same volume and surface area. The surface area (SA) and volume (V) for all the caplets are the same. 259
Figure 5-30. Optical coherence tomography 3D scan for IM caplet (left) and 3DP 0.4 mm caplet (right). 260
Figure 5-31. 2D optical coherence tomography scan for top and bottom for IM caplet, 3DP 0.4 mm caplet and 3DP 0.8 mm caplet. 261
Figure 5-32. Dissolution profiles of the IM caplet, 3DP 0.4 mm caplet and 3DP 0.8 mm caplet, five repetation were averaged with error bars representing the standard deviation and the shaded area represents the range (left), optical coherence tomography scan (right top) and cross-section of IM caplet and 3DP 0.4 mm caplet after being soaked. 263
Figure 5-33. Raman spectra of the outer white surface of the IM caplet and 3DP 0.4 mm caplet after being soaked for different time. 263
Figure 5-34. X-ray diffraction patterns of the IM caplet and 3DP 0.4 mm caplet crushed and dry (top) and after being soaked (bottom). 265

Figure 5-35. DSC traces of the IM caplet, 3DP 0.4 mm caplet and 3DP 0.8 mm caplet. 265
Figure 5-36. Dissolution profiles of cylinder shape tablets printed using 0.4 mm nozzle diameter (blue) and 0.8 mm nozzle diameter (red). Lines averaged from three repetitions. 266
Figure 5-37. Mechanical properties from three-point bend test of old and fresh filaments and heated ones (n= 5, line reresponts the average and shaded area the range). 268
Figure 5-38. X-ray diffraction patterns of old and fresh filaments and heated ones. ...270
Figure 5-39. DSC traces of old and fresh filaments and heated ones. 270
Figure 6-1. Formulation diagram starting from single polymer and the potential outcomes with additive interaction on molecular level (first stage) and on particle-matrix level (second stage). 277
Figure 6-2. Hypothesis and future work to relate molecular interactions with mechanical properties and printability. 278
Figure 6-3. Schematic of some of the printer specification that affect variation in the filament performance between different printers. 279

List of Tables

Table 1-1. 3D printing classes according to ASTM and examples of some subcategories with their abbreviations, schematic, material type input and energy input:.....43
Table 1-2. Melocchi et al [52] FFF sub-processes and material requirement for successful print (table taken from literature):.....52
Table 1-3. FFF filament examples produced using soaking method: 55
Table 1-4. FFF filament examples produced using single polymer and polymer mixture approaches:.....58
Table 2-1. Hot melt extruder zones and process temperature (T_p) for each mixture:.....78
Table 2-2. Synopsis of pure component and binary systems produced on the HME and analysed on the TGA, TA, Raman Low frequency, Raman microscopy, texture analyser and Dissolution: 82
Table 2-3. extrudates of EPO and MFA:EPO at different ratios 10:90, 20:80, 30:70 and 40:60 processed at different process temperature from 120 to 170°C:.....89
Table 2-4. Carboxyl to amine group ratio calculation for MFA:EPO formulae calculation details in (Table Appendix 1-3):.....98
Table 2-5. Raman wavenumber (in cm^{-1}) of MFA and EPO peaks assigned to one functional group and their change in the extrudates samples (detailed list of MFA peaks included in the Appendix Table 1-2 part 1 and part 2): 99
Table 2-6. Raman wavenumber (in cm^{-1}) of MFA peaks assigned to multiple functional groups and their change in the extrudates samples: 100
Table 2-7.Glass transition of the MFA:EPO physical mixtures and extrudates produced at different temperature:.....104
Table 2-8. Statistical study for the HME process temperature impact on the mechanical properties for the MFA:EPO extrudates: 109
Table 2-9. Feed-ability test in the 3D printer:.....111
Table 3-1.Temperature profile of MFA:StA samples on the HSM: 124
Table 3-2.Process and die temperature of the polymer:plasticizer formulae:.....125
Table 3-3.Process and die temperature of the MFA:Polymer:Plasticizer formulae, the additional formulae with StA and the EPO:StA formulae:.....126
Table 3-4.Common plasticizers, HSPs values and differences from both the polymer carrier (Ra_{EPO}) and MFA (Ra_{MFA}):.....130
Table 3-5. (Part 1): HSM miscibility study of EPO:Plasticizers physical mixtures:....134

Table 3-6. Miscibility study of the EPO with different plasticizers namely StA, TWN, TEC, PEG4h and PEG4k using three techniques DSC, HSM and film casting: ..136
Table 3-7. Mass loss of the pure components from the thermogravimetric analysis, two methods were used. One step heating to 240°C (A) and Two phases namely heating then holding at high temperature (B): 139
Table 3-8. extrudates appearance of EPO:plasticizer at 95:5 and 85:15 (%wt) ratios and FA:EPO:plasticizer at 20:76:4 and 20:65:15 (%wt) ratios: 140
Table 3-9. Glass transition of EPO-plasticizer at two ratios 5% and 15% and EPO-MFA-plasticizer system as measured from DSC graphs during the first cooling cycle: 148
Table 3-10. Drug, polymer and plasticizers' molecular volumes (MVol in cm^3/mol) as calculated on HSPiP software: 150
Table 3-11. Comparison of StA WAX peaks from the EPO:StA 85:15 extrudate with literature: 157
Table 3-12. Feed-ability test in the 3D printer for MFA:EPO:StA 20:76:4 formula:... 160
Table 4-1. HME conditions for the studied formulae: 165
Table 4-2. DoE sample levels and actual weight: 167
Table 4-3. DoE responses, abbreviations units, power of transformation (Y^c) and limits: 169
Table 4-4. Mass loss (%wt) of the fillers from the thermogravimetric analysis at 20°C/min heating rate: 174
Table 4-5. Circularity of 50% (median, D0.5) of filler particles per volume and per number: 178
Table 4-6. Comparison between three-point bend test (3PB) and tensile strength (TS) in term of overall coefficient of variation ($\boldsymbol{CV}$) and sample to sample variation ($\boldsymbol{CVss}$): 182
Table 4-7. Pressure and torque values from the HME experiment of DoEs filament: .186
Table 4-8. E/η in 10^{-3} × MPa/%Pas of DoE formulae at 6.283 rad/s and different process temperatures: 191
Table 4-9. Arrhenius equation intercept (eq 4-5) and calculated activation energy (eq 4-7): 193
Table 4-10. 3DP-extrudability test of DoE filaments at three temperatures 150°C, 160°C and 170°C using two feeding method manual and mechanical: 197

Table 4-11. 3D printing test of DoE filaments at three temperatures 150°C, 160°C and 170°C: 199
Table 4-12. 3D printing extrudability 100 mm extrudability test at 130°C, 140°C, 150°C and 160°C printing temperature and four printing speed: 209
Table 4-13. 3D printing test of the optimum formula using two printer and different process temperature and printing speed, ten tablets were printed: 210
Table 5-1. Feeding the physical mixtures in the HME: 220
Table 5-2. Die pressure in the HME of the AZ-HPMCAS and AZ-PEO formulae at different process conditions (table order top-bottom followed the running order): 222
Table 5-3. Shark skinning effect evaluation by measuring the amplitude and length of the shark skinning waves using an optical microscope: 223
Table 5-4. Crossover temperature and E/η ratio at 170°C of AZ-PEO formulae: 240
Table 5-5. Crossover temperature, tan(δ) peak and E/η ratio at 110°C, 130°C and 150°C of AZ-HPMCAS formulae: 240
Table 5-6. 3DP-extrudability test of the AZ-HPMCAS formulae at four nozzle temperatures and a printing speed of 3 mm/s: 241
Table 5-7. 3DP-extrudability test of the AZ-HPMCAS formulae at 180°C nozzle temperatures and different printing speeds: 242
Table 5-8. 3D printing attempts of AZ-HPMCAS filaments at 150°C nozzle temperature and 3 mm/s speed: 244
Table 5-9. AZ-PEO-HPMCAS based formulae processability on the HME and the solid-state result at different process temperatures and screw speed: 252
Table 5-10. 3D-printing test for the chosen filament 30A(25P75H)/S100/T110 at 3 mm/s printing speed, 150°C nozzle temperature and using 0.8 mm nozzle: 256
Table 5-11. 3D printing of 30A(25P75H)/S100/T110 at 3 mm/s and 150°C using a 0.4 mm nozzle and a 0.8 mm nozzle: 258
Table 5-12. Weight of IM caplet, 3DP 0.4 mm caplet and 3DP 0.8 mm caplet: 261
Table 5-13. Feedability of an old and fresh filament: 267
Table 5-14. Mass loss of the pure components, pelletised filament and cryo-milled filament: 267

Chapter 1: Introduction in Fused Deposition Modelling: principle, advantages and pharmaceutical applications

1.1. A need for innovation:

Solid dosage forms are the most used system in pharmaceutics because they are easier to handle, manufacture and administer to patients than other forms [1]. Tablets for example can provide accurate doses for the patients, are safe to administer and easy to carry. Pharmaceutical dosage forms used to be produced in pharmacies and doctor's clinics [2]. Then in the18th century, industrial enhancement and mass production transferred pharmaceutical production lines from the pharmacy bench to manufacturing plants. In the mid-19th century, tableting (via powder compression) was invented and dominated the solid dosage forms [2], [3], [4]. However, big manufacturing machines carried challenges when the tablet design or formula are changed leading to a lack of flexibility in the mass production.

The variation in the human's gastrointestinal system can cause changes in drug dissolution and absorption resulting in deviations in the bioavailability and the drug's effect raising the problem of having one formula for different patients [5]. In 2016, the NHS England has announced that the available drugs are effective in only 30-60% of the cases due to human's individual differences [6]. For example, drugs behave differently in patients' bodies as the gender, body mass, age, ethnicity and age change [7], [8], [9]. According to the FDA report in 2013, 75% of the cancer therapy is not efficient, and customized medication is a possible solution [10].

Improving drug performance requires understanding of three pillars: disease, drug, patient. Moreover, the manufacturing requirements should be considered. The formulation and design of the drug product aim to offer the therapeutic dose for specific period of time in the desirable site [11]. Therefore, altering and masking the biopharmaceutical properties of the drug are common practice. For example, improving the bioavailability of low soluble and high permeable drugs requires enhancement of solubility. This group called class II drugs according to the Biopharmaceutical Classification System (BCS) the literature shows various approach to overcome this issue like reducing the particle size, using a salt, complexing with cyclodextrin and amorphisation [12], [13]. Another example of the formulation challenge is prolonging drug release to reduce the applied dose and the fluctuation in the blood concentration during

the day and increase patient compliance. Encapsulating and a matrix of drug-excipients are utilized to modify the release profile [14]. Although changing formulations were effective, the possible drug release profiles were limited using predesigned standard tablet shapes in conventional methods such as tableting and injection moulding. Moreover, changing formulae required intensive study to find different mixtures that meet the manufacturing technique and release criteria. On the other hand, utilizing the design of tablets showed high promise in changing and optimising drug release profile. Mucoadhesive, floating, high-density and swelling systems are used to increase the gastric retention time and overcome the variation in pH, gastric motility, physiology [15]. In addition to the complexity in the tablet design, the shape and size or surface area to volume ratio can be adjusted to modify the release curve [16], [17]. Since, the conventional manufacturing techniques are not sufficient to alter tablet design [18], there is a need for a technique that opens the opportunity for complex structure and a technique that is modular enough to apply changes in the production line without having the mass production limitation. In the last two decades, researchers focused on 3D printing technology as a perfect candidate to unlock these potentials and start a new era in medicine manufacturing [19]. 3D printing techniques and their advantages are discussed in more details later in this chapter.

1.2. Advantages of 3D printing in different scenarios:

3D printing is a promising technology to customise medication, accelerate clinical trials and as a small to medium scale manufacturing process. Personalised medicine is only one potential application of 3D printing. In clinical trials during developing new molecular entities (NME), it is important to provide correct dose and release for safety, tolerability, toxicity, drug efficacy and pharmacokinetics studies. Thus, drug limitation can be defined to help in the decision making of killing the drug or pushing it forward [20]. This section is an exploration of the advantages that 3D printing is providing over the conventional method and how it could be used for designing solid oral dosage forms.

1.2.1. Alter the drug dose:

Adjusting the dose is a common procedure for delivering of many drugs. Most of the doses are given as a function of the body mass, for example, paracetamol dose is 10-15 mg/kg/dose for children and 15 mg/kg for adults below 50 kg [21]. Moreover, the dose

should be changed for patients with liver or kidney failure when their drugs are liver metabolized or renally excreted, respectively. Simvastatin is halved to 5 mg in case of renal disease and the normal dose might be harmful in case of liver disease [22], [23]. The dose adjustments are not limited to the provided reasons.

Different doses can be printed according to each patient requirement using 3D printing technology. Therefore, an effective dose with the minimum adverse effects can be tailored on demand. This can be crucial for drugs with narrow therapeutic window as the effective dose is close to the toxic one. Cancer drugs are ideal examples for opportunity to improve the treatment using this technology. Martinez et al. was able to produce tablets with different shape and size (weight and as a result dose) but same drug release using stereolithography (SLA) 3D printer (Fig. 1-1-a). Types of 3D printing including SLA will be discussed in the next section. The drug release was correlated with the surface area to volume ratio (SA/V) instead of the surface area only. Such a finding allows us to print different drug dose with different shape without altering the drug release [24].

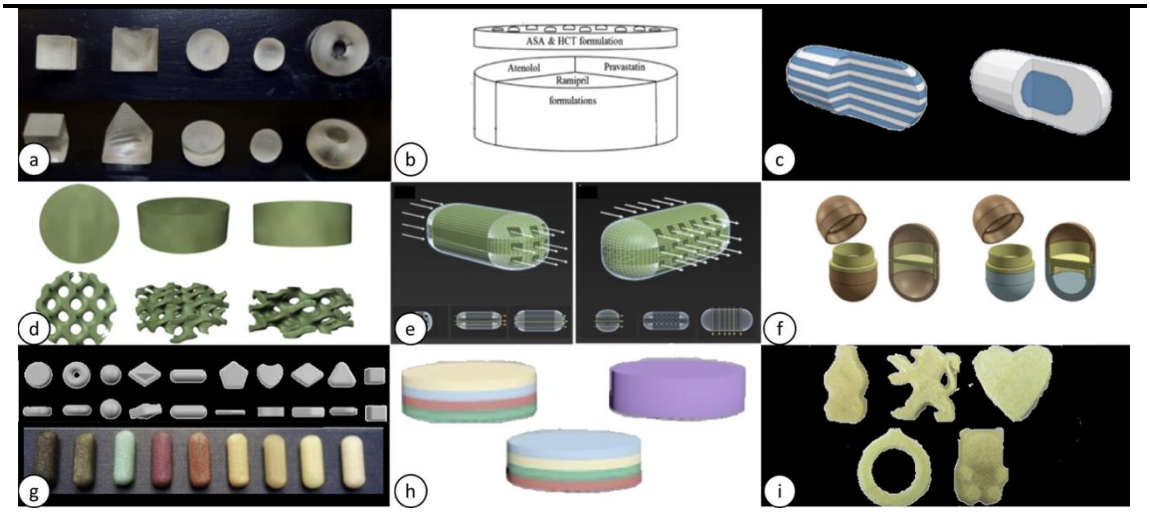

Figure 1-1. Different morphology, size, colour and complexity of printed tablets (all the photos are taken from the original papers). a) tablets with different sizes but similar surface area to volume ratio (SA/V) using stereolithography (SLA) 3D printing (3DP) [24]*. b) Pollypill of five drugs loaded in four compartments, the tablet has dots for distinguishing* [25]*. c) Caplets of two drugs, paracetamol and caffeine, printed by Fused Filament Fabrication (FFF) 3DP in two patterns, the left release both drugs simultaneously and the right delays the one in the core* [26]*. d) tablet with a gyroid shape for improving solubility printed using the selective laser sintering (SLS) 3DP* [18]*. e) Caplets that have channels with different alignments using the FFF-3DP. f) Multi-compartment capsular devices that can contains different drugs or different drug release, the body printed using FFF-3DP* [27] *. g) Placebo tablets with different colours and shapes printed using Hydroxypropylcellulose on FFF-3DP* [28]*. h) Pollypill tablets of four drugs isinopril, indapamide, rosuvastatin and amlodipine printed using FFF-3DP* [29]*. i) Tablets as gummi candies for improving paediatric compliance* [30]*.*

1.2.2. Multiple drug therapy:

Multiple drug therapy is common procedure for patients with chronic diseases or with multiple comorbidities. This therapy can bring better treatment, improving the efficacy and reducing the side effects. However, it increases the number of applied drugs and the complexity of the administration instructions and supply chain. This could be crucial for patients with Alzheimer especially elderly patients who are more likely to have diabetes and hypertension [21]. The main challenge is reducing the number of tablets that patients

take per day to improve compliance and administration. However, the massive number of possibilities of drug combinations is beyond conventional manufacturing capability. 3D printing on the other hand is the best way to print different drugs to get the required doses and release profiles. Khaled et al [25] printed a tablet that contained five drugs for cardiovascular disease (Fig 1-1-b). Predetermined release profiles were obtained, immediate release for aspirin and hydrochlorothiazide and sustainable release for pravastatin, atenolol, and ramipril. The study showed that each drug can release independently as evidenced from the dissolution tests. Another group worked on the same disease but different drugs. They printed a multi-layered tablet of indapamide, rosuvastatin calcium and amlodipine using FFF 3D-printer and poly(vinyl alcohol) (PVA) as a carrier polymer (Fig 1-1-h). The release profile was changed according to the layers' positions [29]. Goyanes et al [26] obtained identical drug release of two drugs, paracetamol and caffeine loaded in PVA, by printing both formulae alternately as multilayers caplet (Fig 1-1-c). A delay in one drug can be achieved by printing the one formulae inside the other a DuoCaplet.

1.2.3. Complex structure:

By utilizing 3D printing technology, dosage forms can be printed in shapes not producible by conventional techniques. This advantage allows the manipulation of product geometry to modify drug release [25], [26]. Fina et al [18] printed paracetamol tablets using SLS 3D printer in a shape of Gyroid improving the dissolution of the drug in comparison with cylindrical shape (Fig 1-1-d). The channels inside the structure provided bigger surface area in contact with the media that passes through the structure. FFF was also used to print channelled caplets. The printed caplets were different in the width and length of the channels (Fig 1-1-e). Faster drug release was obtained with short multiple channels (8.6 mm) in comparison with longer ones (18.2 mm), the acceleration in the release assigned to the reduction in the flow resistance [31] . Maroni et al [27] printed capsules that contain two compartments with ability to have multiple release kinetics (Fig 1-1-f). The capsules produced by FFF 3D printer using hydroxypropyl methyl cellulose (HPMC), HPMC-acetate succinate (HPMC-AS) and Kollicoat IR based formulae, for delayed pulsatile, immediate and enteric release, respectively. Combinations of compartments of the mentioned formulae can be used to get the required release. Producing and utilizing different sizes, shapes and

combinations of cavities in the structure is an advantage of 3D printing technology over conventional ones.

1.2.4. Patient acceptability:

The ability to produce different shapes and sizes with ease allows us to manipulate the shape to improve patient acceptability. Cube, pyramid, cylinder, sphere, disc and torus tablets have been printed with different sizes (Fig 1-1-g). These studies explored the relationship between the geometry and the release and showed the ability to fit the shape and size according to patient preferences [16], [17], [24]. This can be very useful for patients with disabilities to improve their independence and compliance. For example, a smooth oval shape can be customized for patient with dysphagia. Parkinson treatment might be improved if the shape is easy to handle like puffy ended caplet or torus. Goyanes et al [28] conducted a study to understand the picking and swallowing acceptability for tablets with different shape size and colour using FFF 3D printer (Fig 1-1-g). The torus shape was the easiest to swallow and pick. The typical appearance like capsules and cylinder ranked high values. This was attributed to the shape-familiarity. Moreover, the surface structure could be modified for specific purpose, Khaled et al [25] added dots on the surface for distinguishing the tablets by touch. Paediatric treatment can benefit by adopting 3D printing, as this technology can print the colour and the shape that the child likes (Fig 1-1-i). The chewable candy utilized to print indomethacin imitating the Starmix® sweets. Teddy bear, heart, and lion were printed by FFF technology. The bitterness of the drug was masked and immediate release obtained [30].

1.2.5. Prototyping technique:

In addition to the ability to construct complex shapes, the plastic industry utilizes 3D printing to test and visualize designs. Therefore, it was a big leap in prototyping that reduced the development time significantly. From a pharmaceutical perspective, using this technology can reduce development time in preclinical and clinical trials helping to bring the drug to the market earlier. The dose can be modified easily for toxicological studies, also the design is adjustable for the kinetic and formulation studies. Also, coating can be simply applied by adding shell layers masking the drug or modifying the release [20]. The flexibility and efficiency that 3D printing provides during the development stage encouraged companies to adopt this technology like GSK, AstraZeneca, Aprecia and FabRx [32].

1.3. 3D printing a family of many techniques:

3D printing (3DP) is a term applied on different technologies that share the same principle of building the structure layer by layer. It is also so-called Additive Manufacturing (AM), Rapid Prototyping (RP) or Solid Free Form technology (SFF). Each layer is built in two dimensions (X and Y axis) then Z axis changes the position to allow another layer to be added, by repeating this process many times a computer aided 3D structure can be produced.

In general, to create a 3D structure, a design is made defining the dimensions of the structure. Then it is translated to a mathematical representation of replications of specific geometric shapes like quadrilateral or triangular mesh. After that, the produced mesh is processed to generate code scripts such as g-code or z-code. Finally, the scripts are converted to orders by an electronic chip to control the addition process spatially and quantitively. For example, to create a cylinder like shape, the shape can be sketched on Computer-aided design (CAD) software, then exported as .stl file which is the triangular mesh. By using a coding software, g-code scripts can be generated. At the last stage the script lines are read by the instrument as orders to change the X,Y and Z axes, the speed of the material deposition and other controlled parameters depends on the type of 3D-printer [33].

3D printing is a broad umbrella of different instruments that share the same building pattern. However, they have different mechanism for adding the material to the structure. The American Society for Testing and Materials (ASTM) International classifies 3D printing into seven main categories [34]. They are material extrusion, material jetting, directed energy deposition, binder jetting, vat polymerisation, powder bed fusion and sheet lamination [34], [35]. Table 1-1 shows the difference between these classes and the subcategories and schematics.

In general, the machines that are fed from the base are more limited to print a uniform formula. The energy input changes to suit the properties of the added material. From pharmaceutical perspective not all the machines are theoretically able to be used and the available ones have capabilities and limitations. Therefore, understanding the technology is the first step to push these applications forward.

The table does not include all possible subcategories because this work is not to differentiate between all 3D printers but to provide an idea of possible techniques.

Material extrusion 3D printers, are the most used printers in pharma [25], [36], [37], [38], uses temperature to facilitate the extrusion of the softened material from a nozzle. It includes FFF 3D printer which is the main focus of this thesis and will be explained in detail in the coming sections. The Semi-Solid Extrusion (SSE) is different from others in the same class as it uses a paste or thick suspension which loses its water/solvent content to solidify [39]. Material jetting 3D printers use droplets which later solidify by evaporation or polymerisation on the building plate [40], [41]. Direct deposition 3D printers use strong spatial energy to melt metal powder or wire, hence it is not suitable for pharmaceutical application [42].

Binder jetting 3D printers use liquid binder to glue the particles on the powder bed together. This type is used for pharmaceutical applications and the only FDA approved 3D printed oral dosage form, Spritam® are produced using this technique [43], [44]. Vat polymerisation 3D printers use light to induce polymerization reactions, converting monomers or oligomers to solid polymers. The liquid resin consists of oligomer/monomer, a photoinitiator (PI) and additional components. A polymerisation reaction is stimulated by light to convert the oligomers to polymers and solidify the resin. The stereolithography 3D printer (SLA) is utilized to understand the relationship between the shape, size, and volume with drug release [24], [33], [45]. However, the main disadvantage of all photo-polymerisation techniques is the toxicity caused from the radical components, namely the photoinitiator [46]. These active radicals might also cause chemical instability.

All the powder bed fusion machines depend on a laser to move across the X,Y axis and provide heat to bind the material together. The difference between the three types are the feeding material and as a result the degree of melting required to create bonds between the particle. For pharmaceutical purposes, selective laser sintering (SLS) grabbed attention because it can produce high porosity structure [47]. SLS, similar to other the base-based feeding mechanism 3D printers, creates print from a single formula. However, Awad et al [48] was able to overcome this limitation by adding manually the powder for each layer to create pellets consisting of two formulae, a paracetamol one and ibuprofen. However, this manual approach prevents recycling the residual powder (as they have been mixed). Sheet lamination 3D printers of this class are based on stacking and adhering sheets above each other. To the author's knowledge this technique is not applied in drug delivery [49], [50].

For all 3D printers, X and Y resolution is determined by the distance between the printed lines and their thicknesses. While the Z resolution is controlled by the step height and the printed thickness. Changing these parameters will influence the mechanical properties and the porosity of the printed object and as a result the dissolution behaviour. Moreover, adhesion between the layers and lines are also crucial for obtaining the optimum final product properties. Therefore, each layer is added on top of partially cured layer so they weld together. If this process is not sufficient enough, lamination might happen [42].

In this work, we are focusing on the FFF 3D printer and will be discussed in more details later as it is the most used printer and in general the cheapest. The prints do not require post process treatments and are solvent-free making this type easy to operate. Moreover, the acceptable FFF capabilities in term of complexity and resolution and the ability to print multiple materials grasps the attention in pharmaceutical application. Different formulae can be printed with complex geometry and different sizes. However, the main disadvantage of this technique is the heat that the drug experiences and the correlated degradation especially for thermosensitive drugs [51], [52].

Table 1-1. 3D printing classes according to ASTM and examples of some subcategories with their abbreviations, schematic, material type input and energy input:

Class		Examples	Abbr.	Schematic	Material input	Energy input/ process
Material is feed through the head	Material extrusion (MEX)	Fused Filament Fabrication	FFF	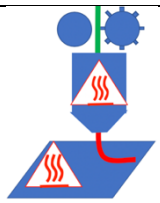	Thermoplastic filament	Heating/ Liquefying then solidification
		Precision Extruding Deposition	PED		Thermoplastic pellets	Heating/ Liquefying then solidification
		Semi-Solid Extrusion	SSE		High viscous/ Semi-solid material	Heating/ Liquid carrier evaporation
	Material jetting (MJT)	Drop on Demand	DOD	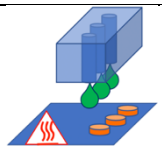	Wax-like material	Heating/ Liquid carrier evaporation
		Material Jetting	MJ	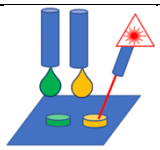	Stereolithographic resin	Laser (Photon) exposure/ Polymerization
		Nano-Particle Jetting	NPJ	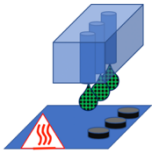	Suspension nano-metal particles	Heating/ Liquid carrier evaporation
	Directed energy deposition	Direct Metal Tooling	DMT	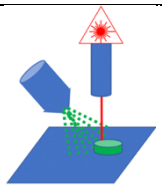	Metal powder	Laser (Photon) exposure/ Melting
		Electron-beam Additive Manufacturing	EBAM	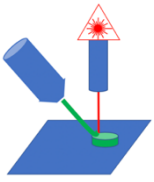	Metal wire	Laser (Photon) exposure/ Melting

Material is fed through the base	Binder jetting	Binder Jetting	BJ	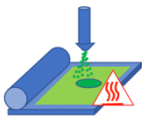	Powder and liquid binder	Heating/ Liquid carrier evaporation
	Vat polymerisation	Stereolithography	SLA	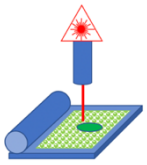	Stereolithographic resin	Laser (Photon) exposure/ Polymerization
	Powder bed fusion	Selective Laser Sintering	SLS	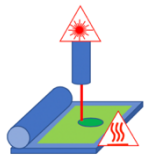	Thermoplastic polymers	Laser exposure/ Particles sintering
		Direct Metal Laser Sintering	DMLS		Powder contains metal	Laser exposure/ Particles sintering
		Selective Laser Melting	SLM		Metal or ceramic	Laser exposure/ Particles Melting
	Sheet lamination	Laminated Object Manufacturing	LOM	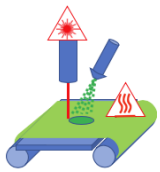	Laminates and binder	Heating/ Liquid binder evaporation (Laser for cutting)
		Ultrasonic Additive Manufacturing	UAM	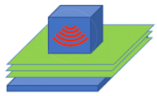	Laminates	Ultrasonic/ Welding

1- Table references [34], [38], [42], [43], [47], [53], [54].

2- Fused Deposition Modelling (FDM) is the Stratasys trademark for FFF type printers.

3- In BJ and LOM, the binder can contain drug to increase the drug load.

4- All powder bed 3D printers use roller to level the powder at same height.
5- ZipDose technology, an BJ 3D printing, is used by Aprecia Pharmaceuticals to produce Spritam, the only FDA approved 3D printed tablets.
6- In LOM, the adhesive material could be activated by heated roller.

1.4. Building quality:

Quality, safety and efficacy are always important concerns for pharmaceutical products. Adopting new technologies carries a lot of challenges especially in terms of meeting regulatory requirements. In 1992, Dr Joseph M. Juran introduced the Quality by Design (QbD) approach to replace the old quality by testing one [55]. In the early 2000s, the U.S. Food and Drug Administration (FDA) began to incorporate QbD principles into pharmaceutical development [56]. In 2013, FDA obligated the QbD approach on a manufacturer for new drug applications except for generic drugs [57]. QbD is a proactive and systematic approach based on scientific analysis and risk management to build product quality across the product life cycle. "Beginning with the end in mind", QbD involves understanding of the product and process requirement and identifying the building blocks to produce the quality, gathering knowledge across the development activities [58]. Other regulatory agencies like The Medicines and Healthcare products Regulatory Agency (MHRA) added the QbD approach in their requirements and the International Council for Harmonization (ICH) supported and promoted it [59].

Due to 3D printing modularity, QbD can be implemented as the final product attributes such as the release and the drug dose can be controlled by changing the geometry of the tablet design [60]. However, there is a need for knowledge-gathering and understanding of the limitation of these new processes. Many researchers have seen this gap and utilised QbD implementing tools like design of experiment (DoE), risk assessment tools, and design space definition. Crișan et al [61] used FFF 3D printer and developed tablet of Diclofenac Sodium:Polyvinyl Alcohol (50:50, wt%). From the risk analysis, they were able to define both the Quality Target Product Profile (QTPP, the desired characteristics) and Critical Quality Attributes (CQA, the measurable properties). Figure 1-2 shows Ishikawa diagram (fish-bone diagrams) that provided representation of material critical attributes and critical process parameters that affect CQA. Three parameters with high CQA impact were selected for further evaluation using DoE. DoE is a statistical tool to investigate the relationship between parameters and the responses.

The chosen parameters were tablet design, tablet size and layer height. While the responses were drug content, the disintegration time and the drug percentages released in 5 min. Then the "design space" and the plot of the probability failure were defined to predict process parameters (optimum condition) that give operational flexibility to keep the system within predefined limits.

Than et al [62] studied indomethacin release from FFF-3D printed tablet by changing the ratios of the formulation which consisted of mixture of hydroxypropyl cellulose, Kollidon VA64 and Soluplus. They found the optimum formulae utilising the DoE. Dos Santos et al [63] also studied the drug release of an FFF-3D printed tablet changing the drug Dexamethasone percentage (5% to 10%, wt%), mannitol percentage (0% to 10%, wt%) and infill from 50% to 100%. Pires et al [64] used the DoE for a. wide range screening study of printing parameters including infill pattern, printer brand, layer height, temperature, printing speed, shape, size, infill density and number of tablets in each run. The last three were the most significant factors on mass, mass variation, printing time and porosity which were taken for optimisation in a further DoE study. Palekar et al [65] utilised the DoE to study the effect of the infill percentage and the tablet size on the drug release. Henry et al [66] also studied 3D printing parameters infill, overlap, number of shells, layer height and layer pattern on CQA like the mechanical properties, dimensions, weight, porosity and dissolution.

Although these papers used DoE established good knowledge about 3D printing process (except Than et al [62] focused on the impact of the formulation) and the impact on the CQA of the final product, the formulae printability was studied using traditional empirical trial and error approaches or by changing one variable at a time. This thesis will focus on the formulation part to achieve a printable formula as it is the bottleneck in the process during drug development on FFF-3D printing. This is because pharmaceutical polymers are not optimised to provide the necessary rheological and mechanical properties for processing. The challenges to formulate 3D printing filament (the FFF 3D printer ink) will be discussed in more detail in the next section.

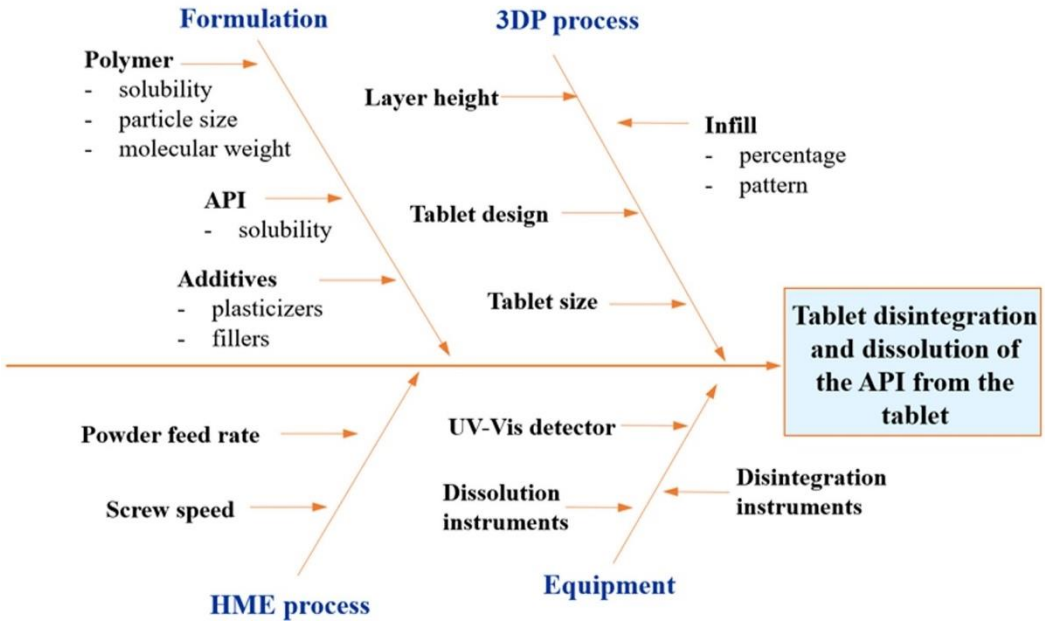

Figure 1-2. Ishikawa diagram material critical attributes and critical process parameters that affect tablet disintegration and dissolution (Figure taken from literature [61]).

1.5. FFF 3D printer ink/filament:

1.5.1. FFF 3D printing machine in details:

Fused Deposition Modelling (FFF), known as a fused filament fabrication (FFF), is advantageous in comparison with other 3D printing techniques for customizing purposes and microscale factories as it is a solvent-free and powder-free process, small machine, relatively cheap and no post processing required. However, there are some drawbacks for FFF-3DP for example unsuitable for heat-sensitive drugs and the difficulties to produce a printable filament with the desired attributes. Therefore, material properties and process parameters are discussed in this thesis aiming to improve the understanding of drug formulations for FFF filaments.

The FFF printer originally came from the plastic industry. It was invented in 1988 by Scott Crump and patented a year later. In 2009 the patent expired, and different parties helped in significantly reducing the machine's cost [51]. Many developers and companies have improved and produce FFF 3D printers. These rapid changes expand the open-source library of the machine [67] but also increase the variabilities between the printers. As a result, the performance of machines varied, and optimisation process should be

done for every printer and each filament. Moreover, the printability might change with machine development; for example, “Flexion Extruder” is able to print rubber-like filaments by applying support for the filament through the whole path. Such filaments were highly likely to fail a few years ago. The 3D printing community and startups have provided many solutions, such as dual extruder 3D printers and increased gear sizes to improve force transferring from the gear to the filament. Additionally, the literature also showed other examples of feeder modifications, such as extending the stiff tubes before the gears, to improve the consistency of filament feeding and partially overcome poor filament mechanical properties [68].

The working principle of the FFF is mainly liquefying plastic-based filament then depositing the material on a 2D layer. By accumulating the layers above each other a 3D structure can be built. Therefore, the machine contains deposition elements and movement ones. To deposit the material, a gear pushes the thermoplastic filament of constant diameter into a liquefier. In the liquefier, the filament is turned into a highly viscous liquid that extrudes under stress through a nozzle typically sized between 0.2 and 0.8 mm (Fig 1-3) [69]. Nozzle sizes below 0.2 mm cause high resistance to flow and potential clogging, while sizes above 0.8 mm result in thicker extruded strings that reduce print precision and detail. The material is deposited on a predetermined place controlled by stepper motors on the X, Y and Z axis. These motors are split between the building plate and the head of the printer, considering the building volume and the vibration caused from the motions. The motors are preferable on the smaller parts (usually the printer head) since it causes smaller dead-zones on the building plate. On the other hand, the motor causes more vibration with each movement when it carries the heaver weight. The print accuracy is limited by the nozzle size and motor steps on the three dimensions. For successful printing, the nozzle should be at a height from the building plate that allows efficient addition. Furthermore, the deposited material should not solidify totally to allow the next layer to adhere on it and avoid lamination. A consistent flow should be achieved to obtain the same radius for deposed filament. Usually, the printed structure does not have a smooth surface because the layer edge takes a stepped ridge shape controlled mostly by Z resolution and nozzle diameter.

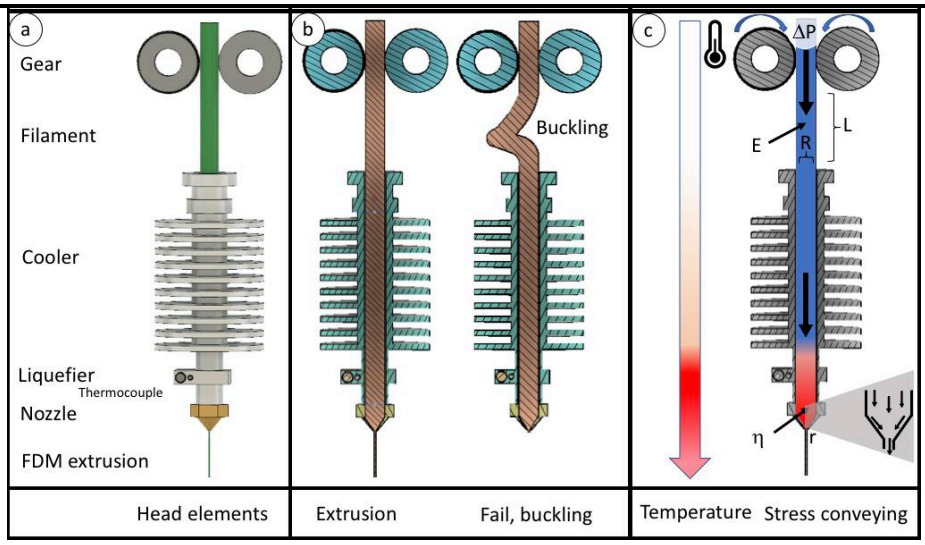

Figure 1-3. FFF head extrusion mechanism. a) The head elements. b) cross section during the extrusion process in both cases success and fail. c) Temperature and stress across the filament where ΔP is the pressure applied through the gears, L is the length between the gear and the liquefier, R is the filament radius, E is the elasticity of the filament at specific temperature and feed rate, r is the nozzle radius and η is the viscosity of the liquified filament at specific temperature.

1.5.2. From process parameters to material properties:

The ejection force is created by the gears and transferred through the solid part of the filament that works as a piston to push the liquified portion out of the nozzle. The viscous molten filament polymer resists flow and requires a stress/pressure to be pushed. However, the solid part of the filament might not be able to tolerate the generated pressure between the gears and the molten polymer in the nozzle causing it to break or buckle. Therefore, the applied pressure must be high to enable liquid flow but lower than critical tolerance of the filament (Fig 1-3-b). This can be summarised in two equations [70]:

$$\sigma_c = \mathrm{E}_\gamma \left(\frac{\pi}{4}\right)^2 \left(\frac{R}{L}\right)^2 \qquad \text{Eq 1-1.}$$

Where σ_c is buckling force or the highest force can the filament tolerate before deformation. E_γ is the young's modulus. R is the radius of the filament and L is the distance between the rollers and the liquefier.

$$\Delta P_c = \left(\frac{8\pi}{k}\right)\left(\frac{\eta_a Ql}{r^4}\right) \qquad \text{Eq 1-2.}$$

ΔP is the stress needed to push that material through the liquefier. k is scaling factor that is used to correlate the values of the viscosity obtained from analyser with the one in the FFF liquefier. η_a is the apparent viscosity of the liquified filament at specific temperature obtained by using capillary rheometer. Q is the volumetric flow rate. r and l are the radius and the length of the liquefier, respectively.

To print, buckling force must be higher than the pressure required to flow the molten material i.e. $\sigma_c > \Delta P_c$. Venkataraman arranged the two equations as follow:

$$\frac{E\gamma}{\eta_a} > Ql\left(\frac{L}{Rr^2}\right)^2 \qquad \text{Eq 1-3.}$$

Therefore, the $\frac{E\gamma}{\eta_a}$ ratio is the minimum critical value for a formula to be extrudable on the 3D printer. From a formulation point of view this relationship (Eq 3.) can act as a guide to improve new drug formulae. It also helps in understanding the role of the additives in the system. Since the equation splits the process parameter and the feedstock filament properties, engineering improvement on the 3D-printers can be done for specific filament. The nozzle radius is the most critical parameter since it is raised to the power four.

Temperature and flow rate can be adjusted to obtain reliable and reproducible performance for accurate drug dose. The relationship between the viscosity and the shear rate and temperature is not linear in polymer-based mixtures and it is complex to model. However, the shear thinning behaviour of the feedstock is assumed to follow a power-law viscosity model [69].

$$\eta = K(\dot{\gamma})^{n-1} \qquad \text{Eq 1-4.}$$

η is the viscosity. $\dot{\gamma}$ is the shear rate. n and K are power-law fit parameters. Many other models were developed in plastic and ceramic industry to understand the process more [69], [71].

Models for heat capacity (c_p), location of melt, feed velocity and nozzle radius, shape and angle, can be found in the literature [69]. Welding, die swell and geometrical quality can be also found [71]. Such models are useful for optimizing the process keeping in mind assumptions that are made. However, the previous equations mainly Eq 1-3 are

used to understand the role of the additives in improving filament extrudability in the 3D printer. Venkataraman et al [70] tested different filaments and found the ratio E_γ/η_a of the printable filaments lies between 3×10^5 to 5×10^5 s^{-1}.

Understanding the process helps to identify the material property requirements. Melocchi et al [52] provided comprehensive review of quality consideration on 3D printing with focus on FFF. The review also reflected experts' opinion and decisions on FFF 3DP sub processes and material requirement for successful print (table 1-2). The process divided into 3 sub-processes: filament supply, feeding and nozzle extrusion and layer by layer deposition and solidification.

Table 1-2. Melocchi et al [52] FFF sub-processes and material requirement for successful print (table taken from literature):

FDM process requirements, relevant material/filament properties and characterization methods.

FDM PHASE	REQUIREMENT	PROPERTY	CHARACTERIZATION METHODS
Filament supply	The filament must be spooled in order to be supplied to the printing facility	Mechanical: - Limited stiffness (limited Young Modulus) - High strength (high stress and strain at yielding/ fracture)	- Tensile tests - Bending tests
Feeding and nozzle extrusion	The filament must be pushed into the heating chamber		
	- Without breaking within the feeding gears	Mechanical: - High strength (high stress and strain at fracture)	- Tensile tests - Bending tests - *Ad hoc* tests (*e.g.* Repka-Zhang test)
	- Without slippage within the feeding gears	Mechanical: - Adequate resistance to yielding to compression (high yield stress) / hardness	- Compression tests - Bending tests - Hardness tests
	- Without breaking after the feeding gears and in the nozzle	Mechanical / rheological: - Adequate buckling resistance (*e.g.* Venkataraman criterion)	- Tensile tests - Rotational/capillary rheometry
	- Without excessive deformation between the feeding gears and the nozzle	Mechanical: - Limited dependence of young modulus on temperature	- Dynamic mechanical analysis
		Thermal: - Limited thermal conductivity/diffusivity	- Thermal analysis (Laser flash method)
	The material must flow		
	- Through the nozzle	Rheological: - Adequate viscosity	- Melt flow index - Rotational/capillary rheometry
	- At a controlled rate	Dimensional: - Circular filament cross section - Constant filament diameter	- X and y axes laser measurements, *e.g.* Ovalization
	- Without degradation	Thermal/chemical: - Degradation temperature higher than process temperature	- Thermogravimetry
	- Without instability	Rheological	- Capillary rheometry
Layer by layer deposition / solidification	Deposited layers		
	- Must have the desired size	Rheological: - Adequate extensional viscosity	- Extensional rheometry
	- Must weld to each other	Physical/rheological: - Adequate macromolecule interdiffusion	- Rotational rheometry (as indirect method)
	- Must keep their shape (control over expansion or contraction post extrusion)	Mechanical: - Limited dependence of young modulus on temperature	- Dynamic mechanical analysis
		Thermal: - Adequate thermal conductivity/ diffusivity	- Thermal analysis (Laser flash method)

1.5.3. Filament production

1.5.3.1. Printable formula:

The filaments in FFF are mainly produced from thermoplastic polymers. For pharmaceutical application the polymers are loaded with the active pharmaceutical ingredient (API) creating a solid dispersion system. The polymer drug dispersion matrix can take three states. The drug can exist in the molecular level which is known as solid solution. While if it is in amorphous or crystalline state in the polymer, it creates amorphous solid suspension or crystalline solid suspension, respectively. These three thermodynamic states are the results of the drug load, the polymer-API interaction, polymer properties and the energy input to create the system. The environmental conditions can lead to changes between these forms according to the stability and time in the exposed ambient conditions [72], [73], [74]. These systems have different physicochemical properties in comparison with the pure polymer. For example, a higher drug load has a stronger plasticizing affect, reducing the glass transition (Tg) of the system. The reduction is bigger with stronger polymer-drug interaction [75]. This interaction causes changes in the Tg, viscosity and mechanical properties. Therefore, understanding the phase diagram of the formula will help in understanding how to improve its printability as well as using other drugs with the same excipients.

To produce FFF filaments hot melt extrusion (HME) is used. HME is a melting technique used originally in plastic industry. The principle is based on transferring the materials in a barrel using screw that rotates while gradually increasing the barrel temperature (Fig 1-4). The energy is added to the system as shear stress from the screw and heat from the barrel. This energy helps to diffuse the drug molecules in the polymer and increase the enthalpy of the system to liquify the ingredients. The HME instrument can have many configurations. The barrel is divided into thermal zones that can be controlled. The machine could also have single or twin screws. The three main roles of these screws are conveying, mixing and compressing the material, which can be modified by changing the screws' elements. Moreover, the twin screw machines can be intermeshing or non-intermeshing and co- rotating or counter-rotating. The rotation speed also controls the residence time and the applied shear stress [76], [77].

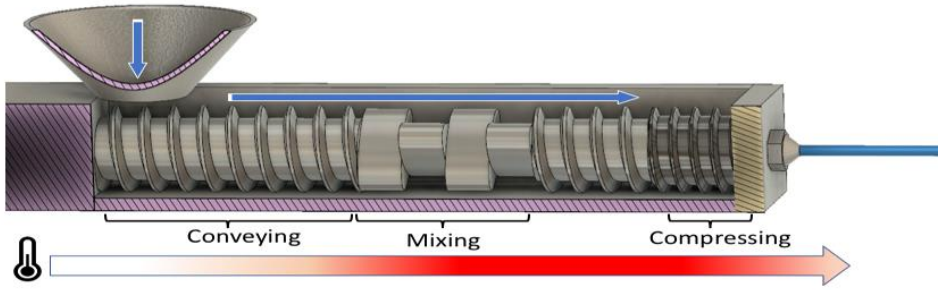

Figure 1-4. Hot melt extruder schematic showing the screw elements and the thermal change in the barrel. The material is passed and mixed through the barrel and extruded to produce filament.

In order to load the filament with drug, two main approaches are used. The first one is to soak the filament in a drug solution for a period of time, so the drug diffuses in the polymer matrix. The concentration of the drug in the solution plays an important role in the final drug content. Therefore, the solvent should dissolve high amount of solute (drug), but without deforming the polymer or changing its properties. The filament is then dried. Although this method using a prepared 3D filament, it re-introduces solvent in the preparation and usually results in a low drug load. Table 1-3 shows example studies that used this method, the drug load ranged between 0.06 to 1.9% [78], [79], [80]. The miscibility of the drug in the polymer (in these cases it was PVA) might have an impact on the drug load, since high miscibility causes easier diffusion. These papers, however, did not discuss the miscibility of the drug in PVA.

Table 1-3. FFF filament examples produced using soaking method:

Polymer	Drug (wt%)	Preparation	Printing T°C	Comment	Ref
PVA	0.06% 5-ASA	15g/50 mL EtOH- for 24h	210°C	-	[79]
	0.25% 4-ASA		210°C	50% degradation during printing	
PVA	0.29% Fluorescein	2%w/v ethanolic solution-24h	220°C	Different infill 0% to 100%	[78]
PVA	1.9% Prednisolone	Saturated methanolic solution-24h	230°C-250°C	Linear relationship between design volume and drug load	[80]

Abbreviations: Polyvinyl alcohol (PVA), Aminosalicylic acid (ASA)

Another way to load the filament with drug is to extrude the drug polymer mixture. The chosen polymer carrier should have good mechanical properties or formula enhancement should be carried out. HPC, PEO, Poly(L-lactic), Polycaprolactone and PVA for example can be used without additives [81], [82], [83]. Such formulae are preferable due to their simplicity, but the optimum drug release might not be achieved (Table 1-4). The literature shows different strategies for improving the mechanical properties by changing the formulae. Zhang et al [84] tested single polymer filament loaded with 30% w/w drug on texture analyzer using the 3-point bend test. This test measures the breaking distance and the stiffness of the single and binary systems. Based on the results of this test, 1:1 mixtures of the polymers used as carriers and the improvement in the mechanical properties was obtained. Finally, different ratios of the mixtures with disintegration agent (Kollidon CL-F) were extruded. Tablets were printed and drug release studies were conducted [84]. Sadia et al [31] used Eudragit EPO in their study. The polymer first plasticized with Triethyl citrate and the highest plasticized ratio was chosen. In order to optimize the strength of the filament a filler of Tri-calcium phosphate was added. Finally, the portion of the filler replaced with the equivalent amount, about 10%, of different drugs. All the formulae were crystalline solid

suspension except with captopril. In both Zhang et al [84] and Sadia et al [31] studies the plasticizing affect of the drug was minimal due to the lack of drug-polymer interaction or the dependance on the additional plasticizer.

Therefore, most of the studies formulation can be narrowed down to one of these three approaches filament soaking (table 1-3), single polymer approach (like Sadia et al [31], table 1-4) and polymer mixture approach (like Zhang et al [84], table 1-4). However, a mixture of polymers (two or more) with plasticizers, fillers and other additives could be found. Although a printable filament was achieved, the formulae were very complex and hard to replicate using other drugs. From QbD perspective, complex formulae have more branches in the Ishikawa diagram and as a result more parameters to control and study in the DoE. Alhajjaj et al [85] used the Hansen Solubility Parameters (HSPs) of the ingrediants (drug, polymers potential additives like tween 80). The difference between the HSPs predicts the miscibility liklyhood. If the difference between two ingrediants indicates miscibility; below 7 $MPa^{1/2}$ is miscible, between 7-10 partially miscible and above that is not miscible. After extuding the potential polymers, they used ones that had good mechanical propertitise as property enhancer for the others and mixture of (drug-polymer-mechanical properties enhancer-plasticizers) was extruded and used in FFF.

Samaro et al [86] used different grades of ethylene-vinyl acetate (EVA) a block copolymer to produce a printable filament. Different polymer grades showed different printability due to different ratios of ethylene (E) and vinyl acetate (VA). Since each block carries the properties, this approach can be categorised under polymer mixture approach.

Elbadawi et al [87] used machine learning to predict FFF printability and both HME extrusion temperature and FFF printing temperature. A total of 614 formulations were used in the model, 75% in the training set. The model succeeded in predicting filament characteristics with 67% accuracy and process temperature with absolute error below 9°C. Using prediction reduce the development time and cost of new printable formulae.

As discussed above filler and plasticizer can be added to improve filament stiffness and ductility, respectively. In the polymer mixture approach, one polymer would be ductile while the other stiff to complement each other. Other additives might be added such as lubricant and disintegration agent [88]. Lubricant might help in reducing the work that is

needed to push the material out of the 3D printer nozzle and in the HME [51]. Mannitol was used as a disintegration agent to create micro channels in the structure and increase the drug release rate [89].

Table 1-4. FFF filament examples produced using single polymer and polymer mixture approaches:

Polymer	Drug (wt%)	Additives (wt%)	T°C$_{(HME/3DP)}$	Comment	Ref
Eudragit EPO	10 % Felodipine	10%Tween 80 + 15%PEG 4000 + 15%PEO WSR N10	100° C/150° C	Ingredients interaction and their impact on drug release	[85]
Soluplus		15%Tween 80 + 10%PEG 4000 + 15%PEO WSR N10	120° C/150° C		
PVA		22.5%Tween 80	130° C/150° C		
Ethyl cellulose	Placebo	10% TEC	160°C/200° C	Insoluble polymer	[81]
Eudragit RL	Placebo	15% TEC	120°C/160°C	Insoluble polymer	
Kollicoat IR	Placebo	12% Glycerol	160°C/180°C	Promptly soluble polymer	
PEO WSR N10	Placebo	-	[90]65°C/160°C	Promptly soluble polymer	
Eudragit L	Placebo	20% TEC	160°C/160°C	Enteric soluble polymer	
HPMCAS (AQUOT-LG)	Placebo	5% PEG 8000	180°C/200°C	Enteric soluble polymer	
PVA	Placebo	5% Glycerol	190°C/225°C	Swellable/erodible polymer	
Soluplus	Placebo	10% PEG 400	120°C/200°C	Swellable/erodible polymer	
HPMC (Affinisol 15cP)	Placebo	5% PEG 400	160°C/200°C	Swellable/erodible polymer	
HPC (Klucel LF)	Placebo	-	165°C/180° C	Swellable/erodible polymer	

PVA	≈ 0.59% Aripiprazole	-	170° C/190° C	Oro dispersible film	[82]
PVA	5% Budesonide	-	170° C/190° C	Overcoated with a layer of enteric polymer	[90]
PEG 6000	5% pantoprazole (thermo-labile drug)	-	≈ 48°C/55°C	2.85 mm filament	[83]
	10% pantoprazole	-	≈ 47°C/54°C	2.85 mm filament	
	5% pantoprazole	5% sodium polyacrylate	≈ 49°C/58°C	2.85 mm filament	
PEG 20000	10% pantoprazole	-	≈ 49°C/60°C	2.85 mm filament	
Poloxamer 407	5% pantoprazole	-	≈ 42°C/60°C	2.85 mm filament	
Kollidon VA64	10% pantoprazole	25% triethyl citrate	≈ 55°C/85°C	2.85 mm filament	
PVP K12	10% pantoprazole	15% triethyl citrate	≈ 49°C/79°C	2.85 mm - Drug is partially miscible in PVP	
	10% pantoprazole	20% triethyl citrate (TEC)	≈ 49°C/78°C	2.85mm-partially miscibility	
	20% pantoprazole	20% triethyl citrate	≈ 50°C/86°C	2.85mm-partially miscibility	
	30% pantoprazole	20% triethyl citrate	≈ 48°C/87°C	2.85mm-partially miscibility	
PVP 40000	10% Dipyridamole or Theophylline	12.5% TEC + 27.5%Talc	90°C/200-220° C	Low HME process makes it potential for thermo-labile drug.	[91]
Eudragit EPO	12.5% Captopril, 5-ASA, Prednisolone	37.5% tri-calcium phosphate (TCP) + 3.2% TEC	90-100°C/135°C	Talc can be replaced with TCP.	[92]

	or Theophylline				
PVA	4% Paracetamol	-	180°C /180°C	Different tablet shapes and SA/V ratio.	[16]
HPMCAS-LG	5% Paracetamol	15% Methylparaben NF + 5% Mg stearate	80°C/190°C	Superior plasticization efficiency of Methylparaben and it causes delayed drug release verses other plasticizers (TEC, PEG, citric acid monohydrate and acetyltributyl citrate). Magnesium stearate was lubricant, reduction in extrusion temperature was noticed. In 50% drug load lower amounts of methylparaben was needed due to the plasticizing effect of the drug.	[93]
HPMCAS-MG	5% Paracetamol		80°C/190°C		
HPMCAS-HG	5% Paracetamol		80°C/190°C		
HPMCAS-LG	50% Paracetamol	5% Methylparaben NF + 5% Mg stearate	110°C/180°C		
HPMCAS-MG	50% Paracetamol		100°C/185°C		
HPMCAS-HG	50% Paracetamol		110°C/180°C		
HPMC E	30% Paracetamol	19.5% CMC E + 5% Kollidon CL-F (disintegrator)	180°C/200°C	Sustainable release formulae.	[84]
HPMC E	30% Paracetamol	19.5% HPC EF + 5% Kollidon CL-F	180°C/200°C	Sustainable release formulae.	
HPMC E	30% Paracetamol	19.5% HPC LF + 5% Kollidon CL-F	180°C/200°C	Sustainable release formulae.	
HPMC E	30% Paracetamol	15% Soluplus + 5% Kollidon	180°C/200°C	Sustainable release formulae.	

		CL-F			
HPMC E	30% Paracetamol	15% Eudragit L + 5% Kollidon CL-F	180°C/200°C	Sustainable release formulae.	
CMC N14	30% Paracetamol	15% Eudragit L + 5% Kollidon CL-F	180°C/200°C	About 9% release after 24h.	[84]
Eudragit E	12.5% Hydrochlorothiazide	3.25% TEC + 37.5 Tri-calcium phosphate	90°C/135°C	Channelled tablet	[31]
Eudragit E	12.5% Hydrochlorothiazide	3.25% TEC + 33.5 Tri-calcium phosphate + 4% disintegrant	90°C/135°C	Disintegrants used were Polyplasdone-XL, Primojel, Explotab, Primellose or Croscarmellose sodium Ac-Di-Sol	
Eudragit RL100	Deflazacort Nanocapsules loaded in the tablet by soaking	20% Mannitol + 10% PEG 6000 + 6% TEC	110±5°C/170°C	Mannitol can be replaced with Avicel® PH 301	[88]
poly(ε-caprolactone) (PCL)			65±5°C/170°C		
Eudragit RL	5% Quinine	-	55°C /155°C	Polymer drug prepared by solvent casting. Then used as a feedstock for the HME.	[83]
Polycaprolactone PCL		-	47°C /53°C		
Ply(L-lactic) PLLA		-	140°C /164°C		
Ethyl cellulose		35% triacetin	59°C /145°C		
Kollidon VA64	3% Ramipril	10% Mannitol + 20% PEG	70°C /90°C	Mg carbonate provides alkaline group	[89]

Kollidon VA64: Kollidon 12PF (3:2)	3% Ramipril	1500 + 2% Mg carbonate	65°C /90°C	to protect from plasticizer and solubility enhancer.	
Kollidon VA64: Kollidon 12PF (1:1)	3% Ramipril		65°C /90°C	The formula contained Kollidon 12PF gave faster release.	
Tecophilic SP-60D-60	60% Theophylline	-	150°C /150°C	Milled and unmilled metformin were used to see the impact of particle size on the formulae. Other Polyurethanes can be used like Tecoflex EG-72D, EG-80A, Tecophilic SP-93A-100 and TG-2000.	[94]
Tecoflex EG-72D	60% Metphormine	-	180°C /180°C		
Eudragit RL PO	30% Theophylline	7% Stearic Acid + 0.4% Anhydrous colloidal silica (Aerosil)	140-180°C/180°C	Filament diameter optimization using DoE on the HME. Stearic Acid can be replaced with 5% or 10% PEG 4000.	[95]
Eudragit RL100	50% Theophylline	5% TEC	120-130/170°C	Eudragit E formula was the fastest release. The RS is less hydrophilic, which led to slower release from RS:RL formula.	[96]
Eudragit RS100	50% Theophylline	7.5% TEC	110-130/150°C		
Eudragit E	50% Theophylline	3.5% TEC	110-130/140°C		
Eudragit RL + RS(1:1)	50% Theophylline	5% TEC	120-130/150°C		
HPC-SSL	50% Theophylline	4% TEC	110-125/160°C		
HPC	-	2, 5 or 10% PEG	150-165/210°C	Capsule shell.	[97]

Kollidon® VA64 + AffinsiolTM15cP (1:1)	10% or 20% Haloperidol	-	150° C (Die 170° C)/210° C	Polymers' miscibility and stability were conducted.	[98]
HPC	Placebo	21.25% Mannitol + 5% Mg stearate	130°C/140°C	Shape acceptability study, Torus found the easiest to pick and swallow	[28]
Kollicoat IR	Radiolabelled Fluorodeoxyglucose (^{18}F- FDG) manually added to the capsules.	20% Mannitol + 20% Methylparaben NF + 10% Talc + 5% Mg stearate	145°C /155°C	Capsule shells from enteric coating ingredient (Kollicoat IR). But, it released the drug in the stomach.	[99]
Klucel EF		21.5% Mannitol + 5% Mg stearate	130° C /160°C	-	
Aqualon N7		20% Methylparaben NF + 5% Mg stearate	120° C /160°C	Delay in the release is observed.	
HPMCAS-LG		15% Methylparaben NF + 10% Talc + 5% Mg stearate	105° C /175°C	Capsules trapped in the stomach for unknown reason.	

Abbreviations and commercial names: Eudragit (methacrylic acid copolymer), TEC (Triethyl citrate), EC (Ethyl cellulose), PVA (Polyvinyl alcohol), HPC (Hydroxylpropyl cellulose, E/L/S viscosity grades), HPMC or Hypermellose (hydroxypropyl methylcellulose), PEG (Polyethylene glycol), PEO (Polyethylene oxide), HPMC-AS (Hydroxypropyl Methylcellulose Acetate Succinate), Soluplus (Polyvinyl caprolactam–polyvinyl acetate–polyethylene glycol), CMC (Aqualon carboxy methyl cellulose), Kollidon® VA64 (Polyvinylpyrrolidone-vinyl acetate copolymer), Aqualon N7 (Ethyl Cellulose), Kollicoat® IR (polyvinyl alcohol-polyethylene glycol graft copolymer), Benecel™ (HPMC E).

1.5.3.1. Formula other consideration:

Some researchers focused on the impact of the formulation on drug release. Solanki et al [98] studied the drug release of Haloperidol in the polymers before they tested the formula for development. However, the best polymer (Kollidon® VA64) was not printable by its own. Therefore, a polymer with better printability (Affinsiol™15 cP) was added. In order to evaluate the miscibility and stability of the formula, film casting of the binary and ternary mixtures was prepared using the solvent evaporation method. The films were kept in a humid and hot environment and evaluated using optical microscope, DSC and XRPD. A solvent-based method also reported in the literature. A polymer-drug film prepared by solvent casting, were used as a feedstock for hot melt extruder to produce filaments [100].

Muñiz Castro et al [37] analysed 968 formulation from the literature using machine learning algorithms. Surface area/volume, weight, infill percentage, pH and volume of dissolution media, drug solubility were used to predict FFF printed formulations. The best model predicted dissolution release (wt%) after 20, 50 and 80 minutes with an error about ±24.29 min.

The FFF filament should have consistent diameter usually 1.75 mm or 2.85 mm. The change in the diameter leads to change in the dispensed amount of the filament per second from the nozzle. Therefore, controlling the filament diameter during the preparation in the HME is crucial. Polymer extrudate swells after leaving the HME die. Researchers used different nozzle diameters to obtain the desired filament, 1.8 mm [81], 1.70 mm [94] and 1.55 mm [98]. Pulling force was also applied to reduce the impact of this phenomenon. For example Kempin et al [83] pulled the filament from the die using a motor with rotation cylinder. Other papers used the design of experiment (DoE) on the HME parameter to control the filament diameter [95].

1.5.4. Engineering the problem

Due to the difficulties of producing new formulae companies and researchers tried to engineer the 3D printer to print powder without the need to make filament. Pellets or powder can be fed into direct powder extrusion 3D printing to deposit molten polymer-drug mixture and produce a printed tablet [86], [101]. Triastek, Inc developed Melt-Extrusion Deposition (MED®) which is capable of printing powder directly at speed up

to 150–200,000 tablets per day [102]. CMAC integrated 3D printer also capable to produce tablets from powder. The work in this thesis does not aim to modify the printer instead exploring the potential of FFF 3D printer and understanding its limitations. Therefore, these machines are not considered or explored in detail here.

1.6. Some material and analytical method background:

In the current work, several drug models and polymers were used. The formulae were studied using different analytical techniques. Therefore, in this section a brief background for these materials and analytical techniques are explored. This section does not discuss the method and how experiments were conducted, instead it explores the general use of the materials and devices and basic principle of the devices.

1.6.1. Materials:

1.6.1.1. Mefenamic acid (MFA):

Mefenamic acid (MFA) is a nonsteroidal anti-inflammatory drug and an analgesic for mild and moderate pain. Its chemical structure is shown in Figure 1-5. The usual oral dose for adults is 500 mg delivered in one tablet or two capsules (250 mg each) [21]. MFA is class II drug in the biopharmaceutical classification system (BCS), meaning it is low soluble high permeable drug. Hence, researchers tried to improve solubility using different techniques like particle size reduction, β-cyclodextrin complexes, creating solid dispersion systems and many others. Solid dispersion system improved MFA solubility and wettability [103] and stabilized the drug in amorphous state (disoriented form) [104].

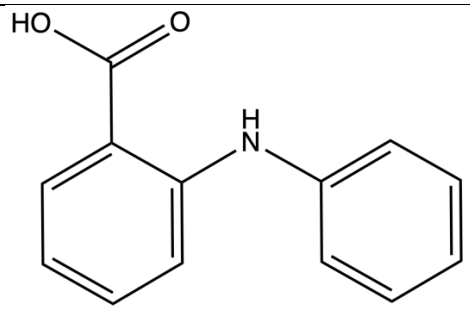

Figure 1-5. Chemical structure of mefenamic acid.

1.6.1.2. Methacrylate-Copolymer Eudragit EPO (EPO):

Eudragit EPO is one of the methacrylate-copolymer family. It is used for tablet coating, taste masking, and most importantly in producing solid dispersion systems with acidic

drugs [105]. Figure 1-6 shows EPO chemical structure. EPO's pKa is 10.0 (Evonik ®) making it soluble in aqueous acidic solution (pH < 5.5) [104].

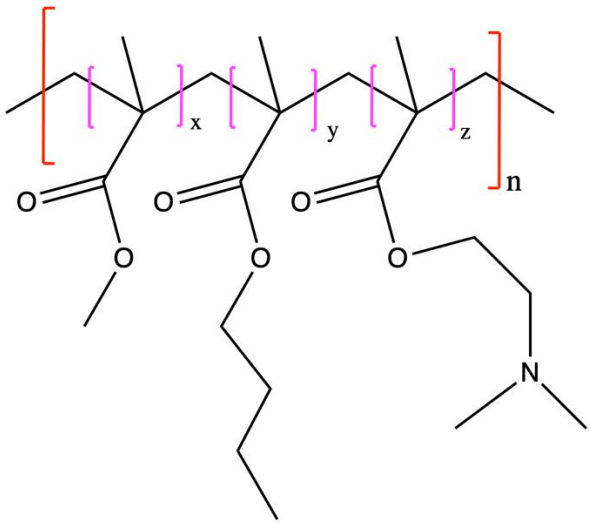

Figure 1-6. Chemical structure of Eudragit EPO.

1.6.1.3. AstraZeneca model drug, AZD0837 (AZ):

AZD0837 is a drug developed by AstraZeneca as coagulation factor II (thrombin) inhibitor for preventing and treatment of thromboembolic diseases. Previously injection molded caplets were produced using PEO as carrier to achieve prolonged release [106]. Another polymer carrier was also explored namely hydroxypropyl methylcellulose (hypromellose) acetate succinate. Data on AZD0837-HPMCAS was shared via email but has not been published publicly. Chemical structure is not available.

1.6.1.4. hydroxypropyl methylcellulose (hypromellose) acetate succinate (HPMC-AS):

HPMCAS is widely used in pharmaceutical application to produce controlled release dosage forms. There are three grades of HPMCAS; LG, MG and HG [107]. The main difference between them is the ratios of acetyl and succinyl groups providing different sensitivity for the dissolution media pH (Figure 1-7). The opening pH are 5.5, 6, 6.5 for LG, MG and HG grades, respectively [108].

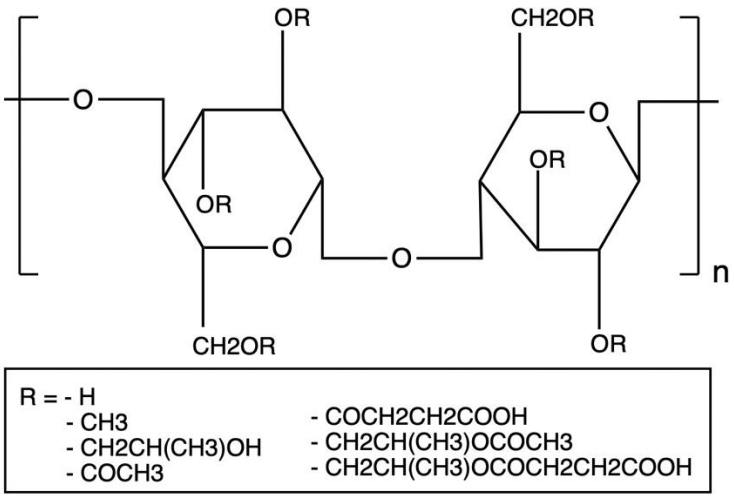

Figure 1-7. Chemical structure of HPMCAS.

1.6.1.5. Polyethylene glycol/oxide (PEG/PEO):

Polyethylene glycol/oxide is widely used in pharmaceutical applications as a carrier in solid dispersion systems, lubricant in tableting and medical devices, vehicle in dermatological applications, base excipient in suppositories, viscosity modifier for parenteral drugs and many others [109]. Figure 1-8 shows the chemical structure of PEG/PEO. It is available at wide range of molecular weights from 100 g/mol to 10 million g/mol [110]. It is worth to note that the name PEO is used for the molecular weight above 20,000 g/mol [111]. The molecular weight can affect the viscosity properties, solubility, wettability, physical state and mechanical properties [109].

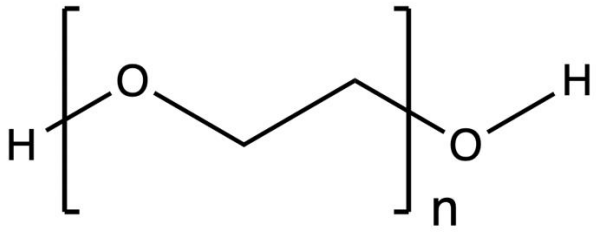

Figure 1-8. Chemical structure of PEO.

1.6.2. Analytical techniques:

There are many analytical techniques that studies the physical state of the filament (as solid dispersion system), molecular interaction of the materials, mechanical properties, viscosity, appearance, thermal behaviour, dissolution and many others. This section is exploring the principle of some of these techniques without the intension to cover them all.

1.6.2.1. X-ray diffraction techniques:

Xray diffractometry is widely used technique in pharmaceutics to study the structure of solid materials. The principle of the technique is to direct an x-ray beam on the sample at a specific angle. The photons interact with the sample (are diffracted) then the photons interfere with each other and are detected by the instrument. The process is repeated at range of angles. If a repeated structure is present in the sample, the corresponding diffraction behaviour is emphasised causing a sharp peak in the collected pattern. While lack of arranged structure causes an amorphous halo (broad peaks) [72], [112].

Wide-angle X-ray diffraction (WAXD) is used to collect information about the atomic and crystal structural levels of materials. In crystalline materials, a repetition of the unit cell with its atomic and plane distances leads to distinctive x-ray peaks for each crystal arrangement or polymorph. According to Bragg's Law, diffraction occurs when the path difference between X-rays scattered from different planes in a crystal is an integer multiple of the wavelength. Amorphous material lacks the periodic structure and sharp X-ray diffraction peaks [112]. For example, on solid dispersion application, Igor Ivanisevic studied the physical stability of 12 amorphous solid dispersions, three of them showed instability using wide angle x-ray diffraction. The sharp peaks appeared after storing under ambient condition indicated the drug crystallisation [113].

If small angle is used bigger structures (nano scale) can be detected. Therefore, small angle x-ray diffraction is used to characterise the materials on nanoscale level [114]. For example, Nagul et al studied the separation of plasticizers and carriers from polymer inclusion membranes using small- and wide- angle x-ray diffraction (SAX and WAX) measurements [115].

1.6.2.2. Thermal behaviour analytical techniques:

Differential Scanning Calorimetry (DSC) is a powerful technique that can measure the release and the uptake in the heat energy of a sample during a controlled change in the temperature. This allows detecting physical state change like melting, crystallisation of polymer, chain unfolding and quantitatively evaluating the heat change associated with it. The DSC device measures the difference in the heat flow between sample (Figure 1-9-q_s) and empty reference (Figure 1-9-q_r), which are exposed to identical temperature profile over time. When an endothermic or exothermic event occurs the heat flow

changes (reduced or increased, respectively) and appears in the final curve (Figure 1-9-Δq) [116]. Some DSC devices can perform thermogravimetric analysis. Thus, weight change can be detected and associated with DSC curve if possible [117].

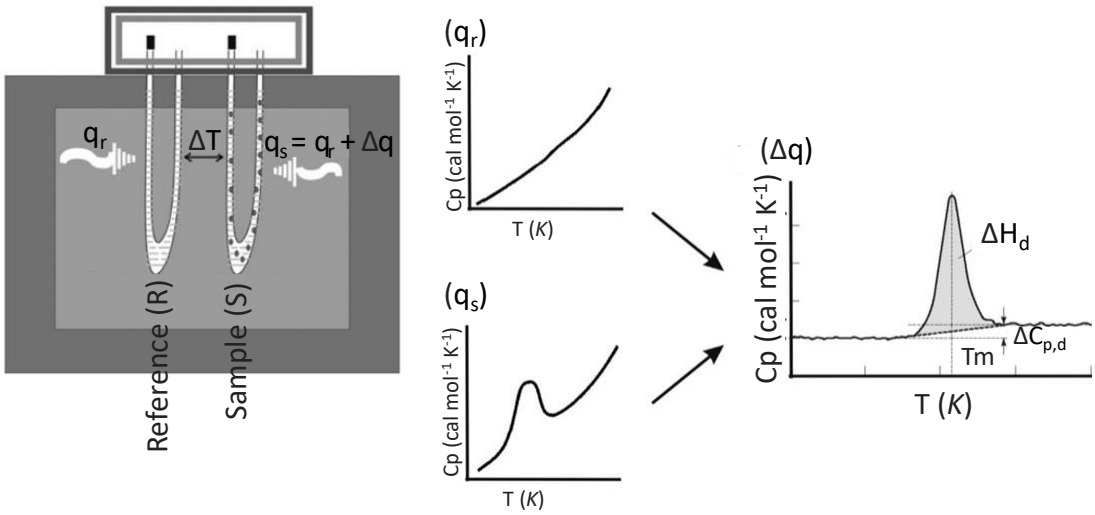

Figure 1-9. Schematic of Differential Scanning Calorimetry showing the principle of the measurement (copied from the literature [116]).

Loss on drying device is a scale with controlled heating chamber to measure the mass change over time. However, it is a scale only i.e. not capable of measuring heat flow like DSC.

1.6.2.3. Texture analyser:

Texture analyser consists of force transducer (moving arm and a load cell), probe and stage (Figure 1-10). It can records force (load cell), distance (traveling distance of the arm) and time. One of the variables is controlled and the other two are measured to obtain force-deformation curve (can be converted to stress – strain curve). The test profile ideally mimics the real-life situation for example applying controlled force, controlled deformation rate or measuring changes after certain time frame. Moreover, wide range of probes and stages are used to apply the test profile to different sample shapes and orientations [118], [119].

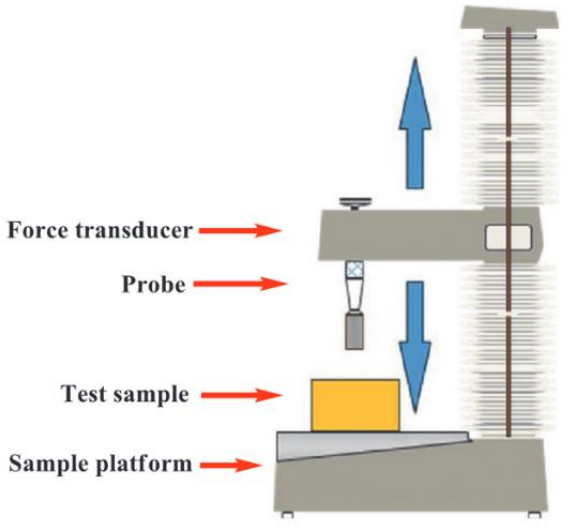

Figure 1-10. Schematic of texture analyser components (copied from the literature [119]*).*

1.6.2.4. Rotary rheometer:

The rheometer measures the deformation and the flow of a material (Figure 1-11). Similar to the texture analyser; deformation, force and time can be measured. However, the deformation in the rotary rheometer is rotational. The amount of rotation applied can vary, from very low (0.01 rad/s) to very high (up to 500 rad/s), depending on the material and the shear rates required. To study the rheology at different temperature equipment can be equipped with a thermostat [120]. Common methods include steady shear tests, oscillatory tests, and creep tests. The main limitation of the rotational rheometers is the difficulty of performing high shear rate measurements, which can be achieved in a capillary rheometer.

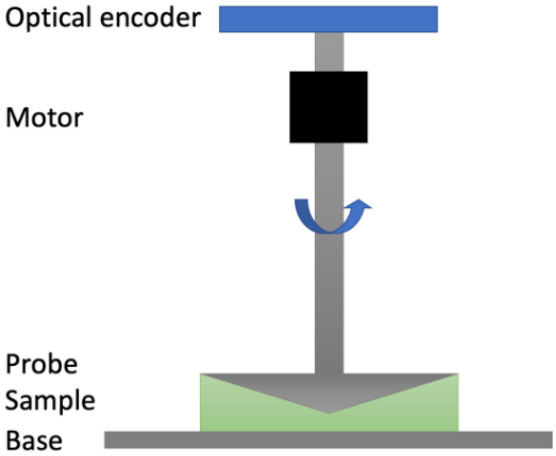

Figure 1-11. Schematic of rotary rheometer.

1.6.2.5. Optical coherence tomography (OCT):

OCT is a non-invasive imaging technique that depends on using a monochromatic light source (Figure 1-12) to capture micrometre-resolution, cross-sectional images. The light splits into reference light and incident light; the last then reflects from the sample. Based on the reference and reflected light interference the depth of the layers can be measured [121]. OCT can be employed to see the 3D printed layer adhesion and alignment and compare it with the digital version created in the slicer software or with other print produced at different settings. Additionally, if the refractive index of the material is known or calculated, OCT can measure the depth of each layer at microscale level. Therefore, the OCT provide subjective and objective evaluation for the 3D printing quality.

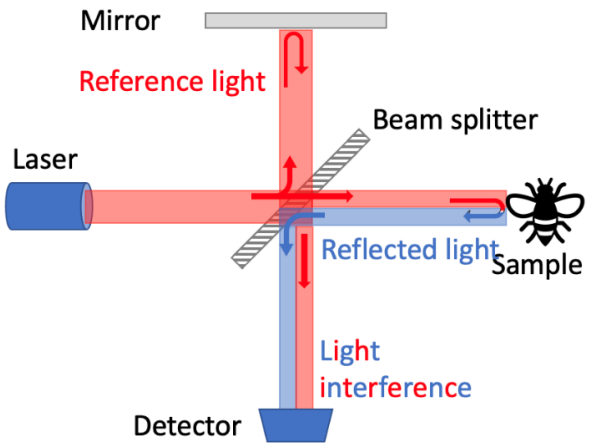

Figure 1-12. Schematic of optical coherence tomography (reproduced [122]).

1.6.2.6. Raman spectroscopy:

Raman spectroscopy is a non-destructive technique that provides information about the chemical structure, polymorphism, and molecular interactions. When a laser beam hits a sample, most of the light is reflected elastically (same energy), which is called Rayleigh scattering, which is not informative chemically. However, only a small quantity (>0.0001%) is scattered inelastically (different energy) and is called Raman scattering [123] (Figure 1-13). The Raman peaks are associated with specific vibrational modes of molecular and functional groups, which are sensitive to molecular arrangement and crystallinity. Therefore, Raman spectroscopy is used to detect changes in the material's physical state that occur during various processes, such as melting in hot melt extrusion (HME), storage, and stability after exposure to ambient conditions. Raman instruments can be used individually for offline analysis, attached to production techniques like HME, or combined with optical microscopy to map a sample.

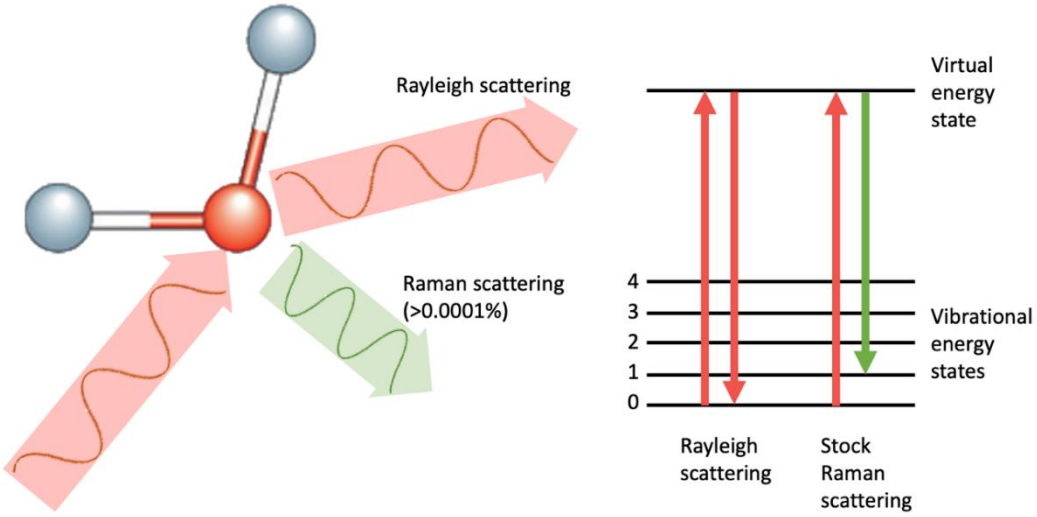

Figure 1-13. Schematic representation of energy transitions in Raman spectroscopy (reproduced [123], [124]).

Aims and objectives:

Despite the efforts in developing new 3D printing filaments, much of this work has relied on a trial-and-error approach. The complexity of formulations often results in a lack of comprehensive studies that cover the entire process from material selection to filament development. Additionally, it is difficult to transfer findings and knowledge across the literature due to the differences in printer specifications used. Therefore, this research adopts a systematic approach to developing 3D printing filaments and using various mechanical and rheological tests to evaluate filament properties and correlate these properties with their behaviour during printing.

The study aims are:

- To explore different drug-polymer combinations for FFF-3D printing filament for pharmaceutical applications and address the challenges in single and polymer blend approaches and understand their formulation space.
- To evaluate the usefulness of the rheological and mechanical properties of the filament for its printability.
- To define the 3D printing limitation and associate these limitations with critical filament properties.
- To explore prediction tools to speed up formula development and reduce material and time requirement to develop new 3DP-filament.

The study objectives are:

1- Analyse the mechanical and rheological characteristics of several drug-polymer blends for use in medicinal FFF-3D printing filament.
2- Examine the molecular interactions of drug-polymer combination using HSPs and Raman spectroscopy.
3- Investigate the physical state of filaments using DSC, XRPD, and Raman spectroscopy to determine how it relates to material behaviour.
4- Identify the limitations of 3D printing and correlate printer specification with critical filament properties.
5- Explore the successful and failure spaces in the formulation space for both single polymer and polymer mixture approaches to address challenges and find printable filaments.

6- Determine the plasticizing effect of different plasticizers on drug-polymer systems and their effect on glass transition reduction.
7- Finding the balance between the drug and excipient ratios of mechanical and rheological properties for a printable filament.
8- Using DoE and HSPs as prediction tools to speed up formula development and reduce material and time requirements to develop new 3DP-filament.

This page is left empty.

Chapter 2: Mefenamic acid filament, single polymer approach: Binary system Drug-Polymer, mefenamic acid Eudragit EPO

2.1. Introduction

This chapter investigates the Fused Filament Fabrication (FFF)-3D printing formulation space using the binary mixture of mefenamic acid as a model drug and Eudragit EPO as a polymer carrier. A range of MFA:EPO physical mixtures were prepared from 0:100 to 40:60 (wt%) drug load and extruded to form extrudates and filaments using a twin-screw hot melt extruder. The extrudate's solid-state properties were then evaluated using a range of techniques DSC, XRPD, Raman microscopy and inline Raman low frequency. In addition, the impact of drug load and process temperature on the filament mechanical properties and intrinsic dissolution rate were examined. These analyses were then evaluated to determine the best filament for further development.

Figure 2-1 identifies physical mixture, extrudate, filament and formula terms used in this chapter. The physical mixture indicated the powder mixture fed into the HME. Extrudate indicated the material that left the HME regardless of its shape, mechanical properties or printability. The term filament was used for the extrudates that had ~ a 1.7 mm diameter and tested on the 3D printer regardless of its printability. The term formula referred to a composition of materials at specific ratios. While the molten formula was used for the molten mixture in the HME and 3D printer heads and the rheometer.

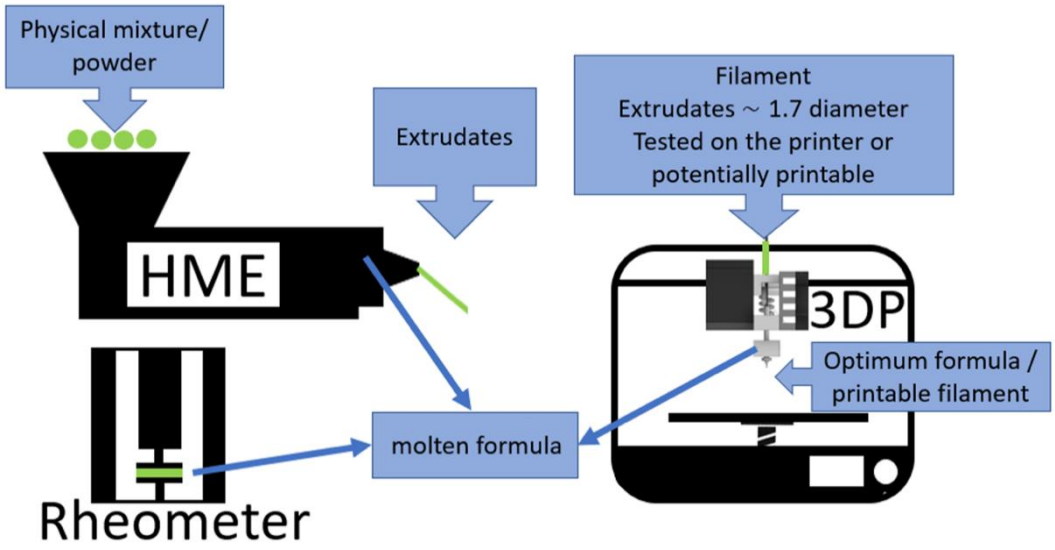

Figure 2-1. Diagram for the extrudate, filament, formula and physical mixture terms used in this thesis.

To satisfy the study objectives, this chapter was designed to answer the following questions:

1. What is the effect of drug concentration and process temperature on the mechanical properties of MFA-EPO extrudates?
2. If a drug plasticizes a polymer matrix, would increasing the drug concentration improve the ductility (strain at break) of brittle polymer?
3. How does the phase diagram relate to extrudate properties? Is there a preferred method to produce the phase diagram?
4. How does brittle matrix break, would the behaviour change by increasing drug load?
5. Is there a printable combination in the formulation space? if not, which one is the best for further development?

2.2. Materials and Methods

2.2.1. Materials

Mefenamic Acid (MFA) was purchased from Sigma-Aldrich (M4267, Riedstr, Steinheim, Germany). Eudragit EPO (EPO), an amino methacrylate copolymer, was kindly donated from Evonik company (Kirschenallee, Darmstadt Germany Evonik Nutrition & Care GmbH). N, N-dimethylformamide and methanol were from Alfa Aesar (Lancaster, UK). The intrinsic dissolution reagents and materials on Sirius inform

were sodium hydroxide pellets (Sigma-S5881 ≥98%, Sigma-Aldrich Gillingham, UK), sodium phosphate monobasic monohydrate (Sigma-71504), sodium phosphate dibasic anhydrous (Sigma-04276), Sodium chloride (VWR-27810.295, VWR, Lutterworth, UK) and Ethanol (VWR-20821.330, VWR, Lutterworth).

2.2.2. Methods

2.2.2.1. Filament and extrudate preparation:

2.2.2.1.1. Hot melt extrusion

Each EPO:MFA mixture (150 g, drug ratio: 0, 10, 20, 30 and 40%, wt%) were mixed using the Pharmatech MB015 AB Blender (Pharmatech, Coleshill, UK) and the Intermediate Bulk Container (IBC) head. The blending speed, agitator speed, blend time, agitator time and agitator delay time were 25 rpm, 500 rpm, 20 min, 19 min and 30 sec, respectively. The polymer and the polymer blends were extruded using a Thermo Scientific® Process 11 twin screw extruder (Thermo Electron/Karlsruhe, GmbH) at a screw speed of 100 rpm. The screw configuration, as found in the literature [125], consisted of elements arranged in the following sequence: 14 feed screws, 6 mixing elements, 7 feed screws, 10 mixing elements, 13 feed screws, and a discharge element, which was used in this study. The powders were fed at 0.1 Kg/hr using Mini Twin (MT-S) Loss In Weight (LIW) Brabender Twin Screw Feeder (Brabender Technologie, Germany). The starting process temperature (T_p) (Table 2-1) was 150°C, which was then decreased in 10°C increments until the extruder failed i.e. torque exceed 90% of the maximum torque, 12 Nm. During experiments room temperature was maintained at 20°C. Samples were collected at each process temperature using a conveying belt to obtain filaments with similar diameters. The belt speed and its relative position to the HME die changed to obtain extrudates with diameters between 1.5-2 mm. Only 40% (wt%) drug loading was extruded at 170°C.

Table 2-1. Hot melt extruder zones and process temperature (T_p) for each mixture:

Formulae		Zone							Die	Unit
		2	3	4	5	6	7	8		
Eudragit EPO	-	20	100	‹—— (T_p = 150 or 140) ——›						°C
MFA:EPO	10:90	20	100	‹—— (T_p = 150, 140 or 130) ——›						°C
MFA:EPO	20:80	20	100	‹—— (T_p = 150, 140, 130 or 120) —›						°C
MFA:EPO	30:70	20	100	‹—— (T_p = 150, 140, 130 or 120) —›						°C

MFA:EPO	40:70	20	100	‹—— (T_p = 170, 150, 140 or 130) —›	°C

2.2.2.2. Solid state study and molecular interaction

2.2.2.2.1. Low frequency Raman Spectroscopy:

To obtain pure component spectra, evaporation crystallisation experiments were performed with Methanol (MeOH) and Dimethylformamide (DMF). MFA (50 mg) was added to 1 mL of solvent in a sample bottle and the mixture heated slightly to ensure complete dissolution. The lid was opened, and the bottle left overnight at 60°C to permit solvent evaporation. Another separate MFA sample was heated to 200°C for 30 min to ensure the transformation of MFA from Form I to Form II [126]. All samples produced were analysed on the same day. Samples were analysed using the Terahertz Raman (THz-Raman) to obtain the spectra with simultaneous form confirmation performed using the X-Ray Powder Diffraction, Bruker D8 Advance II diffractometer (Bruker Corporation, Massachusetts, USA). This was achieved by taking two portions from the same batch of the produced product and analysing them on both machines.

The THz-Raman probe was (Ondax Inc., USA) and was coupled with a RNX1 Raman spectrometer unit (Kaiser Optical Systems Inc., USA). The spectra were collected between Raman shift 0 to 3500 cm^{-1}. The exposure time and accumulation were 3 and 2 sec, respectively. All spectra were smoothed and baselined using the Whittaker smoothing method on Pharma MV software (Weight = 20, Smoothing 80). Raman spectrometer unit was RNX1 (Kaiser Optical Systems Inc., USA).

For crystallinity detection during extrusion, in-line THz-Raman measurement was acquired by attaching the spectroscopy probe to the HME customised die, see Bordos et al. [127]. After two months storage (sealed high density polyethylene bags, at room temperature, approximately 25ºC) all the extrudates samples were re-analysed off-line.

2.2.2.2.2. X-ray Powder Diffraction (XRPD):

Pure components, physical mixtures and extrudates were tested on the XRPD for crystalline form identification. XRPD data was collected on a Bruker D8 Advance II diffractometer with the following experimental setup: range 4-35° 2θ (Cu Ka 50 kV 50 mA) with a 0.015° 2θ step size and 1 s per step count time. After two months storage all samples were re-analysed.

2.2.2.2.3. Microscopy Optical and Raman:

Samples were examined using the Optical Microscopy (Leica DM6000 M F5, Leica Microsystems, Germany) to check the homogenous appearance.

Raman microscopy was performed using a Horiba Xplora Raman Microscope from Horiba Scientific John Yvon (Horiba Ltd., U.K.) and used to check potential sample phase separation. Acquisition conditions were optimised to achieve a spectra with minimal noise interference for the raw MFA and EPO. The acquisition time was 10s with an accumulation setting of 2 and collection range of 50-3500 cm^{-1}. The laser used for this experiment was 532 nm. The grating, filter, slit and hole were 2400 Gr-mm, %25, 50 µm and 500 µm, respectively. All peaks were then assigned and the Raman shift evaluated. Five replicate spectra for pure components and extrudates were collected. The data was presented in a normalised form [0-1], and smoothed and baselined using Penalized least squares method on Python [128]. An identical setup was used for the samples to check the polymer-drug interactions on molecular level. The microscope helped to focus the Raman laser and collect the spectra from the bulk and any potential phase separation, 10X and 50X magnifications were used. Multiple spectra were collected for the bulk and separated areas.

2.2.2.3. Thermal analysis

2.2.2.3.1. Differential Scanning Calorimetry (DSC):

Differential Scanning Calorimetry (DSC) was performed using a Netzsch STA449 F1 Jupiter (NETZSCH-Gerätebau GmbH, Wolverhampton, West Midlands, UK). Analysis was carried out using Aluminium closed pierced lid pans between 0 and 240°C (above MFA melting point) for two cycles at heating and cool rates of 20°C/min. All samples were analysed in duplicate and glass transitions were measured as an onset according to the tangent method. The upper temperature of 240°C was chosen to ensure it is above the melting point of the drug but below the decomposition temperature of the materials. The high heating rate was used to minimize the time at high temperatures, reducing the risk of thermal degradation. The first heating cycle was intended to produce the solid dispersion system, while the second heating cycle was used to check the DSC curve of this system.

2.2.2.3.2. Thermogravimetric analysis (TGA):

Thermogravimetric Analysis (TGA) was carried out using a Netzsch STA 449 F1 Jupiter® (Netzsch, Germany) to measure mass loss with the sample's temperature. The

sample (7-8mg) was tested in duplicate with a temperature profile from 0°C to 300°C and heating at 20°C/min. An empty sample pan was measured as a control, enabling the highest mass fluctuation (maximum – minimum) in the range of the interest (130-230°C) to be measured. Results at temperatures below 130°C were not analysed to avoid instrument fluctuation at the start of the measurement and evaporation of the trapped solvent. Samples were run in duplicate. Measurement error was below 0.011 mg, which was calculated from maximum and minimum mass change of empty pans. A list of pure components and extrudates tested is presented in table 2-2.

2.2.2.3.3. Vapour pressure calculation:

Mefenamic acid sublimation was reported previously in the literature with the vapour pressure (P) of MFA form I measured between 356 to 398 Kelvin (82.85-124.85ºC) [129]. The literature data was analysed to determine the linear relationship between $1/T_k$ and log (P), described by the Clausius-Clapeyron equation. The equation is Log (P) = $0.043(1/T_k)-18.756$ (R^2=0.9983, P in Pascal). Then extrapolation was applied to calculate the MFA vapour pressure values for the HME process temperatures.

Table 2-2. Synopsis of pure component and binary systems produced on the HME and analysed on the TGA, TA, Raman Low frequency, Raman microscopy, texture analyser and Dissolution:

Sample		Powder mixtures	HME process temperature (°C)				
			120	130	140	150	170
MFA	-	●♦▲	-	-	-	-	-
EPO	-	●▲	-	-	■●▲	■▲	-
MFA:EPO	10:90	♦	-	■●▲	■●♦▲	■▲	-
MFA:EPO	20:80	♦	■▲	■▲	■●♦▲	■▲	-
MFA:EPO	30:70	♦	■♦▲	■●♦▲	■●♦▲	■♦▲	-
MFA:EPO	40:60	♦	-	■▲	■●♦▲	■▲	■●▲

Legend: Extrusion, in-line Raman low frequency and texture analyser (■), HSM and TGA (●), Dissolution (♦), XRPD and Raman microscopy and off-line Raman low frequency (▲).

2.2.2.3.4. Hot stage microscopy (HSM):

Hot stage microscopy (HSM) was performed using a HSM Leica DM2700 M optical microscope (Leica Microsystems, Milton Keynes, UK) equipped with Linkam LTS420 Hot Stage and T95 Linkam temperature controller unit (Linkam Scientific Instruments Ltd., Surrey, UK). A temperature profile from room temperature (20°C) up to 200°C at 20°C/min was analysed, before cooling back to room temperature. All extrudates processed at 140°C and all extrudates at MFA:EPO 30:70 ratios were tested (see Table 2-2).

2.2.2.5. Formulae performance

2.2.2.5.1. Mechanical testing using Texture analyser (TA):

Filament mechanical properties were tested on a Texture Analyser TA-XT (Stable Micro Systems, Godalming, UK). The test set up used in this experiment was taken from previous published work [130]. Filaments with a length of 2 cm were tested using a mini 3-point bend rig on the texture analyser (Figure 2-2). Digital callipers

(Axminster.co.uk, 0.01 mm) were used to measure the length and diameter of the samples, which were placed centrally on the two lower support beams with a gap of 8.07 mm. The upper blade speed was set to 0.02 mm/sec until a trigger force of 0.049 N was reached. All filaments were tested except the MFA-EPO 40% (wt%) processed at 170°C, due to the poor filament consistency. The filaments diameters for all the samples ranged between 1.63 and 1.74 mm. All samples were tested on the same day to ensure consistent temperature (20-22°C) and environmental conditions and with the exact same test setup (i.e. including the gap width). Strain at break and Flexural Modulus were evaluated after normalising the strain to the extrudate diameter. Flexural Modulus is calculated as a slope of the curve in the elastic region using Hooke's low. Flexural Modulus (E_f) = Stress (σ) / Strain (ε). Five replicates were run for each sample with a 0.1 mm diameter difference between the replicates. Average and standard deviations values of flexural modulus, strain at break and maximum stress were calculated. Macro function used in Exponent software (version 6.1.20.0) to find the values of interest.

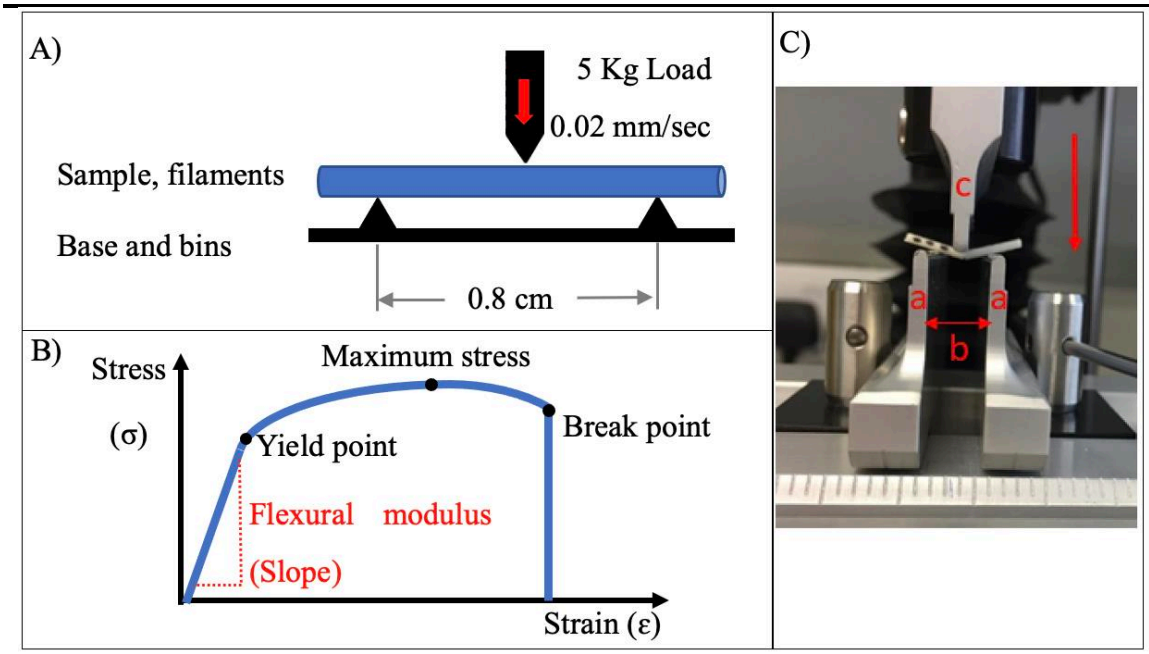

Figure 2-2. Schematic of the 3D point bend test experiment (A), and the mechanical test graph and points (B), picture of the setup (C [130]).

2.2.2.5.2. 3D printing test:

The 3D printer used in this work was Creality Ender 3 V1 (Make: Shenzhen Creality 3D Technology Co. Ltd., China) that has Creality V4.2.7 mainboard with TMC2225

stepper motor driver. The 3D printer framware was Marlin 2.0.1. An MK8 direct driver was installed instead of the original Bowden-style extruder to provide a shorter path between the feeder gear and hot nozzle. The machine spool holder was placed on the front top left of the aluminium frame.

Feed-ability test was conducted by inserting the filaments in the PTFE tube that drove the filament from the spool to the 3D printer extruder head (no printing).

2.2.2.5.3. Scanning electric microscope (SEM):

Cross-sections of the filament feedstock were analysed using a TM4000Plus scanning electron microscope (SEM) (Hitachi High-Technologies Corporation, Japan). Samples were fixed to aluminium stubs using double-sided adhesive carbon tabs before being coated with a 20 nm thick layer of gold using an EM ACE 200 sputter coater (Leica Inc., Germany) to minimise charging during SEM analyses. Samples were then placed inside the SEM and brought under vacuum for analysis. The SEM was operated with an accelerating voltage of 10kV, observation mode 2, and standard vacuum level, with data collected in backscattered electron mode. SEM images were acquired at different magnifications, an initial overview image encompassing the entire cross-section (typically 50x or 60x magnification), as well as zoomed in areas of interest at 250x and 1000x magnification.

To study the impact of the drug load, the following samples were tested; MFA:EPO of 10:90, 20:80 and 30:70 (wt%) and EPO extrudates all processed at 140°C. To study the impact of the HME process temperature the MFA:EPO 30:70 extrudates processed at 120, 130, 140 and 150°C were studied. MFA:EPO 20:80 extrudates processed at 120 and 140°C were also studied.

2.2.2.5.4. Intrinsic Dissolution test using Sirius inForm:

Dissolution tests (see Table 2-2) were conducted using a Sirius inForm (Sirius inForm PAT2000i platform, Pion Inc Ltd, UK), GI dissolution assay at a volume of 40 mL and a constant pH of 5.5 (acetate buffer 0.1 M) at 37°C and 100 rpm. The sample (23 mg of powder, physical mixture or extrudate) was compressed in a 6mm metal holder at 100 Kg for 2 minutes then adjust back to 100 Kg for further 3 minutes. Sample was added to the preheated dissolution media. MFA Molecular extinction coefficient was previously determined in the pH of interest using co-solvent system Yasuda-Shedlovsky

extrapolation. To identify the impact of the drug load and process temperature on the dissolution selected samples were chosen see Table 2-2.

The intrinsic dissolution rate (IDR) was calculated using the following formula:

$$\text{IDR} = (\frac{\sum dm}{n \times dt})/(A \times Ratio) \quad \text{(eq 2.1)}$$

Where m is the mass in mg and n×dt is dissolution time in sec. dt is the sampling time gap and n is the number of samples. A is the area of the disc surface exposed to the media in mm^2 ($A=\pi r^2$: r = 6 mm). Assuming the homogenous distribution of the components, the numerator (A×ratio) is the surface area of MFA only. Average and standard deviation were calculated for each dissolution curve across the running time, 2 hours. All samples were run in duplicate. MFA solubility in the media (pH = 5.5, T= 37°C, Acetate buffer) is 2.2 ug/mL and reached after 30 min [104].

2.2.2.6. Statistical studies

Statistical analysis was performed in Minitab 19.2.

2.3. Results and Discussion

2.3.1. Material selection and extrudates production

The choice of the polymer was based on a previous screening study conducted during a master project in CMAC. MFA miscibility with different polymers were calculated using Hansen Solubility Parameters (HSPs) with the results further evaluated using DSC and HSM [131]. EPO was one of the most soluble candidates $\Delta\delta$ = 4 $MPa^{1/2}$ (<7.0 $MPa^{1/2}$), indicating possible miscibility [132]. To the author's knowledge this the first time MFA:EPO combination was considered for a 3D-printing application.

A pure EPO polymer extrudate was prepared as a drug free control. Although the measured glass transition temperature (Tg) of the polymer was 57°C (DSC result), the lowest EPO process temperature (Tp) achieved on the 11 mm extruder was 140°C due to a high torque value (The recommended EPO process temperature is 150°C but no information was found on the torque value, Evonik Ltd). The processing torque changed according to the material's viscosity in the HME barrel [130] (Figure 2-3 Top). As the temperature increases, the polymer entropy rises, and the polymer-polymer interaction decreases. Therefore, the entangled chains are free to move and slide over each other [133]. However, the big difference between Tg and Tp might be caused by the entanglements of the branched polymer that require additional work to move the

polymer chains. This caused an increase in the resistance in the first few heating zones in the HME, which is reflected in high torque values. Thus, a strong temperature gradient in the first two zones was applied to overcome this polymer property. Parikh et al [134] studied the viscosity and HME-extrudability of Eudragit (polymethacrylic acid) based polymers. Temperature sweep test of EPO showed two crossover points (at which material changed its dominant behaviour from solid-like to liquid-like) at 49°C and 105°C. The first is close to the Tg and assigned to the relaxation of the sidechains. While the second represented the flow of the polymer chains. Their ideal extrusion temperature for the EPO on 11mm HME extruder was between 127°C and 150°C.

Lower torque was observed with increasing process temperature (Figure 2-3 Bottom). The drug ratio, the 20:80 and 30:70 MFA:EPO (wt:wt), had the lowest torque values i.e. highest plasticizing affect. This means that the saturation concentration is between these two values. Above the saturation level the torque lines shifted up again due to the presence of MFA particles in the liquid polymer during extrusion. The presence of the drug molecules reduced the torque values and this was assigned to the plasticizing effect of the drug on the polymer. The interaction of the polymer with small MFA molecules increases the free volume between the polymer chains reducing the polymer-polymer interaction and as a result increases the mobility [135], [136], [137]. Prasad et al observed a reduction of the torque values with increasing paracetamol load due to plasticization effect on hypromellose (HPMC) then there was a modest increase at 30% and 40% (wt%) because of the presence of drug particles [130].

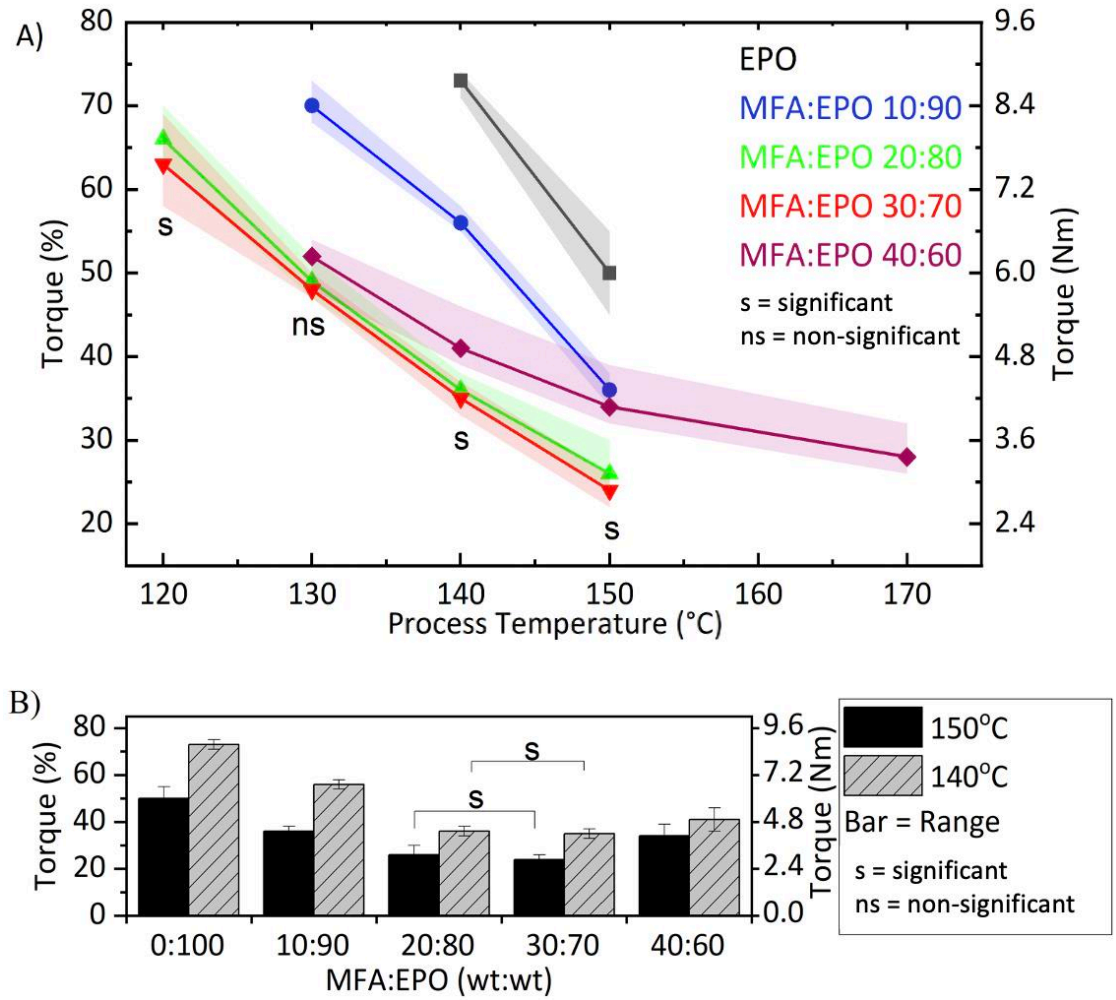

Figure 2-3. Torque against the process temperature for different EPO:MFA drug loads from 0 to 40% (wt%), shaded area represents the range (A). Torque values against the drug load from the HME experiments at 140 and 150°C (B). Mann-Whitney test conducted on the overlapped values, n = 60 (measurement every 5 sec for 5 min), bar and shaded areas are ranges (max-min), s indicated significant difference between the samples (ns = non-significant, P > 0.05).

The die pressures were low in all experiments indicating that resistance was mostly built in the first few zones Figure 2-4. No trends can be noticed except the slight increase in the pressure at lowest process temperature for each value. After the molten material left the HME die, it was exposed to ambient temperature and a conveying belt was used to obtain extrudate diameter around 1.7 mm (filament) by controlling the belt speed i.e. pulling rate. In general, the higher the process temperature the more sensitive the extrudate diameter was to the belt speed, belt speed was increased when the extrudate diameter was >1.7 and vice versa but was not recorded. In contrast, Prasad et

al showed that changing the belt speed does not affect the extrudate diameter for Paracetamol-Affinisol systems due to the low friction at the contact points [130]. The friction between the extrudates and the belt depends on the material properties and the sample temperature on first contact with the belt. A low friction was observed when the Tp dropped to 120°C, i.e. the highest die pressure. Only MFA:EPO 40:60 ratio processed at 170°C showed visible outgassing bubbles and a lack of diameter consistency (Table 2-3).

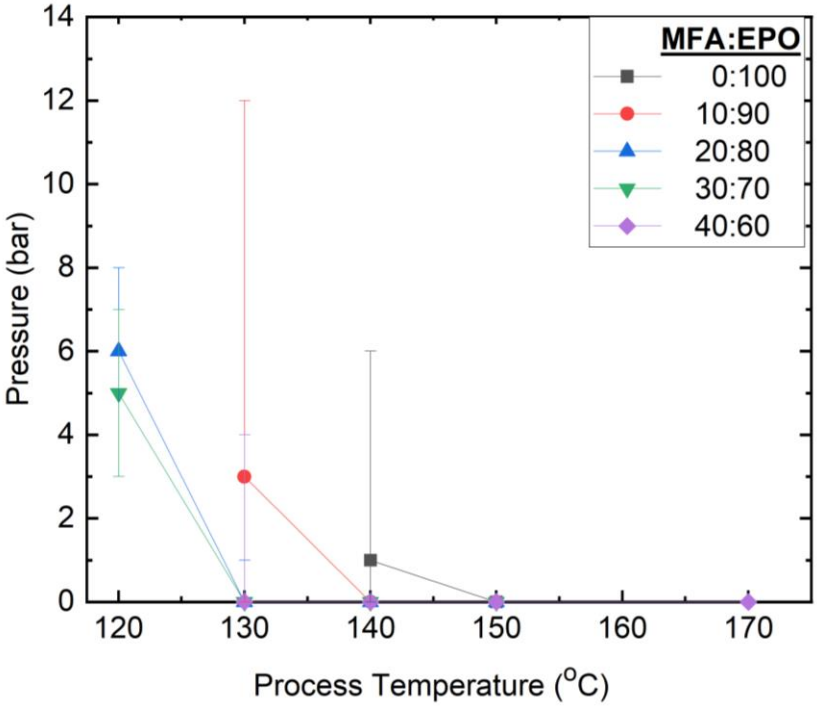

Figure 2-4. Pressure values from the HME die versus the process temperature. Bar represents the range (max-min), n=60 (measurement every 5 sec for 5 min).

Process temperature	120°C	130°C	140°C	150°C	170°C
EPO			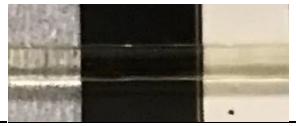	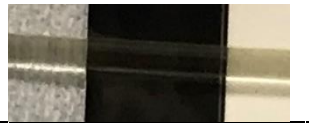	
MFA:EPO 10:90		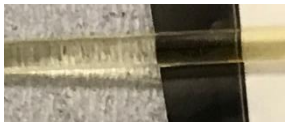			
MFA:EPO 20:80		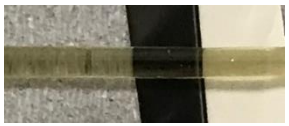	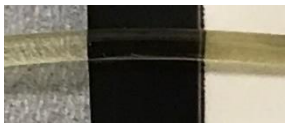		
MFA:EPO 30:70					
MFA:EPO 40:60					

Gray background with black and white plastic strip to visualize the transparency.

2.3.2. Solid state study and Phase diagram

The solid state was studied using different techniques, DSC, Raman Microscopy, inline Raman low frequency, offline Raman low frequency and XRPD. Before analysing the binary systems, pure components and solid form spectra were collected. For MFA, form I is the stable form and transforms to form II at elevated temperature, between 160-190°C [138], [139]. Both forms were obtained using the crystallisation experiment detailed in (*2.1.2.2.2*), but amorphous MFA was not obtainable either by quench cooling from melt or rapid pH reduction from high pH MFA solution.

Low-frequency THz-Raman spectra for MFA form I showed distinct peaks at 33, 48 and 111 cm^{-1} (Figure 2-5). Form II showed distinctive peaks at 43, 51, and 67 cm^{-1}. The peak positions for form I are in agreement with previous study while form II peaks showed small shifting [140]. This variation was assigned to instrumental differences and/or the smoothing and baseline correction method. Both MFA forms showed peaks at 70, 84, 98, 119 and 153 cm^{-1} which were absent in the EPO spectra.

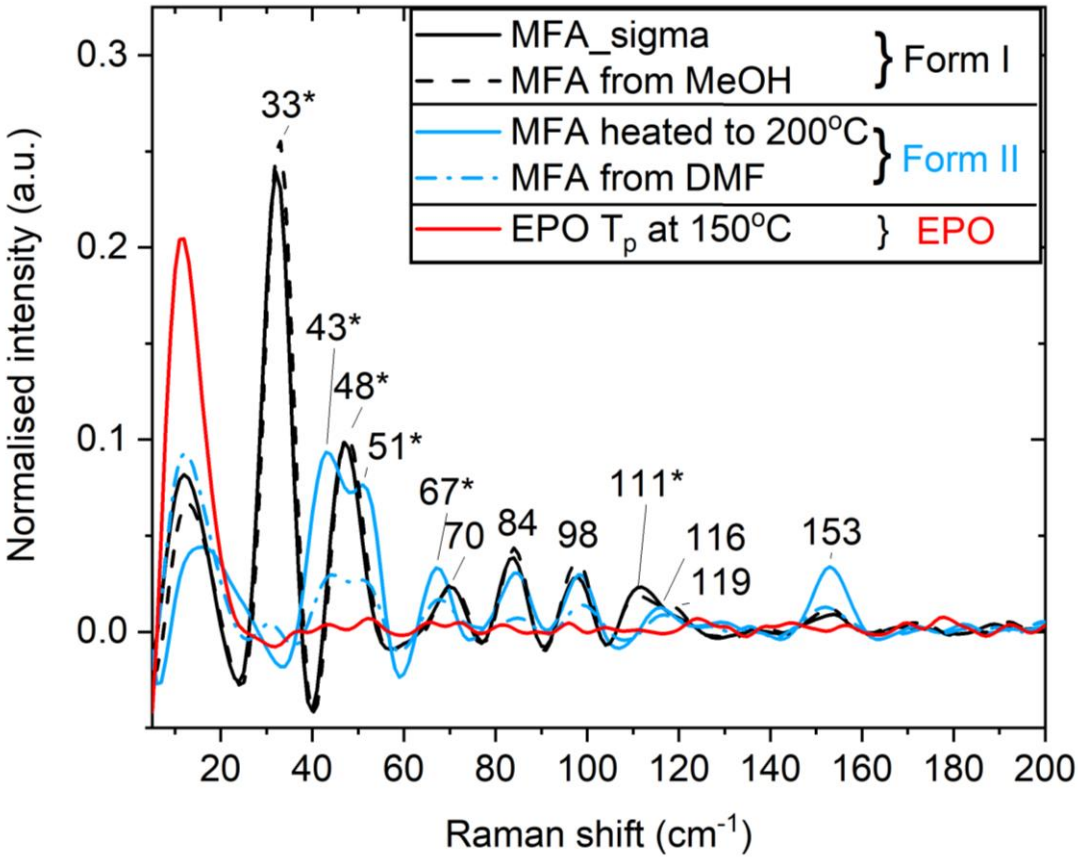

Figure 2-5. low-frequency THz-Raman spectroscopy reference, (Black) MFA form I, (Blue) MFA form II and (Red) EPO. Peaks indicated with stars are the characteristic ones.

Figure 2-6A displays example extrudate spectra at different drug loads and different process temperatures. Peaks at 33 and 48 cm^{-1} Raman shift indicated the MFA form I presence in the samples. All samples of 10:90 and 20:80 did not show MFA crystalline peaks. At 30:70 MFA:EPO the samples produced at temperature higher than 135°C (±5) showed absence of the MFA crystalline peaks while below this temperature peaks of MFA form I are observed in the spectra. At 40:60 MFA:EPO, only above 160°C (±10) MFA form I peaks disappeared.

The disappearance of the crystalline peaks at process temperatures below the melting point (234°C DSC result) and the plasticizing effect of the drug on the polymer (torque result) indicate the amorphisation or dissolution of the drug in the EPO. For the lowest two ratios (10:90 and 20:80), the amorphisation was independent of the process temperature. Critical concentration (Cc) was defined by Bordos et al as the highest API

concentration that formed amorphous solid dispersion regardless of HME process temperature [127]. Thus, for MFA:EPO system 20% (wt%) was assigned as Cc. By increasing the drug load the system was supersaturated and required a higher temperature to dissolve MFA in the polymer. The phase diagram from the THz-Raman is shown in Figure 2-6B. The full set of spectra are included in Figure Appendix 1-1.

Figure 2-6C displays selected XRPD examples of the MFA:EPO extrudates. The offline-XRPD measurements were compared to MFA polymorphic forms found on Cambridge Structural Database (CCDC) [141]. Characteristic peaks at 6.35°, 14.35° and 15.15° (2θ) refer to the presence of MFA form I (XYANAC) [142]. While peaks at 11.97° and 17.89° (2θ) specify MFA form II (XYANAC02) [143]. At 10:90 and 20:80 MFA:EPO all the samples exhibited an amorphous broad peak. At higher drug load 30:70 MFA:EPO, samples processed at 150°C and 140°C were Xray-amorphous, while samples processed at lower temperatures (130°C and 120°C) were form I crystalline solid dispersion. The highest drug load 40:60 MFA:EPO processed at temperature below 160°C were also form I crystalline solid dispersion. All these offline-XRPD findings were in agreement with the THz-Raman spectroscopy results and as a result provide the same phase diagram. The only difference observed is in the sample of 40:60 processed at 170°C which was form II crystalline solid dispersion.

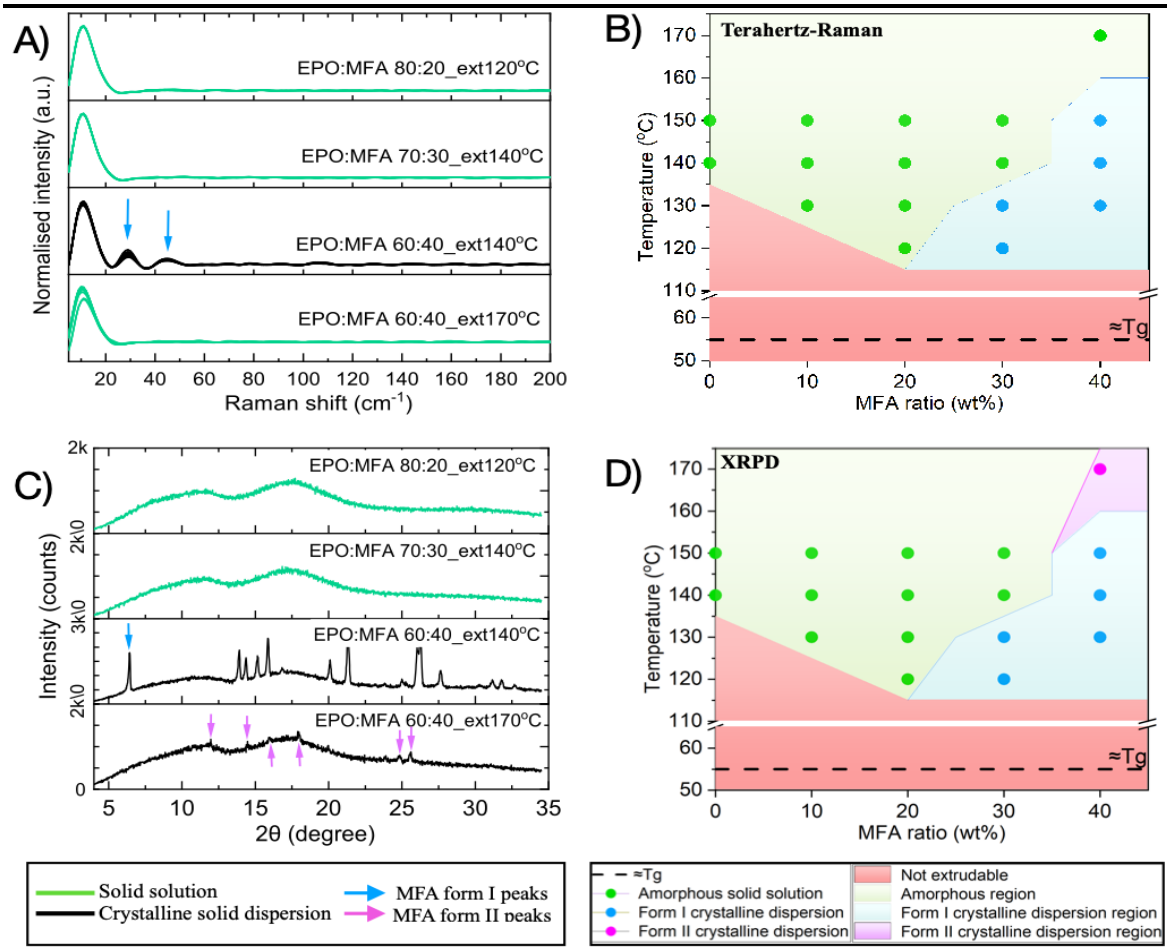

Figure 2-6. Inline-THz Raman Spectra and XRPD examples of EPO:MFA extrudates (A, C) and the corresponding phase diagram from each technique (B, D). In Figures B and D, the borders of the regions are the middle point of the neighbour measurements (accuracy ±10°C, ±5% wt%).

To investigate if this difference was due to stability and re-crystallisation after the extrusion or poor recognition of form II crystals on the THz-Raman, the spectra of the samples were collected offline. Figure 2-7 shows the offline THz-Raman of the extrudates. All samples equal to and below 30% (wt%) drug load were in the agreement with the inline measurements i.e. all 10:90 and 20:80 samples were amorphous and 30:70 below 135°C were form I crystalline solid dispersions. The 40:60 MFA:EPO processed at 170°C demonstrated two spectra with peaks in the same position of MFA form I and II. However, the noise to signal ratio was poor and it was hard to assign these peaks to the noise or to the MFA crystalline forms. In my previous study, a similar onset was observed of both MFA sublimation and form (I → II) transformation indicating a link between both events such as spatial condensation of sublimated MFA

molecules forming MFA form II [131]. Therefore, the MFA might have been sublimed in the HME at high temperature converting MFA form I to gas, upon extrusion and cooling down the supersaturation increased spatially causing re-crystallisation to form II. This aligns with the presence of outgassing bubbles in this sample (Table 2-3). Alternatively, the THz-Raman might have not captured the MFA form II during the HME experiment, especially that it was hard to detect offline as well. The lack of crystallinity detection could be due to multiple reasons, for example sample size, depth of penetration, sample consistency and signal intensity. The XRPD had better detection because the beam size of the Xray is larger than the THz-Raman, 100-200 mm and <15 mm, respectively. The X-ray beams penetrate the sample while the THz-Raman Stokes signals are reflected from the exposed surface. Moreover, the bubbles generated during extruding at 170°C would be expected to move and arrange closer to the walls including the in-line probe surface, this was observed as poor peak intensity consistency of the spectra as the temperature increases to 170°C (Appendix Figure 1-2). Therefore, the main limiting factor for the THz-Raman is the probability of crystalline particles to pass through the beam path. Another reason was the broad and small nature of the MFA form II peaks, which was harder to detect at a higher temperature. This presents as an increase in the background signal which correlated to an increase in the anti-Stokes scattering and a decrease in Stokes scattering i.e. a decrease in the signal to the noise ratio [144]. On the other hand, the XRPD using the current setup cannot detect crystallinity content of beta-lactam antibiotics below 5% [145].

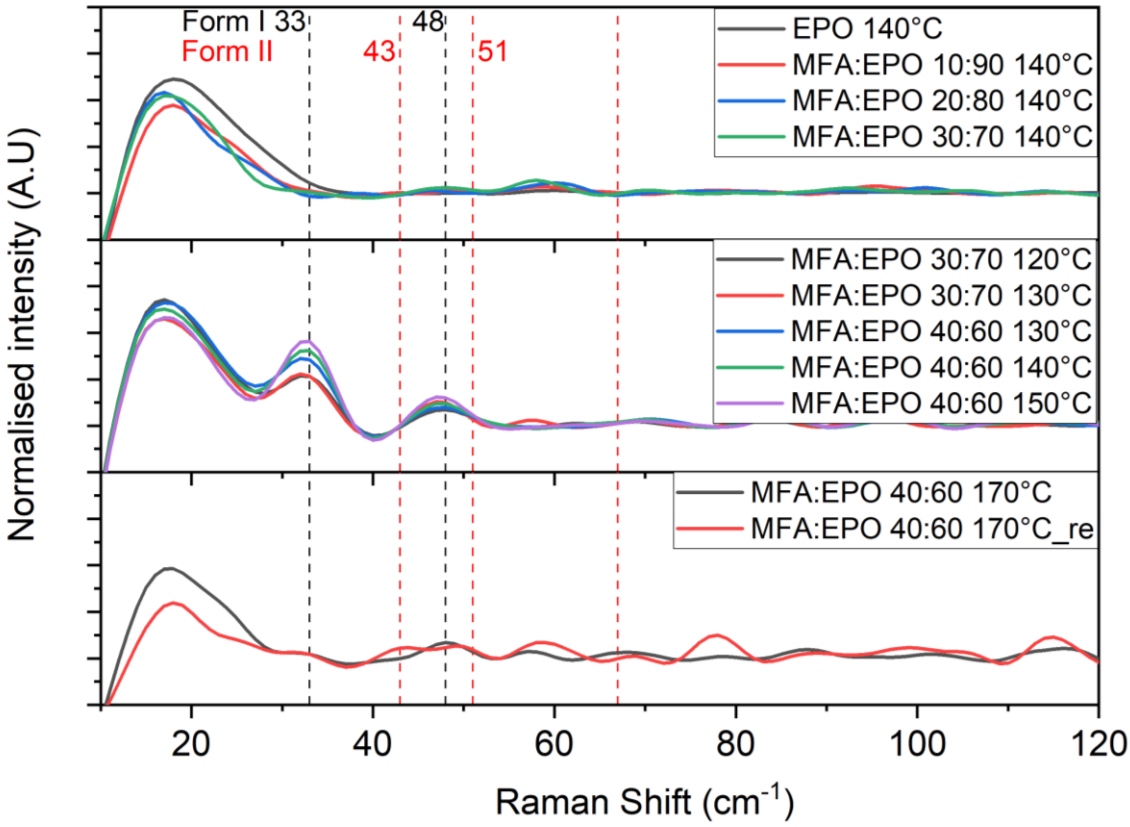

Figure 2-7. Offline THz-Raman of extrudates after two months of the extrusion. First group (top) all spectra that showed no presence of MFA crystalline peaks. Second group spectra with form I MFA peaks indicating crystalline solid dispersion. Third group (bottom graph) shows repetition of MFA:EPO 40:60 extruded at 170°C.

Previous work has reported the formation of an amorphous solid solution of EPO:MFA at 30% and 40% drug load using 16mm HME at Tp of 110°C [104]. The difference with this study might be due to different production or characterisation conditions. However, the literature obtained extrudates at the mentioned ratio were opaque and the corresponding electron scanning microscope showed aggregates suggesting that these finite particles were likely to be drug crystals.

All the amorphous extrudates were clear and transparent by naked eye (Table 2-3). However, under the microscope MFA:EPO 30:70 processed at 140°C (XRPD-amorphous) was found to have small rounded edge particles identified by the Raman microscope, as MFA form I (Figure 2-8). For the 30:70 MFA:EPO (wt%) processed at higher temperature (150°C) two particles were found in 20 cm filament length.

Therefore, all samples above 20% (wt%) drug loading are probably crystalline solid dispersions, but with a very low crystalline material content. This supports the hypothesis suggested earlier of the THz Raman detection limit. It is worth noting that the spectra of the crystalline particles were hard to collect as the particles were not close to the surface. Therefore, a general aspect of THz Raman detection is that a deeper penetration would have a higher probability of crystalline detection. Backscattering Raman spectra for bulk paracetamol tablets showed that 88% of the backscattering is generated from the 1 mm sample layer (97% from 1.5 mm). While transmission mode was insensitive to the depth location of the paracetamol impurity [146]. From the combination of spectroscopic and X-ray diffraction technique results, 20% (wt%) was the solubility limit of the drug in the polymer.

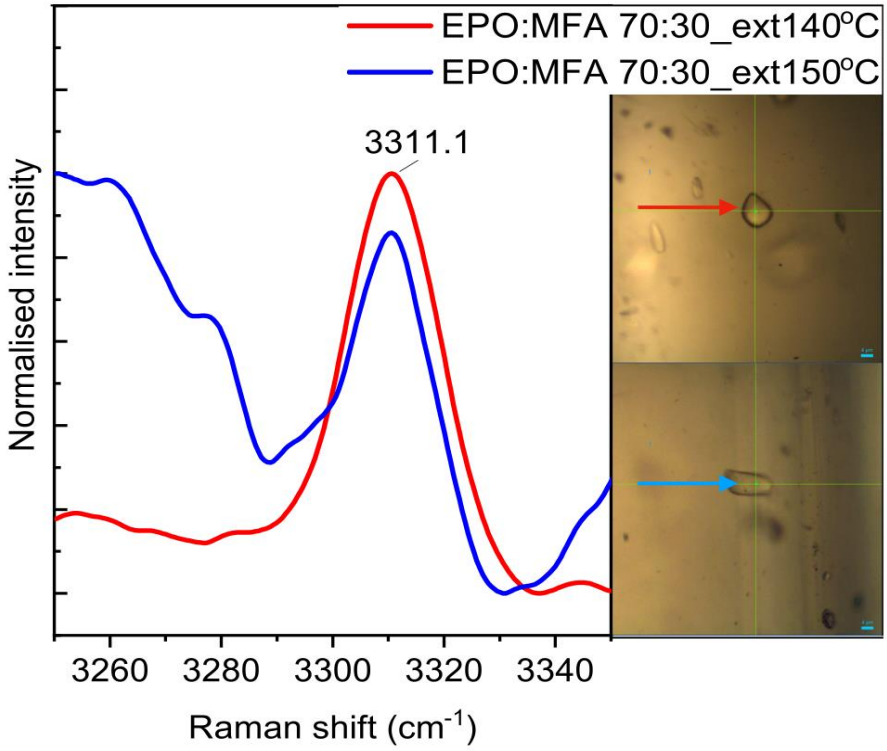

Figure 2-8 . Raman of N-H stretch peak of MFA:EPO 30:70 (wt%) samples processed at 140°C and 150°C showing presence of MFA form I.

2.3.3. Molecular interaction

Polymer-drug molecular interactions control the change in mechanical properties of the amorphous solid solution matrix were investigated using Raman spectra. MFA peak assignments are reported in the literature where atomic group vibrations are associated with specific wavelength [139]. EPO Raman peaks were assigned from literature

references [147], [148], [149], wavelength ranges provided for EPO functional groups. Spectra and peak assignments are included in the Appendix (Figure Appendix 1-4 and Table Appendix 1-1). Changes in the assigned peaks were examined in extrudate spectra and only specific peaks were used for interpretation of the molecular interaction. The specific peaks analysed were those assigned to one type of atomic motion, have strong to medium intensity (except where noted) and showed changes between the samples, Table 2-5 summarises the peaks and their changing patterns.

The MFA peak changes were induced by polymer-drug interactions and breaking the crystalline structure. For example, peaks at 578.1 and 1083.8 cm^{-1} were assigned to the in phase bending of C-C-C in the aromatic ring and C-H bonds respectively. The first peak disappeared in all 10:90 MFA-EPO samples. While the second shifted in all drug-loaded samples about +10 cm^{-1}. These changes in the spectra suggest the presence of an interaction between the aromatic group and the polymer. Peaks at 622.9 and 3311 cm^{-1} were assigned to the N-H bond of form I [139]. The 622.9 cm^{-1} peak was assigned to out of plane bending of N-H and was present only in the crystalline form I solid suspension. The peaks at 3311 cm^{-1} were assigned to the stretching of the same bond and followed the same pattern. Cunha et al. showed that the vibrations of the N-H bond are affected by the hydrogen bond of the carboxyl group [139]. Therefore, the destruction of form I MFA and the interaction between the carboxyl from the MFA and the amine group of EPO might be the reason behind the N-H vibration changes. Other peaks (like 1243 and 1332 cm^{-1}) that correlated to bonds in the carboxyl group also showed changes in the solid solution samples (Table 2-6). This result was supporting the presence of the interaction on the carboxyl group. All changes in the peaks that have been assigned to multiple groups are reported in Table Appendix 1-2.

On the other hand, only few peaks of the polymer changed. This is reasonable as not all the functional groups of the polymer would interact with the drug. The carboxyl to amine group ratio was below 1 up to MFA:EPO 30:70, wt:wt (Table 2-4). EPO showed a medium peak at 601.6 cm^{-1} correlated to the CN stretching vibration. This peak shifted about +[4-5] cm^{-1} for 10% (wt%) drug loading and +[13-15] cm^{-1} for higher MFA concentration (Figure 2-9). This shift was assigned to the hydrogen bond between the carboxyl of MFA and the amine of EPO. A weak peak at 733.6 cm^{-1}, assigned to C-C bond vibrations (namely C-C4 stretching vibration) disappeared in most of the solid solution samples. This might be caused from the molecular interaction with MFA.

Table 2-4. Carboxyl to amine group ratio calculation for MFA:EPO formulae calculation details in (Table Appendix 1-3):

MFA:EPO formulae (wt:wt)	**0:100 (EPO only)**	**10:90**	**20:80**	**30:70**	**40:60**
Carboxyl / amine group ratio	0	0.25	0.56	0.97	1.50

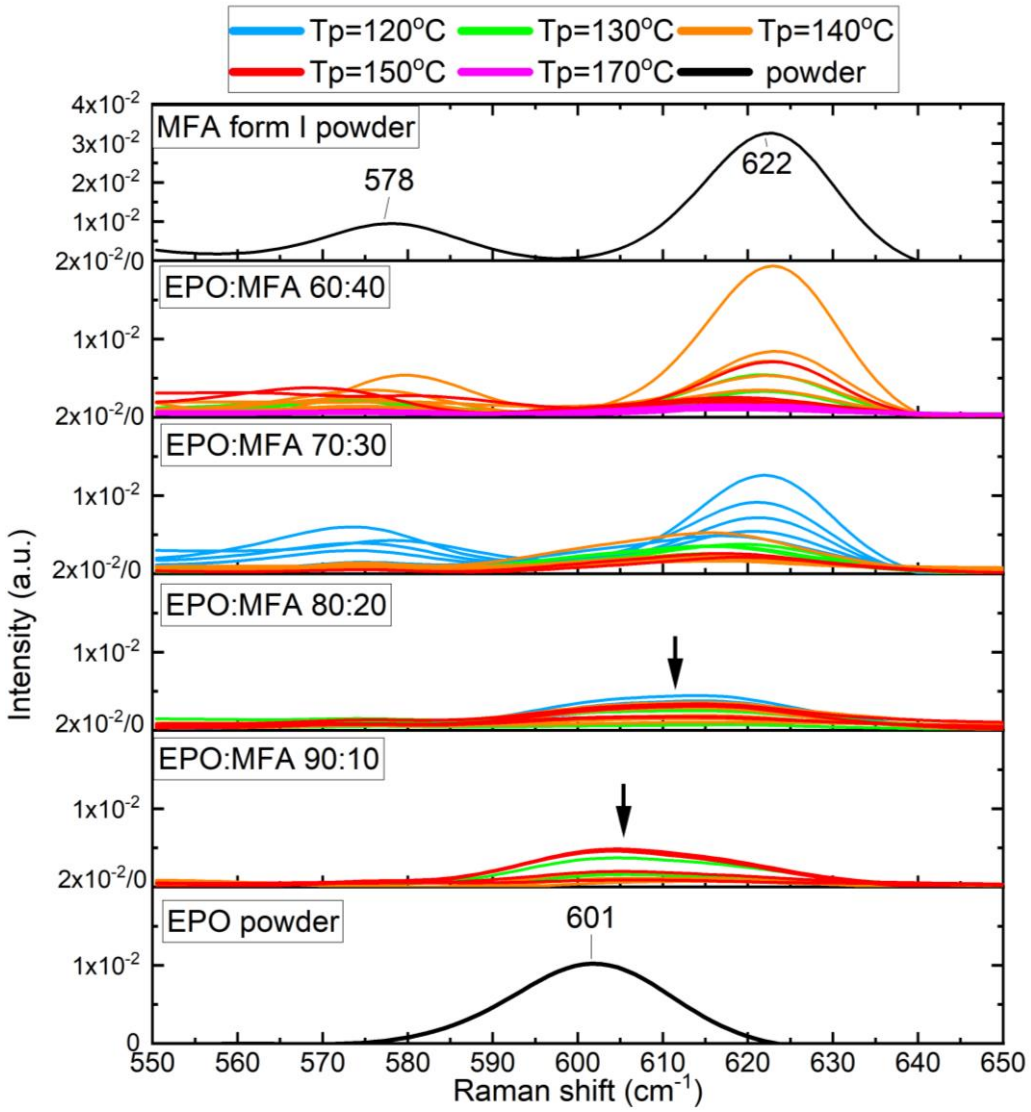

Figure 2-9 . Raman peaks of [Ar] C-C-C in phase bending in the aromatic ring and N-H bending out of plane in the mefenamic acid at 578.1 and 622.9 cm-1 (top) and CN stretching vibration in the Eudragit EPO at 601.6 cm-1 (bottom). Blueshift of the Eudragit peak in the extrudates samples between 10 and 40% (wt%) drug load

The findings on the MFA:EPO molecular interaction are in agreement with two previous studies on the same drug polymer combination . Kojima et al and Higashi et al

prepared amorphous solid solution of MFA:EPO at 24:76 (wt:wt) ratio by cryogenic grinding. Fourier Transform IR (FT-IR) Spectroscopy was used to investigate the molecular interaction in the mixture. Strong molecular interactions between the EPO aminoalkyl group and MFA carboxyl group were found to play an important role in amorphisation and stabilisation the system [104]. Later, Higashi et al. studied in depth the stability of supersaturated solution of this formula and showed the presence of the same type of hydrophilic interaction and hydrophobic interaction between the methyl groups attached to the EPO backbone and the aromatic group of MFA [142]. These findings are in alignment with the Raman results. Consequently, such interactions could be found in our extrudates.

Table 2-5. Raman wavenumber (in cm^{-1}) of MFA and EPO peaks assigned to one functional group and their change in the extrudates samples (detailed list of MFA peaks included in the Appendix Table 1-2 part 1 and part 2):

Raman shift (cm^{-1})		**Peak assignment** [139], [147], [148], [149]	***R.I.**	**Comment**
MFA	578.1	[Ar] C-C-C in phase bending [139]	m	Disappears in 10% (wt%) and higher drug loads
EPO	601.6	CN stretching vibration [149]	m	Shifts at 10% (+5 cm^{-1}) and 20% (+10 cm^{-1}) drug load
MFA	622.9	N-H bending out of plane [139]	s	Only present in crystalline solid suspension samples
EPO	733.6	C-C_4 symmetric stretching [147]	w	Shift in EPO extrudates and disappears in all drug loaded samples
MFA	1083.8	[C-H] bending in plane (Øa, Øb), [CH_3] wagging [139]	m-w	Shift in all samples except few individual spectra. About (+10 cm^{-1}).
MFA	3311.3	[N-H] stretching [139]	m	Present in Form I crystalline solid dispersion only

* R.I. = relative intensity: vs= very strong, s= strong, m= medium, w= weak, vw, very weak

Table 2-6. Raman wavenumber (in cm^{-1}) of MFA peaks assigned to multiple functional groups and their change in the extrudates samples:

Raman shift (cm^{-1})	**Peak assignment** [139], [147], [148], [149]	***R.I.**	**Comment**
MFA 1243.1	[O-H] bending, [C-H] bending and [C-COOH] str	vs	Split in 10% and 20% (wt%) drug loaded samples with a drop in the intensity
EPO 1332.7	[O-H] bending and [C-C] str (¯b)	s	Present in Form I crystalline solid dispersion only

2.3.4. Thermal study

In the HME and FFF 3D printing process the materials are exposed to high temperatures. Therefore, studying the thermal behaviour of the system is important. To understand the thermal behaviour of the MFA:EPO system, DSC, TGA and HSM were used. The pure drug melting peak was about 234 (onset 230)ºC and another peak can be seen at 192ºC assigned to the MFA polymorphism change (I to II) [150]. When the drug is mixed with the polymer, these peaks appeared as one broad peak (between 130-180ºC) (Figure 2-10). The reduction in the melting point confirms once again the strong interaction between the drug and the polymer. In all the physical mixtures a broad peak was observed 120-200ºC. In addition to the melting and form transformation, sublimation can take a place at high temperature [126]. Therefore, due to the difficulties to separate the contribution of the three thermal events (melting, form transformation and sublimation) from the peaks of the physical mixtures, neither the Flory-Huggins equation nor melting enthalpy method were applicable. For example, the MFA:EPO 10:90 which is an amorphous solid dispersion (does not have melting point) showed a peak at 168.5°C. Similarly, the extrudate DSC traces exhibited peaks in the same range (Figure 2-11). The peaks did not show a pattern across the drug load or process temperature suggesting that multi events scenario occurred at high temperature. According to the drug load, the extrudate cuts and HME process temperature, the peaks varied or took different shapes. For example, the 40:60 MFA:EPO processed at 170ºC, there was an exothermal and endothermal events above 130ºC. Since the high drug load and the high process temperature, the MFA might have been supersaturated in the EPO

and upon increasing the temperature and the molecular mobility the MFA crystallised out [151].

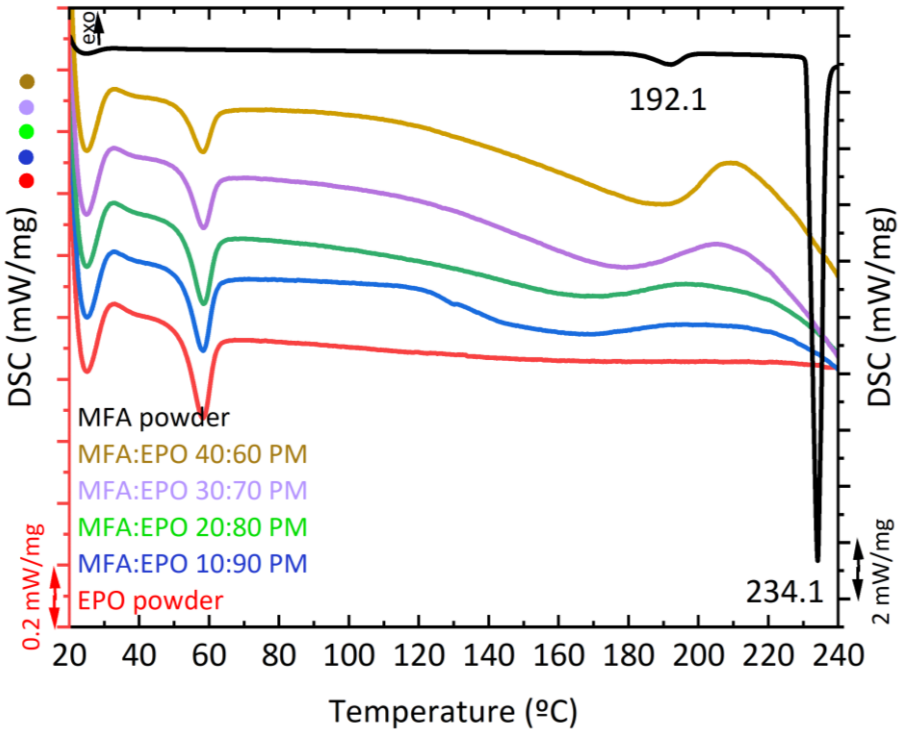

Figure 2-10. DSC first heating cycle of MFA and MFA:EPO physical mixtures (PM) and Eudragit EPO.

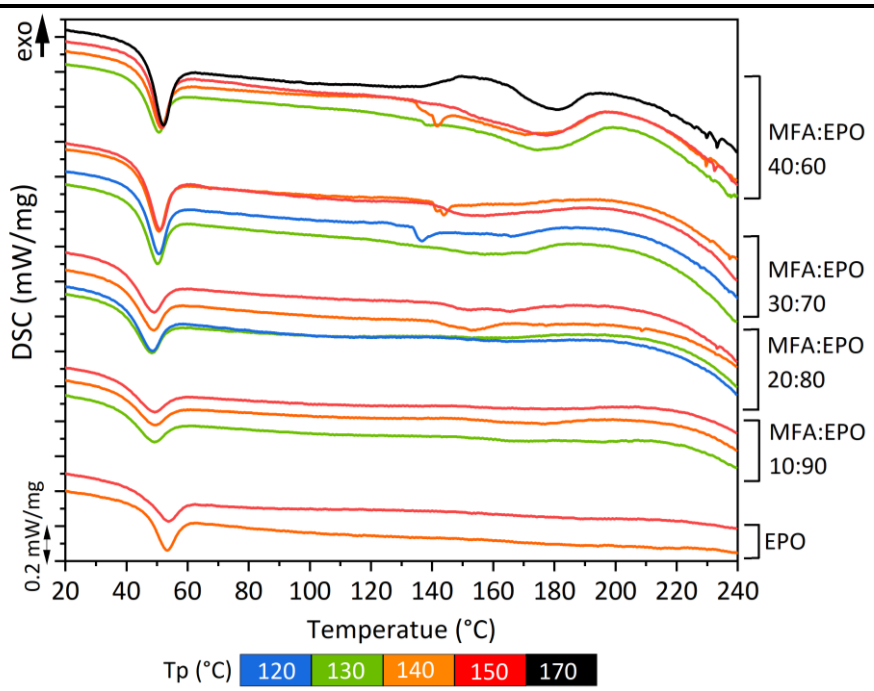

Figure 2-11. DSC first heating cycle of MFA:EPO and Eudragit EPO extrudates processed at different temperature on the HME (Tp).

TGA was used to understand the complex behaviour at high temperature. Figure 2-12 shows the mass loss between 130-230ºC from the extrudates and the pure components. Each of MFA and EPO loss was below 0.5%. The mass loss of the pure component are assigned to the solvent and volatile material trapped from synthesis and crystallisation process and/or water uptake during storage and in the case of MFA additional loss can be a result of the sublimation [129], [152] and potentially some degradation [104], [150]. The mass lost from the binary component systems were higher than the pure components, which was a result of additional process taking place such as increase in the sublimation or degradation. In both cases the presence of the polymer increased the loss due to the lower sublimation energy barrier of the amorphous drug. Hughey et al used a model compound from Roach with each of Eudragit L100 and HPMCAS, in both cases mixture degradation were higher than the sum of pure components degradation [153].

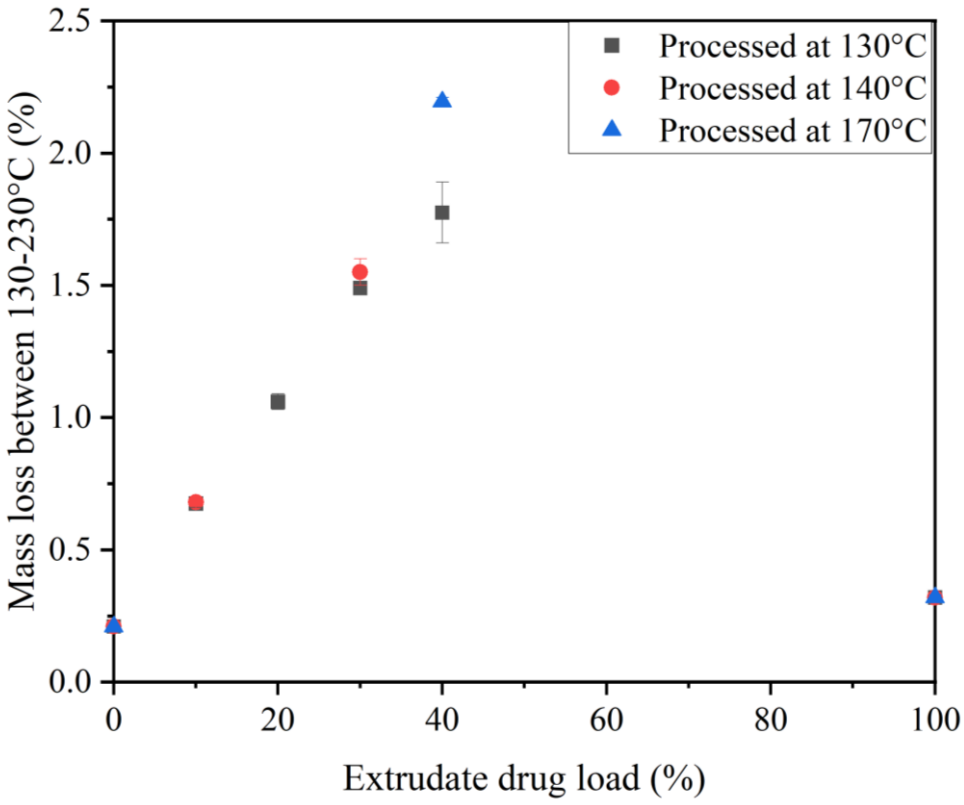

Figure 2-12. Mass loss between 130-230°C from extrudates using TGA (Average value, n=2, bar = SD and max fluctuation of an empty pan below 0.14%).

On the HSM the extrudate samples especially MFA:EPO 40:60 extruded at 170ºC showed out-gassing. Using the data from literature (See Method 2.2.6), the calculated vapour pressure (P) of MFA at 120ºC, 150ºC and 170ºC were about 2, 5.5 and 14 Pa. Such a pressure is small to be detected in the HME but the pressure read for the 40% (wt%) drug loaded samples were 0 bar (Figure 2-5). The runny extrudate and the presence of bubbles at this process temperature suggests that such a pressure was not achieved and caused the diameter inconsistency for this sample (Table 2-3 Figure of 40:60 MFA:EPO processed at 170ºC). Other factors like evaporation of trapped solvent and mixing might induced voids and gas bubbles. However, they have not been seen at lower temperatures.

A measurement of the pure MFA glass transition temperature was not possible as it immediately crystallised out from the melt, hence, the Gordon-Taylor equation was not applicable. For the physical mixtures the glass transition was measured during a cooling cycle after a heating step was used to generate the solid dispersion system. Glass transition temperatures can be found in Table 2-7. The Tg of the 20% (wt%) drug

loaded system was the lowest as more drug molecules dissolved in the polymer matrix. For the extrudates, there was a significant reduction in the Tg between the pure polymer and the 10% and 20% (wt%) drug loaded samples. Then Tg increased again showing no increase in the solubility of the drug in the polymer. Both results from the physical mixture and the extrudates shows a solubility limit around 20% (wt%) drug load and agrees with the previous finding from the XRPD and THz-Raman phase diagram Figure 2-6.

Table 2-7.Glass transition of the MFA:EPO physical mixtures and extrudates produced at different temperature:

MFA:EPO	**Physical Mixture**		**Extrudates, HME process temperature (°C)**					
	Cycle*	-	Cycle	120	130	140	150	170
0:100	Cooling	52.7	Heating	-	-	46.5	45.2	-
10:90	Cooling	48.8	Heating	-	38.8	38.6	37.7	-
20:80	Cooling	43.9	Heating	39.2	39.7	39.2	39.1	-
30:70	Cooling	46	Heating	46.8	48.2	45.9	48.5	-
40:60	Cooling	48	Heating	-	43.7	45	45.6	46.1

* in which cycle the Tg measured.

** theoretical Tg of MFA calculated using Gordon-Taylor equation [107] from extrudates 10:90 and 20:80 wt:wt at 140°C and 150°C, Tg MFA was 39.62°C and 39.89°C, respectively.

2.3.5. Formulae performance

2.3.5.1. Mechanical test and breaking behaviour

The mechanical behaviour of the extrudates is one of the main properties to study for 3D printing applications. Thus, flexural modulus, strain at max and strain at break were studied to evaluate printer head feed ability. Figure 2-13 shows selected examples of the texture analyser graphs and the extracted data from these graphs for all extrudates. Starting with the pure polymer, the extrudates had good elastic modulus (printable formulae 3.1 MPa/% , >1.2 MPa/% [130]) and relatively good maximum stress value (printable formulae >2.2 MPa [86]) but the strain at break values were poor (>12%) indicating brittle behaviour. At 10% (wt%) drug concentration, polymer properties were

dominant and no significant differences (P>0.05) were noticed between EPO extrudates and MFA:EPO 10:90 extrudates in term of flexural modulus and strain at break values. There was only small difference on the maximum stress value. By increasing the drug load to 20% (MFA:EPO 20:80), the impact of the drug on the mechanical properties was observed. An increase in the stiffness (higher flexural modulus) and brittleness (lower strain at break) were recorded for all process temperatures except for the lowest process temperature extrudate, 120ºC. This might be due to the insufficient mixing due to high resistance (Torque value). From the statistical study, it can be seen that all the three mechanical properties of MFA:EPO 20:80 at 120ºC were similar to the lowest process temperature of both EPO and MFA:EPO 10:90 (P>0.05), thus the statistics is supporting the hypothesis (insufficient mixing at low temperature). At higher drug loads which are crystalline solid dispersion, the samples showed significant increase in both brittleness and stiffness. A stronger increase (P<0.05) observed with the MFA:EPO 40:60 extrudates since these samples contained more dug particles. This results could be due to suspending brittle drug particles into the matrix [135]. For example, polypropylene stiffness and brittleness increased when it is filled with flour [154].

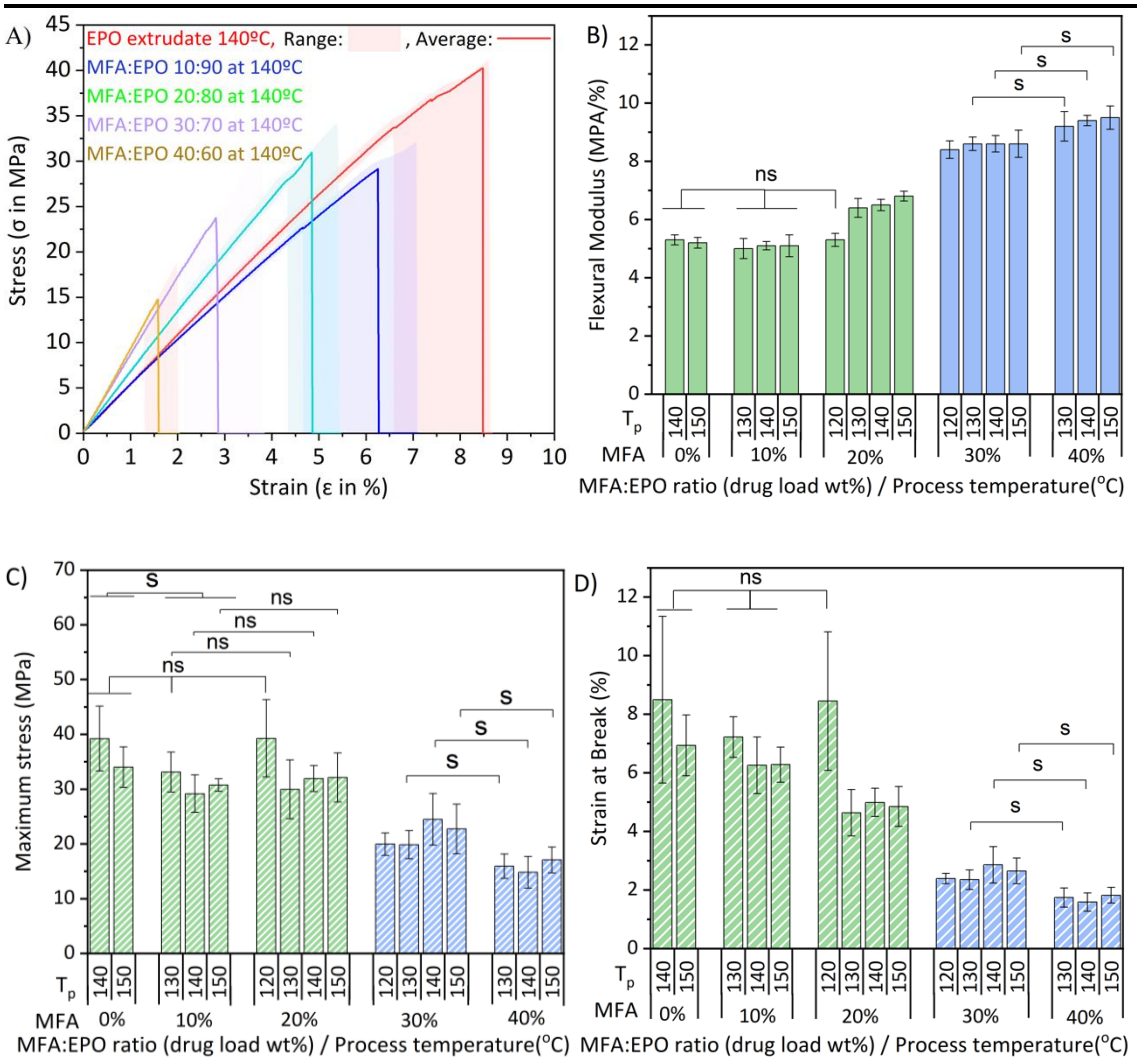

Figure 2-13. Mechanical properties of MFA:EPO extrudates at different drug loadings (0%, 10%, 20%, 30% and 40%, wt%) using the three point bend test. The graphs show examples of 3-point bend test (A) flexural modulus (B), Maximum stress (C) and Strain at break in these systems it was also = Strain at maximum stress (D). Amorphous samples coloured green (≤Cc) and crystalline coloured blue (>Cc). Average value (n=5, error bar = Standard deviation, ANOVA test s = P < 0.05 significant difference and ns = P > 0.05 no significant difference). ANOVA study for the temperature impact are not added to the graph but can be found in table 2-8.

The impact of the process temperature was only observed in the 20% (wt%) drug load (Table 2-8). In the 30% (wt%) drug load there were slight differences in the strain at break value for the samples processed at high temperatures. However, these differences

are not significant (ANOVA test, P>0.05). The difference might be more pronounced in a ductile matrix. In the current work, the polymer was brittle and the presence of the MFA increased this property. Therefore, processing the MFA:EPO 30:70 at higher temperature reduced the particles concentration but increased the matrix brittleness by dissolving more drug. This is in contrast to Prasad *et al.* who showed mechanical properties of extruded Paracetamol:Affinisol systems varied with increasing the drug load, where paracetamol made the affinisol more flexible. The flexural modulus decreased (ductility increased) with increasing the drug concentration in the amorphous solid suspension samples (5-35% of paracetamol (wt%)), including very ductile samples from 25% to 35% (wt%). While in the crystalline solid suspension (40-50%, wt%) the stiffness and toughness increased with higher paracetamol ratios [130]. The dissolved paracetamol molecules soften the affinisol, then un-dissolved solid particles in the ductile matrix increases maximum stress and stiffness and as a result the overall energy tolerance before fracture (toughness). The difference between the impact of the drug on the matrix (increase in the brittleness vs increase in the ductility) could be assigned to the difference in the plasticizing affect and the interaction on the molecular level. In MFA:EPO system, the two types of interactions caused hindering the movement of the polymer chains, as a result increasing stiffness and brittleness. This plasticization affect is believed to be "transmission affect", which was observed previously in polyvinyl chloride (PVC) with tricresyl phosphate (TCP) as transmissive plasticizer. The presence of TCP caused stiffness and brittleness until saturation concentration reached [135].

To be able to evaluate the numerical values of the extrudates an acceptable threshold should be found. However, the mechanical properties are sensitive to the test speed [68], gap and other factors and acceptable values are machine related [70] as a result there are no universal values. Our three-point bend method was same used by Prasad et al who obtained printable filaments equal or above 1.2 MPa for flexural modulus [130]. Zhang et al. 2017 used 2.5 cm gap and 10 mm/s speed and found printable filaments are between 2206-4677 g/mm^2 (21.6-45.9 MPa) [84], the threshold is expected to be lower as a lower speed was used in our work. Although none of the ratios were feedable in the curved bendy filament guide in the 3D printer (Table 2-9) due to the low strain at break value (brittleness), they had good flexural modulus. Lower ratio of the drug was preferable to keep the concentration in the amorphous solid dispersion region since the crystalline solid dispersion were very brittle.

Table 2-8. Statistical study for the HME process temperature impact on the mechanical properties for the MFA:EPO extrudates:

Test group (MFA:EPO wt:wt)		**Response**	**ANOVA test****	
EPO	at 140 and 150°C	FM	No difference	significant
		Stress	No difference	significant
		Strain	No difference	significant
MFA:EPO 10:90	at 130, 140 and150°C	FM	No difference	significant
		Stress	No difference	significant
		Strain	No difference	significant
MFA:EPO 20:80	at 120, 130, 140 and150°C	FM	Significant difference	
		Stress	Significant difference	
		Strain	Significant difference	
MFA:EPO 20:80*	at 130, 140 and150°C	FM	No difference	significant
		Stress	No difference	significant
		Strain	No difference	significant
MFA:EPO 30:70	at 120, 130, 140 and150°C	FM	No difference	significant
		Stress	No difference	significant
		Strain	No difference	significant
MFA:EPO 40:60	at 130, 140 and150°C	FM	No difference	significant

	Stress	No difference	significant
	Strain	No difference	significant

* All MFA:EPO 20:80 extrudates without the one processed at 120°C

** ANOVA test with 95% confidence level ($P<0.05$ indicates significant difference)

Table 2-9. Feed-ability test in the 3D printer:

Formulae		Tp (°C)			
		120	**130**	**140**	**150**
EPO		NA	NA	✗	✗
MFA:EPO	**10:90**	NA	✗	✗	✗
MFA:EPO	**20:80**	✗	✗	✗	✗
MFA:EPO	**30:70**	✗	✗	✗	✗
MFA:EPO	**40:60**	NA	✗	✗	✗

NA = not applicable for example sample not extruded in the HME, ✗ = break in the PTFE tube, / = Extrudate fed into the printer head but fail to print, ✓ = Extrudate successfully printed (3DP-extrudability).

The collected photo of the extrudates cross section under the SEM microscope are shown in Figure 2-14 and 2-15. In general, the extrudates surfaces looked relatively smooth with some fragments settled on the surfaces. The fragments can be differentiated from the surface's defects and impeded objects by black shadow behind the fragments. To compare impact of the drug load on the surfaces cut the neat polymer EPO and drug loaded extruded are exhibited in Figure 2-14. EPO fractured in a brittle manner showing a smooth surface like a mirror and indicating a progress and domination of a primary crack across the extrudate (Figure 2-14-Ax50). Similarly, smooth surface of EPO extrudates observed by Sadia et al on SEM [92]. The edge of the EPO sample showed random ruptures, which are thought to be a result of the stress wave reaching the edges (Figure 2-14-Ax1000). Since no space restriction strings of the matrix teared from the main body and deform plastically. The samples have been taken from the three-point bend test (EPO and MFA:EPO 20:80) or been broken before the SEM analysis (rest of the samples) by similar bending manner. Thus, the cross sections of the extrudates have been exposed to compression in the area from the middle part to the applied force point, while tensile tension, on the other half. A dashed line and force arrow were drawn on the Figures to identify both sections. For the EPO extrudate the start of the crack and the direction of the applied force could not be identified. With the drug loaded samples more brittleness behaviour was observed.

MFA:EPO 10:90 showed development of secondary cracks next to the edges and an offset of the cracked plane in the compression part (Figure 2-14-Bx50 and x250). The secondary cracks are created as a result of the release of an elastic energy that is greater than the energy needed to spread the main crack. Then if its velocity is faster than the main one it dominates the sequenced crack growth [155].

At the higher drug load MFA:EPO 20:80, more fragments are present on the surface. This sample was broken on the three-point bend test like the EPO and did not show secondary cracks (Figure 2-14-Cx50 and x250). But its edges showed smaller ruptured pieces (Figure 2-14-Cx1000). Additional extrudates at same ratio processed at 120°C and 150°C showed similar behaviour, smooth surface with fragments on the top and domination of some secondary cracks (Figure Appendix 1-5).

In the extrudates processed at 140°C, the MFA:EPO 30:70 (wt:wt) one showed a pattern around a central point (Figure 2-14-Dx50). Around the point there is a clear mirror-like area then a relatively rougher area that spread toward the outer surface. This pattern can be found also on another methacrylate polymer derivative, polymethyl methacrylate (PMMA). R. Bortz et al studied toughening the PMMA by loading it with carbon nanotubes and fibres [156]. The crack of the single component PMMA matrix showed three areas the centre of which is the crack flaw (Figure 2-14-D x1000), then mirror region then the mist and hackle region. The crack flaw initiated in the tensile tension area from a weak point and close to the surface where the tension is the highest. The mirror region was associated to the spread of the main crack but it took an ellipse-like shape rather than a circle, which was also observed in the PMMA again due to the untimely appearance of the mist and hackle region [155], [157]. The last area was a result of the appearance of secondary cracks as explained earlier but the primary crack is still dominant. Thus, small secondary cracks appeared causing the surface roughness we see in Figure 2-14-D x250. When the secondary cracks dominate the hackle and crack branching is observed [155].

To study the impact of the temperature on the crack development the MFA:EPO 30:70 (wt:wt) extrudates at 120°C, 130°C, 140°C and 150°C were tested. Extrudates processed at 120°C and 130°C showed similar pattern to the one at 140°C, crack flaw, mirror then mist regions (Figure 2-15 A, B and C x50, next to the stars i.e. in the tension region). Another noticeable difference was imperfection of the matrix surface, which is expected to be caused by MFA crystallinity of the sample (Figure 2-15 A, B and C x250

and x1000). Both MFA:EPO 30:70 (wt:wt) at 120°C and 130°C were crystalline solid dispersion on X-Ray diffraction and Spectroscopic techniques (relatively high crystalline content). Matsushige et al assigned the mist region to imperfection in the PMMA matrix due to microvoids, heterogeneity in microscopic density distribution and other foreign materials from previous processes [157]. The presence of theses structural weaknesses changes the primary crack propagation velocity causing small secondary cracks, the mist region. In our case, the MFA crystallinity was thought to be the cause of the mist. At the 140°C, the sample was harder to visualise but showed mist behaviour which, is in agreement with the Raman microscopy results. The impeded objects in the matrix (MFA crystals) were less abundant. At higher process temperature 150°C, the mist pattern disappeared again as a result of reduction in the MFA crystallinity. However, an MFA crystal-like shape was captured in this extrudate (Figure 2-15 D x1000).

The patterns observed in the Scanning Electron Microscopy (SEM) findings are consistent with the patterns identified using other techniques, such as X-Ray Powder Diffraction (XRPD) and Raman spectroscopy. The sample with the lowest drug load (MFA:EPO 90:10, wt:wt), which was a solid solution, displayed the most uniform crack propagation, characterized by a mirror pattern. As the drug load increased to MFA:EPO 80:20 (wt:wt), the brittleness of the sample increased, as evidenced by the emergence and dominance of secondary cracks. Upon further increasing the drug load and reaching the crystalline solid dispersion space (MFA:EPO 70:30, wt:wt and above), the surface roughness increased, particularly in what is termed the mist region.

Our results are in agreement with previous study that showed the SEM Figures of MFA:EPO extrudates processed at 110°C at ratio 20:80, 25:75 and 30:70 (wt:wt). The first extrudates were smooth cut while the higher drug load had rough surfaces that might have been from MFA residual crystallinity [152]. It is not clear if the SEM images from the outer extrudate surface, its cross section or crashed extrudates, and no further discussion was provided. Thus, the results and discussion presented in the current work describes the system behaviour more in depth.

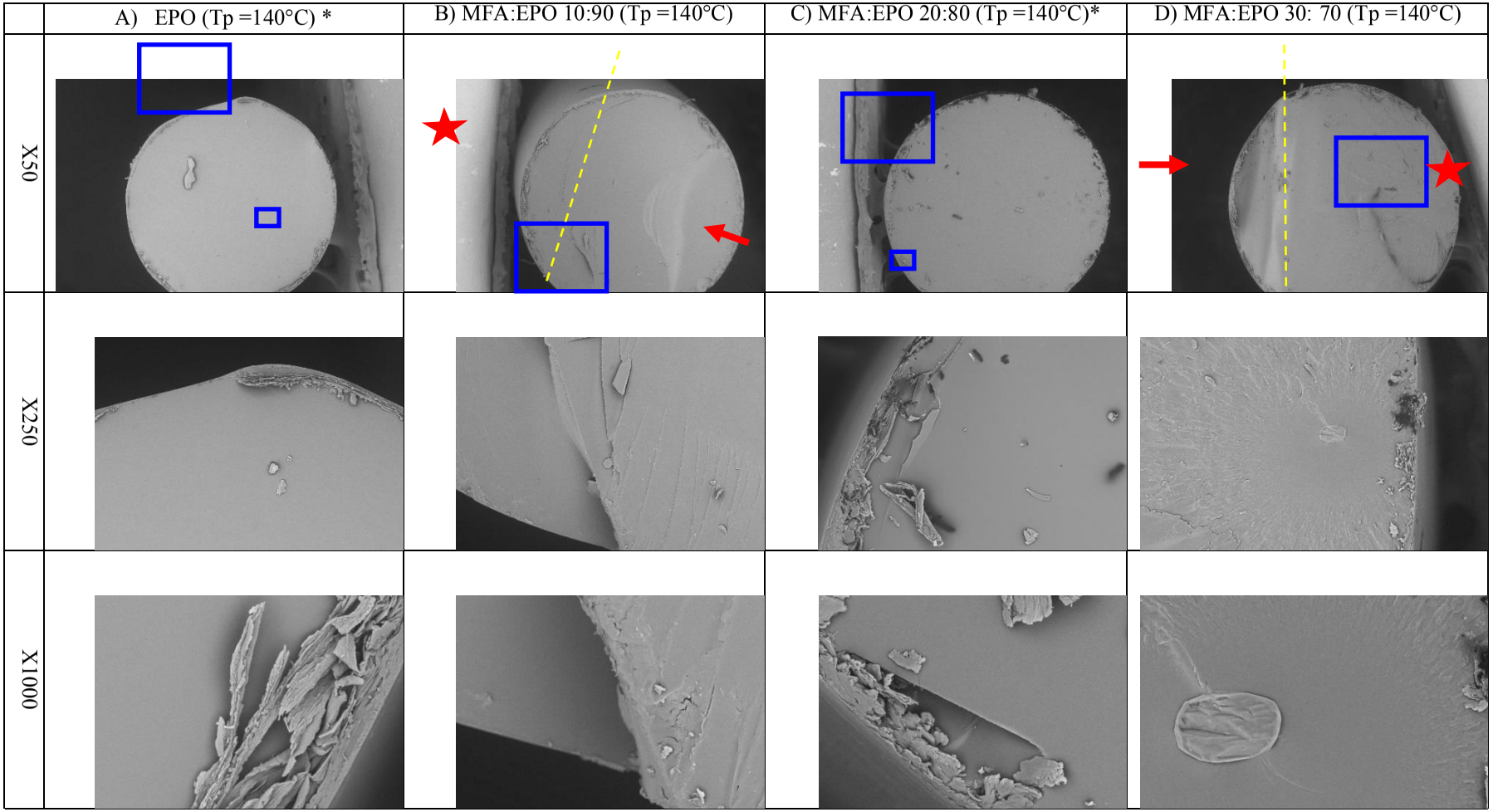

*Figure 2-14. Cross section images from the SEM of the net polymer EPO extrudate (A) the MFA:EPO extrudates at different drug load (B - D). Red arrows (stress direction), dashed line (separate the compression and tension areas) and stars (toward the tension area). * samples broken using three point bend test.*

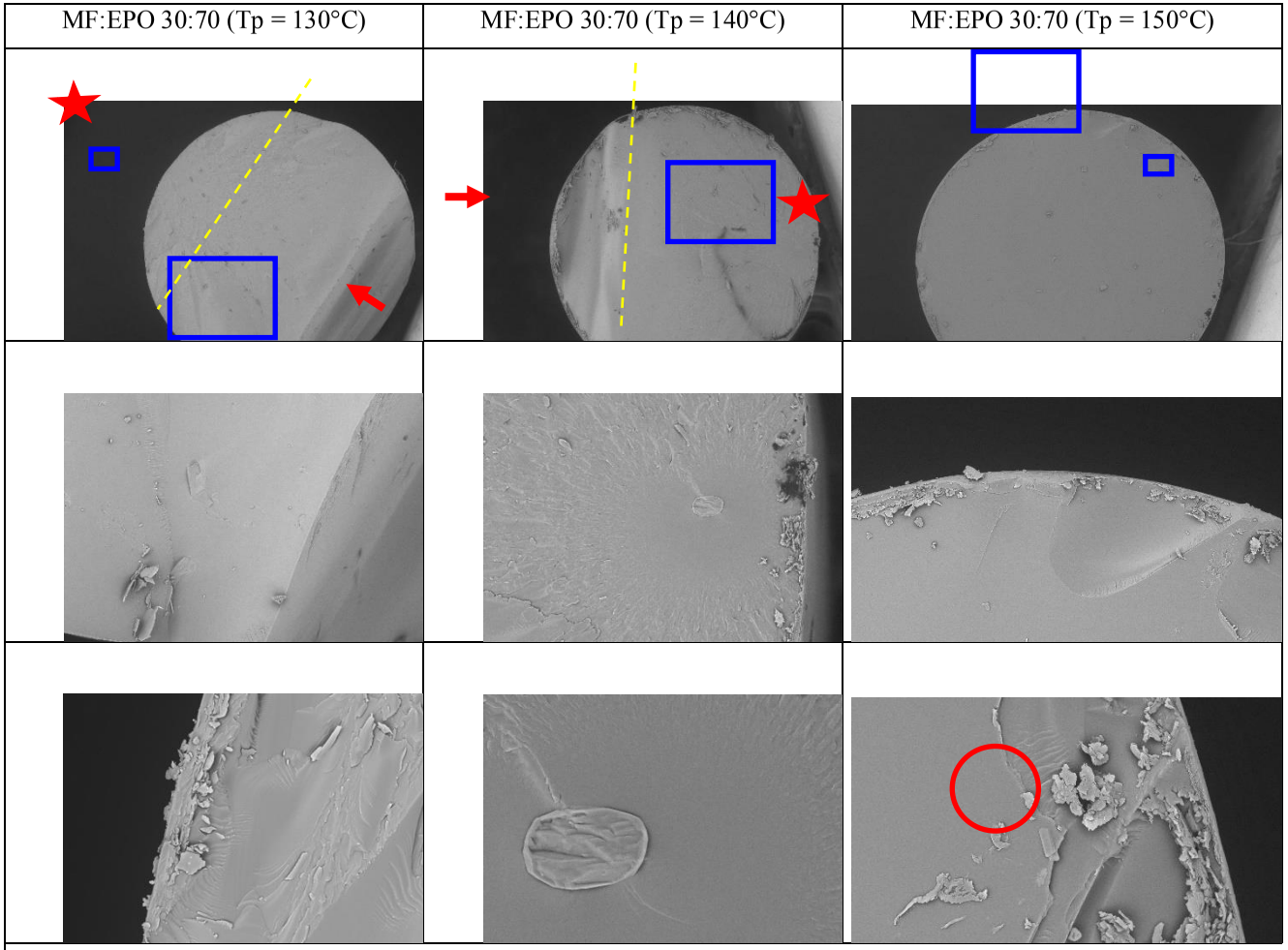

Figure 2-15. Cross section images from the SEM of the MFA:EPO 30:70 (wt:wt) extrudates at different process temperature 120-150°C (A – D, respectively). Red arrows (stress direction), dashed line (separate the compression and tension areas) and stars (toward the tension area).

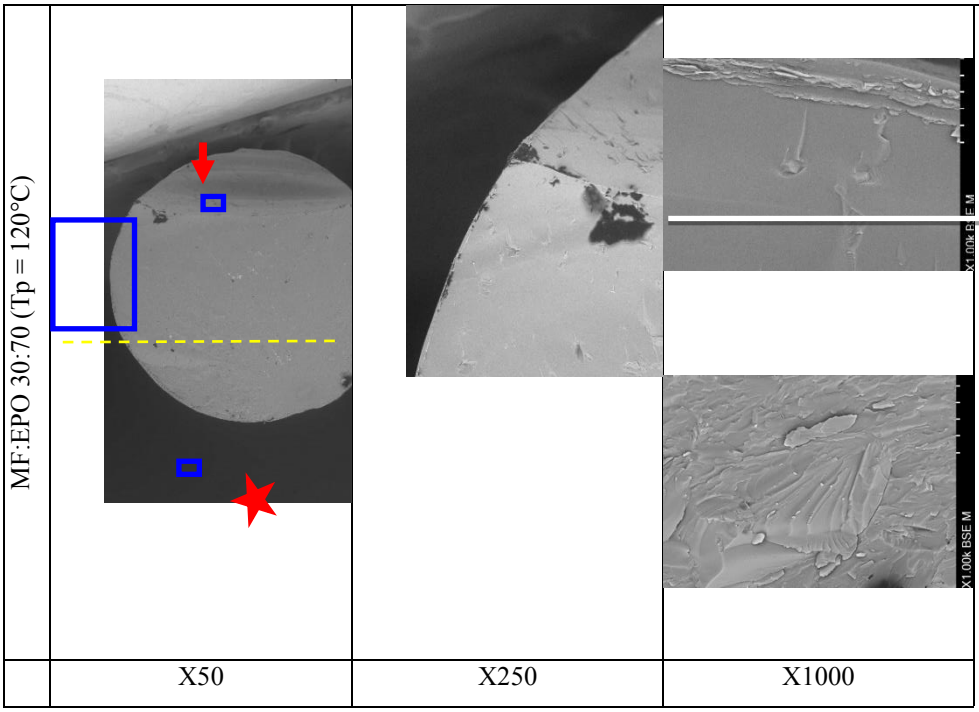

2.3.5.2. Intrinsic dissolution rate

The Intrinsic Dissolution Rate (IDR) and the amount of the drug released versus time from the surface of the 6 mm compressed desk were plotted in Figure 2-16 (raw dissolution data and the calculated IDR according to eq 2-1). The dissolution of the pure drug was very slow due to the low wettability of the BCS Class IIa especially at acidic pH [103], [125]. However, it is improved with presence of Eudragit EPO at all tested ratios. The polymer facilitated the wetting of the hydrophobic MFA particles [103], [125]. Comparing the physical mixtures with the extrudates, it was clear that the distribution of the MFA at the molecular level in the polymer significantly increased drug dissolution. This can be attributed to the amorphization of the drug which is easier to dissolve [12], [73], [74]. MFA:EPO 24:76 physical mixture showed improved dissolution in comparison with pure MFA and the solid solution MFA:EPO produced by cryogenic grinding method showed 200 times (in one hour) greater concentration than crystalline MFA (in 30 minutes) [104]. In the current work, solution saturation has not been achieved at the end of the dissolution test (2 hours). Number of factors caused this difference between the literature and the current study like manufacturing techniques and amount of MFA and volume of the dissolution media but most importantly was surface area. In the literature powder with particle size below 6.5 µm and in this work inform 6 mm compressed disk. For the dissolution rate, the physical mixture of MFA:EPO 20:80 (wt:wt) and 30:70 (wt:wt) showed increase up to 58 fold in comparison with MFA form

I crystalline powder. The extrudates of the same ratios (20:80 and 30:70, wt:wt) increased 507 and 267 times, respectively.

The MFA:EPO 10:90 and 20:80 processed at 140°C (solid solution samples ≤ Cc), MFA extrudates showed the fastest release followed by MFA:EPO 30:70 then 40:60 (wt:wt) processed at 140°C (crystalline solid suspension > Cc). These results are in agreement with previous work using same system (MFA:EPO) but on the USP apparatus II, 20% (wt%) drug load was the fastest release followed by 30% and 40% (10% was not analysed, wt%) [152]. Saboo et al studied the release behaviour from two solid dispersion systems namely polyvinylpyrrolidone-co-vinyl acetate with nilvadipine and cilnidipine at different ratios. They found that the release of the drug is polymer-controlled below the amorphous solubility limit, and drug-controlled above the solubility limit [158]. Similarly in this study, 20% (wt%) drug load exhibited the highest release rate (507 times higher than MFA) which was thought to be controlled by the EPO. By increasing the drug load above the amorphous solubility of MFA in 30% and 40% (wt%) systems (267 and 137 times higher than MFA, respectively), the drug load increased the hydrophobicity of the exposed surface and MFA crystalline stable form. Thus, a reduction in the release rate was observed.

To understand the impact of process temperature on the drug release, extrudates at 30% (wt%) drug loading processed at different temperatures were tested. The crystallinity content of MFA in the solid dispersion was expected to be the major effect controlling dissolution and higher temperature would dissolve greater amounts of drug in the matrix and also reduce the drug particle size of remaining solid drug. As a result, increasing the dissolution rate. However, the highest process temperature showed the lowest dissolution rate. The reason of the inverse effect of the temperature is not clear, it might be due to the increase of matrix hydrophobicity due to dissolved drug. Ouyang suggests that the drug interacts with the exposed polymer coil functional groups instead of being distributed uniformly. Ouyang's argument explained that the high energy barrier to release the drug from a uniform matrix would not justify the dissolution enhancement [159]. On the other hand the energy input in the process (heat and shear stress) allows the polymer chains to slide and expose to the neighbouring molecules [133], [135], [136]. As a result, a possible explanation is that the higher temperature was the reason to trap more MFA molecule in the polymer matrix. Although this could justify the result, this hypothesis requires further investigation which is out of the scope of this study.

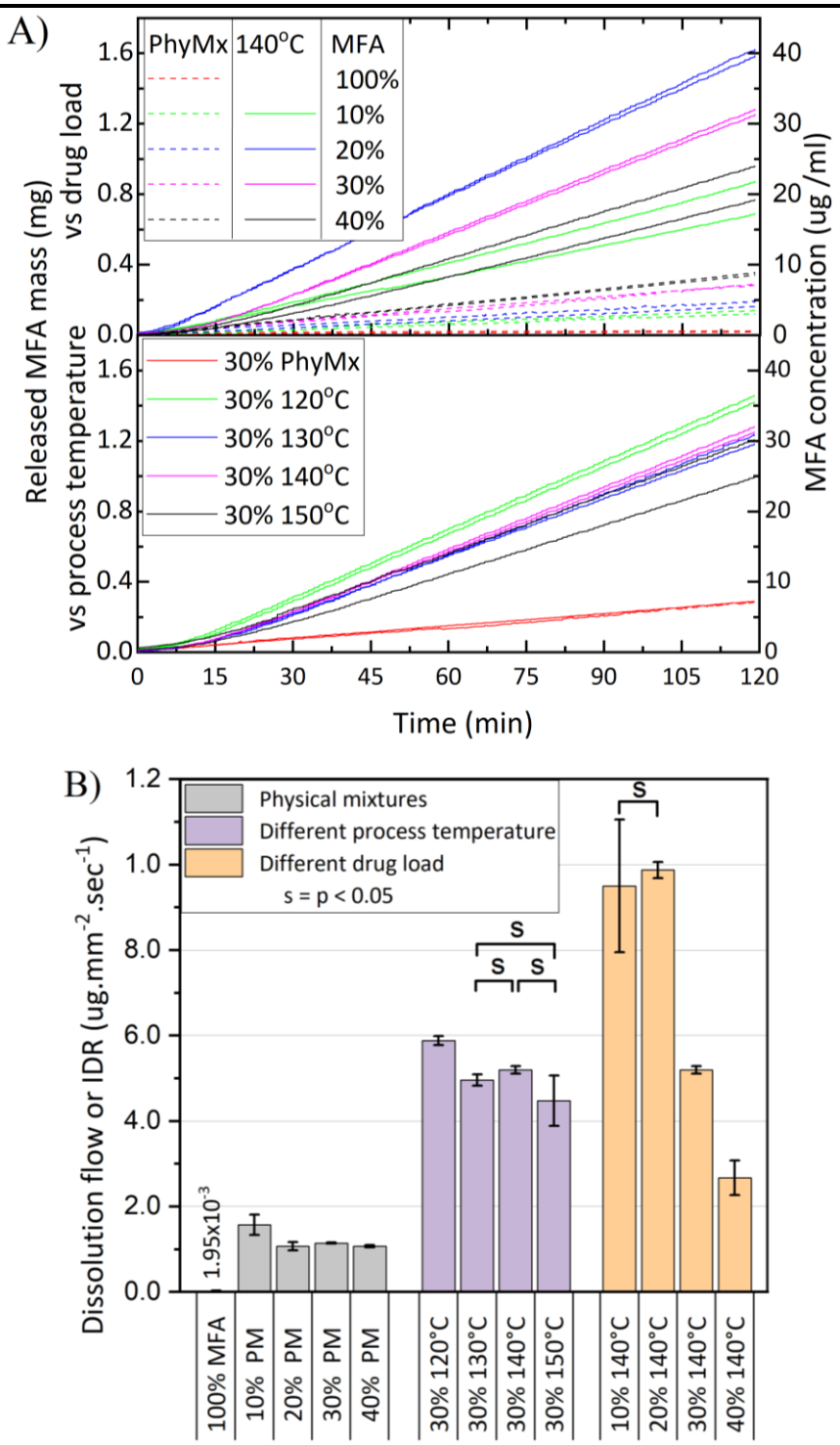

Figure 2-16. The Amount of MFA (A) and the calculated intrinsic dissolution rate of MFA (B) from the 6 mm compressed tablets of the MFA powder and MFA:EPO physical mixtures, and extrudates loaded with drug at different concentration or processed at different temperatures. IDR values calculated according to eq 2-1. Average (n = number of data points in graph A, 200), Mann-Whitney test (s = P < 0.05 significant difference).

2.4. Conclusion

MFA-EPO extrudates at drug loads between 0-40% (wt%) were extruded using an 11 mm HME at process temperatures between 120-150°C. Both presence of the drug and higher temperatures reduced the resistance in the HME barrel. However, above the solubility limit of MFA in EPO increasing the drug concentration increased the resistance for process temperatures below the MFA melting point. High temperature is not recommended due to potential for MFA sublimation and poor control of extrudate diameter. A cooling belt can be used to control the diameter, but it is less effective at low temperatures due to the low friction and pulling force on the extrudate.

To study the phase diagram, Raman Low frequency analysis detects MFA form I crystalline material both in-line and offline, but the detection limit was restricted due to the low penetration depth into the matrix. Thus, lower concentrations of crystalline material coupled with the absence of crystal next to the extrudate surface limited the detection ability. The Raman microscopy provides information on the molecular level and can identify the potential phase separation. Also transmission technique is preferable over the reflective one, since it gives better idea of the bulk.

All MFA-EPO systems were not feedable into the printer due to brittleness. Which is caused due to polymer properties, molecular interaction in the solid solution and particle ratio in the crystalline solid dispersion. The polymer properties affect the mechanical properties especially in the solid solution region since it constitutes about ≥ 80% (solubility limit 20%, wt%) of the system. In the solid solution, the drug interacts with the polymer in two ways, causing a reduction in the polymer mobility and as a result an increase in the flexural modulus and brittleness. In the crystalline solid dispersion, the particles increased the brittleness significantly. The influence of process temperature on the mechanical properties was not significant at all drug loads except the 20% (wt%) system.

The fraction progression can be visualised on the SEM to understand the brittleness behaviour of the system. EPO fractures in a brittle manner. MFA increases the stiffness releasing more elastic energy that causes secondary crack propagation and increase in brittleness. If MFA particles presences in the matrix, they work as weak points to form crack flaw and mist region.

EPO increases the dissolution rate of the MFA due to improving the hydrophobic MFA particles wettability for the physical mixtures and amorphization of the crystalline drug for solid dispersion systems. The highest dissolution rate is achieved in by the solid solution samples, whilst in the crystalline solid dispersion, the presence of MFA crystals reduced the rate significantly. A higher HME process temperature surprisingly reduced the dissolution rate in the 30% (wt%) drug load extrudates, even although the sample contains less MFA particles.

Since all samples are brittle, additives should be considered to improve the mechanical properties. The best formula for further development was the 20:80 MFA:EPO, because it achieved high release rate and is the highest concentration in the solid solution region. The higher drug load (>20%, Crystalline solid dispersions) are not considered for the next stage because of the poor mechanical properties and slower dissolution rate.

This page is left empty.

Chapter 3: Multicomponent systems (Drug-Polymer-Plasticizer), mefenamic acid-Eudragit formula development:

3.1. Introduction

As discussed in Chapter 2, the MFA-EPO binary system is not printable due to filament brittleness arising from poor polymer mechanical properties, MFA-EPO molecular interaction and the presence of MFA crystals in the matrix. To improve the best MFA-EPO formula (20:80, wt%), addition of plasticizers and fillers were considered. Different plasticizers were tested to improve the strain at break value (reduce brittleness).

The terms physical mixture, extrudate, filament and formula used in this chapter have the same meaning in previous chapter (Figure 2-1).

To satisfy the study objectives, this chapter was designed to answer the following questions:

1- Which plasticizers are suitable candidates for use in MFA-EPO blends for FFF-3D printing filament?
2- Can HSPs predict plasticizer compatibility for drug-polymer blends to produce FFF-3D printing filament?
3- What effects do various plasticizers have on the glass transition temperature and mechanical characteristics of drug-polymer filaments?
4- How do the different plasticizers affect the solubility of MFA in EPO, and how does this impact the mechanical properties of the 3D printing filament?
5- What is the most promising plasticizer for further development of MFA-EPO filament, and why?

3.2. Materials and Methods

3.2.1. Materials

For EPO and MFA see Chapter 2. Tween® 80 (TWN; supplier product code (PC) #P1754), poly(ethylene glycol) MW 400 (PEG4h; PC #P3265), poly(ethylene glycol) MW 4000 (PEG4k; PC #81242), triethyl citrate (TEC; PC #w308307) and stearic acid (StA; PC #175366) was purchased from Sigma-Aldrich (Leicestershire, UK).

3.2.2. Methods

3.2.2.1. Plasticizer screening

3.2.2.1.1. Hansen Solubility Parameters (HSPs):

HSPs were calculated for common pharmaceutical plasticizers using Y-MB method on HSPiP software version 5.4.02 [160]. For Eudragit EPO, the software blend function was applied to take into account the ratio of each monomer in the copolymer. Distance (Ra in $MPa^{1/2}$) between each of MFA and EPO from the plasticizers were calculated.

$$Ra = \sqrt{[4(\delta_{D2} - \delta_{D1})^2 + (\delta_{P2} - \delta_{P1})^2 + (\delta_{H2} - \delta_{H1})^2]} \qquad \text{(eq 2.1)}$$

The constant 4 was previously determined to fit the prediction more accurately for solvent-polymer systems [161] and therefore applied in this work. δ_P δ_D δ_H are the energy from dipolar intermolecular, dispersion and hydrogen bonding forces between molecules.

HSPs were also normalised to be used in Teas plot [162]. The normalisation equations are eq 2.2, eq 2.3 and eq 2.4

$$f_D = \frac{100 \times \delta_D}{\delta_D + \delta_P + \delta_H} \qquad \text{(eq 2.2)}$$

$$f_P = \frac{100 \times \delta_P}{\delta_D + \delta_P + \delta_H} \qquad \text{(eq 2.3)}$$

$$f_H = \frac{100 \times \delta_H}{\delta_D + \delta_P + \delta_H} \qquad \text{(eq 2.4)}$$

These values were calculated for all the following materials MFA, EPO, stearic acid, polyethylene glycol, triacetin, Tween® 80, methylparaben, triethylene glycol, propylene glycol, urea, ethyl glycol, triethyl citrate, glycerol, xylitol and D-mannitol. For comparison purpose, HSPs of Lumefantrine, a drug, were also calculated [163].

3.2.2.1.2. Hot stage microscopy and DSC:

For the binary physical mixture 85:15 ratio of EPO:plasticizer a miscibility study was conducted using the hot stage microscope (see section 2.2.2.3.4) and DSC (see section 2.2.2.3.1) combined. The temperature profile was designed to mimic the target process temperature (150°C except 120°C for TEC formulation), heating at 20°C/min then holding for 9 minutes, before finally cooling down to 20°C.

Table 3-1.Temperature profile of MFA:StA samples on the HSM:

State	Start	Heating	Heating	Heating	Cooling
Target temperature (°C)	25	60	80	130	20
Rate (°C/min)	-	20	20	20	20
Holding time (min)	-	2	2	10	-

3.2.2.1.3. Film casting:

Film casting was employed to confirm the miscibility results obtained from DSC and HSM. A solution of EPO in isopropanol (3.4 mL at 14.3%, wt%) was mixed with plasticizer in isopropanol (1.2 mL at 6.8%, wt%), sealed in a sample bottle and sonicated for 5 hours, 3.5 mL was added to a petri dish (radius 52 mm) and left open to evaporate the solvent and create a film with a 85:15 (wt%) mixture of EPO:plasticizer. Phase separation within the film was assessed using the optical microscope. Mixtures with homogenous appearance considered miscible (See result section Figure 3-4).

3.2.2.2. TGA, Pure component thermal degradation

Stability of the pure components (plasticizers and fillers) were examined using thermogravimetry (see section 2.2.2.3.2). Heating profile was from 20°C to 240°C at 20°C/min heating rate. Plasticizer was also run at the potential HME process temperature using an isothermal stage at 150°C with a holding time equal to the residence time in the hot melt extruder for EPO (9 min) to investigate the degradation of the components. All samples were analysed in duplicate.

3.2.2.3. Production of the filaments (Hot melt extrusion):

HME details can be found in section 2.2.2.1.1. The following paragraphs indicates the changes to these parameters for the formulae examined in this chapter. The chosen plasticizers from the HSPs calculation were either solid like PEG4000 and StA or liquid like PEG400, TEC and TWN. For the solid materials, flakes of PEG4k and StA were milled using mortar and pestle then sieved using 300 µm mesh. Then powder mixtures were prepared and extruded as described in section 2.2.2.1.1. Process temperature and die temperatures are provided in table 3-2. The liquid materials were added using a syringe pump calibrated for each liquid (mg vs time), with the flow rate checked for 20

min and before each experiment. The pump connected to the HME in the first quarter of the HME barrel after the hopper.

Table 3-2.Process and die temperature of the polymer:plasticizer formulae:

		Tp (°C)	T die (°C)*
EPO:PEG4k	**95:5**	150	130
EPO:PEG4k	**85:15**	150	115
EPO:StA	**95:5**	150	120
EPO:StA	**85:15**	150	105
EPO:PEG4h	**95:5**	150	120
EPO:PEG4h	**85:15**	150	110
EPO:TWN	**95:5**	150	130
EPO:TWN	**85:15**	150	115
EPO:TEC	**95:5**	120	115
EPO:TEC	**85:15**	120	100

* T die was changed experimentally to achieve extrudates with diameters between 1.6-1.9 mm.

In the second stage the MFA:EPO:plasticizers except PEG4k was extruded at ratio of 20:76:4, respectively. Zone 8 and die temperature was changed to obtain a consistent diameter. Table 3-3 shows the process temperature, zone eight and die temperatures for these formulae. More filements with StA (Table 3-3) were produced to understand the impact of the StA on the mechanical properties.

Table 3-3.Process and die temperature of the MFA:Polymer:Plasticizer formulae, the additional formulae with StA and the EPO:StA formulae:

	T_p (°C)	T_{Zone8} (°C)	T_{die} (°C)
MFA:EPO:plasticizer (20:73:4, wt%)			
MFA:EPO:StA	150	115	110
MFA:EPO:PEG4h	150	120	105
MFA:EPO: TWN	150	120	115
MFA:EPO:TEC	120	120	115
MFA:EPO:plasticizer (20:65:15, wt%)			
MFA:EPO:StA	150	115	100
MFA:EPO:PEG4h	150	115	100
MFA:EPO: TWN	150	115	100
MFA:EPO:TEC	120	115	100
MFA:EPO:StA additional formulae			
0:90:10	130	115	110
72:20:8	130	115	110

3.2.2.4. Phase separation:

3.2.2.4.1. Optical Microscope:

Two optical microscopes were used during the studies, a Leica DM2700 and Leica DM6000. DM2700 is attached to the hot stage (see section 2.2.2.3.4), the DM 6000 was used for checking phase separation in the film casting method (see section 3.2.2.1.3) and in the produced filaments. The microscope was Leica DM6000 M F5 Optical microscope (Leica Microsystems, Wetzlar, Germany).

3.2.2.4.2. Differential scanning calorimetry (DSC):

DSC (see section 2.2.2.3.1) was used to investigate the compatibility of 95:5 and 85:15 ratios of EPO:plasticizer. The same temperature profiles used on the HSM (3.2.2.1.2.) for these mixtures were used on the DSC, 5-6 mg of the physical mixtures or pure components were tested in duplicate.

The extrudates of EPO:plasticizers were analysed using a heating and cooling cycle between 20-160°C without an isothermal hold step, collecting two replicates for each extrudate. For the extrudates of the MFA:EPO:plasticizer (PEG4h, TWN, TEC and

StA) two methods were applied. The first was similar to that used for the binary system i.e. up to 160°C. The second was used with MFA:EPO formulations taking the temperature up to 250°C to check for the absence of the MFA melting peak. The different methods were used to measure the glass transition temperature and check the presence of an MFA melting point. Glass transitions in all studies were measured using onset of the glass transition according to the tangent method.

3.2.2.4.3. X-ray Diffraction techniques (XRPD, SAX and WAX)

StA powder and all ternary systems MFA:EPO:Plasticzer were analysed using the xray diffractometer, details of the instrument and method can be found in 2.2.2.2.2.

For EPO-StA compatibility investigation, small and wide angle Xray diffraction (SAX and WAX) were collected simultaneously using Xeuss 2.0 (Xeuss 2.0 SAX/WAX laboratory beamline "16370504", Xenocs, France). Source radiation was Cu of wavelength 1.5406 Å. Operation voltage and current were 40kV and 0.6 mA, respectively. Single reflection multilayer optics with 2D collimation was used. While slits were two 2.0 scatter-less motorised slits with variable aperture. Transmission stage was used at 170 mm distance from the detector. Collection time was four hours. For the background signal, the diffraction signal of air was collected. Extrudates of EPO, EPO:StA at ratio of 95:5, 90:10 and 85:15 (wt%) were mounted on a sample holder for analysis.

Data was normalised for transmitted intensity and integration performed over the whole two theta range using Foxtrot data reduction software (Version 3.4.9, Xenocs, Grenoble), and presented as a 1D diffraction pattern.

3.2.2.5. Performance and mechanical properties

3.2.2.5.1. Three-point bend test:

All samples of EPO:Plasticizer and MFA:EPO:Plasticizers, prepared by HME (3.2.2.3.1) were tested on the 3-point bend test (see section 2.2.2.5.1).

3.2.2.4.2. Scanning Electric Microscope:

Method details can be found in section 2.2.2.5.3.

3.2.2.5.2. 3D printing test:

Details of Creality Ender 3 3D printer can be found in Chapter 2, section 2.2.25.2. Dimensions of the MK8 extruder elements can be found in Figure 3-1. The MK8 extruder contained a single spur geared (26 teeth) and stainless steel M6 throat with polytetrafluoroethylene (PTFE) tube inside.

Relevant samples were tested on the printer after manually inserting the filament, a 10 mm piece was marked, using a G-Code order to extrude 10 mm at a speed of 60 mm/min and 120 mm/min. Filament tested at 150°C and 160°C printing temperature. Initially, the tension from the spring was set to apply the minimum tension on the filament. If the 10 mm was not extruded, the test failed and was then repeated after the spring tension was increased to improve the friction between the gear and the filament. The tension was increased until buckling or breaking occurred. The rationale was to find a tension high enough to provide friction to push the filament forward but below a limit that can cause damage to filament's cross section.

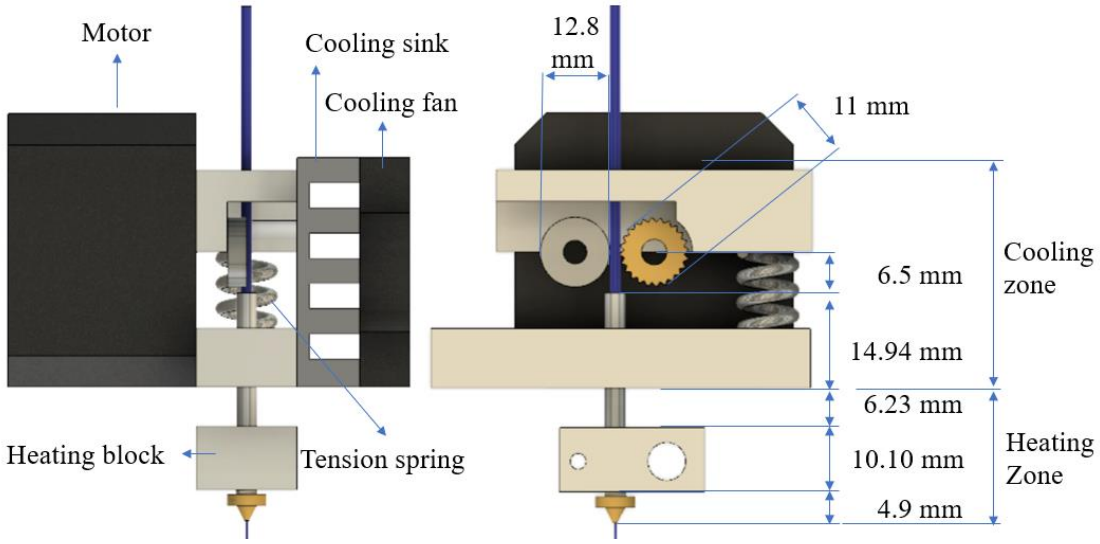

Figure 3-1. Schematics from two sides of the direct extruder of the 3D printer used in this study, main elements defined (left), and main dimensions indicated (right).

3.3. Results and discussion

3.3.1. Binary system Polymer – plasticizer

3.3.1.1. Plasticizers compatibility study

The previous chapter demonstrated that all the MFA:EPO binary systems are not suitable for printing due to their brittleness. Therefore, additives are required to improve

the mechanical properties [105]. Common plasticizers have been considered and included with their HSPs values in table 3-4. Distance of the HSPs values from MFA and EPO (Ra $_{MFA}$ and Ra $_{EPO}$, respectively) were calculated using equation 2b.1 (Table 3-4). Polyethylene glycol (PEG), stearic acid (StA) and triacetin were the closest to EPO, their Ra EPO below 7 $MPa^{1/2}$. While Tween 80 (TWN), triethyl Citrate (TEC) and MFA were in Ra $_{EPO}$ range of 7 to 10 $MPa^{1/2}$. The differences between the value for the remaining plasticizers were larger. All the plasticizers with Ra $_{EPO}$ below 10 $MPa^{1/2}$ also had Ra $_{MFA}$ below 10 $MPa^{1/2}$, with triacetin and TEC being the closest to MFA. Moreover, all the Ra $_{EPO}$ above 10 $MPa^{1/2}$ had Ra $_{MFA}$ above 10 $MPa^{1/2}$, with one exception methylparaben which had Ra $_{MFA}$ of 4.56 $MPa^{1/2}$.

Greenhalgh et al found that the miscibility likelihood of a drug and a carrier can be predicted using the HSPs where values fall below a difference value [164]. Melting and evaporation methods were applied to produce solid dispersions followed by DSC and XRPD analysis to confirm their prediction. HSPs were also calculated for solid dispersions from the literature to broaden their findings on other systems. Three categories can be identified based on the difference of the overall HSPs values; <7 $MPa^{1/2}$, 7-10 $MPa^{1/2}$ and >10 $MPa^{1/2}$. These regions corresponding to miscible, partially miscible and immiscible drug-polymer, respectively [164]. Utilising these findings, it can be concluded that PEG, StA, triacetin, TWN, TEC were compatible plasticizers for the MFA:EPO formulae. This result is in agreement with the literature where these plasticizers except triacetin have been used for Eudragit polymers (E and RL grades) to produce 3D printing filaments [81], [85], [92], [95]. Triacetin was used to plasticize Eudragit E for tablet coating applications [165].

Based on a literature survey the other plasticizers have not been used with Eudragit EPO, except xylitol. Fanous et al produced filaments for 3D printing application using Eudragit EPO as a polymer carrier, Lumefantrine as a drug, xylitol as a plasticizer and maltodextrin as a pore former. In this study, the placebo and 5% formulae were brittle, while higher drug loadings were flexible [163]. By calculating the Lumefantrine HSPs (19.5, 3.3 and 5.4 for δ_D, δ_P and δ_H, respectively), it was found to have similar values to EPO (Ra $_{EPO}$ = 3.4). Therefore, the drug is most likely to be the plasticizer instead of the xylitol, while the xylitol interacted with the maltodextrin due to the high presence of hydroxyl groups. This hypothesis aligned with the mechanical properties trend indicating a drug plasticization effect.

Table 3-4.Common plasticizers, HSPs values and differences from both the polymer carrier (Ra $_{EPO}$) and MFA (Ra $_{MFA}$):

	δ_D	δ_P	δ_H	Ra $_{EPO}$	Ra $_{MFA}$	Closer to
	(MPa$^{1/2}$)					
Eudragit-EPO	18.2	2.5	3.2	0	7.47	EPO
Polyethylene Glycol	17.9	3.4	2.6	1.24	7.98	EPO
Stearic Acid	16.2	2.8	5.2	4.52	8.81	EPO
Triacetin *	16.8	5.8	8.7	6.95	6.19	MFA
Mefenamic Acid	19.9	5.3	9.2	7.47	0	MFA
Tween 80	16.3	5.5	9.5	7.96	7.21	MFA
Triethyl Citrate	16.8	6.0	10.1	8.23	6.4	MFA
Methylparaben	19.0	9.1	11.0	10.35	4.56	MFA
Triethylene Glycol	17.0	9.8	16.9	15.69	10.6	MFA
Propylene Glycol	17.3	10.2	22.1	20.49	14.76	MFA
Urea	19.7	19.8	21.3	25.2	18.87	MFA
Ethyl glycol	17.8	13.5	27.4	26.53	20.33	MFA
Glycerol	18.3	12.7	27.8	26.66	20.27	MFA
Xylitol	17.7	11.5	28.9	27.29	21.16	MFA
D-Mannitol	17.3	11.2	29.9	28.12	22.1	MFA

Scale from 0-30 MPa$^{1/2}$, values ≤7 considered miscible (in green), between 7-10 partially miscible (in orange), >10 immiscible (in red).

* Only miscible plasticizers with EPO were considered for further investigation. Triacetin (glycerol triacetate) was the only plasticizer that was miscible and was not used.

Molecular volume can be found in table 3-10 and table appendix 2-1.

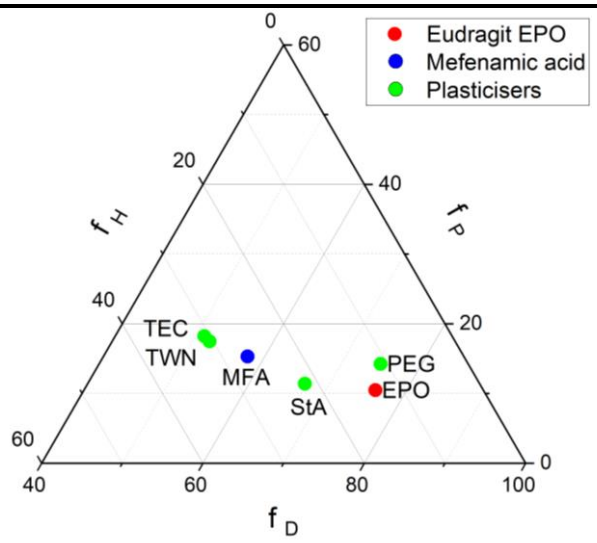

Figure 3-2. Teas Plot of chosen plasticizers (green), MFA (blue) and EPO (red) showing the relative distances between the pure components' solubility parameters.

Based on the analysis above five plasticizers (TWN, TEC, StA, PEG4h and PEG4k) were selected for further testing. The various grades of Eudragit, such as EPO, L, and RL, were plasticized using some of those plasticizers, including PEG4h, PEG4k [81], [85] and TWN, to produce 3D printing filament at ratios of 16.7%, 16.7%, and 11% (wt%), respectively [105]. Therefore, miscibility studies were conducted using DSC, HSM and film casting techniques on EPO:Plasticzers at 95:5 and 85:15 (wt%) to confirm the miscibility prediction.

Forster et al [132] coupled the HSPs miscibility prediction with DSC and HSM to provide a small scale screening method before HME experiments. Figure 3-3 shows the DSC traces of both first cooling cycle and second heating cycle i.e. after producing solid dispersion (first heating cycle) of EPO:Plasticizer. PEG4k separated from EPO on both EPO:PEG4k 95:5 and 85:15 (wt%) ratios since both crystallisation and melting peaks were observed on the cooling and heating cycles, respectively. StA did not show phase separation due to absence of the melting peak. While TEC, TWN and PEG4h are liquids and no melting peaks presented in the corresponded formulae to detect phase separation. Tg(s) of EPO and binary mixtures can be found in table 3-6. Glass transitions ranged between 43°C to 52°C. All plasticizers except PEG4k caused either decreasing or total absence of Tg. This impact was a result of polymer-plasticizer molecular interaction and the increase in the free space between the molecular chain [135]. At 85:15 (wt%) for EPO:PEG4h, EPO:TWN and EPO:TEC, the change in the heat

flow was not pronounced or did not occur in the studied range, thus Tg(s) were not recorded.

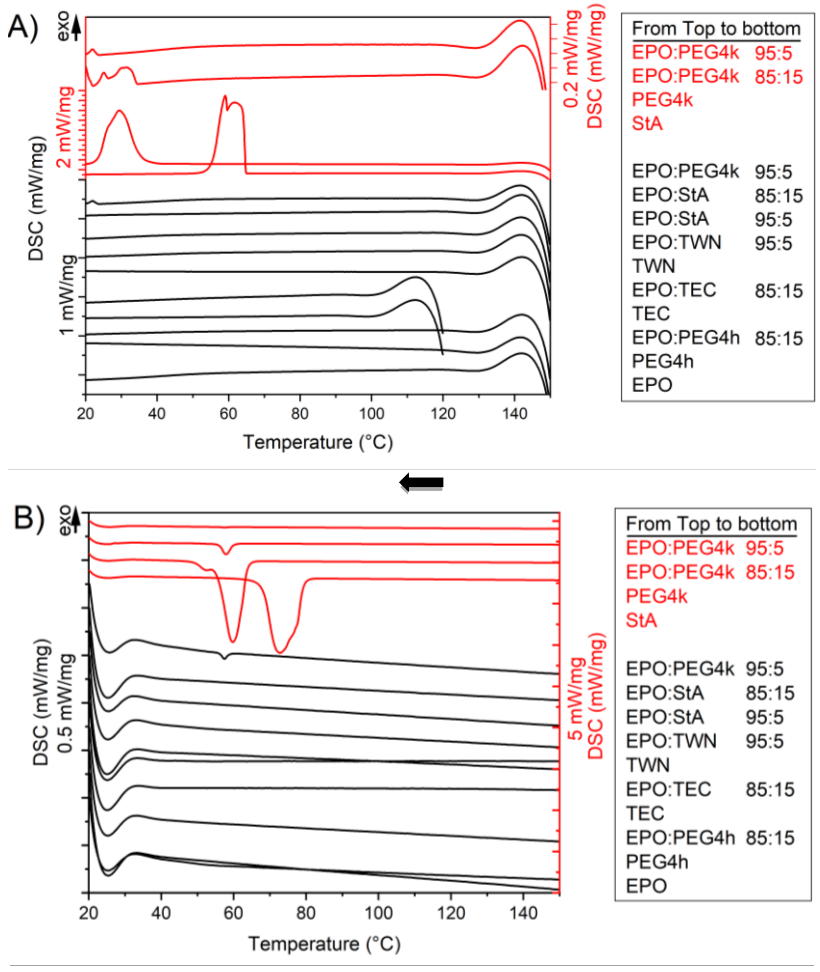

Figure 3-3. DSC traces of EPO:Plasticizer formulae (mixtures not extrudates) and the pure component from thermal profile of two cycle. Cooling graphs from melt of the first cycle (A), Heating graphs of the second cycle (B).

On the HSM the impact of the plasticizer on EPO liquification and phase separation at both high temperature and after cooling could be observed. Table 3-5 exhibits microscopic images of the pure components and binary mixtures. EPO particles kept a sharp-edged appearance until 98°C (> 52°C, Tg). Which is thought to be a result of the complex side chain and structural entanglement that also caused the torque build up during HME (Chapter 2: 2.3.1). Branched metallocene low-density polyethylenes (mLLDP) had higher zero-shear viscosity and flow activation energy in comparison with linear mLLDP [166]. Similar to the DSC results, PEG4k did not produce a homogeneous mixture with EPO and had neglectable impact on its observed

liquification. While StA (at EPO:StA 85:15, wt%) dropped the liquification of EPO to below 90°C and formed a homogenous mixture at high temperature. But at low temperature droplet-like shapes appeared. PEG4h, TWN and TEC had a stronger impact on EPO liquification and homogenous appearance. Due to the absence of physical mixing in the DSC and HSM, film casting experiment were conducted to confirm the results. Microscopic images from the film casting experiment can be found in Figure 3-4. EPO:TEC and EPO TWN at 85:15 (wt%) had smooth and homogenous appearance. While EPO:PEG4k, PEG4h and EPO:StA 85:15 showed phase separation. The film casting was used as a supporting experiment and not considered in isolation for decision-making due to the potential of trapped solvent in the film. It is acknowledged that isopropanol may not completely evaporate at room temperature, which could affect the results.

Table 3-6 is a summary of the miscibility study. Although PEG4k and PEG4h are same in terms of the chemical structure the miscibility results were different. This was due to the impact of the molecular volume and the difference of diffusion of the molecules in EPO [161]. Honary and Orafai prepared films using different molecular weight and ratios of PEG with hypromellose (HPMC). Phase separation was observed as molecular weight and PEG ratio increased [167]. StA and PEG4h can be considered as partially miscible with EPO since some techniques showed interaction with the main polymer. TEC and TWN were miscible at all ratios up to EPO:Plasticizer 85:15 (wt%). Alhijjaj et al investigated a mixture of EPO, PEG4k, PEO WSR N10 and TWN for a placebo 3D printing formula [85]. The complexity of the formula made it hard for direct comparison. Melting peaks appeared in their filament and printed tablet between 60°C and 70°C. Which was associated with PEG/PEO crystallinity and indicating phase separation. The presence of both PEO and TWN might also reduce or increase the enthalpy. Sadia et al used DCS to scan TEC ratios between 5% to 10% (wt%) by measuring Tg from heating cycles [92]. Although the miscibility results are in agreement with their observation of Tg reduction, the measurement of a low Tg during the heating cycle was found to be problematic, since the instrument switches off nitrogen cooling stream and activates the heating, resulting in an artificial peak and affected values at low temperature. Therefore, a cooling cycle was used in the current work and determined that 6.5% was the optimum ratio of TEC [92]. Korte and Quodbach used StA to plasticize Eudragit RL, another amino methacrylate copolymer and found it to interact and reduce the Tg of the polymer [95].

Table 3-5. (Part 1): HSM miscibility study of EPO:Plasticizers physical mixtures:

	Start (°C)	Heating (°C)	Target T (°C)	Cooled (°C)
EPO	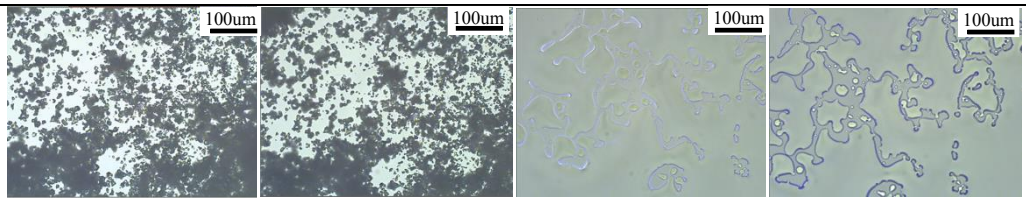			
	20	70	150	20
PEG4k	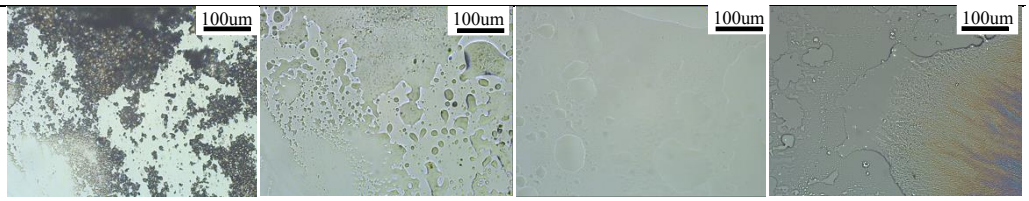			
	20	69	150	20
EPO:PEG4k 85:15	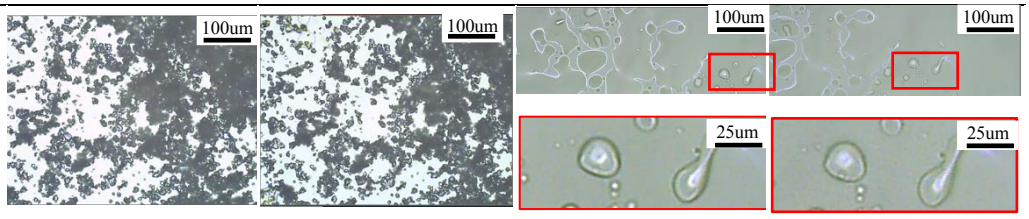			
	20	70	150	20
StA	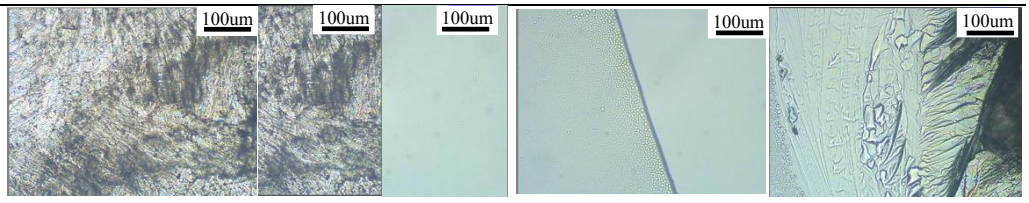			
	25	70 – 84	150	20
EPO:StA 85:15	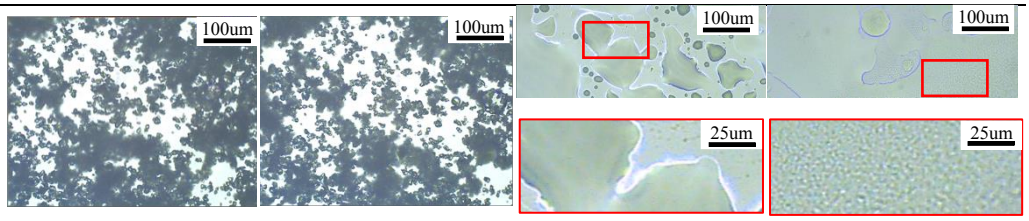			
	25	84	150	20
EPO:PEG4h 85:15	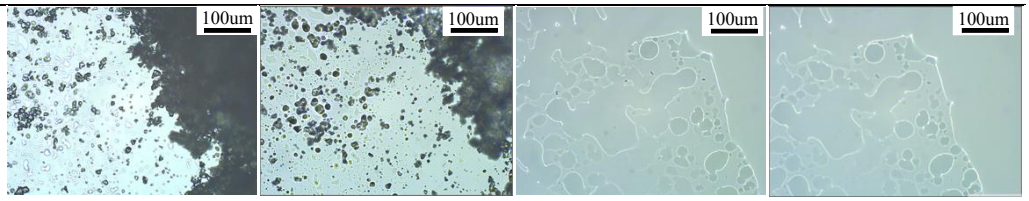			
	25	70	150	25
EPO:TWN 85:15	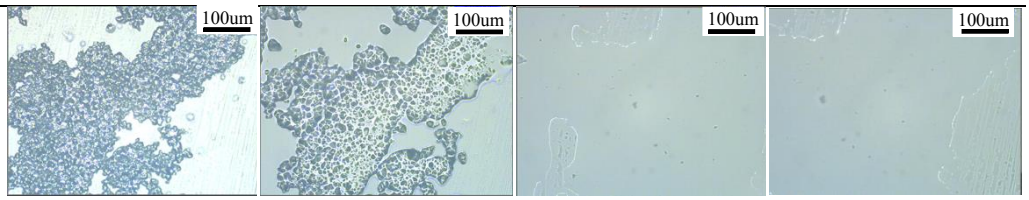			
	25	70	150	25

Table 3-5. (Part 2): HSM miscibility study of EPO:Plasticizers physical mixtures:

	Start (°C)	Heating (°C)	Target T (°C)	Cooled (°C)
EPO:TEC 85:15	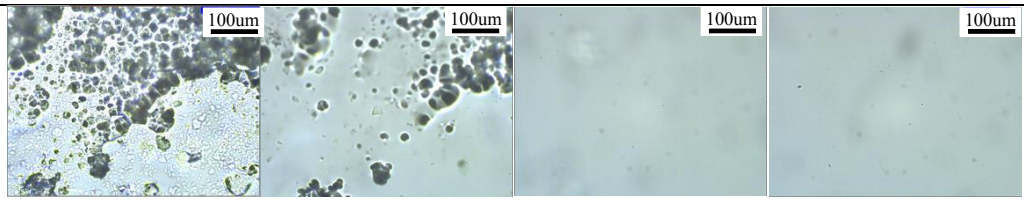			
	25	70	120	25

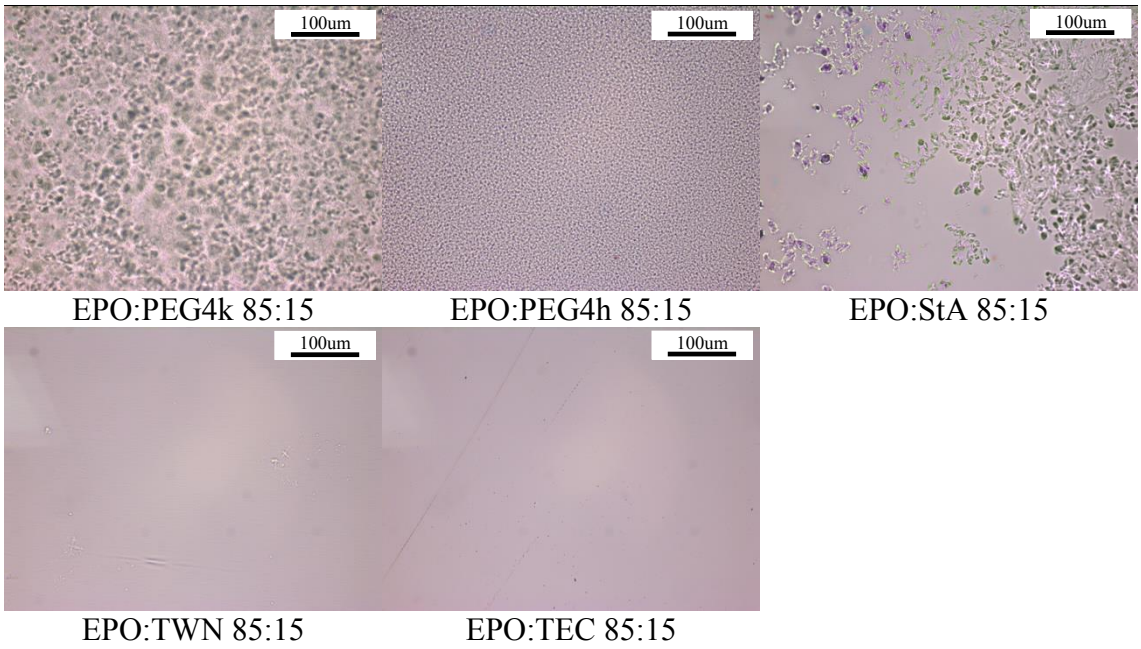

Figure 3-4. Microscopic images from the film casting of EPO:Plasticizers at 85:15 (wt%) ratios.

Table 3-6. Miscibility study of the EPO with different plasticizers namely StA, TWN, TEC, PEG4h and PEG4k using three techniques DSC, HSM and film casting:

	Ratio	Tg* (°C)	HSM ** of 15% mixture	Film Casting ** of 15% mixture	Miscibility ***
EPO	-	52	-	-	-
EPO:PEG4k	95:5	52	Phase separation	Phase separation	Immiscible
	85:15	50			
EPO:PEG4h	95:5	43	Some cloudy zones	Undulate surface	Partial miscibility
	85:15	-			
EPO:StA	95:5	47	Clear	Phase separation	Partial miscibility
	85:15	49			
EPO:TWN	95:5	52	Clear	Clear	Miscible
	85:15	-			
EPO:TEC	95:5	48	Clear	Clear	Miscible
	85:15	-			

* Glass transition = average of two replicates, Tg measured as tangent onset from the cooling cycle. Some replicates showed about 3°C difference. No Tg observed at TEC, TWN and PEG4h high ratio (85:15).

** Phase separation was shown as liquid or solid spots in the polymer matrix, cloudy appearance of the mixture or separation on the surface of the film.

*** The material considered; miscible if the 15% ratio created clear mixture, partial miscible if only small separation was shown at high additive ratio, immiscible if clear separation noticed.

3.3.1.2. Pure components degradation

Before HME experiments, pure component thermal stability was studied by measuring the mass loss, Figure 3-5 and Table 3-7, using two methods. The first was a one step dynamic heating to high temperature and the second was two steps including a holding at a potential HME process temperature. The mass loss up to 120°C (heating rate 20°C/min) was considered due to water and/or volatile material. All the five plasticizers were studied including PEG4k, despite the phase separation, in order to assess the impact of different molecular weights on HME mixing and extrudate mechanical properties.

Between 120°C and 170°C (potential process temperature), only PEG4h had mass loss above 1% (1.6%). At higher range (170°C - 240°C), StA, PEG4h and TEC mass losses were ≥ 1%. In the HME process temperature, shear stress and time affect the degradation of processed material [130]. Shear stress cannot be mimicked in the TGA but time was mimicked by holding the materials at potential process temperature chosen based on the first method, 150°C. If the TGA mass loss was less than 1% the material was considered to be stable. Based on these criteria during the holding stage all pure components were stable except for TEC. For TEC the experiment was repeated at lower temperature, 120°C, where the mass loss was less than 1%. In the literature both PEG and StA degradations have been studied, StA degraded in one step with initial degradation temperature at 216ºC (10ºC/min heating rate) [117]. In similar manner, PEG/PEO polymer (molecular weight of 3400, 1×10^5, 3×10^5, 1×10^6 and 5×10^6) degradation happened in the range from 330ºC to 450ºC. T5% which represented the mass loss of 5% of the initial weight was 358ºC and did not change with molecular weight [168]. TEC totally degraded between 120ºC and 250ºC [169]. Tween 80 thermogravimetric analysis was not found in the literature. However, TWN specification document indicated 3% (wt%) water content. Based on this thermal stability study, a HME process temperature of 150°C was chosen for all binary EPO:Plasticizers systems except for TEC where 120°C was applied.

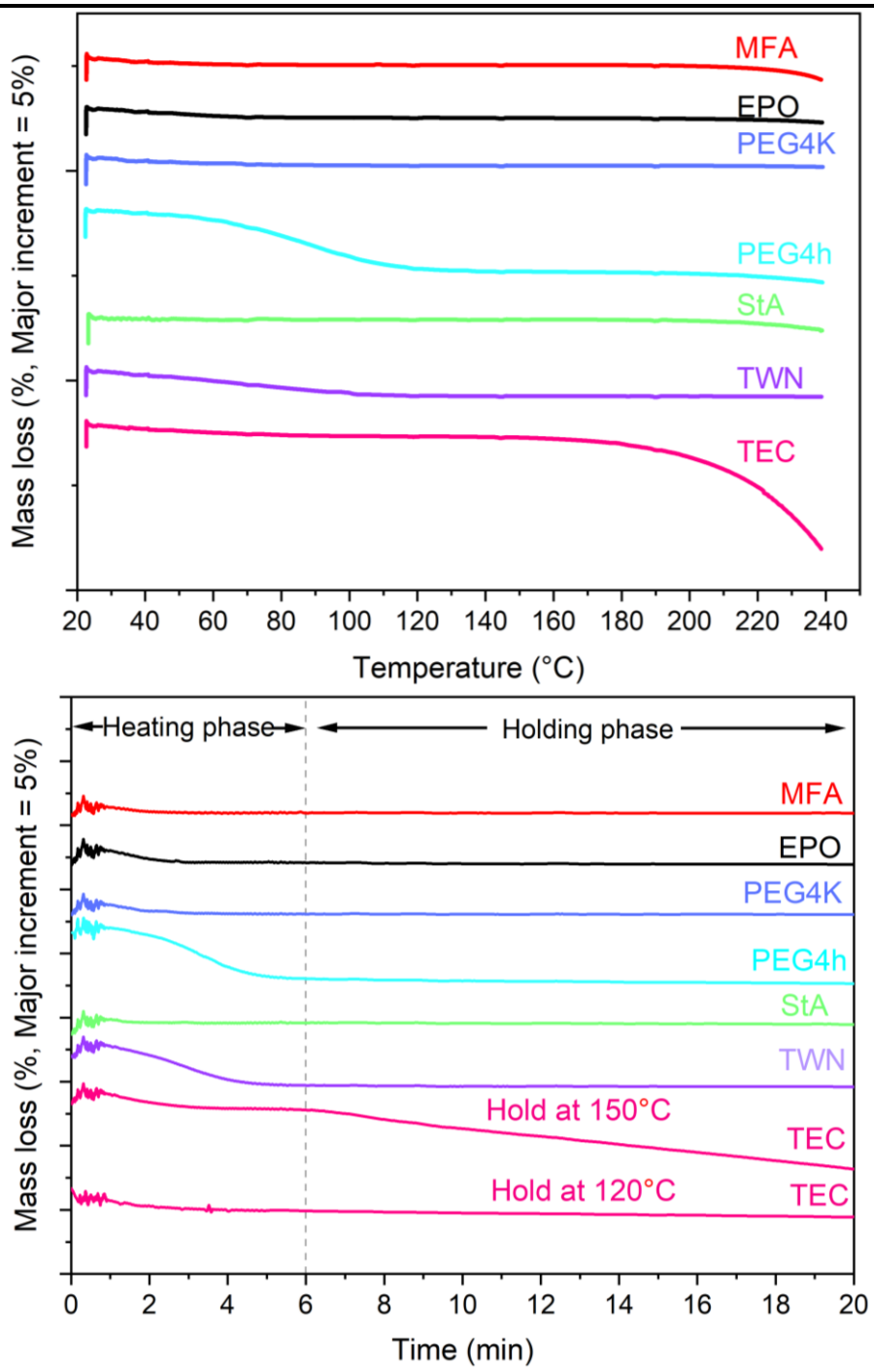

Figure 3-5. Mass loss of the pure components by two thermogravimetric analysis methods. One step heating to 240°C (Top) and Two phases namely heating then holding at high temperature (Bottom).

Table 3-7. Mass loss of the pure components from the thermogravimetric analysis, two methods were used. One step heating to 240°C (A) and Two phases namely heating then holding at high temperature (B):

	A- Mass loss (one heating step)			B- Mass loss (two heating phases)	
Material	**20-120°C**	**120-170°C**	**170-240°C**	**Heating phase**	**Holding phase**
MFA	0.5%	0.2%	1.2%	0.3%	0.3%
EPO	0.7%	0.1%	0.4%	0.8%	0.1%
PEG4k	0.5%	0.1%	0.1%	0.5%	0.00%
PEG4h	4.3%	1.6%	1.0%	2.6%	0.5%
StA	0.1%	0.1%	1.0%	0.4%	0.1%
TWN	1.7%	0.4%	0.1%	2.9%	0.2%
TEC	1.1%	0.4%	10.2%	1.1%	3.9% (150°C)
TEC				0.8%	0.3% (120°C)
Rounded to a decimal place. Silica powder has low density therefore the total sample mass was below 1.6 mg.				Rounded to a decimal place. All holding temperatures 150°C. TEC was analysed using different holding temperature 120°C. Holding time was 9 min (residence time of the EPO in the HME).	

3.3.1.3. Production and EPO:plasticizer performance

Tables 3-2 and 3-8 presents the HME process temperature and the extrudates appearance of EPO:Plasticizers. EPO:PEG4k 95:5 and 85:15 (wt%) were white, EPO:PEG4h 85:15 (wt%) and EPO:StA 85:15 (wt%) were cloudy and the remainder were transparent. The loss of transparency appearance might be due to phase separation. These results agree with the findings in the miscibility study (Figure 3-4). The mechanical properties of all EPO:Plasticizer formulaes are presented in Figure 3-7. All plasticizers except PEG4k improved the flexibility (strain at break). EPO:PEG4k 95:5 and 85:15 (wt%) were more brittle than the EPO which assigned to the solid-solid phase separation in these extrudates. All plasticizers reduce flexural modulus in comparison with pure EPO extrudates. With PEG4k, the modulus reduction was due to the poorer mechanical properties of PEG4k (waxy material i.e. low stiffness and maximum stress). Other EPO:Plasticizer extrudates had lower flexural modulus indicating higher

molecular mobility due to EPO-plasticizer molecular interaction and increase in the free space between polymer chains. At EPO:plasticizer 95:5 (wt%) the formulae from the stiffest to the softest were PEG4k, PEG4h, TWN, StA then TEC. At EPO:plasticizer (except PEG4k) 85:15 (wt%) the stiffness dropped significantly and formulae were over plasticized. Maximum stresses for the binary systems were lower than EPO maximum stress. EPO:PEG4k formulae broke before reaching plastic flow. While the rest of EPO:plasticizer 95:5 (wt%) were in the same order of stiffness (PEG4h, TWN, StA then TEC). At EPO:plasticizer (except PEG4k) 85:15 (wt%) the maximum stress were also very small due to over plasticization. For EPO:TWN and EPO:TEC 85:15 the extrudate-like shape deformed after three months due to plastic flow under storage temperature (25ºC) and weight of other samples (table 3-8). Weight of the samples were not measured as this phenomenon observed accidently rather than studied on purpose. From the screening study, Tgs of these two samples were not detected (DSC trace reached 20ºC) suggesting that molecular mobility was possible at storage temperature (storage temperature > Tg) [170].

Table 3-8. extrudates appearance of EPO:plasticizer at 95:5 and 85:15 (%wt) ratios and FA:EPO:plasticizer at 20:76:4 and 20:65:15 (%wt) ratios:

	**EPO:Plasticizer (wt%)**		**MFA:EPO:Plasticizer (wt%)**	
1 cm	**95:5**	**85:15**	**20:76:4**	**20:65:15**
PEG4k				
	White cloudy	White	/	/

PEG4h				
	Clear	Cloudy	Clear	Clear
StA				

	Clear	White cloudy	Clear	White cloudy
TEC	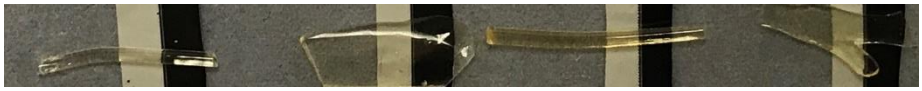			
	Clear	Clear	Clear	Clear

TWN				
	Clear	Clear	Clear	Clear

Four plasticizers PEG4h, TWN, TEC and StA were considered suitable for improving EPO flexibility. The most interesting system was EPO:StA. In the previous chapter, the carboxyl group of MFA was determined to interact with the amine group of EPO and a similar interaction is assumed for the StA carboxylic group. However, the impact of MFA and StA on EPO mechanical properties were different, increase in brittleness and flexibility, respectively. In StA the carboxyl group is attached to long hydrophobic linear carbon chain i.e. no polar or hydrogen interaction with other molecules was expected. While the MFA carboxyl group is linked to the aromatic ring, which is thought to have an interaction with EPO. As a result, MFA reduces the EPO molecules mobility and plastic flow due to its plasticization transmission affect as explained in Chapter 2 (2.3.5.1) and represented in Figure 3-6-D. While StA had an interaction from the carboxyl side and week Van der Waals interaction from the other side allowing EPO chains to slide (Figure 3-6-F). This affect is the so called plasticization separation affect [135] and StA was used at 2.5% (wt%) to plasticize EPO for placebo 3D printing filament (Evonik) [171].

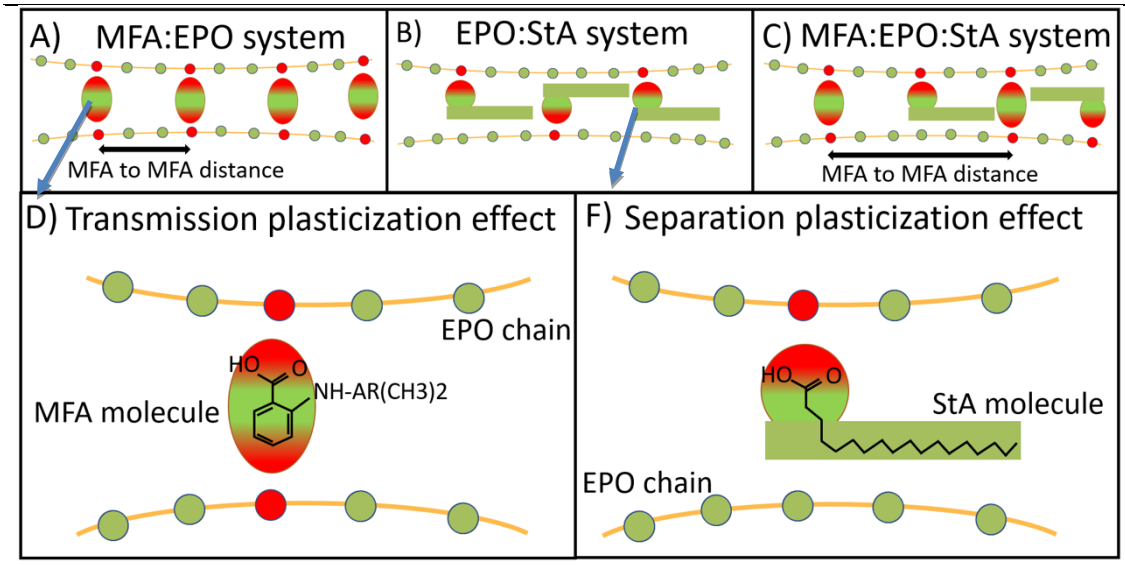

Figure 3-6. Schematic of MFA and StA interaction with EPO, MFA:EPO system (A), EPO:StA system (B) and MFA:EPO:StA system (C), and plasticization effect associated with both molecules, transmission plasticization effect (D) and separation plasticization effect (F). Strong bonds like hydrogen bond (red), while Van der Waals bonds (green).

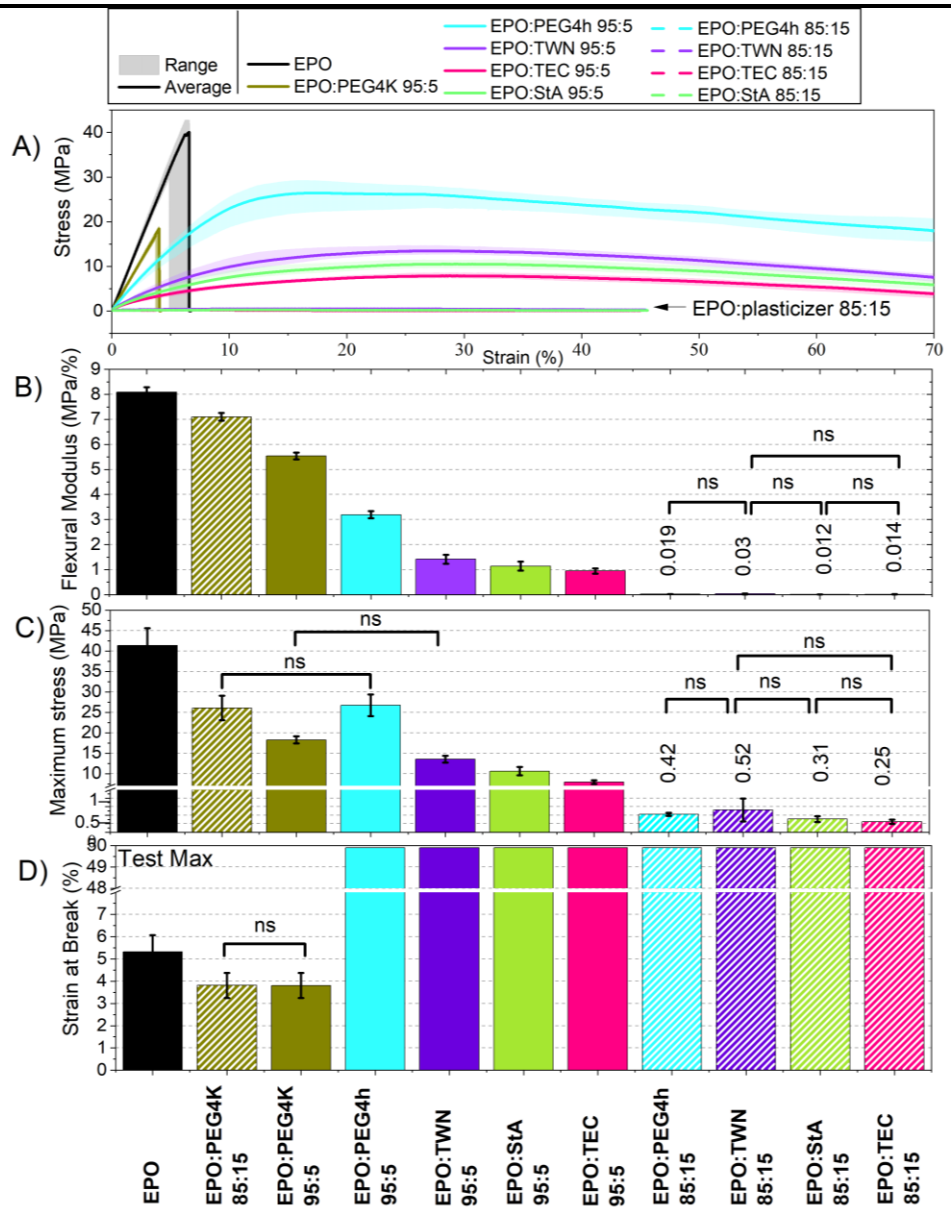

Figure 3-7. Mechanical properties from 3 point bend test for pure EPO, EPO:Plasticizers 95:5 and 85:15 (wt%). Stress-strain curves (A), flexural modulus (B), maximum stress (C) and strain at break (D). Average value (n=5, error bar = SD), ANOVA test only non-significant difference (ns, P>0.05) added to the graph i.e. all the rest are significant.

3.3.2. Binary to Ternary system: drug - polymer – plasticizer

The four chosen plasticizers were further investigated keeping the same EPO/Plasticizer ratio with an MFA loading of 20% (wt%) of the total formula, i.e. MFA:EPO:plasticizer ratio was 20:76:4 (wt%). HME 11 mm was employed to produce the extrudates taking into account ingredient stability (process temperature was 150ºC except for TEC 120ºC)

as measured above. All extrudates were transparent. Figure 3-8 shows EPO:plastitcizer and MFA:EPO:plasticizer formulae under the optical microscope. EPO:plasticizer 95:5 (wt%) extrudates had smooth surfaces except EPO:PEG4k where the difference is thought to be due to solid-solid phase separation. At the higher plasticizer ratio (EPO:plasticizer 85:15, wt%), phase separation was observed with PEG4k, PEG4h and StA. Optical microscope results of separation in EPO:platicizer extrudates were in agreement with screening study mentioned above. When MFA was added, crystal-like shapes were noticed in MFA:EPO:TEC and MFA:EPO:TWN indicating a reduction in the MFA solubility in EPO. MFA:EPO:StA showed a homogenous appearance, and MFA:EPO:PEG4h appeared homogenous but with a few small solvent or air pockets.

From the HSPs prediction (Table 3-4 and Figure 3-2), the TEC and TWN were closer to the MFA than EPO. Moreover, MFA was located between EPO and the plasticizers but closer the plasticizers. Thus, plasticizer-MFA interaction is thermodynamically thought to be more favourable. It was not clear if MFA was not dissolved during heating in the HME or crystallised out during post-extrusion cooling. On the other hand, PEG4h and StA were closer to EPO and formed homogenous extrudates.

Review [172] of using surfactant as plasticizer for solid dispersion systems can be found in the literature and surfactants increase drug-polymer miscibility. However, reducing the Tg of the system increases the molecular mobility and might cause recrystallisation. In the original research paper, the presence of sodium lauryl sulphate was thought to increase the mixing efficiency resulting in intensity reduction of the drug peaks on the IR [173]. The justification might have been simplified by considering only the surfactant impact on mixing. However, the ternary system miscibility from thermodynamic perspective should be considered as described above. HSPs have been applied to find co-solvents and anti-solvents for a targeted material [174]. Good miscible reduce Tg of the system (increasing molecular mobility). But high molecular mobility after extrusion leads to recrystallisation, thus, Tg is recommended to be 50ºC above the storage temperature [132]. PEG4k and poloxamer 188 showed strong plasticization effect on hypromellose acetate succinate (HPMCAS) with StA exhibiting a lower effect on the polymer. It was found that drugs in HPMCAS:PEG4k and HPMCAS:poloxamer were not stable physically, while StA did not impact storage stability and interestingly boosted the drugs disintegration and dissolution [175]. None of these studies linked the solid state of the dispersion system with HSPs.

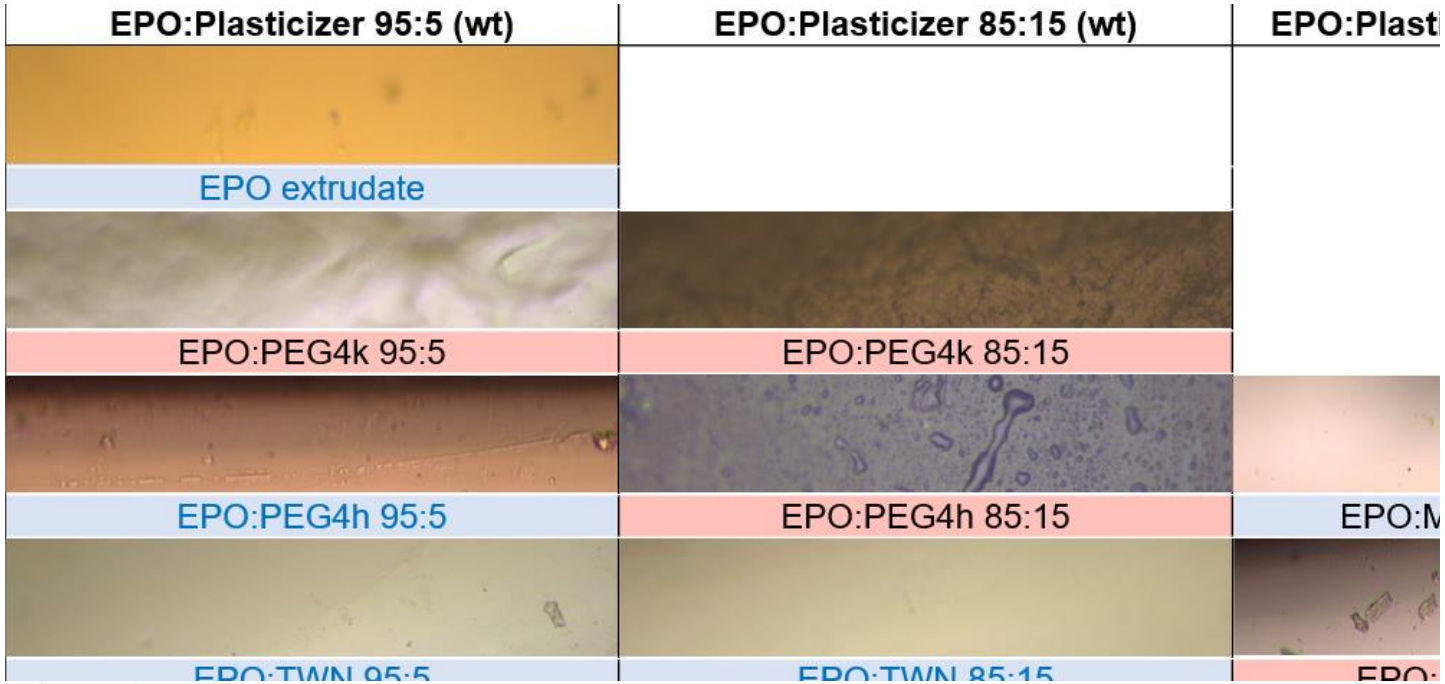

indicated phase separation blue colour indicated homogenous system.

Table 3-9 and Figure 3-9 show the glass transition temperature onset measured from the extrudate cooling cycle, with values between 40ºC and 49ºC. For EPO:plasticizer 95:5 extrudates the Tg's rank order did not follow the order of any of the mechanical property values. The Tg(s) verses Ra $_{EPO}$ and molecular volume (MVol) did not follow similar pattern nor having strong correlation values, -0.54 and -0.28 (table 3-10), respectively. Ghebremeskel et al [176] found that Tg depression associated to partial HSPs of plasticizers with Plasdone-S630 and hypromellose-E5 but this was not seen with other polymers namely hypromellose acetate succinate or polyvinylpyrrolidone-K30. Their calculation was missing the experimental constant 4 (see section 3.2.2.1.1, eq 3.1). The volume (molecular volume) and the 3D structure of the plasticizer might cause different free space between polymer chains [177]. In the current work, the lack of direct relationships might be due to the impact of multiple factors together (both Ra and MVol) or unconsidered ones like plasticization effect type.

Tg's of extrudates at 85:15 ratio (except PEG4k) was not measurable due to over-plasticization. When MFA was present two trends were observed, for TWN and TEC Tg's were higher with MFA than without, while for EPO:StA and EPO:PEG4h Tg's were lower with MFA. From the HSPs calculation and microscopic images the StA/PEG-MFA-EPO systems EPO plasticized by both drug and plasticizer. While with TEC/TWN-MFA-EPO systems, plasticizer thermodynamically prefer MFA (phase separation under the microscope) hence less plasticization affect observed (higher Tg). Thus, plasticizers with HSP values that are closer to EPO and further from MFA were better.

Table 3-9. Glass transition of EPO-plasticizer at two ratios 5% and 15% and EPO-MFA-plasticizer system as measured from DSC graphs during the first cooling cycle:

Plasticizer *	**Tg (ºC) of EPO-Plasticizer 95-5 extrudates**	**Tg of (ºC) EPO-Plasticizer 85-15 extrudates**	**Tg of (ºC) EPO-MFA-Plasticizer 76-20-4 extrudates**
PEG4k	47.9	48.6	NA
PEG4h	46.6	/	43
StA	46.3	/	40.7
TWN	41.9	/	43.2
TEC	40.1	/	42

***** Tg of EPO extrudate was 57°C and for MFA:EPO 20:80 (wt%) was 46°C.
Duplicate DSC experiments were conducted and average value is presented.
NA = extrudate was not produced. / = Tg could not be measured.

Table 3-10. Drug, polymer and plasticizers' molecular volumes (MVol in cm^3/mol) as calculated on HSPiP software:

	MVol		MVol
EPO *	369.3	**StA**	324.3
PEG *	39.4 (PEG4h = 354.6)	**TWN**	586.7
MFA	200.6	**TEC**	238.9

* For polymer the value is calculated for the monomer/s not for the whole molecule.

Correlation values for Tg-Ra $_{EPO}$ and Tg-Mvol were -0.54 and -0.28, respectively.

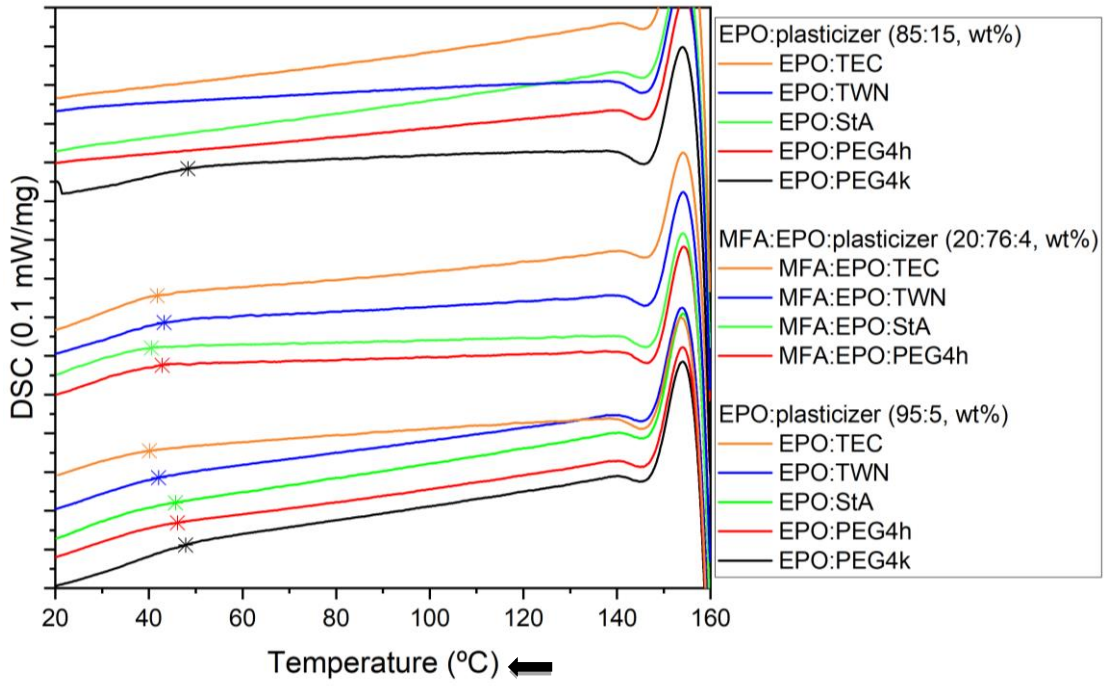

Figure 3-9. DSC traces of EPO-plasticizer at two ratios 5% and 15% and EPO-MFA-plasticizer system during the first cooling cycle, glass transition (star).

X-ray diffraction patterns of ternary systems MFA:EPO:plasticizer are plotted in Figure 3-10. All samples at MFA:EPO:plasticizer 20:76:4 (wt%) ratio (Figure 3-10, L) exhibit the same pattern with two wide amorphous peaks and an absence of MFA crystalline Bragg sharp peaks. The X-ray was not able to detect the phase separation observed earlier in MFA:EPO:TEC or TWN 20:76:4 (wt%). Thus, a higher plasticizer ratio was examined MFA:EPO:plasticizers 20:65:15 (wt%), however similar patterns were obtained and no MFA peaks were detected.

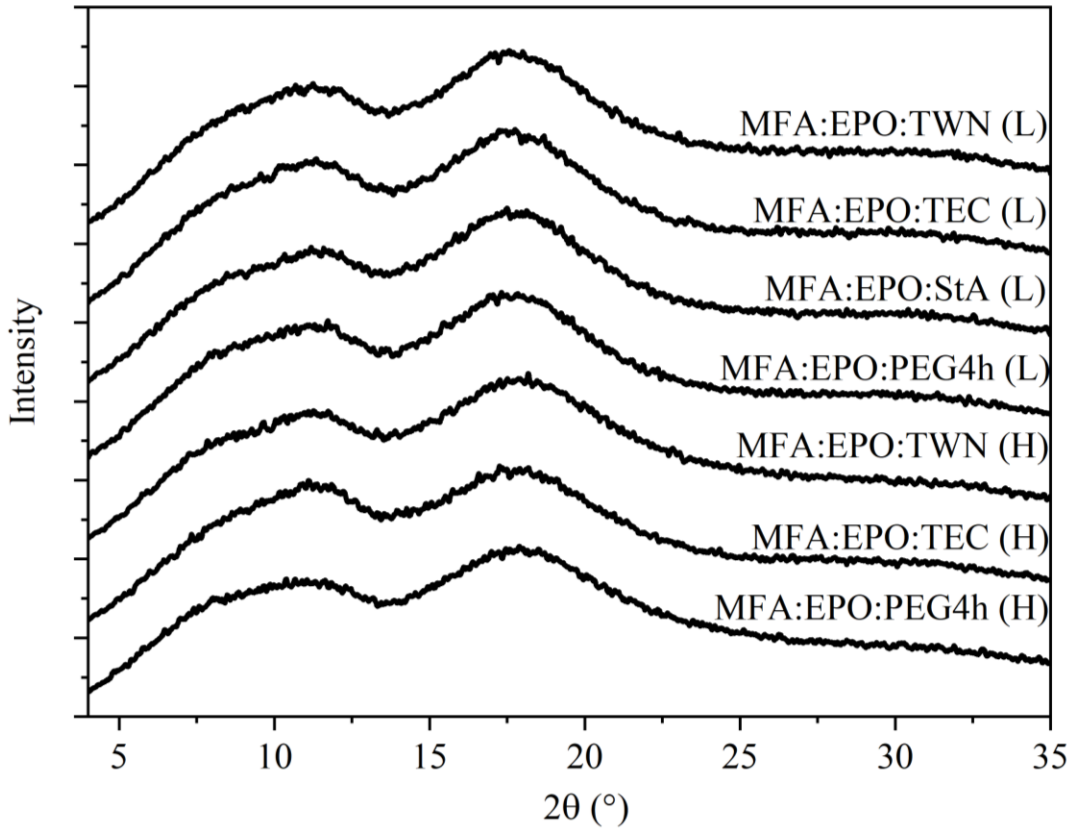

Figure 3-10. Xray diffraction pattern of ternary systems at two plasticizers ratio MFA:EPO:plasticizer 20:76:4 (L) and 20:65:15 (H).

Mechanical properties of MFA:EPO:plasticizer 20:76:4 (wt%) extrudates versus EPO, MFA:EPO 20:80 (wt%) and EPO:plasticizer 95:5 (wt%) extrudates were compared. Figure 3-11 presents stress-strain curves, flexural modulus, maximum stress and strain at break results from 3-point bend test. In the previous chapter, MFA increased both stiffness (higher flexural modulus) and brittleness (lower strain at break) of EPO and this was assigned to the molecular interaction of EPO with MFA. Both TEC and TWN produced a similar effect MFA:EPO:TEC or TWN 20:76:4 (wt%) were significantly and drastically stiffer and more brittle than EPO:TEC or TWN, Figure 3-11 b and d, purple and red bars. Moreover, strain at break of MFA:EPO:TWN was significantly lower than MFA:EPO. MFA:EPO:TEC was also lower than MFA:EPO but the difference was insignificant. These differences in the mechanical properties assigned to the MFA-EPO molecular interaction as well as solid-solid phase separation observed under the microscope. Moreover, maximum stress for MFA:EPO:TWN and MFA:EPO:TEC were higher than corresponding binary systems (without MFA).

With PEG4h as plasticizer, the flexural modulus was identical with or without MFA (Figure 3-11, blue curves and bars). However, the strain at break of MFA:EPO:PEG 20:76:4 (wt%) was lower than without MFA and with no significant difference than MFA:EPO 20:80 (wt%). Maximum stress of PEG4h-ternary system dropped with MFA presence. The mechanical properties changes attributed to an accumulation of both PEG4h effect and MFA effect on EPO. At the beginning the elastic behaviour of the ternary system was dominated by the effect of PEG4h (same of EPO:PEG4h Flexural modulus). Until specific strain MFA restrained EPO chains to deform further causing structural break (same of MFA:EPO strain at break). Due to the early break of the extrudates maximum stress was low.

With StA as plasticizer, the flexural modulus and maximum stress of the ternary system MFA:EPO:StA 20:76:4 (wt%) were between EPO:StA 95:5 (wt%) and MFA:EPO (wt%) values. Strain at break however was not measured as maximum strain was not reached in this test. The mechanical properties of this ternary formula were a direct combination of both StA and MFA interaction with EPO, since both carboxylic acids interact with the amine group on EPO. Thus, StA provided distances between MFA-EPO strong interaction allowing plastic deformation to occur (Figure 3-6-C). Hence, strain at break was high. The result was not proportional to the ratio in this test setup since the properties was closer to EPO with StA (4-5% of the total formula) than EPO with MFA (20% of the total formula). StA which is the recommended plasticizer from Evonik [178] was the best plasticizer for the MFA-EPO combination. In the literature, TWN was applied to develop 3D printing filaments. However, there were no comparisons between the formulae with and without the plasticizer. Formulae were also complex consisting of five components including drug, EPO, PEG4k and PEO WSR-N10 [85], [179]. Research papers using TEC for 3D printing did not include a mechanical test [31], [92], [96], [180], [181], [182].

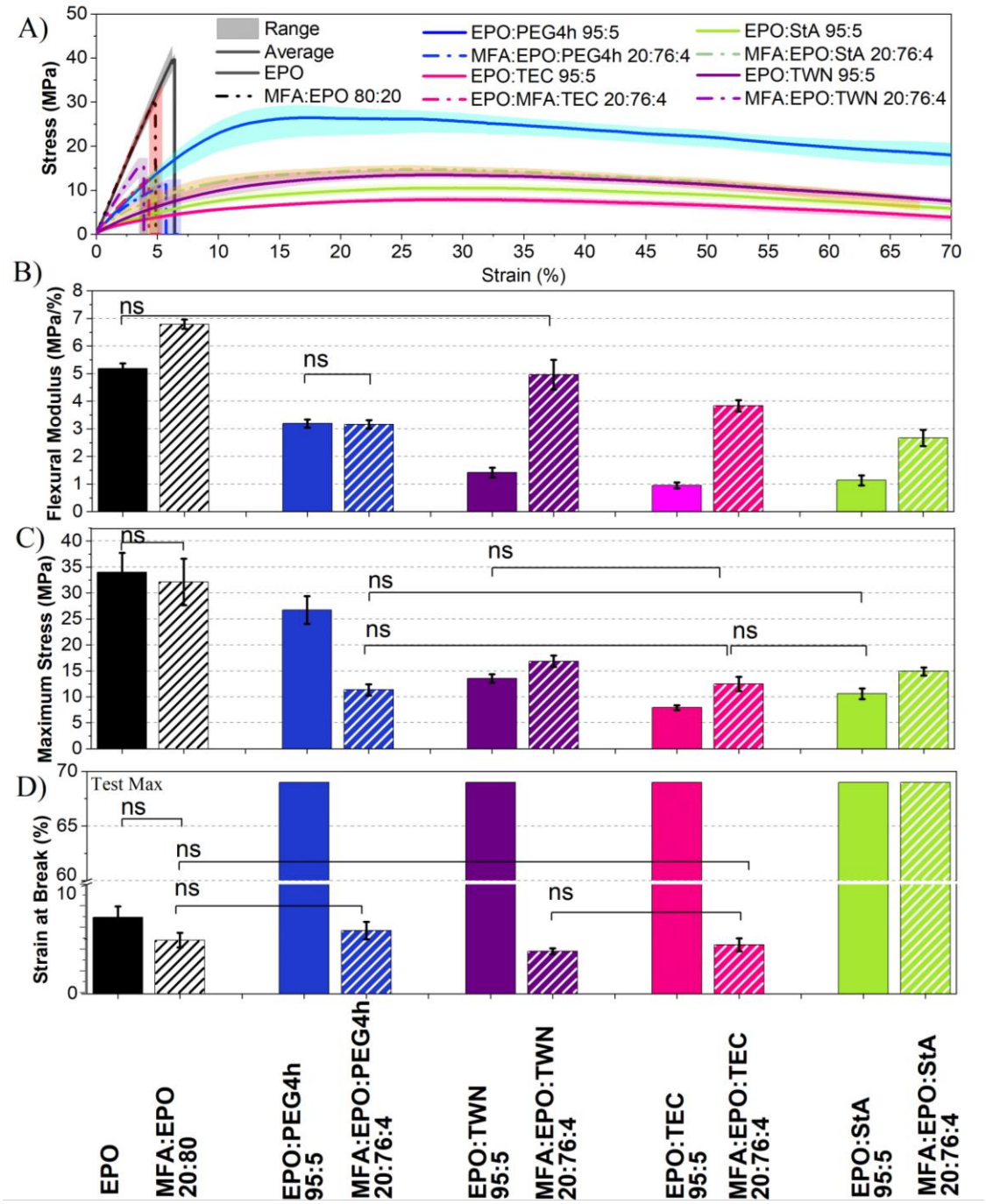

Figure 3-11. Mechanical properties of EPO and EPO:plasticizer 95:5 (wt%) versus the corresponded formulae loaded with 20% (wt%) MFA. Stress-strain curves, flexural modulus, maximum stress and strain at break. Average value (n=5, error bar = SD), ANOVA test only non-significant difference (ns, P>0.05) added to the graph i.e. all the rest are significant.

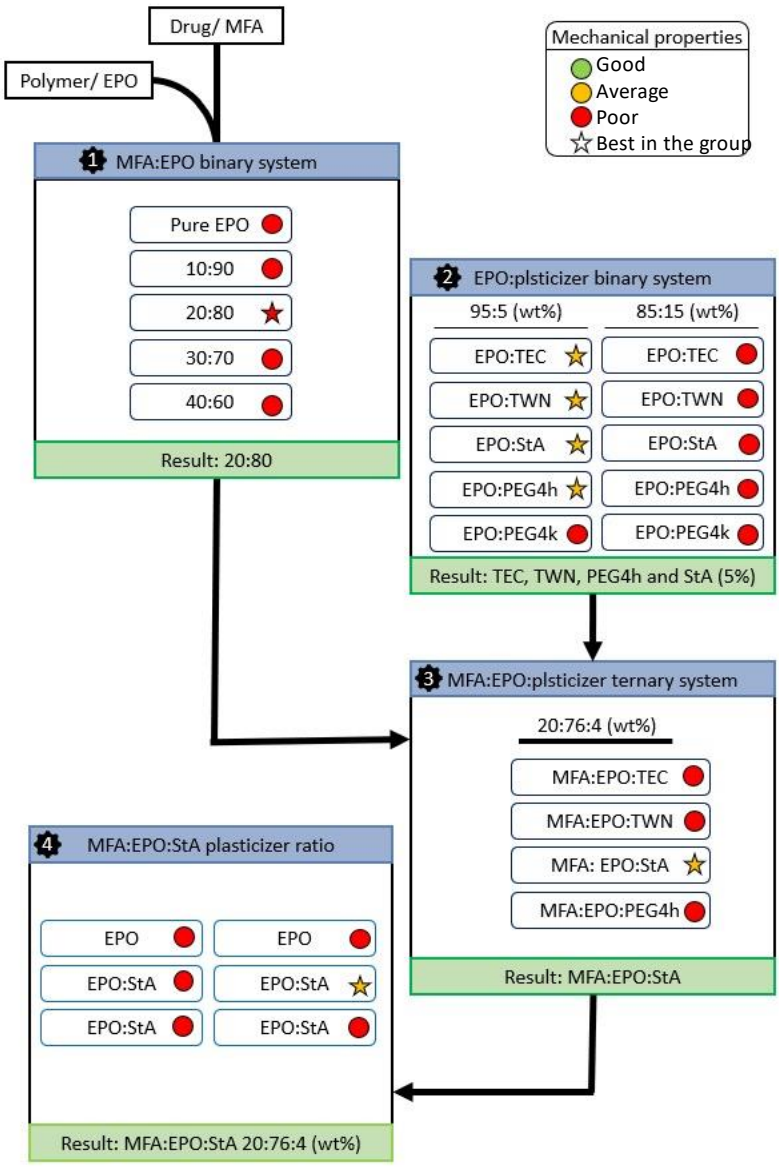

Figure 3-12. Schematic of MFA-EPO formula development.

From the SEM images shown in Figure 3-13, only MFA:EPO:TWN has a clear origin of the crack, mirror and mist regions (Figure 3-13 X50). MFA:EPO:TEC showed some roughness on the edges (Figure 3-13 X50, red ellipse). Both MFA:EPO:PEG4h and MFA:EPO:StA showed smooth surfaces. In the MFA:EPO:TWN or TEC samples, the pattern and roughness assigned to the presence of interruption of the crack spread that might be due to MFA crystals in the samples. While the other two samples did not show a pattern indicating homogenous crack spread. Moreover, there was less development of secondary cracks in comparison with MFA:EPO binary systems (Chapter 2, 2.3.5.1). The reduction of the elastic modulus might reduce the released stress and as a result less probability for secondary crack development.

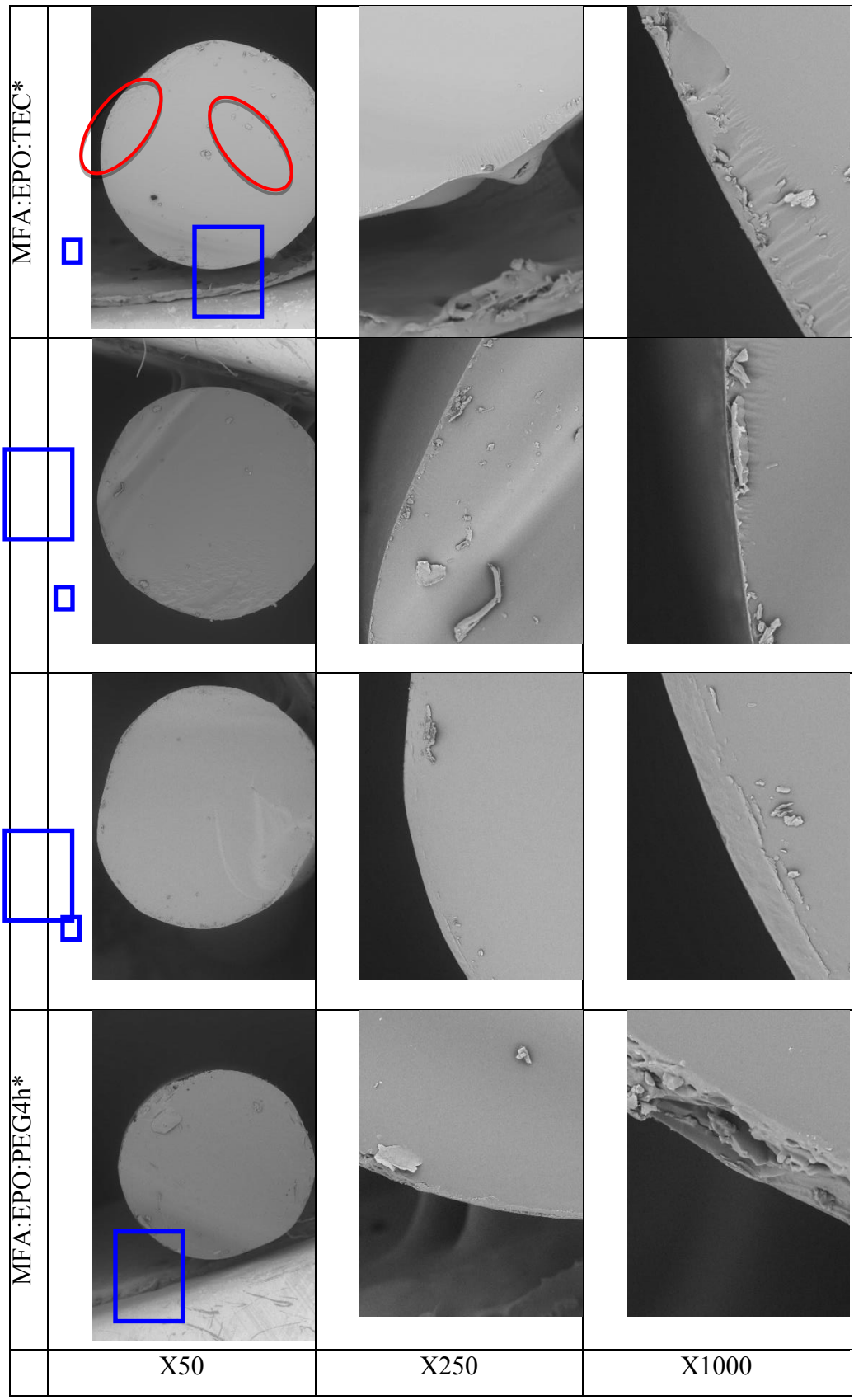

*Figure 3-13. Cross section images from the SEM of MFA:EPO:plasticizer 20:76:4 (wt%) extrudate. * samples broken using three point bend test.*

Korte and Quodbach used StA at 7% (wt%) with theophylline – Eudragit RL (ERL) formula to achieve good mechanical properties for 3D printed application. StA reduced

stiffness and brittleness of ERL but it showed phase separation at 7% (wt%) [95]. Therefore, the interaction of StA with EPO might be different from Eudragit RL. Eudragit RL contains quaternary ammonium groups while EPO has amine groups [105]. SEM, XRPD, optical microscope and DSC of EPO:StA -based extrudates did not show phase separation of EPO:StA 95:5 (wt%) but the screening results indicated separation in 85:15 (wt%). For further investigation a 90:10 (wt%) ratio was extruded and compared with other samples (Figure 3-12) on small and wide-angle X-ray diffraction (SAX and WAX).

Figure 3-14 shows the diffraction patterns of blank-air, EPO, EPO:StA at 95:5, 90:10 and 95:15 (wt%). From SAX data, Blank, EPO, EPO:StA at 95:5 and 90:10 (wt%) were identical with no peaks presented. This suggests no significant structural arrangement on nanoscale level and these extrudates were one block piece. However, a higher StA ratio, EPO:StA 85:15 had a peak around q value of 0.158. This was thought to be from the StA phase separation and creation of lamellar structure, the Wax data was similar. The pure polymer, EPO:StA at 95:5 and 90:10 (wt%) were similar with no sharp peak instead very broad peaks. This was due to the amorphous nature of the extrudates and lack of arranged repetitive pattern. At higher StA ratio (EPO:StA 85:15) sharp peaks appeared. These peaks referred to crystalline material presence in the extrudate.

In the literature SAX and WAX signals were collected for the StA powder during heating from 25 to 80°C. In agreement to our study, one SAX peak of StA was detected around q value of 0.15 which disappeared at 80°C (melting of StA). At room temperature StA had six WAX peaks (Table 3-14). These peaks shifted to lower scattering angle during the thermal expansion until they disappeared due to melting [183]. The values are slightly different from the ones measured in the current work, which might be due to change in StA polymorphism or presence of the Eudragit EPO that impacts the molecules arrangement to return to its equilibrium state. From SAX and WAX analysis StA-EPO produces homogenous amorphous solid dispersion up to 10% (wt%) StA load and might be promising to produce MFA:EPO:StA 3D printing filament.

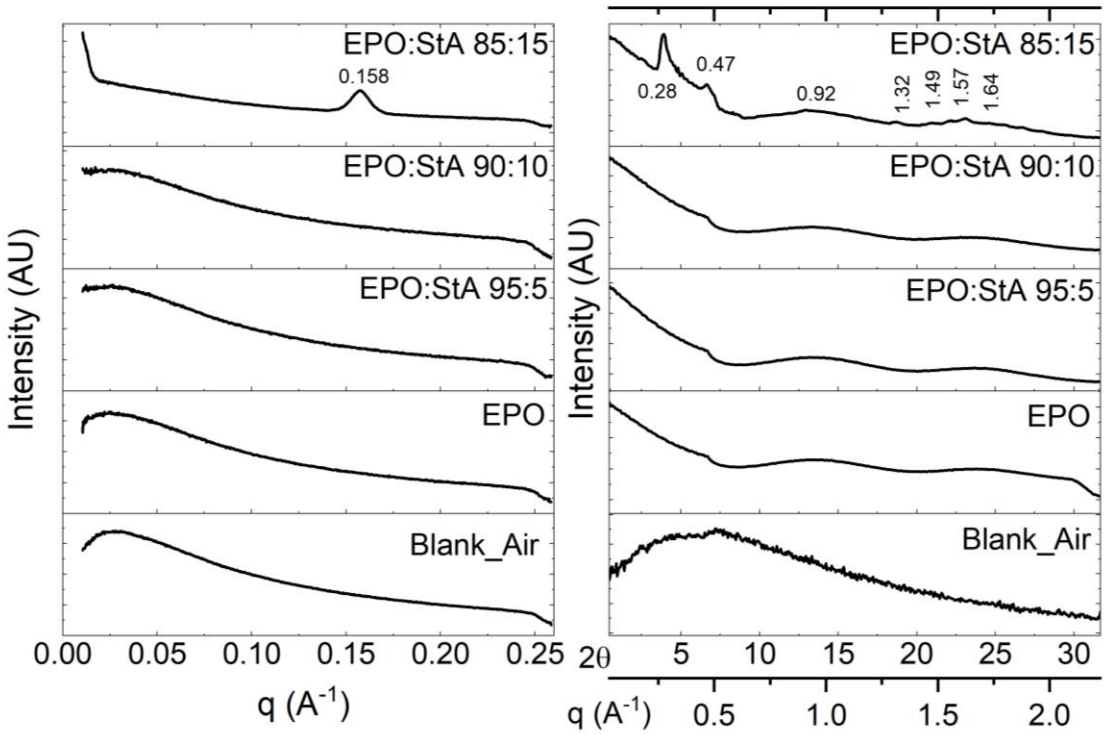

Figure 3-14. SAX (left) and WAX (right) data of the EPO extrudate, EPO:StA at ratio of 95:5, 90:10 and 85:15.

Table 3-11. Comparison of StA WAX peaks from the EPO:StA 85:15 extrudate with literature:

EPO:StA 85:15	0.28, 0.47, 0.92	1.34	1.40, 1.44	1.52, 1.57	1.70
StA literature	Signal not collected	1.32	1.49	1.57	1.64

3.3.3. MFA:EPO:StA systems potential for 3D printing

Thus far EPO, EPO:StA at 95:5 (wt%), 90:10 (wt%), MFA:EPO 20:80 (wt%), and MFA:EPO:StA 20:76:4 (wt%) were studied. Since MFA:EPO:StA 20:72:8 (wt%) provided better understanding and navigating in the formulation space, it was extruded and analysed using the 3-point bend test (Figure 3-15). The flexural modulus increased with the presence of MFA but reduced with StA. In the studied range, MFA changed the flexural modulus up to 1.6 MPa/%. While increasing of StA ratio caused 6.3 MPa/% reduction. Maximum stress followed almost similar pattern with an exception, MFA reduced the maximum stress in MFA:EPO 80:20 (wt%) in comparison with EPO.

Increasing each of MFA and StA ratios caused up to 7.3 increase and 36.9 MPa reduction respectively in the studied range. Strain at break reached the maximum value with all plasticized samples with StA. Without StA extrudates were brittle (low strain at break). The change in the mechanical properties was more sensitive to the StA change than MFA. StA had lower R_{EPO} (Table 3-4) and bigger molecular volume (Table 3-10) in comparison with MFA (4.52 versus 7.47 $MPa^{1/2}$ and 324.2 verses 200.6 cm^3/mol, respectively). However, as explained earlier (section 3.3.2) a direct relationship was not possible. Since higher mechanical properties values were preferable for 3D printing, MFA:EPO:StA 20:76:4 was the best formula.

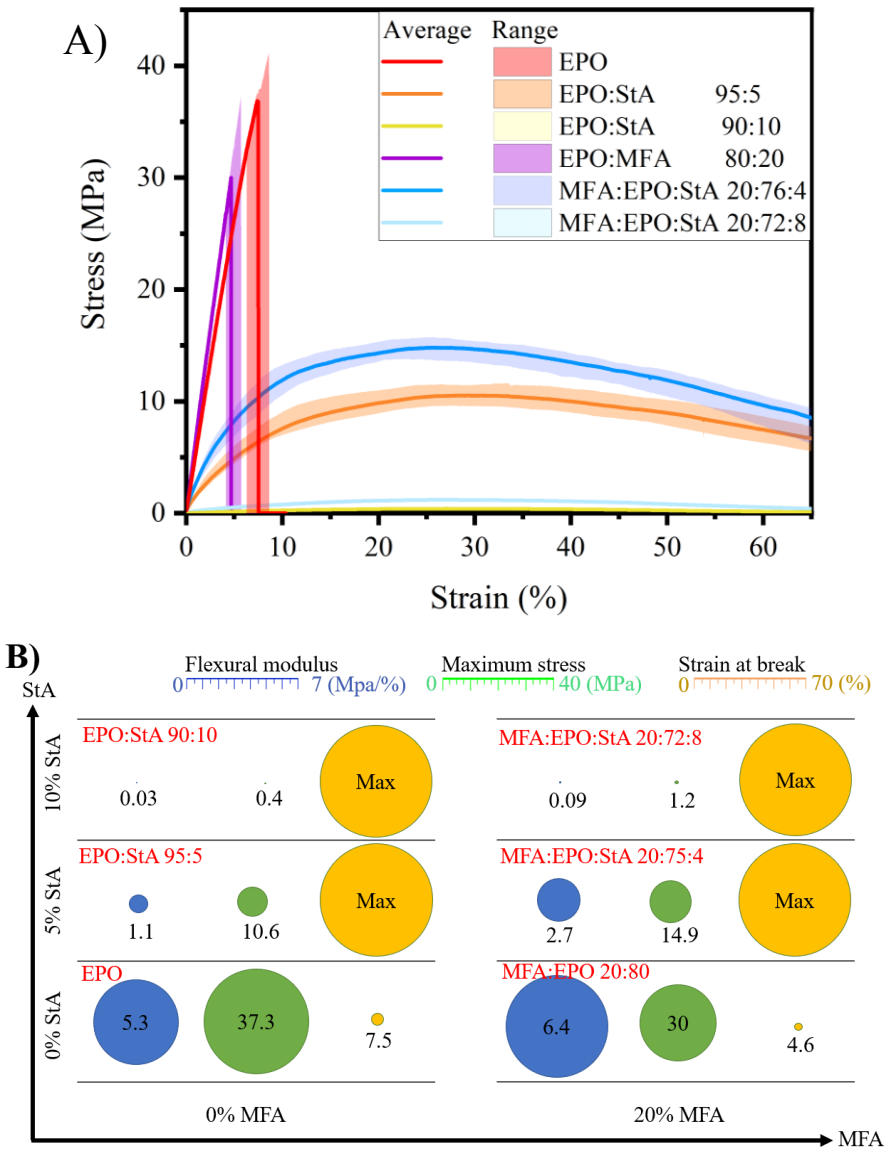

Figure 3-15. 3-point bend test of six different EPO formulations using StA as plasticizer and MFA as a drug. StA ratios were 0, 5 and 10% (wt%) while MFA ratios were 0 and 20% (wt%). Stress-strain curve (A) and extracted mechnical property values (B).

Printing test results are presented in table 3-12. The chosen formula was flexible enough to be inserted in the printer and travel through the PTFE tube however, the tension from the gears caused filament breaking or filament erosion. Reducing the tension was not successful to push the filament and extrude the formula at a printer head temperature of either 150°C or 160°C.

Table 3-12. Feed-ability test in the 3D printer for MFA:EPO:StA 20:76:4 formula:

Conditions 3DP T°C - speed	Feed-ability	Tolerance to gears' stress*	3DP-extrudability
150°C - 180 mm/min	✓	✗	✗
150°C - 60 mm/min	✓	✗	✗
160°C - 180 mm/min	✓	✗	✗
160°C - 60 mm/min	✓	✗	✗

Feed-ability = Pass through the PTFE tube,

Tolerance = the initial gear tension was set to a minimal level to ensure the filament could be fed into the printer head. If the gears failed to push the filament due to insufficient grip, the gear tension was incrementally increased by rotating the tension screw one full turn per trial. This process was repeated until the filament was either successfully fed into the printer head or deformed/broke due to excessive tension.

3DP-extrudability = filament was efficiently working as piston to push molten formula out (to not been confused with HME-extrudability).

3.4. Conclusion

Degradation of the pure components is temperature and time related. TGA can be used to mimic HME process conditions and evaluate potential degradations. PEG4h, TWN, StA were stable at 150°C while TEC was stable at 120°C.

StA, TEC, TWN and PEG4h can be used as plasticizer for EPO. HSPs are able to predict the plasticizer compatibility however this calculation does not take in to account the molecular weight. For example, PEG4k (same HSPs of PEG4h) separates or does not mix well with EPO. However, HSPs are not useful to evaluate the Tg reduction, change in the mechanical properties. Thus, experimental approach is needed for checking product properties. All the studied plasticizers reduced the EPO brittleness. Stearic acid has different plasticizing effect (separation effect) on the polymer than MFA (transmission effect), see Figure 3-6 d and f.

MFA solubility in EPO is reduced with the presence of TWN and TEC since they are likely to interact with MFA more than EPO based on HSPs calculation. Thus, phase separation observed in the correlated ternary systems (drug-polymer-plasticizer). As a result, a significant increase in the brittleness is noticed. StA up to 10% (wt of EPO) is the most promising plasticizer for MFA-EPO formula since it improves flexibility of EPO and does not cause MFA phase separation. Moreover, StA increase the distance between weak points from MFA-EPO interaction, see Figure 3-6 a and c .

Based on the plasticizer screening study MFA:EPO:StA 20:76:4 was the best formula explored in this chapter. Although the formula is flexible enough to be inserted in the printer it breaks due to the tension of the gears.

To make MFA:EPO a printable filament, it is necessary to enhance its tolerance to the stress exerted by the gears.

This page is left empty.

Chapter 4: Quaternary systems ratio optimisation, mefenamic acid-Eudragit EPO- Stearic acid and Fumed silica formula development:

4.1. Introduction

In chapter 3, StA was the optimum plasticizer for the MFA-EPO system, with the best formulae MFA:EPO:StA 20:76:4 (wt) flexible enough to unroll from filament coil and feed into the printer head. However, the filament did not tolerate the feeding gear pressure in the printer. In this chapter, the flexible matrix tolerance to stress will be examined by loading stiff (high elastic modulus) and strong (high maximum stress) filler particles. Four fillers will be screened: talc 45 µm (talc45), talc 75 µm (talc75), fumed silica and silk powder with a Design of Experiment (DoE) applied to screen formulation space. Two levels of three factors (ratios of MFA, StA and filler) were used to predict and find a printable formula. Figure 2-1 identifies physical mixture, extrudate, filament and formula terms used this chapter.

To satisfy the study objectives, this chapter was designed to answer the following questions:

1- What is the effect of incorporating filler (silica, talc45, talc75 and silk) on the mechanical properties of FFF-3D printed pharmaceutical filaments? What are the impacts of particle size and particle shape?
2- What are the critical filament attributes that affect the success of 3D printing and what are their limits for a specific printer?
3- What are the mechanical and rheological tests that are useful to evaluate 3D printing filament?
4- How does the drug, plasticizer and filler content affect the rheological and mechanical properties of the 3D printing filament?
5- Can 3D-printability be predicted using DoE to find new 3DP-filament?
6- After printable filament is there stability consideration to be taken into account?

4.2. Materials and Methods

4.2.1. Materials

Details of MFA, StA and EPO are in sections 2.2.1 and 3.2.1. Fumed silica was purchased from Sigma-Aldrich, UK (S5505, <44µm), talc with two particle sizes, <75µm and <45µm (product numbers 10503244 and 11383878, respectively) from

Fisher Scientific, UK. Based on product data sheet, the particle sizes specified for the silica and talcs were determined using sieves with designated mesh sizes. Silk powder was purchased from Biorigins (MADAR Corporation Ltd) Hampshire, UK.

4.2.2. Methods

4.2.2.1. Thermal analysis

4.2.2.1.1. Thermogravimetric analysis (TGA), pure components:

TGA was conducted on all the fillers (talc45, talc75, fumed silica and silk powder) using the one heating step method detailed in section 3.2.2.2.

4.2.2.1.2. DSC:

Thermal behaviour of the extrudates were studied using the method detailed in section 3.2.2.4.2, samples were analysed in duplicate and average Tg recorded.

4.2.2.1.3. Particle size:

Particle size and shape were measured using Malvern Morphologi G3-ID (Malvern Panalytical, Malvern, UK). Powder (500 mg) was placed on dry dispersive unit, the dispersion parameters were injection pressure of 0.8 bar, injection time 20 ms and settling time 60 s. For image capturing and analysis, the following parameters were applied; optical lens 5X (6.5 µm – 420 µm), overlap value 40%, threshold 105 Gray scale, minimum trash size 10 pixels and capturing area 2894.348 mm^2. The segmentation method was disabled, and hole filling was enabled. No filters or classification settings were selected.

4.2.2.2. Extrudate preparation

Fillers (silica, silk, talc45 and talc75) were used to prepare EPO:StA:Filler blends at a ratio of 72:8:20 (%wt). Blending and extruding methods are detailed in section 2.2.2.1.1. The HME process and die zone temperatures were varied depending on the mixture (table 4-1) to obtain slightly soft extrudates (not runny or solid) after leaving the HME nozzle. Thus, the extrudate diameter was controlled by pulling the thick ones.

A Noztek filament winder 1.0 (Noztek, UK) was used to coil and collect the flexible extrudate. The winder's motor speed is controlled by light sensors (Figure 4-1), which detect the filament elevation, and varied to maintain the filament at specific elevation to the winder. After the HME reached the steady state, the filament was under constant

stress (its own weight) and the position and height of the rig changed to obtain a 1.7 mm radius filament, size was checked using digital callipers (Axminster.co.uk, 0.01 mm resolution).

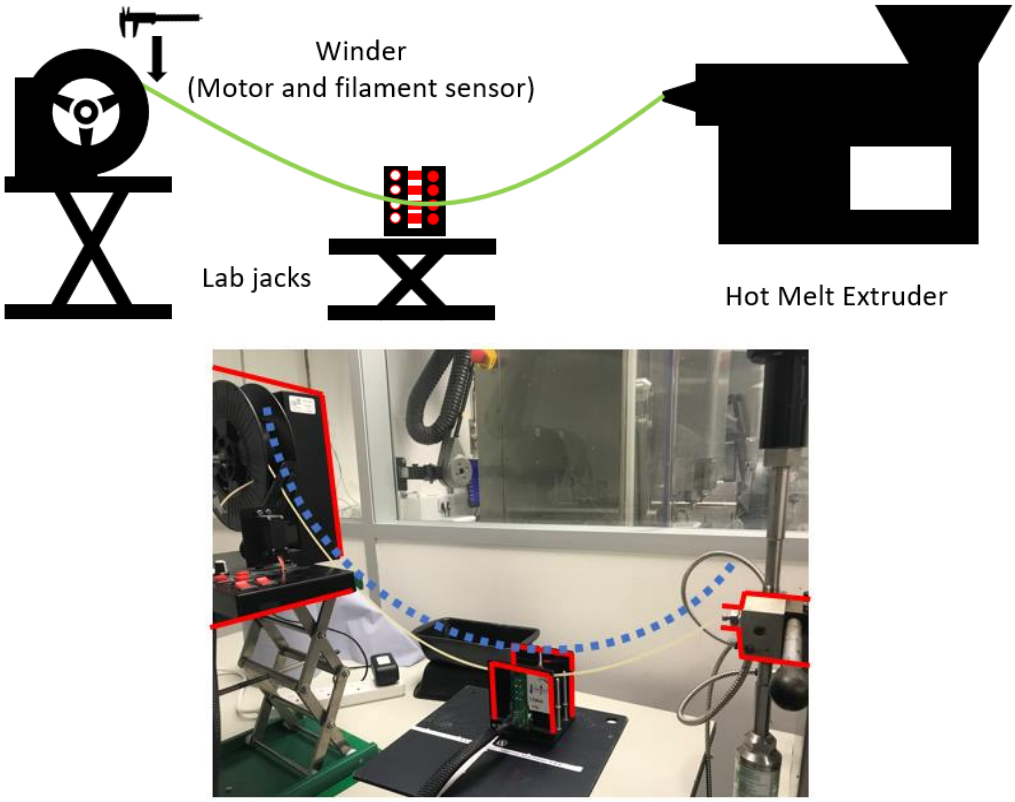

Figure 4-1. Schematic and photo of filament collection and diameter adjustment.

Table 4-1. HME conditions for the studied formulae:

*	T_p (°C)	T_{Zone8} (°C)	T_{die} (°C)
EPO:StA:Filler 72:8:20 (wt)			
EPO:StA:Filler	115	115	110
DoE 1-10			
(MFA:EPO:StA:Silica different ratios)			
DoE 1, 2, 3, 4, 5, 6, 8	130	115-120	110-120
DoE 7, 10	130	145	147-150
DoE 9	130	150	150
Predicted formula			
MFA:EPO:StA:Silica			
	120	120	120

T_p = process temperature, Zone 8 and die temperatures were changed to obtain

filament with diameter of 1.7 mm.

4.2.2.3. Design of Experiment (DoE)

For ratio optimisation, only silica was utilised as a filler in the DoE (Figure 4-2). A full factorial design was established using MODDE version 12.1, which included two levels and three factors (MFA, StA, and Silica ratios), in addition to two central points.

The interaction between the drug and the plasticizer with the polymer occurs at the molecular level. As a result, their ratios are calculated relative to the polymer, marking the first step in the calculation. On the other hand, the filler ratio is calculated as a percentage of the total formula, as the filler interacts with the matrix (MFA:EPO:StA). This marks the second step in the calculation.

To illustrate this (refer to DoE2 Table 4-2), if we start with 75 g of polymer and aim to add 10% of MFA and 10% of StA (first step), this implies the addition of 7.5 g of MFA and 7.5 g of StA, resulting in a matrix weight of 90 g. If we then consider a filler ratio of 10% (i.e., the MFA:StA:EPO matrix is 90 g, equivalent to 90% wt of the total formula), the filler amount would be 10 g (second step), yielding a total formula amount of 100 g.

The two levels for StA, high and low, were set at 10% and 5%, respectively, as a weight percentage of EPO. Similarly, the two levels for MFA were set at 20% and 10%, as a weight percentage of EPO. For silica, the two levels were set at 30% and 10%, weight percentage of the total formula. The levels and ratios of the ingredients are displayed in table 4-2 and Figure 4-2, which includes a 3D plot representing the DoE samples. The DoE formulas were combined and extruded in the HME, as detailed in section 4.2.2.2.

DoE responses were obtained from three-point bend point tests, tensile strength tests, frequency sweep test (viscosity measurement on the rheometer) and temperature sweep test (Tg measurement on rheometer to evaluate the stickiness). Actual mefenamic acid ratio (wt% of total formula) was a calculated value (table 4-2). However, it was added in the DoE to be able to show it with other responses in the contour and sweet spot plots. Both mechanical tests and rheological tests provided numerical values that fed into the DoE. Stickiness was observed in some filaments coiled and stored at 25°C in sealed High -density polyethylene (HDPE) bags. These observations were given a numerical value between -5 to 0, where -5 very sticky and 0 not sticky. Glass transitions

from both DSC and rheometer were compared with the evaluation and used in the DoE as a response. Response limits, inclusion and exclusion will be discussed in the result sections.

Multiple linear regression (MLR) was used. Fitting improvement done by deleting the non-significant coefficients (when error was bigger coefficient value) that do not reduce the model fitting and applying power transformation to the responses (table 4-3).

Table 4-2. DoE sample levels and actual weight:

	Level*				g in 100 g formula			
Experiment	**(MFA**	**StA**	**Silica)**		**MFA**	**StA**	**Silica**	**EPO**
DoE1	(0	0	0)		9.8	4.9	20	65.3
DoE2	(-	+	-)		7.5	7.5	10	75.0
DoE3	(+	+	+)		10.8	5.4	30	53.8
DoE4	(-	-	-)		7.8	3.9	10	78.3
DoE5	(0	0	0)		9.8	4.9	20	65.3
DoE6	(+	+	-)		13.8	6.9	10	69.2
DoE7	(-	-	+)		6.1	3.0	30	60.9
DoE8	(+	-	-)		14.4	3.6	10	72.0
DoE9	(-	+	+)		5.8	5.8	30	58.3
DoE10	(+	-	+)		11.2	2.8	30	56.0

StA levels were 5 (-), 7.5 (0) and 10 (+) % of EPO amount

MFA levels were 10 (-), 15 (0) and 20 (+) % of EPO amount

Silica levels were 10 (-), 20 (0) ad 30 (+) % of the total formula

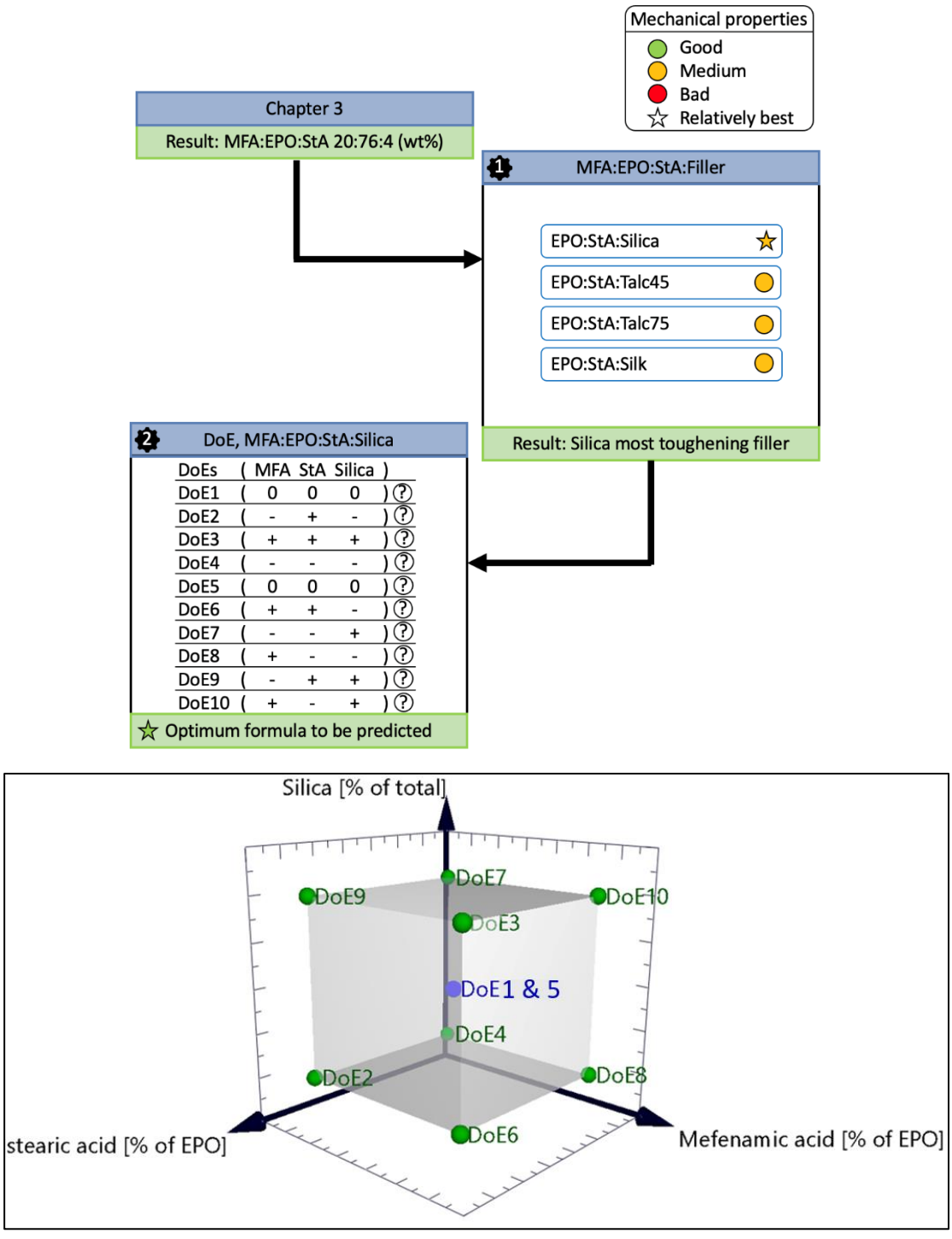

Figure 4-2. Schematic of formulation development (completion of Figure 3-12) and 3D scatter plot of the DoE experiments.

Table 4-3. DoE responses, abbreviations units, power of transformation (Y^c) and limits:

Response	Abbr.	Unit	Y^c	Min	Target	Max
$E/\eta_{150°C\text{-}6.28rad/s}$	En	MPa/%.Pas	$Y^{0.2}$	0.0008	0.0015	-
Maximum stress 3PB	MxSt	MPa	$Y^{0.65}$	22.9	24.2	-
Strain at break TS	Brk	%	$Y^{0.612}$	35	42.1	-
Tg (Rheometer)	TgR	°C	Y^1	73	78	-
MFA content	MFAc	%(wt of total)	$Y^{1.23}$	8	9	-
Tan(δ)- 150°C	TanD	/	$Y^{0.042}$	1	-	-

Maximum limit left empty as higher value is preferable, while target was calculated as minimum limit + standard deviation from the corresponding tests. Except MFAc, minimum and target values were arbitrary.

4.2.2.4. Formulae performance

4.2.2.4.1. Mechanical properties 3-point bend test and tensile strength:

For filler screening only the three-point bend test (3PB) as detailed in sections 2.2.2.5.1 and 3.2.2.5.1 was used. While both 3PB and tensile strength (TS) tests were used to measure the DoE extrudates.

The tensile strength conducted on a Texture Analyser TA-XT (Stable Micro Systems, Godalming, UK) with load cell of 30 KG. Extrudates with a length of 30 mm were mounted on A/MTG Miniature Tensile grips (Stable Micro System LtD, Surrey, UK). The distances between the grips were 20 mm (actual sample length). The sample sandwiched and cantered between two layers of rubber and sand sheet to improve the gripping. Figure 4-3 is schematic and actual photos of the tensile strength accessory loaded with the sample. The gripper tension tightened using torque screwdriver at 0.5 Nm. The upper blade speed was set to 0.1 mm/sec until a trigger force of 0.049 N was reached. Then test started at 0.05 mm/sec (higher than 3-point bend test, 0.02 mm/sec).

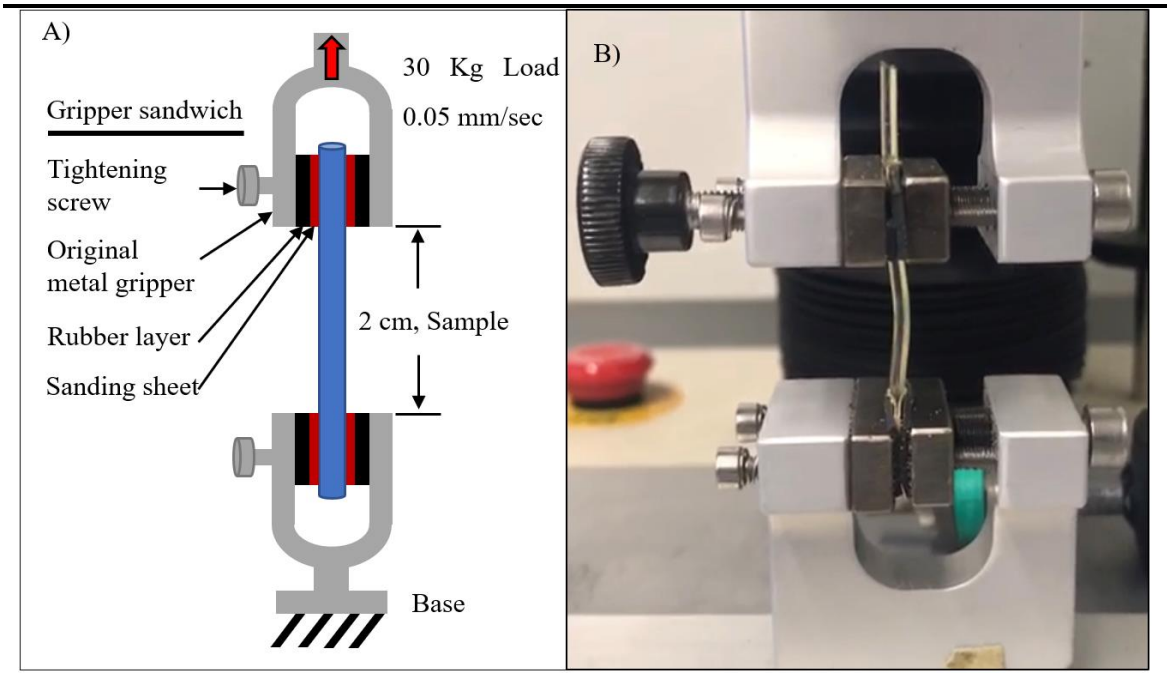

Figure 4-3. Schematic of the tensile strength test experiment (A) and picture of the setup (B).

The extrudate diameters for all the samples ranged between 1.65 mm and 1.77 mm. Data processing is done as detailed in section 2.2.2.5.1. Only DoEs filaments were tested on the tensile strength test.

To compare between both mechanical tests, mechanical values should provide differentiation between the samples and contain minimal deviation between sample repetitions. To evaluate the variation within sample repetitions, the coefficient of variation (CV) which is the normalised sample standard deviation of the average was calculated (eq 4.1). Then the overall variation was calculated as an average for these CVs (eq 4.2).

$$CV = \frac{s}{\bar{x}} \times 100\% \qquad \text{(eq 4.1)}$$

$$\overline{CV} = \frac{1}{N}\left(CV_1 + CV_2 + CV_3 + .. + CV_N\right) \qquad \text{(eq 4.2)}$$

Where $\bar{x}$ is the average of interest (elastic modulus, strain at break, … etc), s is the corresponding standard deviation, N is the total number of samples (10 samples in the DoE). The lower the $\overline{CV}$ is better (less error and better reproducibility). A good test is a test that differentiate between the samples. Thus, the test that showed biggest variation

between samples (different DoE filaments) was favourable. Therefore, sample to sample variation was calculated as the coefficient of variation for the samples (CV_{ss}) using the following formulae (eq 4.3, 4.4 and 4.5).

$$\bar{X} = \frac{1}{N}(\overline{x_1} + \overline{x_2} + \overline{x_3} + .. + \overline{x_N}) \quad \text{(eq 4.3)}$$

$$S_{ss} = \sqrt{\frac{\sum(\bar{x}_i - \bar{X})}{N}} \quad \text{(eq 4.4)}$$

$$CV_{ss} = \frac{S_{ss}}{\bar{X}} \times 100\% \quad \text{(eq 4.5)}$$

Where $\bar{X}$ is the average of all DoE's samples. S_{ss} is the corresponding standard deviation. The bigger the variation between the samples (CV_{ss}) the better the test. In addition to the numerical evaluation, physical meanings of mechanical values were also considered in the comparison.

4.2.2.4.2. Rheological properties:

Haake Mars III Rheometer (Thermo Scientific, HAAKE Technik Co, Germany) equipped with heating chamber was used for all rheological measurements. Zero gap height calibrations were performed prior to measurements with 25 mm diameter parallel plate geometry accessory attached. The chamber was preheated, an excess amount of sample added, after liquification, the top plate was brought down to the measurement position (1 ± 0.05 mm), the sample trimmed and kept in standby for 2-3 minutes, if the sample was stable (no leaking) the measurement was then conducted.

An oscillation amplitude sweep test was performed at the lowest and highest temperature, 120°C and 170°C respectively. Test parameters were controlled, deformation (from 0.01 to 100%) at 1 Hz (6.2832 rad/s) with three repetitions for each data point. The linear visco-elastic region (LVR) was found for each sample-temperature using Haake RheoWin (version 4.87.0010) software.

An oscillatory temperature sweep test was performed starting from the high temperature 170°C to 25°C at a cooling rate of 2°C/min. Controlled deformation mode at a constant amplitude within the LVR limit and frequency of 1 Hz (6.2832 rad/s) was used. Each data point generated from five repetitions.

Oscillatory frequency sweeps were conducted at each of 170°C, 160°C,150°C, 140°C, 130°C and 120°C. Similar amplitude of the oscillatory temperature sweep test was used across a frequency range from 0.1 to 100Hz.

The shift factor (aT) of G', G" and viscosity at different temperatures (120°C, 130°C, 140°C, 150°C, 160°C and 170°C) for frequency sweep tests (time-temperature superposition principle, TTS) can be calculated using MATLAB-based program [184]. From aT (eq 4.6), Arrhenius flow activation energy (Ea, kJ K^{-1} mol^{-1}) can be calculated (Eq 4.7). Ea is the energy required for a molecule to overcome the friction of neighbouring molecules to initiate a motion [185].

$$ln(aT) = a + b(\frac{1}{T}) \qquad \text{(eq 4.6)}$$

a and b are the constants of the linear fit between the shift factor and 1/T : T in Kelvin.

$$Ea = \frac{R_G lnaT}{\frac{1}{T}-\frac{1}{T_R}} \qquad \text{(eq 4.7)}$$

Where R_G is the gas constant (0.008314 kJ K^{-1} mol^{-1}), T is temperatures of interest, T_R is reference temperature used in TTS.

Shear thinning behaviour was evaluated by comparing viscosity at low versus high frequencies [86]. Although in the cited study, the highest and the lowest values were used, here the first and last points were excluded (e.q 4.8). Avoiding the initial step and last step of the test helped to reduce the artificial error at the start and the end of the oscillation part of the test.

$$|\Delta\eta^*| = |\eta^*_{\omega=0.92} - \eta^*_{\omega=428.1}| \qquad \text{(eq 4.8)}$$

4.2.2.4.3. 3DP:

Filament printer feeding was tested using two methods as detailed previously in sections 2.2.2.5.2 and 3.2.2.5.2: manually by hand and G-code order (10 mm at 180 mm/min). The tests were performed at nozzle temperatures of 150°C, 160°C and 170°C with a nozzle diameter of 0.4 mm. 3D printing experiments to print the DoE formulae were conducted using cylindrical tablet shape at 180 mm/min. When it was possible the reason of failure was identified as breaking before the gears, breaking or erosion on the gears, breaking or buckling after the gears.

The predicted optimum formula from the DoE was tested at different speeds ranging from 60 to 240 mm/min at printing temperature from 130°C to 160°C and bed temperature of 25°C. After motor calibration, G-code order to extrude 100 mm at the test temperature and speed sent to the printer. If less than 100 mm was printed, one of the following reasons was considered: slippage, buckling and breaking. When slippage occurred, the test was repeated with increasing gear tension on the filament by rotating the tension screw one full turn per trial.

A caplet with a flat base was designed on Fusion 360 (Version 2.0.12670) and converted to STL file (using Meshmixer 3.5.474). Then G-code files were created using Ultimaker Cura 4.9.0 slicer with default Creality ender-3 printer setting. The printing setting were: two layers for wall (0.8 mm), top and bottom, lines infill pattern at 100% infill, 0% overlap, and 0.4 mm infill distance, 0.2 mm layer height, 0 cooling fan speed and 25°C build plate temperature. Cold extrusion checking was disabled to allow printing below 170°C. Printing test conducted at 150°C nozzle temperature and 180 mm/min speed, at 155°C and 240 mm/min speed and at 160°C nozzle temperature and 420 mm/min speed.

Optimum formula was also tested on an additional printer used by other research groups [66], [186]. The printer was Prusa i3MK3S (Prusa, Czech Republic). Tests were conducted by printing 10 tablets at 150°C and 900mm/min speed, 160°C and 420 mm/min speed and 160°C and 900 mm/min speed.

4.3. Results and discussion

4.3.1. Filler screening

Filler degradation was tested before HME extrusion (see Figure 4-4 and table 4-4). The mass loss from room temperature 25°C until 120°C (heat rate 20°C/min) were assigned to water and solvent residual in the sample. In this temperature range only silica showed value above 1% (wt) due its ability to adsorb water at low humidity level [187]. Above 120°C, mass loss was assigned to degradation. From previous chapters the potential process temperature was below 170°C. From 120°C to 170°C, all fillers were stable (mass loss below 1%, wt). Above 170°C, only silk showed degradation (more than 13%, wt). The degradation started at 190°C showing an agreement with a previous study by Zhang et al who studied the thermal properties of silk fibres reporting no

weight change from 98°C to 190°C, while gradual then sharp loss was observed at higher temperatures [188].

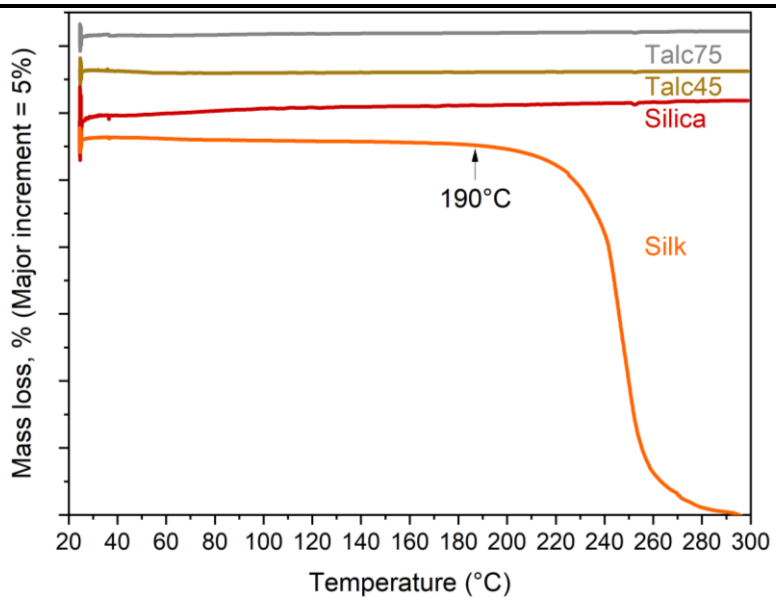

Figure 4-4. Mass loss (%wt) of the fillers from the thermogravimetric analysis at heating rate of 20°C/min.

Table 4-4. Mass loss (%wt) of the fillers from the thermogravimetric analysis at 20°C/min heating rate:

Material	**20-120°C**	**120-170°C**	**170-240°C**
Talc75	0.4%*	0.1%	0.2%
Talc45	0.0%	0.1%	0.1%
Silk	0.3%	0.3%	13.4%
Silica*	1.6%	0.4%	0.4%

Rounded to a decimal place.

Silica powder has low density therefore the total sample mass was below 1.6 mg.

The HME process temperature was chosen to avoid degradation of the components at 115°C (<150°C, section 2.3.4). To study the potential mechanical properties improvement (impact of the filler on the matrix), a very ductile formula was chosen i.e. no MFA and high ratio of StA (10:90 wt:wt of StA:EPO, section 3.3.2). A 20:80 wt:wt of filler:polymer-matrix (where polymer matrix s the plasticized polymer) ratio was

used for initial screening. The appearance of the filaments can be seen in Figure 4-5, all filaments were opaque except for silica. This was due to the high load of the filler (20:80 filler:matrix, wt:wt) and the transparent appearance was assigned to the nanoscale of the silica particles [189].

Filler:	Silk	Talc (<45 µm)	Talc (<75 µm)	Silica

Figure 4-5. EPO:StA:filler (72:8:20) filaments, fillers (silk, talc < 45 µm, talc <75 µm and Silica), scale (1 mm increment).

Mechanical properties of the filler containing and filler free extrudates are plotted in Figure 4-6. All fillers showed significant improvement in mechanical properties. Both flexural modulus and maximum stress were higher for filler containing (reinforced) extrudates and followed the same increasing pattern. Silica showed the highest increase at approximately thirteen times when compared to the filler free systems and for talc values were five (for 45 µm) or six (for 75 µm) times higher than EPO:StA 90:10 (wt:wt). Silk's values were only four times higher. The impact on the strain at break was not clear as the test reached the maximum deformation, however all systems retained good flexibility.

In the second chapter the presence of the MFA particles increased the stiffness. There was a reduction in the strain at break (increase in the brittleness), and breakage occurred in the elastic region affecting the maximum stress value. The different behaviour with the filler containing systems is due to the base flexible matrix (MFA-EPO matrix was brittle). To achieve the reinforcement the following requirement applied [135]. The filler is stiff (high elastic modulus) and strong (high maximum stress) like talc [190] and silica [189] and the matrix is ductile (high strain at break). Thus, the examined fillers improved the EPO:StA formula.

The impact of the particle size on the mechanical properties was revealed by using talc45 and talc75. The bigger particle size improved both flexural modulus and maximum stress more (Figure 4-6 bar charts). This impact was explored previously in the literature using polyethylene and styrene-butadiene polymers with different fillers.

The elastic modulus, yield stress and maximum stress increased proportionally with particle size increase for each filler (linear relationship) [191]. Although the silica particle size was smaller than talc45 (aggregated form smaller than 43 μm according to the material datasheet), the mechanical properties were drastically improved. However, the reinforcing effect depended on the filler chemical structure, particle shape, filler-matrix adhesion [135]. The slope of the linear relationship between particle size and mechanical properties depended on the filler and polymer types [191]. The branched aggregated structure of the fumed silica might have improved the particle-matrix adhesion (higher circularity value, table 4-5). Fumed silica had a stronger reinforcing effect on poly(2-vinylpyridine) in comparison with colloidal spherical silica. The mechanical reinforcement assigned to the strong adherence between silica and polymer making the fumed silica behave as node centres and polymer chains as connecting bridges between these nodes [192]. Silk (74μm average particle size, material data sheet) showed the lowest reinforcing effect (lowest maximum stress); however, it was better than filler free extrudate.

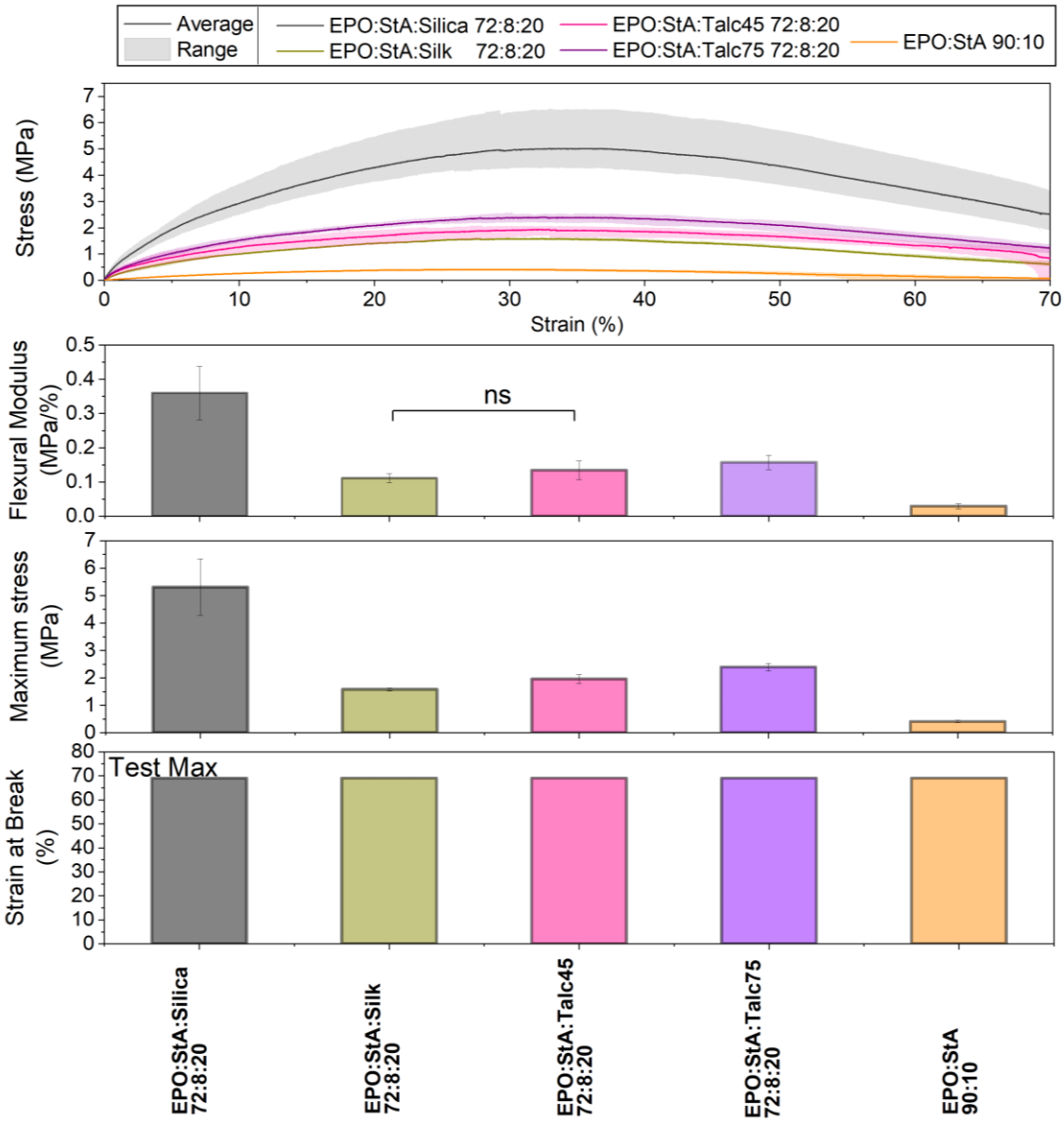

Figure 4-6. Mechanical properties from 3-point bend test for filler containing and filler free extrudates. Stress-strain curves (A), flexural modulus (B), maximum stress (C) and strain at break (D). Average value (n=5, error bar = SD), ANOVA test only non-significant difference (ns, P<0.05) added to the graph i.e. all the remainder are significant.

Table 4-5. Circularity of 50% (median, D0.5) of filler particles per volume and per number:

	Circularity D[n, 0.5]	Circularity D[v, 0.5]
Talc 45	0.552	0.4033
Talc 75	0.582	0.4934
Fumed silica	0.452	0.258
Silk	NA	NA

NA values not available, sample was not measured.

4.3.2. Quality attributes for 3D printing filament

4.3.2.1. Evaluation of mechanical properties from 3PB and TS

From previous experiments, StA and silica were the best plasticizer and filler respectively for MFA-EPO system. Both StA and MFA interact with EPO on a molecular level and separated at ratios above 10% (wt, of EPO) and 20% (wt, of EPO), respectively. Silica suspended in the matrix as particles and showed reinforcement effect at 20% (of total formula weight, wt). Therefore, a DoE of the three ingredients (MFA, StA and Silica as drug, plasticizer and filler, respectively) was conducted around these ratios (table 4-2).

DoE filaments mechanical properties were tested using three-point bend test and tensile strength test to extract mechanical values from the DoE formulae. A comparison between the tests was conducted according to equations 4.2 and 4.5 (section 4.2.2.4.1). $\overline{CV}$ and CV_{ss} values are shown in table 4-6. Extracted data are plotted in Figure 4-7 and 4-8, with the full data set presented in appendix 3 (Figure appendix 3-1, 3-2, 3-3 and 3-4). In addition to the mathematical evaluation, the physical relationship to 3D-printing process for each value was considered. The importance of these values to predict printability and using it in DoE will be discussed later.

From the strain-stress curve of the mechanical tests all the values presented in table 4-6 were extracted. The elastic modulus (flexural modulus for 3PB test and Young's modulus for TS test) represented the stiffness, i.e. the resistance of the material to deform under the applied stress. Results from both tests were able to differentiate between the samples. 3PB test was preferable as it showed a lower $\overline{CV}$ and higher CV_{ss}, 9.6% and 69% (13.8% and 64.9% for TS), respectively. The elastic modulus values also showed the same pattern with difference between the tests for the same sample below

1.2 MPa/% (Figure 4-7). The maximum stress for both tests showed similar trends with the optimum the 3PB values due to its better reproducibility (lower $\overline{CV}$). Stress at yield point from 3PB was also preferable over TS, however strain at break from 3PB was not useful as the test did not differentiate between the formulae (14%, low CV_{ss}). While TS was better to apply to compare formulae (68.7%). Similar to strain at break, strain at maximum stress from the TS test was preferable (higher CV_{ss}). Strains at yield points had low CV_{ss} from both TS and 3PB tests, thus did not differentiate between samples. In general, 3PB test showed better results for stress values while TS test were superior for strain values. This was assigned to the test's setups and speeds. Sample placement in the texture analyser for 3PB was easier in comparison for TS where samples sandwiched, centered and aligned straight between the grippers. On the other hand, strain values were preferable in the TS, as the test maximum deformation was not limited (more than 800%). In this case TS test speed was faster than the 3PB one. A faster test speed increased plastic deformation and induced earlier failure of polypropylene random copolymer [193].

Resilience modulus, maximum strength modulus (area under the curve until maximum stress) and modulus of toughness represented the energy the system can take until yield point, maximum stress point and break point, respectively. Since the modulus values were calculated as area under the curve, the correlated strain and stress values defined the size of these areas. For example, modulus of resilience defined by both strain and stress of yield point, the $CV_{ss}$of both resilience modulus and yield stress (yield strain did not show differentiation, low CV_{ss}) were very close (CV_{ss} of 69.6% and 68.6% for 3PB, and 52.8% and 53% for TS, respectively). Similar principles applied on other area under the curve values, where variation either associated with stress or/and strain values defining it ($CV_{ss}$for TS test were 68.6% and 68.7% for modulus of toughness and strain at break, respectively). Moreover, the area under the curve values had higher $\overline{CV}$ suggesting lower reproducible results (higher error).

In term of the physical meaning, elastic modulus describes the elastic relationship between deformation and stress i.e. the amount of stress generated with specific strain [194]. The higher the value the better the filament worked as a piston to push the molten material out. Venkataraman et al found that a critical value of elastic modulus on viscosity ratio at specific shear rate must be exceeded for the material to flow out of the printer nozzle (section 1.5.2) [70]. Although the elastic modulus in the mentioned work

was obtained from compression test rather than TS or 3PB tests and pharmaceutical literature generally used 3PB and TS tests because they were more reliable [186]. In 3PB test, both tension and compression forces were applied on the filament cross section (bottom and top, respectively) as described in section 2.3.5.1. Some researchers used elastic modulus from compression and tensile test interchangeably to describe material stiffness as the elastic region from the tests were essentially similar [186]. While others argued that elastic modulus will be sensitive to potential polymer rearrangement due to shear stress in the HME process, however, they used combination of TS and 3PB test to evaluate printability [95]. The same elastic modulus pattern from TS and 3PB with a small difference in the values (<1.2 MPa%) suggested that the rearrangement was not significant for amorphous polymer. Moreover, TS conducted at slightly higher test speed hence lower elastic modulus value obtained. Semicrystalline polymer is more sensitive to shear stress as this potentially affect polymer rearrangement and the amount of crystallinity in the system [135]. However, Samaro et al [86] used TS, 3PB and compression tests on seven different grades of ethylene-vinyl acetate (EVA) copolymers with different VA ratios (different crystallinity ratios), similar mechanical property trends were observed for all samples on the three tests, except 18% VA on compression test.

Using stiffness only without linking to rheological behaviour might not reveal good comparison between the formulae. Hence, researchers used both to predict their formula printability [186]. It is worth noting that the relationship between elastic modulus on viscosity ratio and the extruder specification of the 3D printer did not describe formulae printability. The ratio represented the filament's ability to work as a piston to push the viscous molten material [70]. However, this was one step of the printer process representing the part from where the filament leaves the gears until the tip of the printer (the third step). To avoid confusion this ratio will be termed in this work 3DP-extrudability. The filament also gripped by the extruder gears (the second step) and bent in the feeding tube between the spool and extruder head (the first step). Samaro et al [86] differentiated between two steps (feedability and printability) on FFF 3D printer. Other researchers used strain at break in their printability evaluation as the filament needs to be flexible [84], [195]. As discussed earlier only strain at break and strain at maximum stress from TS test were useful mathematically to compare the formulae. Both values showed a similar pattern except for DoE8 (+ - -) (Figure 4-7). Since the aim is to assess the filament's ability to bend (the first step) the strain at break was chosen as response

in the DoE. Several researchers have evaluated the strain at break using two test speeds. Examples of using TS tests at two speed, [186] 3PB tests at two speed [68], combination of TS and 3PB [94], [95], [195] can be found in the cited papers.

In the second step, the gears should provide sufficient stress on the filament to transfer the rotation to linear motion and avoid slippage. The stress should not exceed the filament maximum stress to avoid breakage, erosion or drastic impact on filament cross section. Thus, maximum stress was chosen as response in the DoE. It was preferable over yield point stress as small indentations on the filament were commonly noticed for good filaments [195]. Although 3PB test does not mimic gear indentation on the filaments, researchers used it for their printability evaluation [84], [195], [196], [197]. However, extracting this value directly from cutting test, indentation test [198] or stiffness test (Repka-Zhag method [199]) might be more useful. In the current work maximum stress from 3PB was used as response in the DoE. For brittle filament (like MFA:EPO systems, chapter 2) the maximum stress might not follow a reasonable trend since extrudates broke in the elastic region. However, brittleness (strain at break) evaluation can exclude brittle formulae in printability prediction.

Resilience modulus, maximum strength modulus and modulus of toughness represent energy needed to produce the associated deformation. Since these moduli defined by the associated strain and stress values and carried the same sample to sample variation (differentiation) but with higher error, using the stress and strain values directly were more beneficial. Especially that variation could be decreased or increased by the associated strain and stress values. Therefore, these moduli were not included in the DoE. The elastic modulus, maximum stress and strain at break were only used for DoE prediction. The same points defined material toughness which is in agreement with previous literature. Xu et al compared between 3PB, TS and stiffness tests for printability prediction and found that toughness from stiffness tests were predicting the printability [200]. However, their work did not consider the rheological behaviours which is included in the current work as elastic modulus on viscosity ratio. Moreover, using the values as separated responses might be better to define the formula weakness and define the required changes. Analysing the responses are covered in later section (section 4.3.3). Bar chart presentations of the data also are in appendix (Figure Appendix 3-4).

Table 4-6. Comparison between three-point bend test (3PB) and tensile strength (TS) in term of overall coefficient of variation ($\overline{CV}$) and sample to sample variation (CV_{ss}):

	Variation between repetitions ($\overline{CV}$, %)		Sample to sample variation (CV_{ss}, %)	
	3PB	**TS**	**3PB**	**TS**
Elastic modulus	9.6	13.8	69.0	64.9
Maximum stress	5.4	7.6	59.0	41.0
Strain at break	8.7	14.0	24.4	68.7
Strain at maximum stress	11.5	17.0	18.7	78.4
Strain at 0.2% yield point	10.2	7.9	9.3	8.4
0.2% Yield stress	11.0	11.0	68.6	53.0
Resilience modulus	19.3	16.3	69.6	52.8
Maximum strength modulus*	16.0	24.1	57.6	74.7
Modulus of toughness	13.2	20.5	47.6	68.6

Eq 4.2 and 4.5 were used to calculate both $\overline{CV}$ and CV_{ss}, respectively.

Green font refers to optimal results (low $\overline{CV}$ or high CV_{ss}).

Maximum strength modulus was calculated as the area under the curve until reaching the maximum stress.

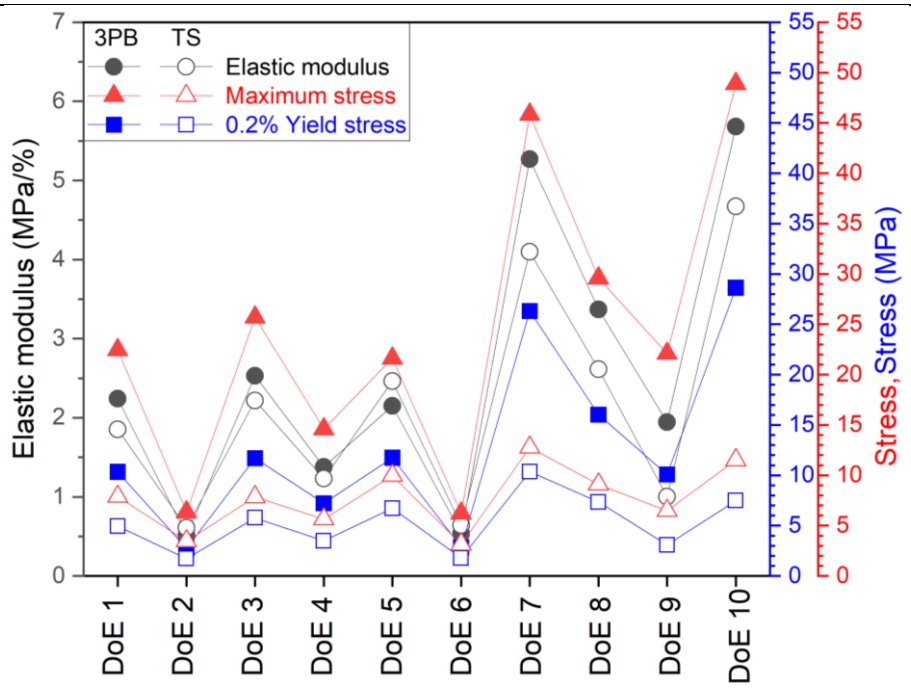

Figure 4-7. Elastic modulus and stress values of DoE filaments from both three-point bend (3PB) tensile strength (TS) tests.

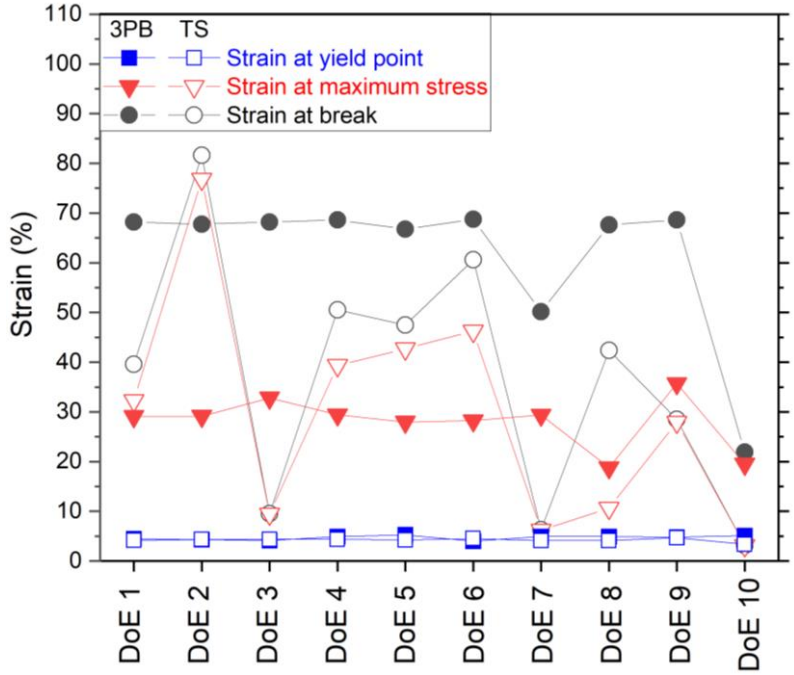

Figure 4-8. Strain values of DoE filaments from both three-point bend (3PB) tensile strength (TS) tests.

4.3.2.2. Rheological properties

Figure 4-9 shows a representation of the amplitude sweep test (appendix 3-5 for all DoEs). From the amplitude sweep test, all samples showed complex viscosity behaviour (shear banding) as the loss (G") and storage (G') moduli had another event (Figure 4-9 arrow) before dropping at high amplitude. This complex behaviour might be due to presence of lubricant (StA), branched copolymer (EPO) or suspended particles (fumed silica) inside the matrix [120]. As a result, the linear viscoelastic region (LVR) was identified on both G' and G" curves and the lowest were chosen as LVR limit (arrows in Figure 4-9). The following temperature sweep and frequency sweep tests were conducted within the LVR region.

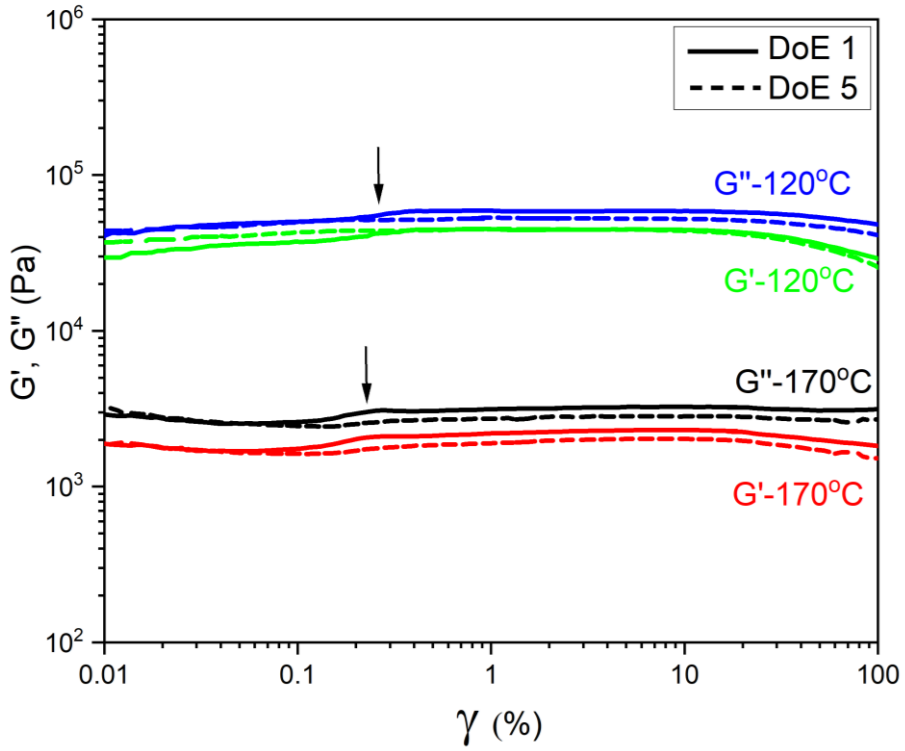

Figure 4-9. Storage (G') and loss (G") moduli of DoE central points (1 and 5) from the amplitude sweep test showing complex behaviour and linear viscoelastic region limit (arrows), data from other samples are shown in Figure appendix 3-5.

Results of the temperature sweep test are shown in Figure 4-10. For all formulae, as temperature decreased the viscosity increased. This was a result of increase in molecular interaction at low temperature and decrease in the molecular mobility. Comparison between the formulae below 70°C was not feasible as good contact with the rheometer plate cannot be assured. At low temperature (<70°C) samples solidified and, in some

cases, lose the grip with the plate. Above 70°C, formulae with high silica ratio (DoE 7, 9, 10 and 3) showed the highest viscosity. Central point formulae (DoE 1 and 5) had lower viscosity followed by formulae with low silica content (DoE 4, 8, 2 and 6). StA and MFA reduced the viscosity but their effects on viscosity were less than silica. Formulae with low StA and MFA had higher viscosity than formulae with one of them. While formulae with both StA and MFA was the least viscous ones (DoE 7 vs 9 and 10 vs 3 and DoE 4 vs 8 and 2 vs 6). Both drug and StA plasticized the polymer as indicated earlier in Chapter 2 and 3. The HME torque and die pressure value were in agreement with the viscosity results in term of silica impact (table 4-7) i.e. viscosity was primarily sensitive to silica content. However, due to the change in the process temperature to obtain the desirable filament diameter the impact of MFA and StA was not captured in the HME experiments. Die pressures and torque values were high for formulae with high silica ratio. Increasing zone 8 and die temperatures were required to reduce the viscosity and as a result die pressure and torque values below 100 (bar and %, respectively). In Figure 4-10 (red box), these formulae had viscosity above 10000 Pas. While DoE 6 and 2 were on the edge or below 1000 Pas, thus reducing the die temperature to 110°C and 112°C respectively was needed.

Gupta et al [201] found that found that viscosity between 1000-10000 (dashed lines Figure 4-10) was the ideal viscosity range for HME-extrudable polymer. In this work they used different grades of polyvinylpyrrolidone (PVP) and PVP-based grafted copolymer namely Soluplus® (polyvinyl caprolactam-covinylacetate-ethylene glycol) and Kollidon® VA 64 (PVP-vinyl acetate). In another study Gupta et al [202] and Parikh et al [134] confirmed the same viscosity limit applicable on Soluplus® loaded with up to 30% (wt%) carbamazepine and polymethacrylic acid based polymers (including EPO). In these studies, increasing temperature and drug content reduced both the viscosities and the torque values.

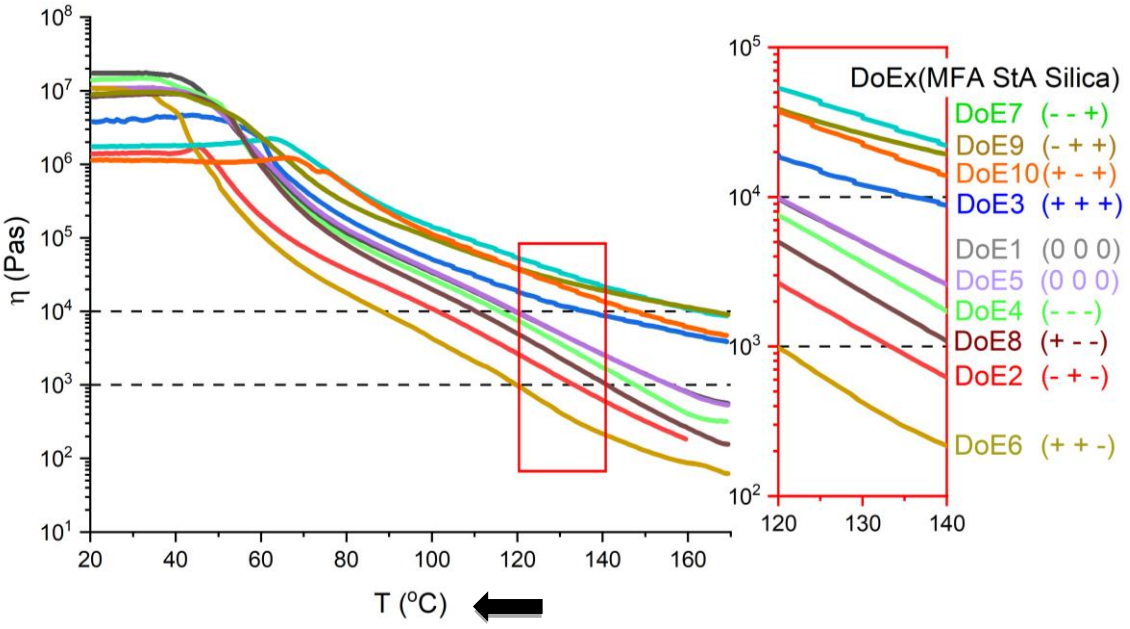

Figure 4-10. Viscosity of all DoE formulae at different temperature plotted together, zoom in box (right side). Central points (DoE1 and 5) were overlapping.

Table 4-7. Pressure and torque values from the HME experiment of DoEs filament:

		Zone 3-7	Zone 8	Die Zone	Pressure	Torque	**
		(°C)	(°C)	(°C)	(bar)	(%*)	
DoE 7	**(- - +)**	130	145	147	52.9	61.8	B
DoE 9	**(- + +)**	130	150	150	36.4	51.1	B
DoE 10	**(+ - +)**	130	145	150	45.0	53.5	B
DoE 3	**(+ + +)**	130	130	130	67.7	48.2	-
DoE 5	**(0 0 0)**	130	120	120	38.2	43.8	-
DoE 1	**(0 0 0)**	130	115	110	72.2	48.5	-
DoE 4	**(- - -)**	130	120	119	23.0	40.0	S
DoE 8	**(+ - -)**	130	120	117	24.5	35.8	S
DoE 2	**(- + -)**	130	120	112	22.8	34.5	S
DoE 6	**(+ + -)**	130	120	110	23.5	33.0	S

* % of the maximum torque value for the extruder, 12 Nm.

** B = filament break during winding, S = filament sticking on each other

Figure 4-11- A and B show storage (G') and loss (G") moduli for the DoE filaments. The components effect on the moduli were similar to the effect on the viscosity. Silica increased in G' and G" and presence of drug and/or plasticizer reduced them. Thus, around process temperature (130°C) the sample orders were similar to the one in the viscosity, from highest to lowest DoE 7, 9, 10, 3, 1 and 5, 4, 8, 2 and lastly 6. G' and G" represented the energy for material to move elastically and plastically, respectively [203]. Graphene nanoplatelets increased the storage modulus for the polyether ether ketone. The additional restriction in the movement attributed to the adsorption of the nanoparticles on the polymer chains [204].

Dump factor (tan(δ)), calculated as the division of G" on G', are plotted in Figure 4-11-C. Thus, the tan(δ) represented the domination of solid like behaviour (1>tan(δ)) or viscous liquid like behaviour (1<tan(δ)). Crossover point (tan(δ) =1) for all formulae were identified in Figure 4-11-C. Dump factors of formulae with high silica content (DoE 7, 9, 10 and 3) were below 1 across the temperature from 20°C to 170°C i.e. G' dominant. Thus, filler increased the solid like behaviour and reduced tan(δ). Other formulae (low silica) with both StA and MFA showed highest tan(δ) value. The values at HME process temperature followed the opposite order seen in η (viscosity), G' and G" i.e. from highest to lowest DoE 6, 8, 2, 4, 1 and 5 then high silica formulae. Nanoclay increased G', G" and viscosity of polymethyl methacrylate but reduced tan(δ) [205]. The reduction in the dumping factor of poly styrene co butyl acrylate – nanocellulose composites were stronger with high filler content (ranged from 0 to 15%, wt%) [189]. One to two crossover points found with low to medium silica content, the first cross over ranged from 52°C to 68°C and the second from 89°C to108°C. Which were assigned to the relaxation of the side chains and polymer flow, respectively [134]. The second cross over of DoE 8, 2 and 4 (low silica and high MFA or/and StA) were lower than 105°C showing the plasticization effect of both MFA and StA on EPO.

Some polymers like hypromellose did not follow the viscosity range (1000 to 10000 Pas) role for HME-extrudability, as this polymer showed strong shear thinning behaviour (shear stress dependent) therefore, frequency sweep test was necessary [206]. Although EPO-based systems followed the rule, frequency was conducted.

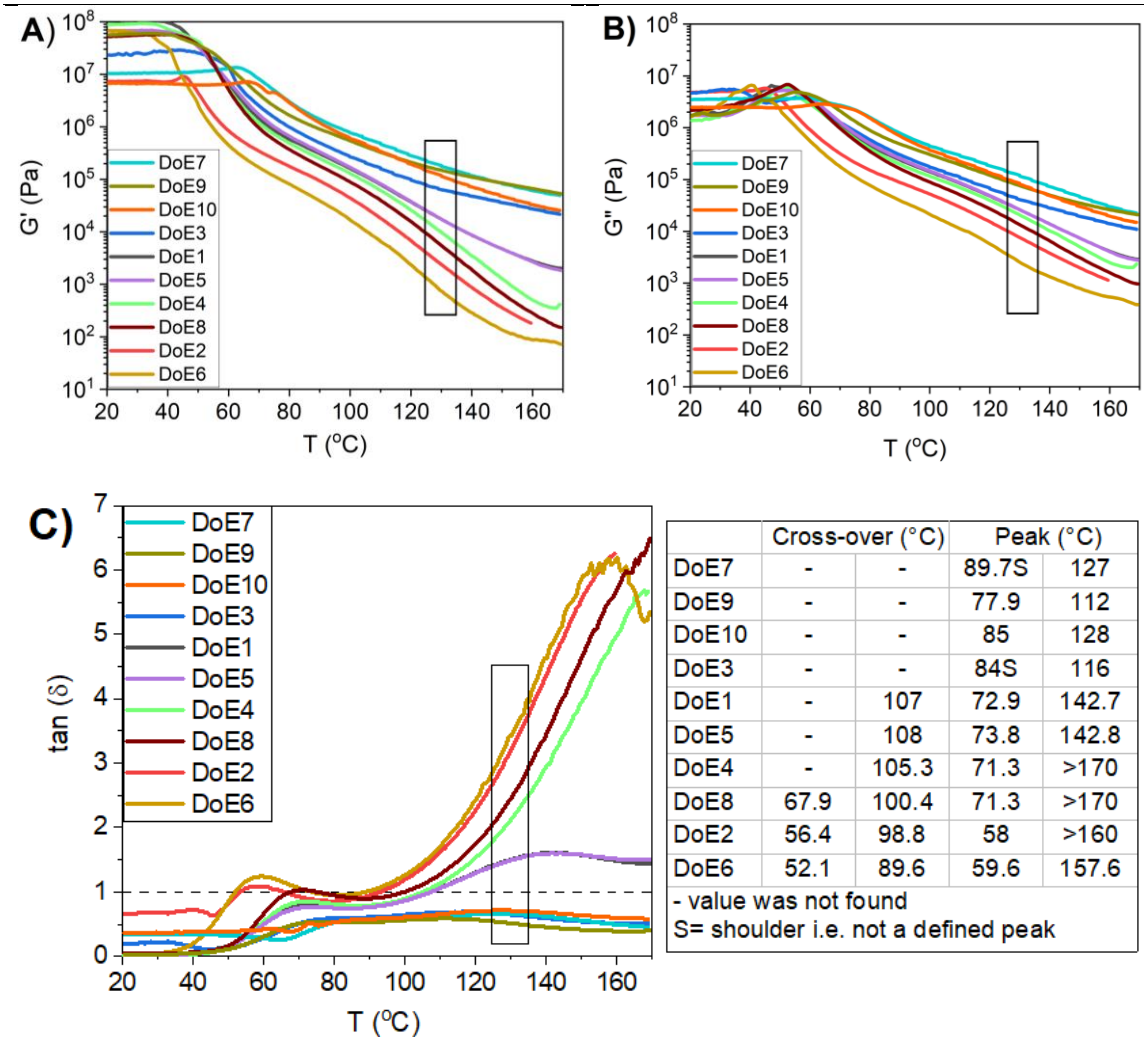

	Cross-over (°C)		Peak (°C)	
DoE7	-	-	89.7S	127
DoE9	-	-	77.9	112
DoE10	-	-	85	128
DoE3	-	-	84S	116
DoE1	-	107	72.9	142.7
DoE5	-	108	73.8	142.8
DoE4	-	105.3	71.3	>170
DoE8	67.9	100.4	71.3	>170
DoE2	56.4	98.8	58	>160
DoE6	52.1	89.6	59.6	157.6

- value was not found
S= shoulder i.e. not a defined peak

Figure 4-11. Storage modulus (A), loss modulus (B) and tan(δ) with the crossover points and peaks (C) of the DoE filaments.

Complex viscosities profiles are presented in Figure 4-12 (low silica content formulae and central points) and 4-13 (high silica content formulae), with additional data in Figures appendix 3-7 to 3-12. In Figure 4-11, liquid-like behaviours (1<tan(δ)) were dominant mostly. But at high frequency and at low temperature solid-like behaviour became more dominant (1>tan(δ)). For high silica formulae (DoEs 7, 9, 3 and 10) tan(δ) were below 1 across the tested frequencies. All formulae, viscosity reduced at higher temperature (similar to temperature sweep test) and at higher frequency due to shear thinning behaviour. As indicated earlier the threshold of elastic modulus on viscosity ratio must be exceeded for formulae to be 3DP-extrudable [70]. Although the viscosity measured using capillary rheometer in the mentioned study, multiple researchers used rotary rheometer for 3D printing [86], [186]. Moreover, Coogan et al [207] measured the viscosity on a 3D printing nozzle inline and verify it with offline measurement on rotary

rheometer. Prasad et al [208] calculated the apparent shear rate of a 0.4 mm nozzle at printing speed 0.5 to 2 mm/s for 1.75 mm filament to be between 20 to 100 s^{-1}. However, the apparent shear rate is different from the actual shear rate due to non-ideal (non-Newtonian) polymer behaviours [207]. Thus, this range was not used and Cox-Merz rule was not checked to match shear rate with frequency. Figure 4-14 shows the elastic modulus on viscosity ratio for all DoE formulae at 150°C (Figure appendix 3-13 at 170°C, 160°C and 140°C). At high frequencies the samples were overlapping and difference between the samples were hard to detect. Thus, viscosity value was chosen at 6.283 rad/s for the comparison. Table 4-8 shows the E/η values at the chosen frequency for all DoE formulae. These results will be discussed in the 3D printing test in further details. Since viscosity is the denominator the formulae with high viscosity showed lowest E/η value. However, the value was not exactly negatively correlated of the viscosity due to the elastic modulus (the numerator) differences between the formulae. For example due to the strong impact of the StA on the mechanical properties (reducing E,) the high StA content had lower E/η in comparison with the one with low StA content (DoE 8 vs 6, DoE 4 vs 2, DoE 10 vs 3 and DoE 7 vs 9).

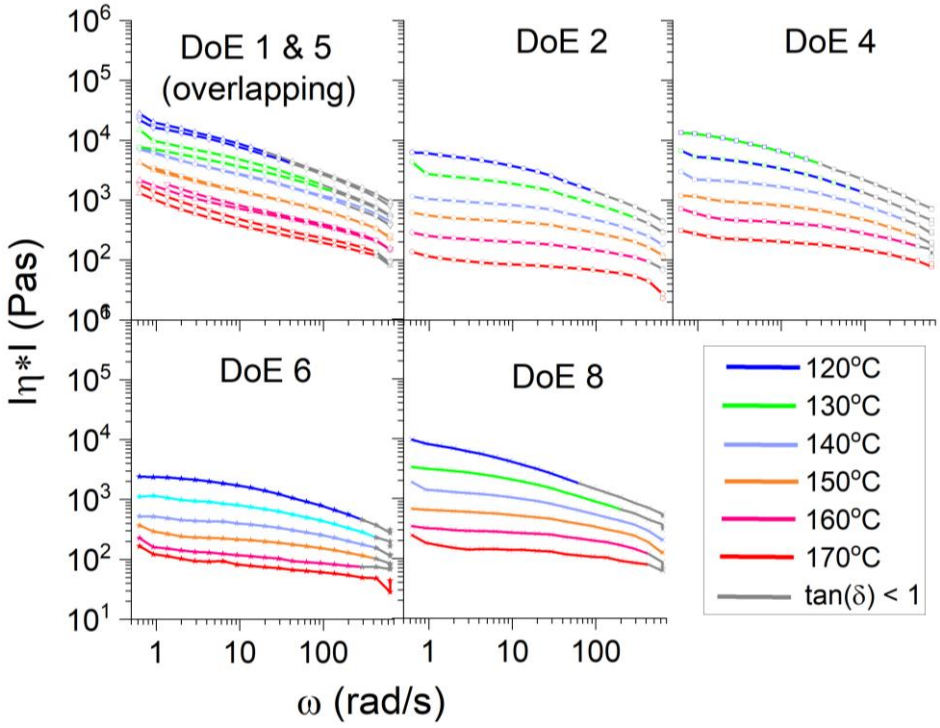

Figure 4-12. Complex viscosity from frequency sweep test of DoE formulae 1, 2, 4, 5, 6 and 8 at different temperatures, if G' was dominant curves coloured with grey (1>tan(δ)).

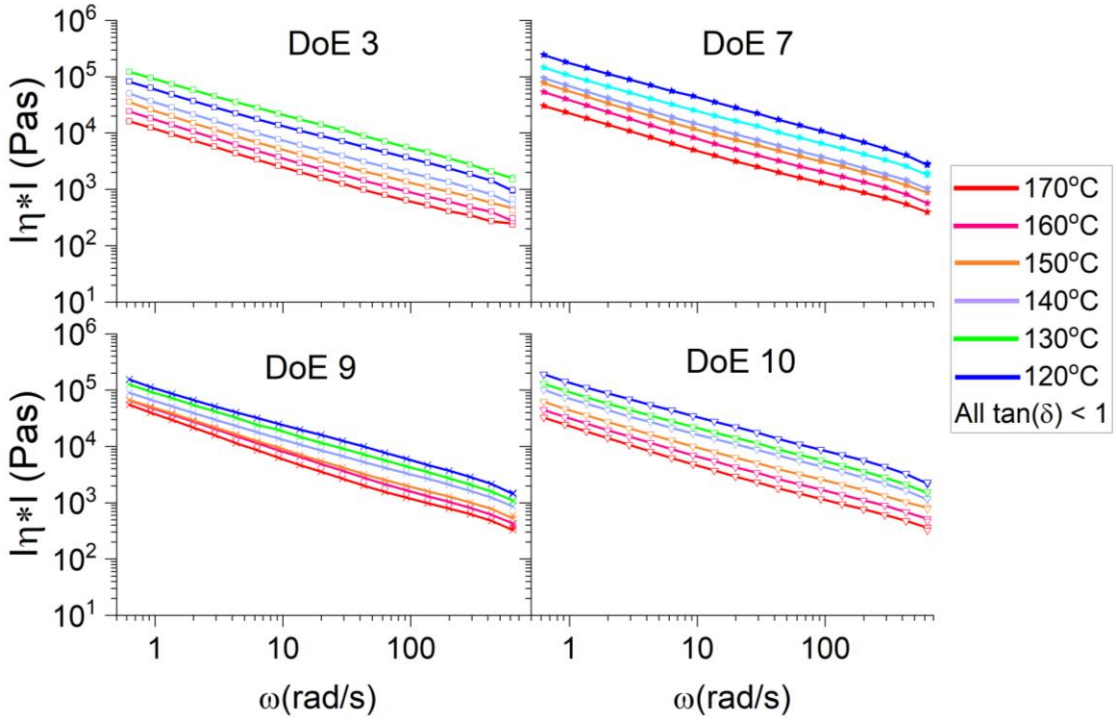

Figure 4-13. Complex viscosity from frequency sweep test of DoE formulae 3, 7, 9 and 10 at different temperatures, in theses formulae G' was always dominant (1>tan(δ)).

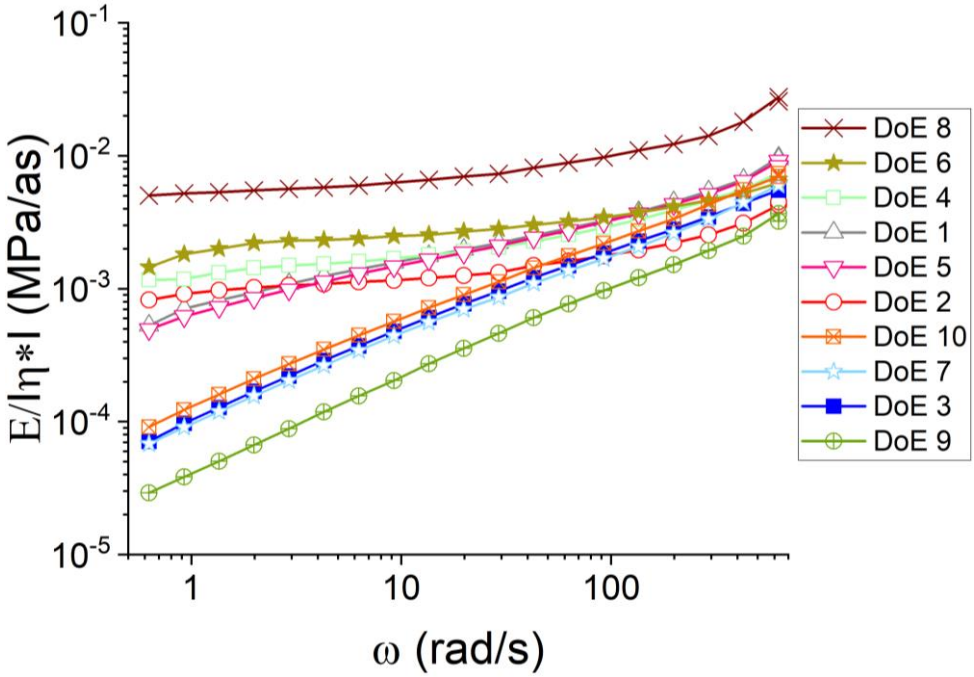

Figure 4-14. E/η in MPa/%Pas of all DoE formulae at 150°C and different frequencies.

Table 4-8. E/η in 10^{-3} × MPa/%Pas of DoE formulae at 6.283 rad/s and different process temperatures:

		140°C	**150°C**	**160°C**	**170°C**
DoE 8	**(+ - -)**	2.99	5.97	12	23.56
DoE 6	**(+ + -)**	1.25	2.38	4.28	5.73
DoE 4	**(- - -)**	0.76	1.6	3.08	6.5
DoE 1	**(0 0 0)**	0.72	1.4	2.71	5.05
DoE 5	**(0 0 0)**	0.7	1.3	2.25	3.76
DoE 2	**(- + -)**	0.59	1.12	2.46	5.85
DoE 10	**(+ - +)**	0.27	0.45	0.64	0.91
DoE 7	**(- - +)**	0.27	0.34	0.49	0.81
DoE 3	**(+ + +)**	0.26	0.37	0.53	0.76
DoE 9	**(- + +)**	0.11	0.16	0.17	0.23

Figure 4-15 is the Arrhenius plot of the shift factor (aT) versus 1/T. Table 4-9 shows the linear fit constants and the calculated (eq 4-7) Arrhenius flow activation energy at 120°C and170°C. Ea values ranged from 53.8 to 76.7 kJ K^{-1} mol^{-1}, with a range of

22.9 kJ K^{-1} mol^{-1}. In general, the samples with higher silica had higher $Ea_{120°C}$ and $Ea_{170°C}$ (except DoE9). However, the difference between Ea values for central points (DoE1 and 5) were up to 7.9 kJ K^{-1} mol^{-1}. Therefore, the comparison between the formulae could not be made and Ea values were excluded from the DoE model. Henry et al [186] used Ea for their formulae comparison, their Ea values for different polymers ranged from 34 to 114 kJ K^{-1} mol^{-1}. The used polymers were polyurethanes, ethylene–vinyl-acetates, polycaprolactone (PCL), polyethylene-oxide (PEO), methacrylates, hydroxypropylcellulose and copovidone based polymers. Using the same based polymer and the close values in the current study might have limited the importance of this value for printability prediction. Henry et al [186] also found the Ea for Ibuprofen-PCL and Ibuprofen-PEO at 20:80 (wt:wt) and 40:60 (wt:wt) ratios, the differences between the two ratios were 8.16 and 0.95 kJ K^{-1} mol^{-1}, respectively.

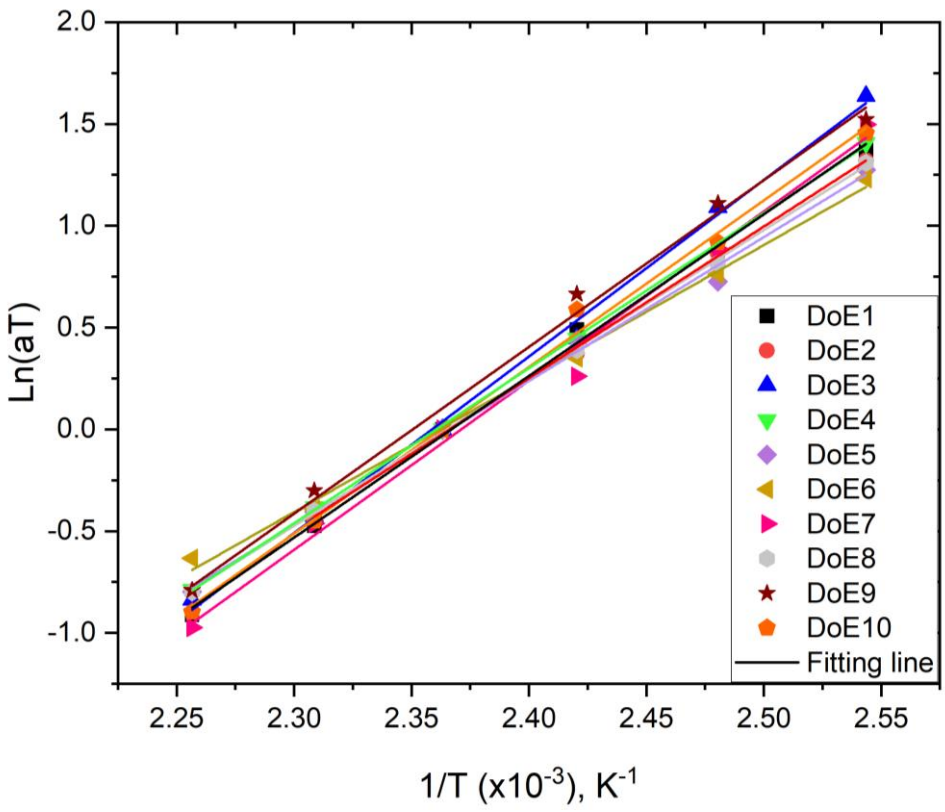

Figure 4-15. Logarithm the shift factor (aT) against the inverse temperature (1/T in Kelvin), the Arrhenius fit was performed at 150°C.

Table 4-9. Arrhenius equation intercept (eq 4-5) and calculated activation energy (eq 4-7):

		eq 4.5 constants			Ea (eq 4-7)	
		Intercept	**Slope**	**R^2**	**$Ea_{120°C}$**	**$Ea_{170°C}$**
DoE1	**(0 0 0)**	-18.8	7939.5	0.99781	63.6	70.4
DoE2	**(- + -)**	-17.6	7446.7	0.99912	59.8	65.7
DoE3	**(+ + +)**	-20.5	8672.1	0.99673	72.4	71.6
DoE4	**(- - -)**	-18	7616.6	0.99972	63.1	63.7
DoE5	**(0 0 0)**	-16.7	7065.5	0.99612	56.6	62.5
DoE6	**(+ + -)**	-15.5	6556.9	0.99676	53.8	55.8
DoE7	**(- - +)**	-19.7	8308.8	0.99126	64.9	76.7
DoE8	**(+ - -)**	-17.2	7261.7	0.99961	58.4	63.9
DoE9	**(- + +)**	-19.3	8190.4	0.99298	71.8	61.5
DoE10	**(+ - +)**	-19.3	8180.7	0.99560	66.9	70.0
Range		**5**	**2115.2**		**18.6**	**20.9**
SD		**1.5**	**617.4**		**5.8**	**5.7**
DoE1-5		**-2.1**	**874**		**7**	**7.9**

Shear thinning was evaluated using the difference between viscosity at high and low frequencies (eq 4-8). Figure 4-16 shows the $|\Delta\eta^*|$ values of the DoEs' formulae. Shear thinning behaviour was observed in all formulae. Silica's impact on the shear thinning was dominant, all high silica content formulae (DoE 7, 9, 10 and 3) showed highest $|\Delta\eta^*|$ followed by central points (DoE 1 and 5) then low silica content (DoE 4, 8, 2 and 6). This might be due to the presence of solid particles in the matrix that as indicated earlier increased G'and G". Therefore, the energy input will be transferred across the matrix.

Both StA and MFA reduced reduction in the shear thinning affect for example DoE 6 vs DoE 2, 8 and 4 and DoE 3 vs DoE 7, 9 and 10. Using StA or MFA only with high silica content did not show a strong affect, which might be due to silica domination on the shear thinning behaviour. However, at low silica content, StA reduced the shear thinning affect more than MFA, for example DoE 2 vs DoE 8 vs DoE 4. The increase of G" in these samples ($1<\tan(\delta)$) suggested the loss of the energy as heat.

As the temperature increased all formulae showed less shear thinning since the formulae liquified more. This was less pronounced at high silica content as the solid content was not affected by temperature. Samaro et al [86] found that formulae with high shear thinning showed less consistency in the tablet shape. This was attributed to the higher sensitivity of the flow at different shear stress during feeding and retraction in printing process.

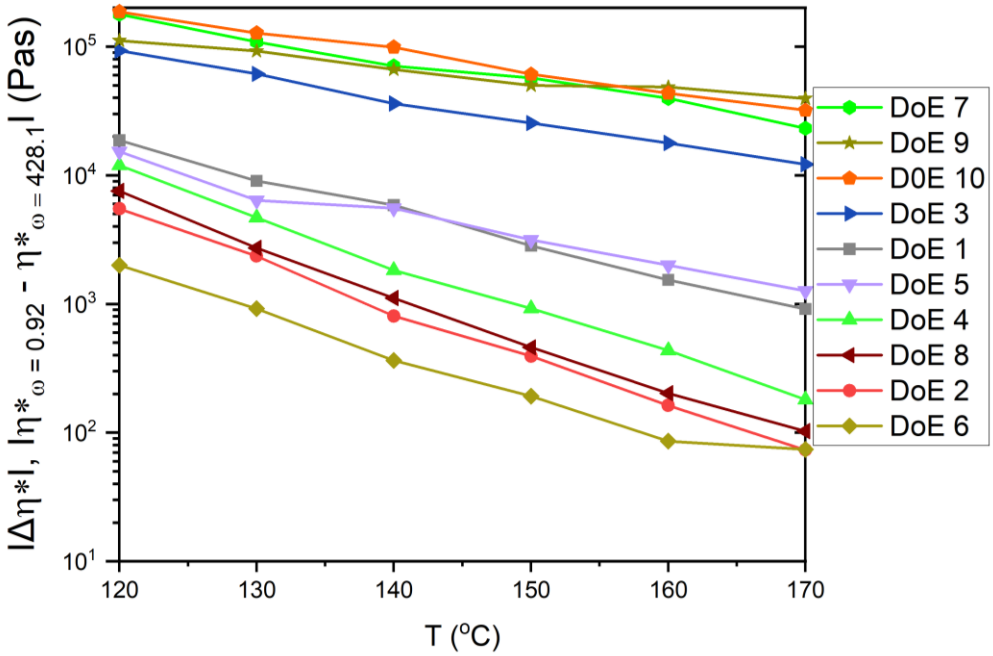

Figure 4-16. Viscosity difference between high shear rate (428.1 rad/s) and low shear rate (0.92 rad/s).

4.3.2.3. Stickiness

Following the HME-extrusion process, the filaments were coiled using the filament winder, as detailed in the methods section. During this process, we observed distinct issues. Some filaments, specifically those from DoE 7, 9, and 10, broke and could not be coiled at all, while the filament from DoE 3 was prone to breaking during winding and coiling. Separately, there were instances of stickiness: filaments from DoE 2 and 6 adhered to each other during the winding process, while filaments from DoE 1 and 5 exhibited stickiness after two months of storage. On the other hand, filaments from DoE 4 and 8 were more able to be coiled and did not exhibit stickiness during the study period. Filament stickiness is therefore another issue which requires consideration in order to produce printable filament. Stickiness was given a subjective score where -5

was very sticky and the filament adheres to itself after extrusion and 0 was not sticky and exhibited no adherence after two months storage (Figure 4-17-top).

To avoid the subjectiveness in the DoE data entry, another numerical evaluation had to be considered. When neighbouring filaments stick on each other during cooling down after extrusion a possible reason was the presence of the material in the rubbery state. Thus, high molecular mobility presented which could be evaluated by the glass transition [135]. Glass transitions measured on both DSC (Tg_{DSC}) and rheometer (Tg_{Rhe}), Figure 4-17 were assessed. Tgs reduced with presence of StA (DoE 4 vs 2, DoE 8 vs 6, DoE 7 vs 9 and DoE10 vs 3). While they increased with presence of silica (DoE 9 vs 2, DoE 3 vs 6, DoE 10 vs 8 and DoE 7 vs 4). MFA increased the Tgs in all the cases (DoE 6 vs 2, DoE 8 vs 4 and DoE 3 vs 9) except DoE 7 vs 10.

Across all formulae, DoE 1, 2, 5, 6, 7 and 10 followed same pattern on both techniques. DoE 3, 4, 8 and 9 showed different pattern. Tg_{DSC} ranged from 33.3°C to 43.7°C (10.4°C) while Tg_{Rhe} from 58°C to 89.7°C (31.7°C). The difference in the Tgs between the two techniques assigned to using different heating rate and detected signal (heat flow in DSC and phase shift δ in rheometer). Moreover, in the DSC the onset (start of the glass transition region) was used since the deflection was hard to measure (fig 4-18), while in rheometer peak of tan(δ) was used (middle of glass transition region).

Ascending order of the Tg_{Rhe} showed agreement with the stickiness ranking (Figure 4-17-middle). Filaments that had Tg_{Rhe} below 72°C showed stickiness. Hancock and Zograf [209] suggested that molecular mobility was present in amorphous systems stored at (Tg - 50)°C, and although their study discussed it from molecular stability perspective, the molecular mobility might occur across two neighbouring filaments with good contact and produce stickiness. Since the Tg_{Rhe} showed same order of the stickiness evaluation spread it across wider range and showed better reproducibility (DoE 1 vs 5), Tg_{Rhe} was applied as a response factor in the DoE model.

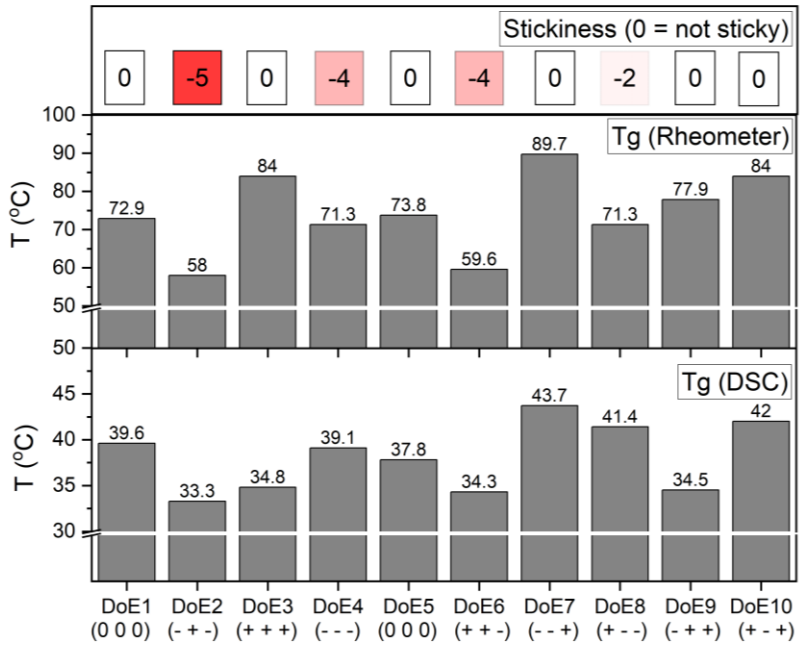

Figure 4-17. Glass transition measured from cooling cycles from both DSC (using onset value) and temperature sweep test (using peaks of tan(δ)) and stickiness evaluation of the DoEs filaments.

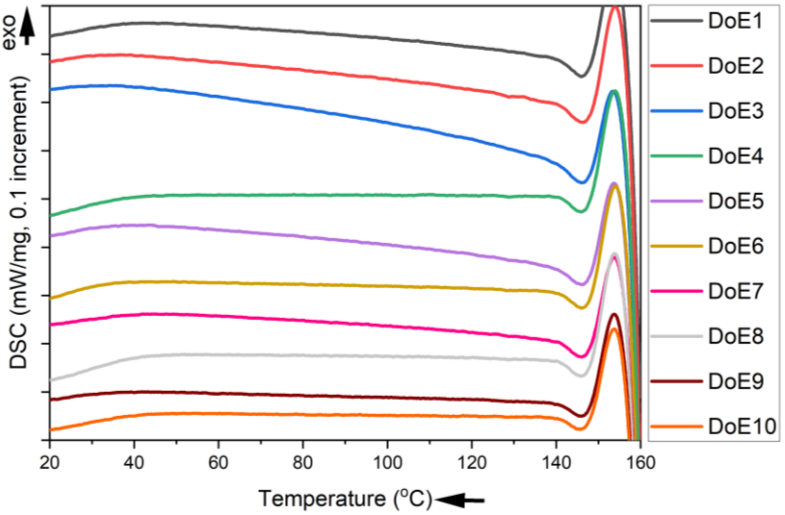

Figure 4-18. Cooling cycle of the DoE filaments DSC traces.

4.3.3. Define quality attributes limits

From previous experiments E/η, strain at break (from TS), maximum stress (from 3PB) and Tg_{Rhe} were chosen for DoE responses. Therefore, selected experiments (section 4.2.2.4.3) were conducted using the 3D printer to match these responses with the printing process. The filaments were fed into the 3D printer and failure modes were

identified (table 4-10). Most of the filaments were 3DP-extrudable at the tested temperatures (150°C, 160°C and 170°C). The filaments that failed at one of the temperatures were DoE 3, 7, 9 and 10. Manual feeding showed more successes due to using the hand to gently push the filaments. Increasing the temperature increased the possibility to successfully 3DP-extrude. As the temperature increased the viscosity dropped the pressure required was less and solid filament mechanical properties was sufficient to work as a piston. Comparing these results (table 4-10) with table 4-8, filaments of E/η below 0.8 $\times 10^{-3}$ MPa/%Pas were not 3DP-extrudable. Therefore, this threshold was chosen as minimum limit in the DoE. From the equation 1-3 (section 1.5.2) the E/η threshold is printer specific [70] and the value was for the current printer set up (section 3.2.2.5.2).

Table 4-10. 3DP-extrudability test of DoE filaments at three temperatures 150°C, 160°C and 170°C using two feeding method manual and mechanical:

	150°C		160°C		170°C	
	MF	**AF**	**MF**	**AF**	**MF**	**AF**
DoE1	✓	✓	✓	✓	✓	✓
DoE2	✓	✓	✓	✓	✓	✓
DoE3	✓	✗	✓	✗	✓	✓
DoE4	✓	✓	✓	✓	✓	✓
DoE5	✓	✓	✓	✓	✓	✓
DoE6	✓	✓	✓	✓	✓	✓
DoE7	□	✗	✓	□	✓	✓
DoE8	✓	✓	✓	✓	✓	✓
DoE9	✗	✗	✗	✗	□	✗
DoE10	✗	✗	✗	✗	✓	✗

✗ = fail, ✓ = succeeded, □ = inconsistency

MF is manual feeding, AF is automatic (gcode) feeding

DoE 7, 9 and 10 were very brittle to coil on the spool, while DoE 3 showed difficulties and broke during pulling (table 4-7). From strain at break experiments these filaments had strain at break below 28%. The rest of the filaments were flexible enough to be

collected using the winder and the strain at break of these filaments were 39% and above. Thus, 35% was chosen as minimum limit in the DoE and 42% was chosen as a target (minimum limit + maximum standard deviation). Yi Zhang et al [210] studied the breaking behaviour of spaghetti rod and found that the breaking point occurred at the maximum curvature. The maximum curvature limit was correlated to the rod diameter to the length ratio.

All formulae with Tg_{Rhe} of 71.3°C and below showed stickiness. While formulae of 72.9°C were stable over two months period. Thus, 73°C was chosen as limit in the DoE model, with 78°C chosen as a target (minimum limit + 5°C as buffer). Which was higher than the recommended Tg for stable solid solution assuming 20°C as storage temperature [209].

In addition to the 3DP-extrudability study, experiments were performed to assess the 3D printing properties of the DoE filaments covering a longer run time including the stop-start processes which occur during a typical printing process. Table 4-11 shows the result of the printing tests and at 150°C nozzle temperature that all printing tests failed, except DoE 8 which only successfully printed the first tablet layer. At 160°C and 170°C, DoE 8 and central points (DoE 1 and 5) were printable might be a result of the viscosity drop. DoE 4 was printable at 170°C and showed low consistency at 160°C. Three failure scenarios were observed, in the first scenario, filament buckled and escaped from the gap between the gears and the guidance tube (chapter 3 Figure 3-1) (DoE 1, 2 and 5). In the second scenario, filaments broke due to gear pressure (DoE 3, 4 and 6) and in the third filaments broke after the gear (DoE 7, 9 and 10).

The first and second scenarios were assigned to poor maximum stress value that caused fracture or serious plastic deformation. Although this work aimed to separate each cause of failure and assign it to one property, few samples showed complex behaviour. For example, DoE 4 tolerated more gear pressure by increasing process temperature as back pressure reduced (viscosity reduced) [211]. While DoE 3 failed regardless of the good mechanical properties due to poor E/η ratio. This complexity was assigned to the interaction between the factors. For example, the total stress on the filament was a result of the stress from the gears and stress due to the back pressure in the hot end. Schematic of the total force on the filament is presented in Figure 4-19. Limits for maximum stress selected to be 22.5 MPa and 24.2 MPa as a target (minimum limit + maximum standard deviation).

The difference between scenario two and three is the filament break point in relation to the gears, either before or after respectively. Breakage before the gear allows the filament to be pulled from the print head, while after can be assigned to the poor E/η ratio as the gears still grip the filament and it cannot be pulled from the print head. If in scenario two the filament remains in the correct alignment it can be re-engaged by the gears and the broken sections can be pushed together. Gottschalk et al [68] modified the printer by adding a rigid guide tube, this allowed good force transfer from the feeding filament to the filament loaded in the hot end and reduces scenario 2.

Table 4-3 summarises the responses limits including MFA content that was assigned an arbitrary limit of 8% (wt, of total). This ratio is low for a feasible therapeutic formula since a 250 mg to 500 mg MFA dose is in the marketed product [21] (equivalent to 3125 to 6250 mg tablet weight for 8%wt of MFA in minimum limit formula). However, the aim in this study is to use MFA as a model drug and understand the technology limitations.

Table 4-11. 3D printing test of DoE filaments at three temperatures 150°C, 160°C and 170°C:

	Break/Buckle	$E/\eta_{160°C}$*	Maximum stress	150°C	160°C	170°C
DoE1	Buckling	2.71	22.5	✗	✓	✓
DoE2	Buckling	2.46	6.3	✗	✗	✗ ☐
DoE3	Break	0.53	25.7	✗	✗	✗
DoE4	Break	3.08	14.6	✗	✓ ☐	✓
DoE5	Buckling	2.25	21.6	✗	✓	✓
DoE6	Break	4.28	6.2	✗	✗	✗
DoE7	Break after the gear	0.49	45.8	✗	✗	✗
DoE8	Break occasionally	12	29.6	✗ ☐	✓	✓
DoE9	Break after the gear	0.17	22.1	✗	✗	✗
DoE10	Break after the gear	0.64	48.9	✗	✗	✗

✗ = fail, ✓ = success, ☐ = inconsistent (symbol combination indicates likelihood).

* E/η in 10^{-3} × MPa/%Pas

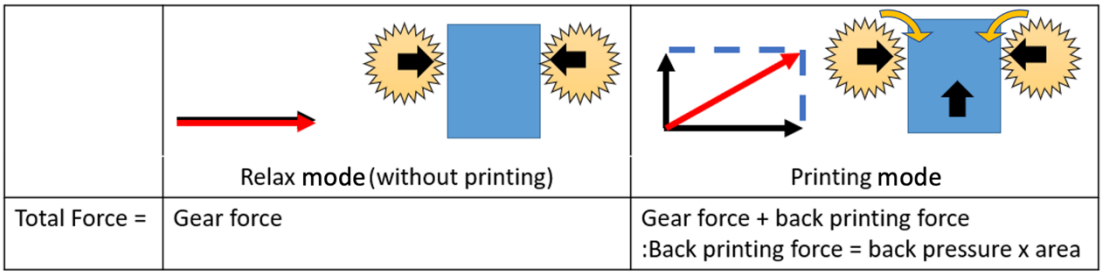

Figure 4-19. Effect of the viscosity on the Gears pressure limit.

4.3.4. DoE results

4.3.4.1. Comparing mechanical properties using MODDE

To identify the formula ingredients property contributions coefficients between mechanical properties and ingredients were calculated and presented in Figure 4-20 for the stiffness, yield stress and maximum stress from both 3PB and TS tests. StA reduced both stiffness and stress values, while silica increased them. MFA caused increase in elastic modulus in 3PB and TS tests and all stress values in 3PB. Although the error bar was bigger than the coefficient values. However, deleting this coefficient reduces the model quality. This result is in agreement with previous findings in chapter 2 and 3 about MFA impact on stiffness.

An interaction between StA and silica affected the stiffness negatively, which might be due to changes in the matrix properties and its adherence to the silica particles [212]. For maximum stress and yield stress using the TS test, the only important factors were StA and silica. TS was less sensitive to stress values (low CV_{ss}) than 3PB which might lead to undetectable MFA affects.

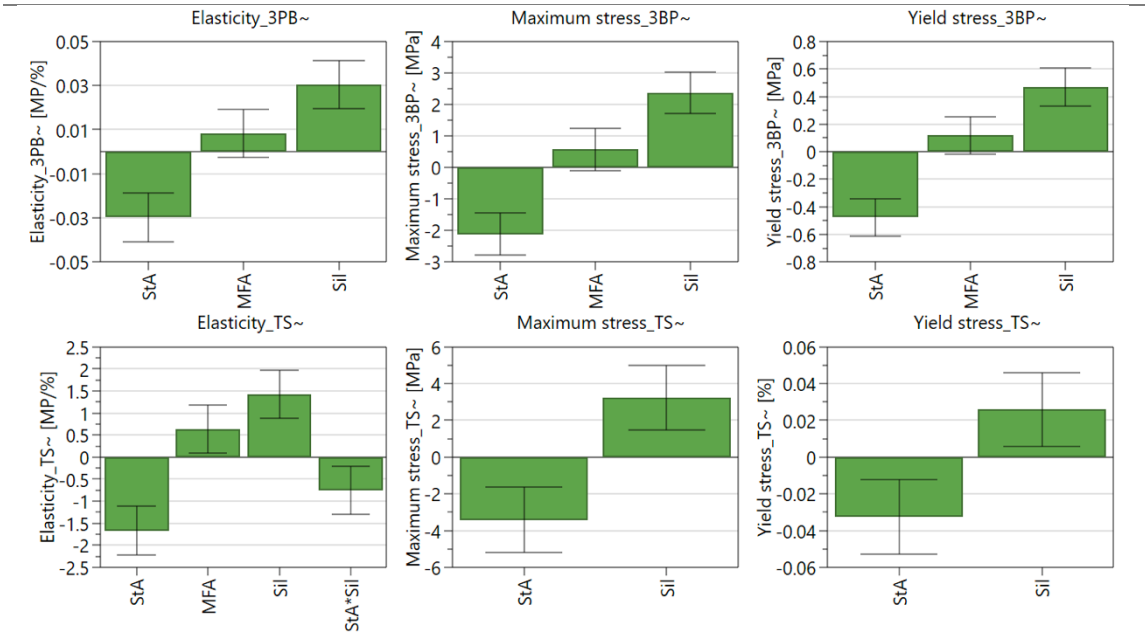

Figure 4-20. Coefficients plots (coefficients scaled and centred) of elastic modulus (left), maximum stress (middle) and yield stress (right) from both 3PB test (top) and TS test (bottom). Non-significant coefficients were removed and confidence level was 0.95, for numerical values see table Appendix 3-1.

For the components impact on the strain values only TS test was considered as 3PB test was limited, see section 4.3.2.1. Strain at maximum stress and strain at break showed almost similar patterns (Figure 4-6 and Figure appendix 3-15). In contrast to the stress values, StA increased strain values while silica reduced them (Figure 4-21) and MFA also reduced the values. This result is in agreement with the previous finding in chapter 2 and 3 that formula brittleness increases with increasing MFA ratio. Other square and interactions factors were included to improve the model fitting for both strain at max and strain at break, respectively.

Using machine learning, Elbadawi et al [87] ranked that feature importance (how useful the feature to predict a variable) for mechanical properties from the most important to the least. The highest ranking were polymer choice, plasticizer and drug, respectively, while filler was relatively minor. Although the prediction of the mechanical property prediction was accurate, the model depended on literature data using a polymer blend approach, with no filler used and this might have influenced the filler ranking.

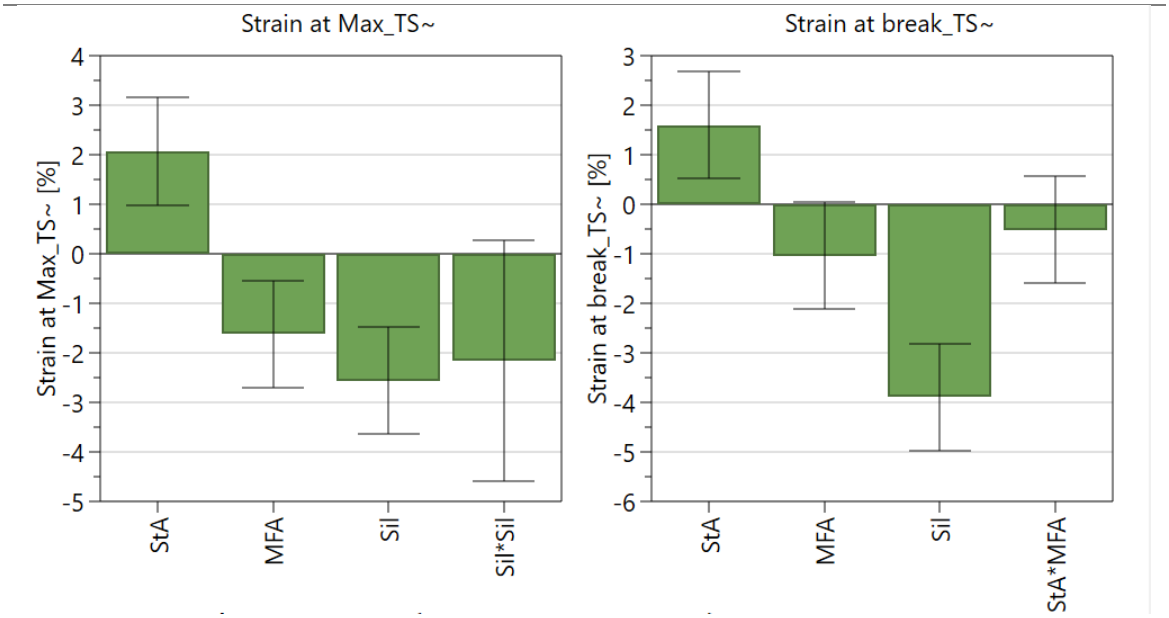

Figure 4-21. Coefficients plots (coefficients scaled and centred) of strain at maximum stress (left), strain at break from TS test. Non-significant coefficients were removed , For numerical values see table Appendix 3-1.

Tan(δ) at printing temperature values were fitted using an MLR model (Figure 4-22) and although the R2, Q2 and reproducibility showed good values (>0.9), the model validity was missing. The difference of tan(δ) of central points (pure error) was lower than the model error i.e. a source of variation was not explained by the model [213]. For this reason, tan(δ) was not used in the DoE model. However, due to the importance of this value for explaining the likelihood of the material behaviour (solid-like or liquid-like) it has been presented in this section. The coefficients values were in agreement with the previous discussion (tan(δ) increased by increasing MFA and reducing silica). For the contour plots, all formulae from 10% to 20% (wt of total) silica were 1.5 (tan(δ)) and above. Thus, formulae were expected to behave more like a liquid and flow. Tan(δ) of 1 could therefore be used as a limit for formulae suitability assessment. When tan(δ) was above 1, the viscosity value provides a better assessment of material behaviour and when tan(δ) below 1, G' and G" were preferable [120].

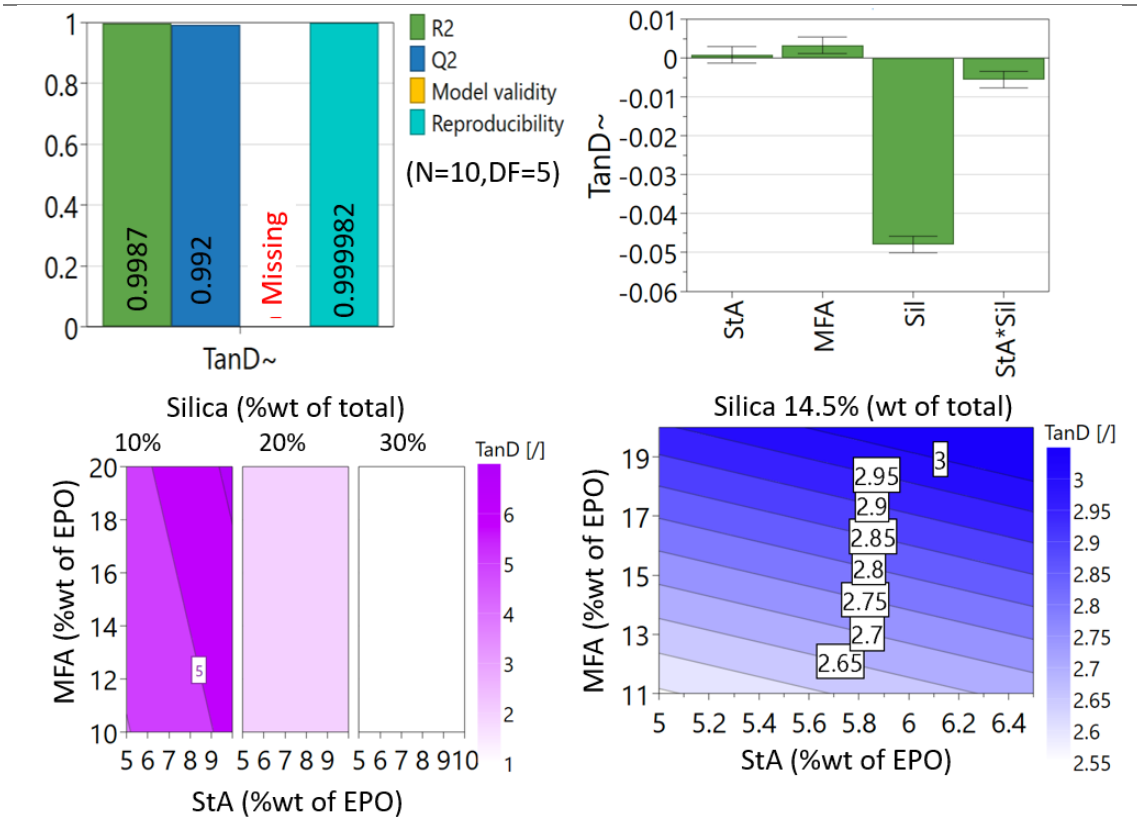

Figure 4-22. Tan(δ) summary fit, coefficients and contour plot, N is the number of the samples (10), DF = degree of freedom.

4.3.4.2. DoE model for 3D printability

The DoE fitting summary is presented in Figure 4-23, the root mean square errors of calibration (R2) are above 0.95 and of prediction (Q2) above 0.79 with the difference between R2-Q2 below 0.177. For a good model R2 and Q2 should be above 0.5 with difference below 0.2 [213]. Model validity values are above 0.46 and with a value above 0.25 indicating acceptable performance. MFA content was an exception as the MFA content was a calculated value not experimental. Thus, there was no difference between central points and no error can be calculated therefore model validity was missing. Finally, the reproducibility also was good (>0.5) which represented the variation in the central point in comparison with all data points in the formulation space.

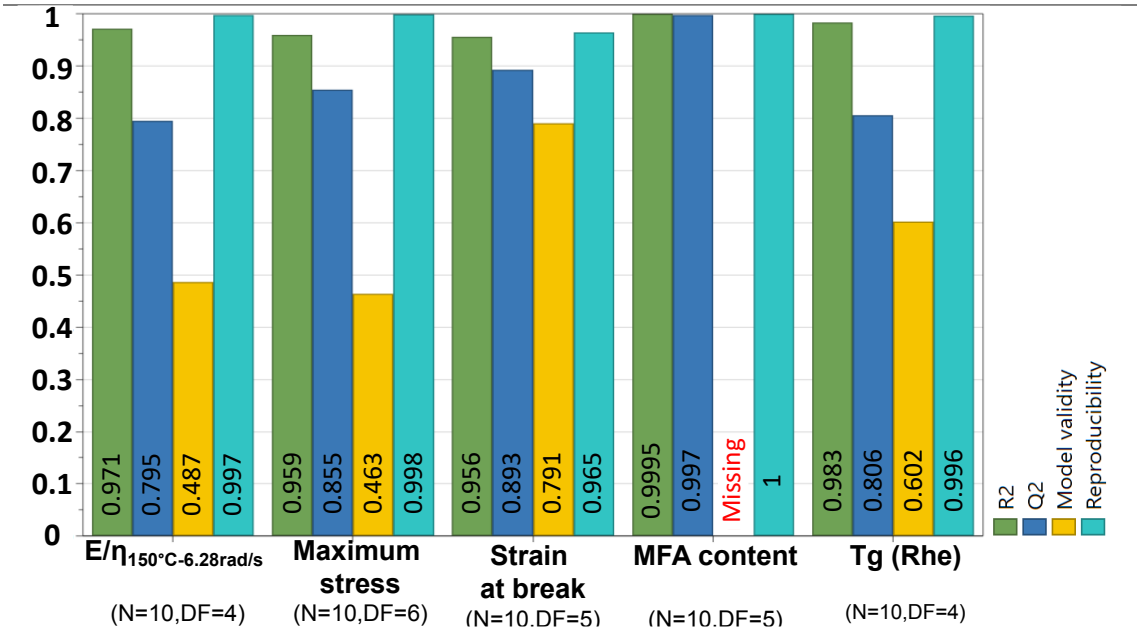

Figure 4-23. Summary of fit plot for the five responses (from left to right; $E/\eta_{150°C}$, maximum stress, strain at break, MFA ratio and stickiness), N is the number of the samples (10), DF = degree of freedom.

Correlations between factors and responses are presented in Figure 4-24. For $E/\eta_{150°C}$, both silica and StA had negative influence and MFA was positive. StA reduced η (denominator) but reduced E (numerator) more, while silica increased E but increased the denominator (η) more. Only MFA increased E and reduced η showing a favourable effect as the filament would be more efficient in pushing the molten material out. Other correlations MFA-silica interaction and silica square terms were applied to improve the fitting. Both affected negatively the $E/\eta_{150°C}$ value but the standard deviation for both terms were high to form a strong conclusion.

Both maximum stress from 3PB and strain at break from TS were previously discussed in section 4.3.4.1. The total MFA content decreased with increasing other formulae components. StA reduced Tg_{Rhe} while silica increased it. Other terms MFA, StA-MFA and StA-silica interactions had standard deviation bigger than the correlation values.

Plasticizer, lubricant, drug and polymer were the highest ranked features of importance in the machine learning model for printing temperature and printability [87]. However, once again filler was not ranked high for same reason presented for predicting mechanical properties (section 4.3.4.1).

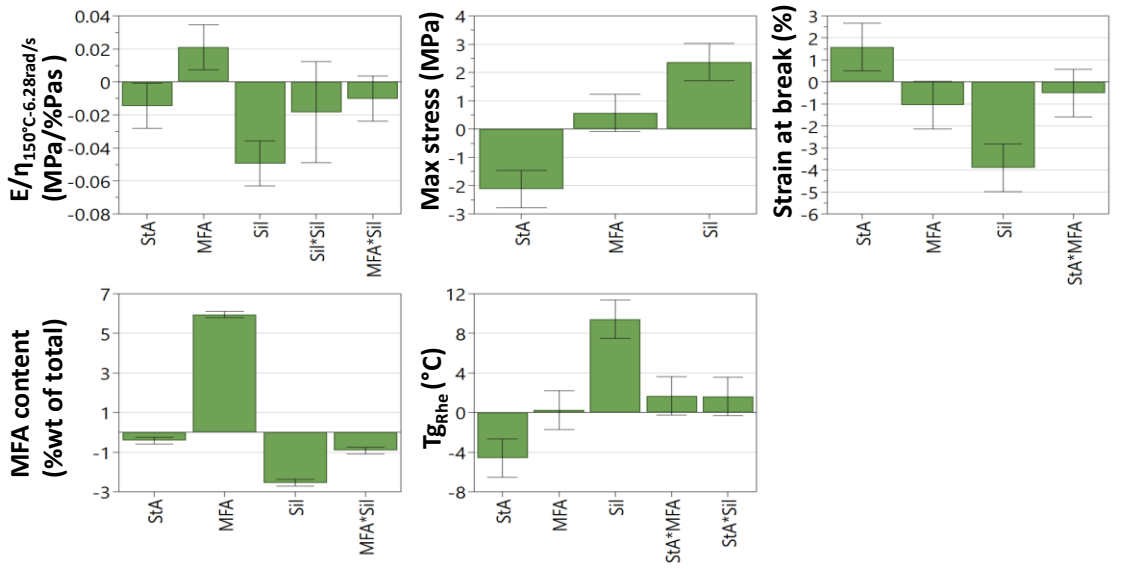

Figure 4-24. Coefficients plots (coefficients scaled and centred) of DoE responses, non-significant coefficients were removed. For numerical values see table Appendix 3-1.

4.3.4.3. Prediction of DoE responses

Figure 4-25 shows the contour level of maximum stress (from 3PB test), strain at break (from TS test), $E/\eta_{150°C}$ and Tg_{Rhe}. MFA actual ratio (%wt of the total formula) was included to identify the total MFA content in the formulation space. High values of the responses were preferable to provide high tolerance to gear pressure, flexible filament to collect and feed in the printer, reliable 3DP-extrudability, low stickiness and stable formula, and high drug load. In the contour plots, the strong saturated colour indicates higher values. Each of the responses were increasing in different directions in the formulation space. For maximum stress, moving toward high-silica, high-MFA low-StA region was preferable. While for strain at break, low-silica low-MFA high-StA region was preferable. 3DP-extrudability ($E/\eta_{150°C}$) showed better values in low-silica high-MFA low-StA region. Tg_{Rhe} evaluation was better for high-silica low-StA region. MFA actual concentration (calculated) was highest in low-silica high-MFA low-StA region.

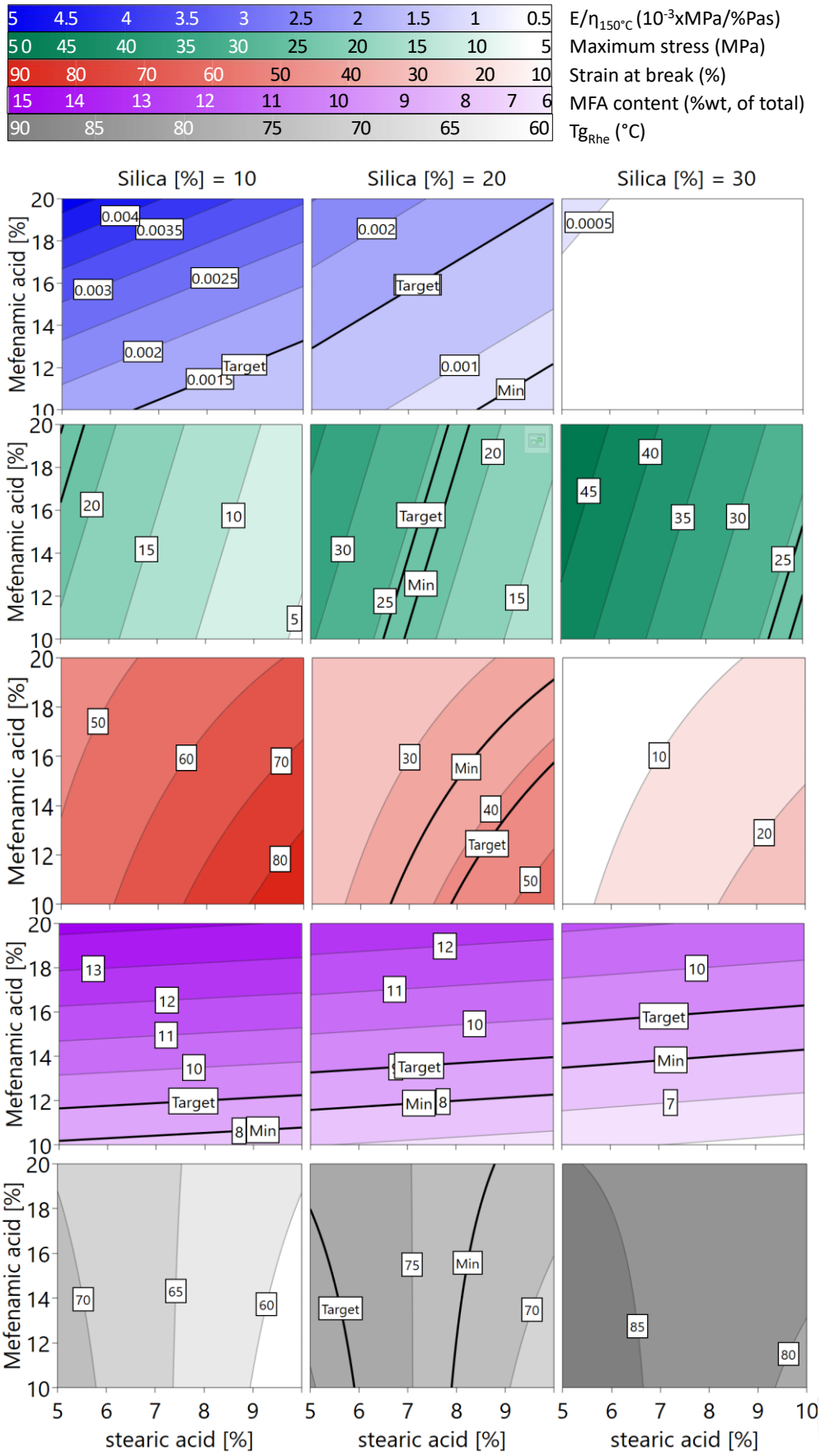

Figure 4-25. Contour plots of the DoE responses, maximum stress from 3PB test (green), strain at break from TS test (red), E/η at 150°C (blue) and $\boldsymbol{Tg_{Rhe}}$ *(gray).*

Figures 4-26 and 4-27-left illustrate the 'sweet spot' within the formulation space. In the DoE, each response was improved in different directions within the space. Therefore, the sweet spot was identified, where any point within this area has all responses higher than the minimum required. At high and low silica content most of the criteria were not met. In Figure 4-26-left plot (silica 10% wt), Tg_{Rhe} and maximum stress were below the minimum, MFA content and E/η criteria were met in part of this space and only strain at break was acceptable. In Figure 4-26-right plot, E/η and strain at break criteria were not met, while MFA content and maximum stress were partially met. While at medium silica content (20% wt of total) more zones overlapped and a small sweet spot was detected. The biggest sweet spot was found at 14.5% (wt of total) silica. Probability of failure was calculated and no robust formulation was found see Figure 4-27-right, with the lowest probability failure about 37%. Thus, a formulation from the 37% probability failure space was chosen for further work. The chosen (optimum) ratios were 5.1% (wt of EPO) for StA, 13.2 (wt of EPO) for MFA and 14.5% (wt of total) for silica.

Samaro et al studied printability of ethylene-vinyl acetate (EVA) copolymers with different VA ratios. Low VA ratio (9%wt) failed due to high initial viscosity while high VA ratio (40%wt) had poor mechanical properties. A balance between these properties was required for a printable filament [86].

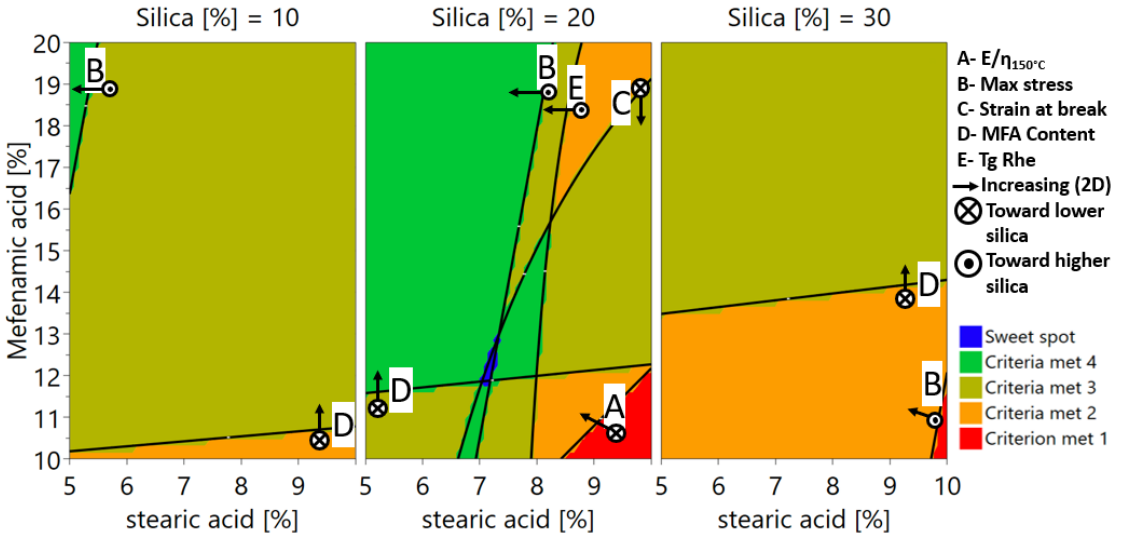

Figure 4-26. Sweet spots (responses above the defined limits/criteria) at low, high and medium silica content and different MFA and StA ratios.

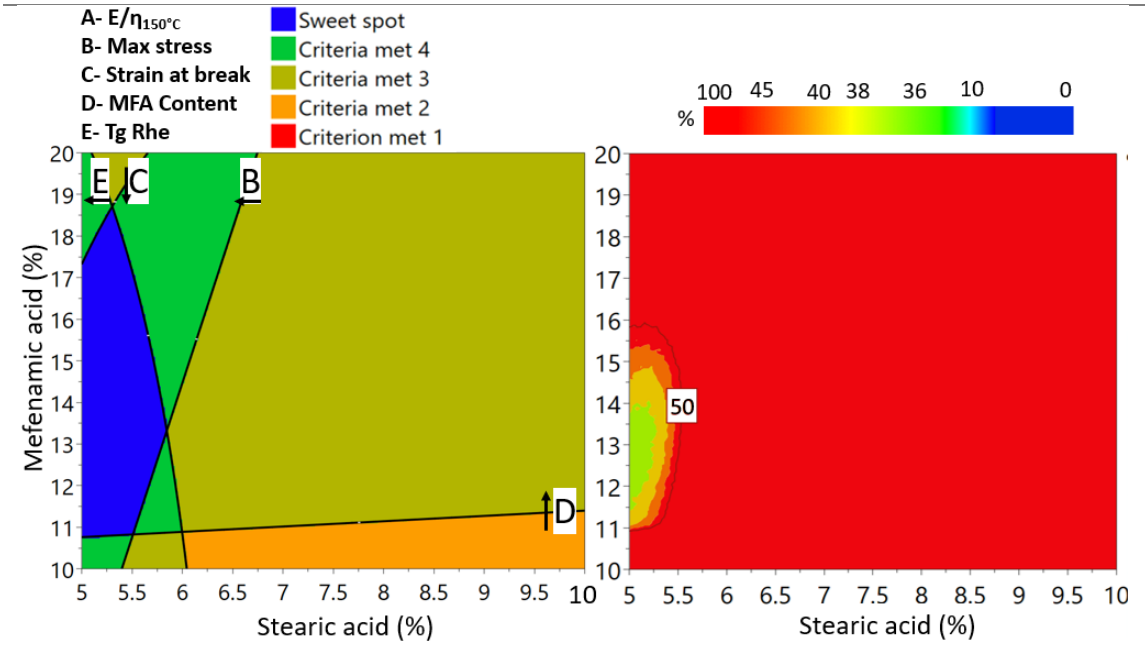

Figure 4-27. Sweet spot plot (left) and design space plot (right) at 14.5% (wt of total) silica showing the space where all criteria were satisfied and failure probability.

4.3.4.4. Best formula printability test

The chosen (optimum) formula was HME extruded then tested using the Ender 3 3D printer using G-code to 3DP-extrude 100 mm of the filament. Table 4-12 shows the results of the test conducted at different temperatures and printing speeds. At 160°C the printer extruded 100% of the filament up to 240 mm/min. At 150°C, the filament started to break at 180 and 240 mm/min printing speed. At 140°C, slippage occurred using 60 mm/min while higher printing speed failed due to breakage. Lower temperature (130°C) failed regardless of the printing speed.

Increasing temperature, nozzle size and/or reducing the printing speed was successful to print formulae that was not printable [186]. This was due to reducing shear rate and viscosity [207], [208].

Table 4-12. 3D printing extrudability 100 mm extrudability test at 130°C, 140°C, 150°C and 160°C printing temperature and four printing speed:

3DP-T (°C)	Speed (mm/min)	Speed (mm/s)	Continuous 3D-extrustion (mm of 100 mm)
160	60	1	100%
160	240	4	100%
150	60	1	100%
150	120	2	99%
150	180	3	95% (break sometimes)
150	240	4	88.5% (break more often)
140	60	1	96.5% (slippage 3.5%)
140	120	2	Fail - break always
130	60	1	88% (break often + slippage 12%)
130	120	2	Fail - break always

At 150°C, the printing failed due to repeated breakage (second scenario). During printing the printer stops and starts to change nozzle location, when changing a line or layer, which caused the filament to break and printing to fail. However, the filament was successfully printable at 155°C-240 mm/min and 160°C-420 mm/min (Figure 4-28).

In an experiment conducted on a different printer (Prusa i3MK3S), the optimum filament was printable at both 150°C and 160°C at printing speed up to 900 mm/min. Cracking noises could be heard during printing, which was filament breaking inside the cooling sink. However, due to well supported path the filament was aligned in the narrow tube and pushed out of the nozzle to print successfully. The Prusa printer has a longer cooling sink than the Ender 3, which forced the coiled filament to experience additional stress in the tube.

The two printers had different specifications and as a result limitations. The variation in machines specification and methods to evaluate printability was challenged in the machine learning model [87]. Alternatively generating the data in house would limit the data entry in the model [37]. This is highlighting the importance of linking the acceptable

limits with printer specification for universal findings and to accelerate the 3D printing formulation.

Table 4-13. 3D printing test of the optimum formula using two printer and different process temperature and printing speed, ten tablets were printed:

Printer	3DP-T (°C)	Speed (mm/min)	Time	Comment
Ender 3	160	420	13 min	Print successfully*
Ender 3	155	240	22 min	Print successfully
Ender 3	150	180	30 min	Failed at the last ~40%
Ender 3	150	120	45 min	Failed at the last ~60%
Prusa	160	900	5 min	Print successfully
Prusa	160	420	-	Print successfully
Prusa	150	900	5 min	Print successfully

* Printing all 10 the tablets without process failure such as filament breakage, buckling, slippage, blockage … etc

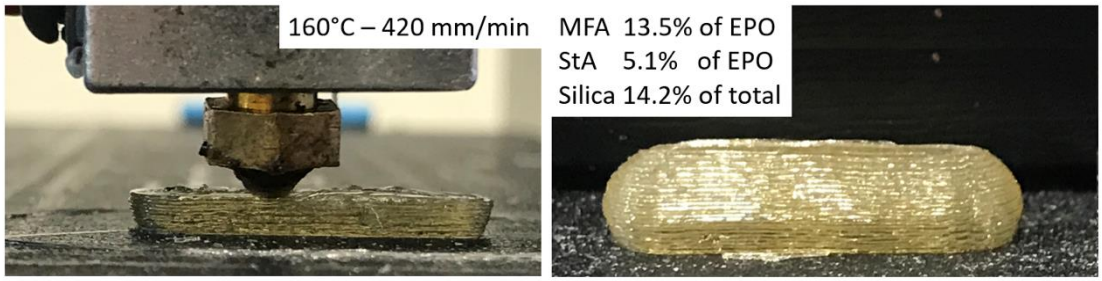

Figure 4-28. Optimum formula printed on Ender 3 3D printer at 160°C.

4.4. Conclusion

Incorporation of any of the fillers (silica, talc45, talc75 and silk) improved the mechanical properties of the ductile matrix by increasing the elastic modulus and maximum stress in a manner dependent on particle size, filler surface properties, and filler-matrix adhesion. For the MFA-STA-EPO matrix, silica increased mechanical properties the most. The three-point bend test provides valuable stress and elastic modulus data, while the tensile strength test is preferable to evaluate the strain at break since the filament displacement during the test is not limited. MFA (miscible drug) and

StA (plasticiser) reduce η, G' and G" and decrease dumping factor (tan(δ)), while silica (filler) increases η, G', and G" but reduces tan(δ). Silica increases the shear thinning effect; however, filaments with high silica content were less affected by temperature. Stickiness is correlated with Tg_{Rhe} and stable filament should have Tg_{Rhe} 50°C above storage temperature. E/η, strain at break, maximum stress, Tg_{Rhe} and drug content are defined as critical quality attributes for successful printable filament. Limits for these attributes are defined for the used printer (table 4-7). Then, printable filament was predicted successfully. However, the limits are specific to the printer, and different printers require different limits. To develop new formulae for certain printers, users should define the threshold of the critical quality attributes using filaments with different strain at break, maximum stress, and E/η properties. This will provide the formulator with insight into in which direction to move in the formulation space when using different polymers to find the sweet spot and/or what part of the printer can be modified to increase the area of the sweet spot. Additionally, the report of these values and printer specification should be encouraged, as the research community collects more values of thresholds and printer specification imperial or/and machine learning models can be developed to correlate these thresholds with the specification. These models will allow to transfer the knowledge between different printers and unify the efforts toward well-engineered machines and developing new formulations, moving closer to wider implementation for this technology and personalised medicine.

This page is left empty.

Chapter 5: AZD0837 3D printing filament using polymer blend approach:

5.1. Introduction

This chapter was part of an industrial placement organised with AstraZeneca and placed in the CMAC research centre at the University of Strathclyde. Polyethylene oxide (PEO) and hypromellose acetate succinate (HPMCAS) were examined with an AstraZeneca development compound, AZD0837 (AZ)[106], to produce an extended release solid dispersion caplet. The 3D printing formulation space was explored for binary mixtures, AZ with each of PEO, a flexible polymer, and HPMCAS, a brittle polymer. If neither of the formulae was printable, the best formulae were utilised for further development using the polymer blend approach (section 1.5.3.1).

To satisfy the study objectives, this chapter was designed to answer the following questions:

1- What is the effect of drug concentration and process temperature on the mechanical properties of drug-polymer filaments?
2- Is there a printable combination in the formulation space of drug-polymer filament if not, which one is the best for further development?
3- How does the mixing ratio of HPMCAS and PEO polymers (polymer blend approach) affect the mechanical properties of the filament and do the product properties get affected by HME process temperature?
4- Assuming a similar surface area to a volume ratio of the final caplet shape, is there a difference between 3D printed caplet and injection moulding?
5- After printable filament is there stability consideration to be taken into account?

5.2. Materials and Methods

5.2.1. Materials

AZD0837 (AZ), a basic drug, was used received from AstraZeneca (Gothenburg, Sweden). AQOAT® MMP (HPMCAS: hypromellose acetate succinate) was kindly donated by Shin-Etsu Chemical Co., Ltd. (Wiesbaden, Germany). Polyox™ WSR 1105 NF (PEO, MW 900,000 g/mL) was kindly supplied by ChemPoint.com Inc (Supplier: Chempoint, Maastricht, Netherland. Manufacturer: DOW Inc, USA).

To prepare phosphate buffer pH 6.8 (0.1 M), sodium phosphate monobasic dihydrate $NaH_2O_4P.{}_2H_2O$ and sodium phosphate dibasic Na_2HPO4 were purchased from Sigma-Aldrich, UK (Product number 71500 and S9763, respectively).

5.2.2. Methods

5.2.2.1. HME extrusion

HME details can be found in section 2.2.2.1.1. The following paragraphs indicate the changes to these parameters for the PEO- and HPMCAS-based formulae examined in this chapter. To achieve a total weight between 300 and 500 mg for 150 mg dose [106], three drug loads were considered 30%wt, 40%wt and 50%wt with each of the polymers, PEO and HPMCAS. Concave screws are used to feed all formulas except PEO-based formulas to avoid feeding instability, while a spiral screw is used at a rate of 0.1 kg per hour.

The labelling for binary mixtures (drug-polymer) in this chapter used the weight ratio, then the initial of the material, followed by (pw) for powder or physical mixtures or screw speed (S) and HME process temperature (T) for extrudates. For example, 30%wt of AZ with 70%wt of HPMCAS extruded at 100 rpm and 170°C process temperature was labelled as 30A70H/S100/T170, while the physical mixture of the same sample was labelled as 30A70H/pw. Optical microscopy (Leica DM6000, section 2.2.2.2.3) was used to evaluate the surface of PEO-based filaments.

For polymer mixture-based formulae, drug loading was always 30%wt and polymer blends were 70% wt. The 70% polymer blend was a mixture of PEO and HPMCAS at ratios of 0:100 (only HPMCAS), 25:75, 50:50, 75:25 and 100:0 (only PEO), respectively. The same labelling method used for the binary mixture was applied here. For example, an extrudate that contained 30% (wt of the total formula) of AZ and 70% (wt of the total formula) of a polymer blend of 25:75 (wt:wt of the polymer blend) PEO:HPMCAS processed at 100 rpm and 170°C was labelled as 30A(25P75H)/S100/T170.

Powder mixtures were prepared and extruded as described in section 2.2.2.1.1. Process temperature and die temperature were the same and ranged from 160°C to 120°C for HPMCAS-based formulae and from 180°C to 120°C for PEO-based formulae. The screw speed was 100 rpm for the HPMCAS-based formulae, but it was reduced from 100 to 15 rpm for PEO-based formulae to reduce the shark skinning effect. A filament

winder or cooling belt was used to obtain around 1.7 mm in diameter (Section 2.2.2.1 and 4.2.2.2). The shark skinning effect was evaluated under the microscope while filament diameter was measured using a digital calliper.

Ternary mixtures AZ-HPMCAS-PEO were prepared and extruded in the same manner at die temperatures ranged from 180°C to 110°C. While the screw speed was always 100 rpm except for low PEO ratios, i.e. 30A(25P75H), the screw speed was 15 rpm.

5.2.2.2. Solid state

5.2.2.2.1. Low frequency Raman Spectroscopy:

Low frequency Raman spectroscopy (section 2.2.2.2.1) was used for inline solid state investigation. Both polymers and drug Raman signals were collected offline at room temperature (25°C) and 120°C on a heating plate. During the HME experiments, the spectroscopic probe was attached to the HME die and signal acquisition started.

5.2.2.2.2. XRPD-D2:

XRPD was collected on a Bruker D2 phaser second generation benchtop diffractometer (GX000815) with the following experimental setup. 10 to 50 mg of powder or extrudates were placed in a sample holder that rotated to increase sampling and decrease preferred orientation. The source radiation was Cu of wavelength 1.5406 Å with Ni filter.

5.2.2.2.4 DSC:

Extrudates and physical mixtures were tested on the DSC (section 2.2.2.3.1). For extrudates, one cycle was used (heating-cooling), while for physical mixtures two cycles were used.

PEO crystallinity was calculated using the following equation:

$$PEO\ crystallinity = \frac{\Delta H\ of\ the\ formula \times PEO\ ratio}{\Delta H\ of\ 100\%\ crystalline\ PEO} \quad \text{(Eq5.1)}$$

Where ΔH is the enthalpy of the melting in J/g, for 100% crystalline PEO 205 J/g [214].

5.2.2.3. Physical properties

5.2.2.3.1. Mechanical properties:

PEO-based extrudates HPMCAS-based extrudes and polymer mixture-based extrudates were tested on the texture analyser three-point bend test using the same method from previous chapters (section 2.2.2.5.1, 3.2.2.5.1 and 4.2.2.4.1-3PB).

5.2.2.3.2. Rheological properties:

The amplitude sweep test and temperature sweep test were used for measuring the viscosity in the linear viscoelastic region details of the methods can be found in section 4.2.2.4.2.

5.2.2.3. Caplets production

5.2.2.3.1. 3D printing temperature

Thermogravimetric analysis was used to check the stability of the pure components. Instrument details are found in section 3.2.2.2. The temperature profile (Figure 5-1) consisted of two stages, the first stage represented the water and trapped solvent content and the second stage evaluated the degradation. The first stage was heating up to 105°C (above the water melting point) and then holding for two minutes. The second stage was heating up to the potential process temperature and holding for 20 min.

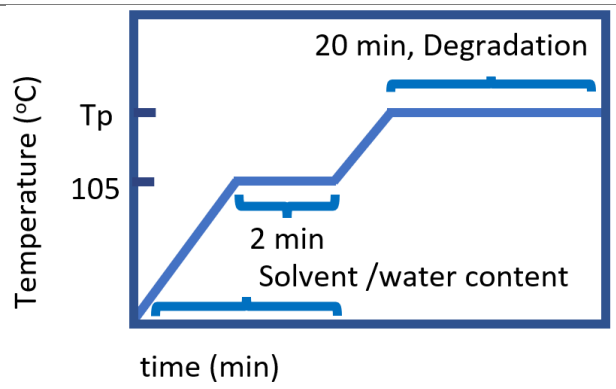

Figure 5-1. Thermogravimetry temperature profile.

5.2.2.3.2. 3D printing

Ender 3 creality 3D printer (sections 2.2.2.5.2, 3.2.2.5.2 and 4.2.2.4.3) was used to test the formulae.

Three tests were used. The 3DP-extrudability test involved extruding 10 mm of the filaments at different temperatures between 110°C and 180°C and evaluating the flow of the molten material from the nozzle. Prolong 3DP-extrudability test to evaluate by

extruding 100 mm at the chosen temperature at speed that between 0.8 to 3 mm/s. 3D printing of caplet designs (Figure 5-2) is described below (Section 5.2.2.3.3). Printing temperature and printing speed were chosen for each formula based on the previous 3D printing tests.

5.2.2.3.3. Injection moulding

Caplets were produced using the HAAKE MiniJet Pro Piston Injection Moulding (IM) System (Thermo Fisher Scientific, USA), which is an upright air-pressurised injection moulder. A single cavity caplet shaped metal mould was used to define the shape and volume of the produced caplets. Machine parameters were set to 150°C for heating chamber temperature, 25°C for mould temperature, 100 bar for injection pressure, 10 sec for injection time, 30 bar for post-injection and 5 sec for post-injection time.

5.2.2.3.4. Caplets design

For 3D printing, different designs were used (Figure 5-2). The size and weight variation of caplets printed with 0.4 mm and 0.8 mm nozzles were investigated using a flat top and bottom caplet design (F-design). IM-design was initially used to compare 3D printed caplets with IM caplets. The IM equivalent design (IME-design) was an alternative shape that has the same volume and surface area as the IM-design but with a flat bottom surface to avoid a steep overhang structure. The cylinder-like design was used as a simple geometrical shape.

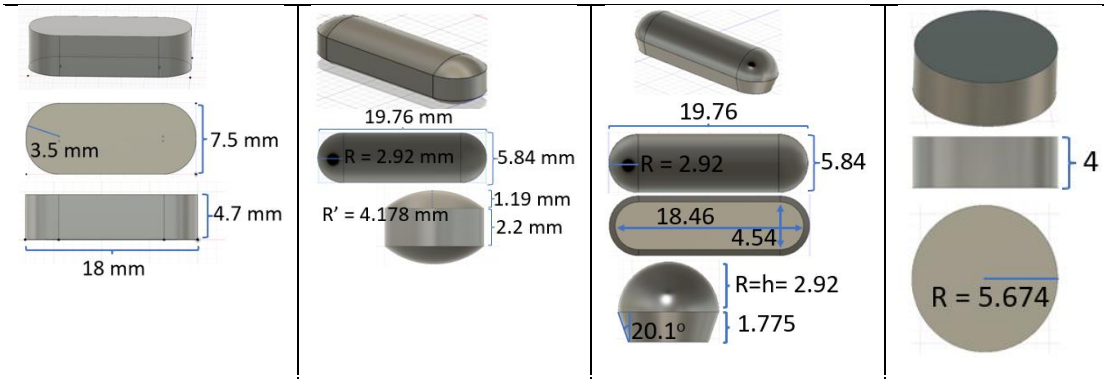

F-design	IM-design	IME-design	C-design
Flat top and bottom caplet	IM caplet	IM-equivalent	Cylinder

Figure 5-2. tablet and caplets design with their dimensions printed using 3D printing.

5.2.2.4. Caplets characterisation

5.2.2.5.1. Dissolution

Dissolution testing was performed using an ADT8i Dissolution bath (USP II) paddle on a closed loop setting with a T70+ UV/Visible spectrophotometer (Automated Lab Systems, UK). For each design, 3 to 5 caplets were tested for drug release in 900 mL of phosphate buffer at pH 6.8 (0.1 M) using a USP dissolution apparatus 2 (paddle) at 50 rpm and 37°C. The amount of AZ released is determined using a spectrophotometer at 258 nm. An automatic sampling was used to measure the concentration every 5 min (first two hours) to 15 min (until 24 hours). The automatic system sampled 20 mL at a 20 mL/min flow rate through a 20 µm cannula filter (ALS, UHMW PE, Part No. 50831).

5.2.2.5.2. Optical Coherence Tomography (OCT):

An optical coherence tomography (OCT, GAN620C1-SP4, 900 nm, HR, 248 kHz, Thorlabs, GmbH, Dachau, Germany) equipped with an OCT-LK3-BB electronic scanning lens to investigate the caplet porosity and printed line alignment. ThorImage OCT software was used for image acquisition, analysis and visualisation.

5.2.2.5.3. Roman microscope

A Raman microscope was used to examine the dried caplets and after they had been soaked in a dissolution medium for two hours. For acquisition parameters, see section (section 2.2.2.2.3).

5.2.2.6. Filament stability

5.2.2.6.1. Mass loss analysis

Sartorius Moisture Analyser (Sartorius MA160, Goettingen, Germany), which is loss on drying (LOD) equipment was used to analyse the trapped moisture and solvent in the extrudates. 2 g of a two-month old and fresh 30A(25P75H)/S100/T115 filaments were pelletised and placed on an aluminium tray in the moisture analyser. A few grams of each filament (fresh and old) were frozen and milled using cryomill for 20 minutes at 5 Hz for two cycles (Retsch GmbH, Germany). Then 2 grams of the milled powders were placed in the moisture analyser. The temperature profile was heating up to 110°C (gentle drying) until the mass became stable (deviation less than 0.05%).

5.2.2.6.2. Mechanical properties

Fresh and old filaments were heated up to 40°C for 20 min, and then all heated and unheated samples were tested on the texture analyser. Mechanical tests, namely 3-point bend tests, were run for the old and new filaments similar to section 5.2.2.3.1.

5.2.2.6.3. Physical state

Fresh and old filaments and heated ones were analysed using DSC (section 2.2.2.3.1) and XRPD (section 5.2.2.2.2).

5.3. Results and Discussion

5.3.1. Binary mixtures

Figure 5-3 shows the workflow to explore the 3D printing formulation space of each of the AZ-PEO and AZ-HMPMCAS based formulae at ratios from 30% (wt) to 50% (wt) drug load (maximum tablet weight 500 mg). Formulae extrudability was studied experimentally on the 11 mm HME. The solid state was then studied using DSC, XRPD and spectroscopic techniques. To evaluate the printability, mechanical and rheological properties were evaluated. Then, these results were linked with the results from the 3D printing test.

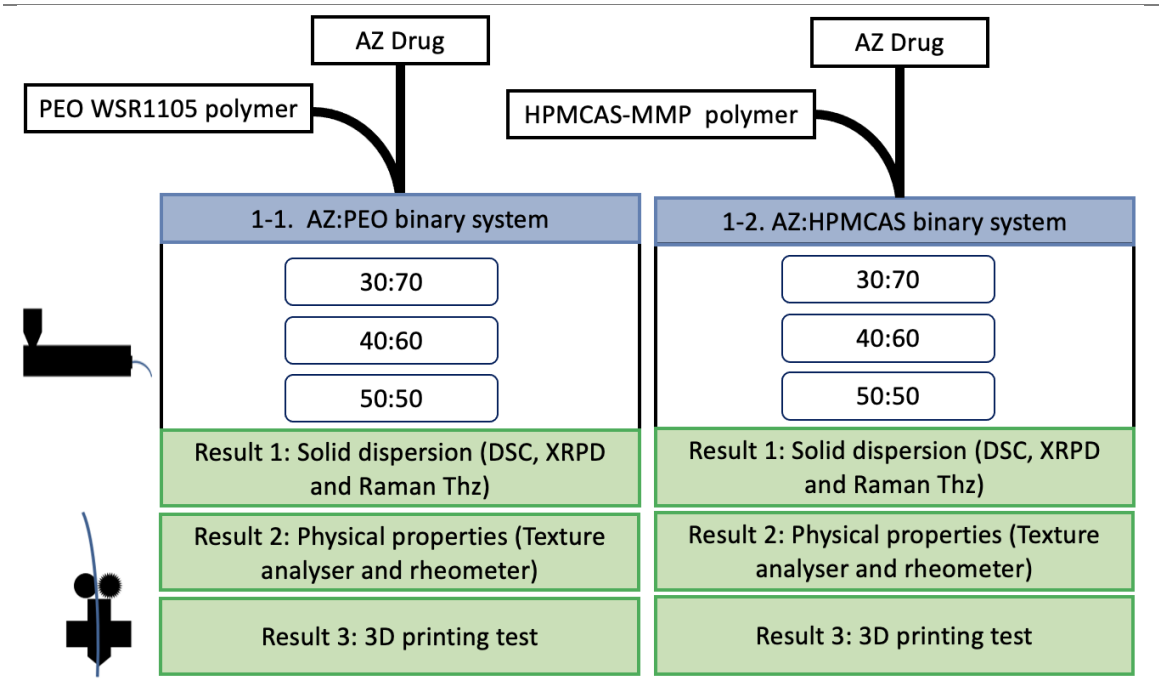

Figure 5-3. First stage workflow for exploring the 3D printing formulation space of AZ-PEO and AZ-HPMCAS formulae.

5.3.1.1. Filament production:

Feeding the physical mixture in the HME was challenging especially using a high ratio of the drug (Table 5-1). The balance of the feeder frequently gave error messages as the feeding rate was not stable. At 30% (wt) drug load the formulae fed continuously to the HME without issue. Increasing the drug load to 40% (wt) an excessive amount of the formula stayed in the feeder hopper. This might be due to the poor flowability of the drug powder. At 50% (wt) drug load the issue was clearer and caused a lack of feeding consistency and could not deliver 0.1kg/hr. Reducing the feeding rate to 0.5 kg/hr or using a spiral screw shape for a 0.1 kg/hr feed rate solved the issue. Both polymers were engineered to have good flowability. Even though reducing the feeding rate and using a spiral screw shape helped improve flowability, feeding remained difficult. The drug powder, which was in its early stages of development, contained numerous clumps. To address this issue and ensure a uniform blend, the drug powder was passed through a sieve (< 1 mm) prior to mixing.

AstraZeneca studied the flowability of AZ, AZ:HPMCAS-LG 50:50 (wt%) AZ:PEON750:HPMCAS-LG 35:15:50 (wt%) and 20:30:50 (wt%). Mixtures with drug ratios of 35-50% (wt%) exhibited an angle of repose of 47 to 49.2 degrees, indicating poor flowability, thus, agitation was used to improve the flow. At a drug load of 20% (wt%), fair flowability (angle of repose of 36.5 degree) was achieved without agitation (unpublished paper, internal AZ report).

Table 5-1. Feeding the physical mixtures in the HME:

Formulae	Feeder error (concave screw)	Solution/Feeder screw type
30A70P	-	Concave screw used
40A60P	The feeder hopper should be full	>0.1Kg/hr: spiral screw shape needed 0.05Kg/hr: concave screw used
50A50P	Frequent feeding stability error	>0.1Kg/hr: spiral screw shape needed 0.05Kg/hr: concave screw used
30A70H	-	Concave screw used
40A60H	-	Concave screw used
50A50H	Feeding stability error at low	Concave screw used

load

HPMCAS-based formulae were extrudable at 100 rpm screw speed, 0.1 kg/hr feeding rate and range of temperatures (Table 5-2). As the drug load and/or process temperature increased, the die pressure decreased. A higher temperature reduced the interaction between the molecules and as a result lowered the die pressure. Although the drug load reduced the die pressure, it could not be attributed to a reduction in molecular interactions between polymer molecules in this case. Because all process temperatures were above the drug's melting point, 111°C (as indicated by the manufacturer, AstraZeneca). Thus, the drug might have plasticized the HPMCAS or/and drug liquefication worked as a thinning agent for the viscous polymer.

PEO-based formulae were more challenging. Initially, the aim was to keep the screw speed constant at 100 rpm for all formulae. However, 30A70P and pure PEO were not extrudable at 100 rpm screw speed (pressure >100, table 5-2). To reduce the die pressure, a bigger nozzle size (lower shear rate) and a higher drug load (lower viscosity) were tested. 50A50P was successfully extruded at 145°C and 155°C with 1.74 mm and 3 mm nozzle sizes. However, a shark skinning effect was observed and the filament surface was not smooth or suitable for 3D printing (Table 5-3). The wavelength (L) and amplitude (A) of the shark skinning were measured. Both A and L were reduced with a higher drug load, higher process temperatures, a lower screw speed and a lower feed rate. When both values were small enough the surface became smooth (Table 5-3, 40A60P/S30/T180-0.05Kg/hr).

The shark skinning effect arose from a localised stress concentration at the extruder nozzle tip [215]. The polymer chain oscillated between engagement and disentanglement, causing a periodic slip-stick mechanism (oscillation in the flow). The phenomenon was presented in linear polymers like polyethylene and was associated with high die pressure.

Table 5-2. Die pressure in the HME of the AZ-HPMCAS and AZ-PEO formulae at different process conditions (table order top-bottom followed the running order):

Formulae	Nozzle (mm)	Feed rate (Kg/hr)	Extruder speed (rpm)	Extruder temperature (°C)	Pressure (bar)
30A70H	1.74	0.1	100	150	43
	1.74	0.1	100	140	58
	1.74	0.1	100	130	>100
40A60H	1.74	0.1	100	150	25
	1.74	0.1	100	140	37
	1.74	0.1	100	130	48
50A50H	1.74	0.1	100	140	25
	1.74	0.1	100	130	33
30A70P	1.74	0.1	100	150-180	>100
PEO	1.74	0.1	100	150-180	>100
	1.74	0.05	100	150-180	>100
50A50P	3	0.05	100	155	60
	2	0.05	100	155	70
	1.74	0.05	100	155	90
50A50P	1.74	0.05	100	155	70-90
	1.74	0.05	50	145	85
	1.74	0.05	30	145	80
40A60P	1.74	0.05	30	160	77
	1.74	0.05	30	170	55
	1.74	0.05	15	180	14
30A70P	1.74	0.05	15	170	92
	1.74	0.05	15	180	61
40A60P	1.74	0.05	15	180	43-55
	1.74	0.05	15	170	52
	1.74	0.05	15	160	95
50A50P	1.74	0.05	15	180	36
	1.74	0.05	15	170	43
	1.74	0.05	15	120	92

Table 5-3. Shark skinning effect evaluation by measuring the amplitude and length of the shark skinning waves using an optical microscope:

	Filament (1cm)	**Filament under the optical microscope** (1 mm)	Length (L) Amplitude (A) **µm (SD: N=3-5)**
50A50P/S100/T155 0.1Kg/hr			L=947 (± 99) A=181 (± 51)
50A50P/S50/T145 0.1Kg/hr			/
50A50P/S30/T145 0.1Kg/hr			/
40A60P/S30/T160 0.1Kg/hr			L=1069 (± 54) A=428 (± 17)
40A60P/S30/T170 0.1Kg/hr			L=606 (± 106) A=169 (± 19)
40A60P/S30/T180 0.05Kg/hr			L=445 (± 65) A=55 (±12)

Another extrusion challenge of the PEO-based formulae was to obtain the correct filament diameter. After the extrusion, the filament especially at a high drug load (50A50P) showed rubber-like behaviour (Figure 5-4). The fresh filament was elongated elastically under tension and shortened back after removing the tension. Thus, changing the distance between the filament winder and extruder to alter the tension on the filament (filament's weight, Figure 4-1) was not successful in controlling the filament diameter. This rubbery-like behaviour was lost after a few hours and was less obvious with 30A70P i.e. only a 50A50P filament diameter of 1.75 mm could not be achieved.

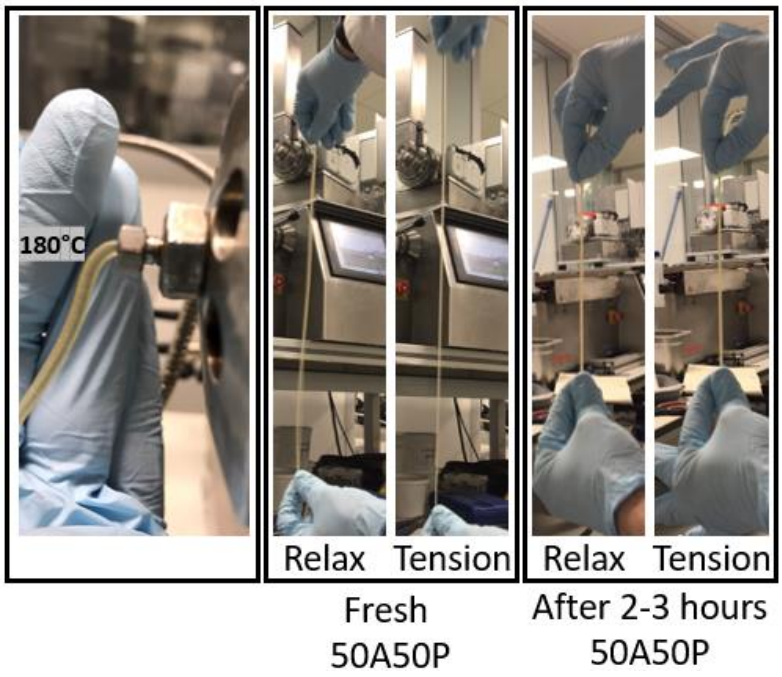

Figure 5-4. 50A50P/S100/T180 immediately after extrusion (left and middle) and after a few hours (right) showing rubber-like behaviour after extrusion that disappeared over time.

5.3.1.2. Solid state

5.3.1.2.1. DSC:

Pure components and physical mixtures of the AZ-PEO and AZ-HPMCAS formulae were tested using DSC. In the HPMCAS-based formulae (Figure 5-5), the first heating cycle did not reveal any interactions between the drug and the polymer since the drug's melting peaks did not change in the physical mixtures. This was attributed to the high glass transition of the polymer. The AZ drug melted at 120°C (onset 109°C) while the HPMCAS glass transition onset was at 119°C (end 128°C). Thus, the drug started to melt before the polymer was liquified. The fitting of the melting enthalpy values plotted in Figure 5-5-C shows an intercept with the x-axis (drug load % wt) at 1.58% i.e. practically HPMCAS did not dissolve the AZ drug. However, the first cooling and the second heating showed one Tg for the physical mixtures (50-74°C, cooling) which was between the Tg of the AZ (54°C, cooling) and Tg of the HPMCAS (126°C, cooling).

For PEO-based formulae (Figure 5-6), the melting of PEO (72°C) occurred before the melting of AZ. The melting enthalpy of the drug decreased with PEO presence. The linear fitting of the enthalpies showed an x-intercept at 24.9% (wt), which was the amount of the drug that did not contribute to the melting enthalpy. Based on the melting

enthalpy method [74], this value was considered the solubility of AZ in PEO. The first cooling and second heating showed only a melting peak of PEO but no Tgs.

In general, the drug was relatively stable in the amorphous state by itself without the assistance of polymer [106]. Thus, the absence of crystallisation during the first cooling or melting during the second heating could not be attributed to the polymer presence.

The extrudates showed trends similar to the second heating cycle of the physical mixtures with no melting peak for AZ (Figure 5-7). However, the Tgs of the HPMCAS-based formulae dropped to about 50°C (heating cycle), while PEO formulae showed a decrease in PEO crystallinity with the presence of AZ. Interestingly, the AZ decreased or delayed the PEO crystallisation during cooling (Figure 5-7-B). This means a longer time in the rubbery state. At 50A50P (the highest AZ ratio), the crystallisation did not occur during cooling (Figure 5-7-B), which might have caused the rubber-like behaviour of this formula after extrusion (Figure 5-4).

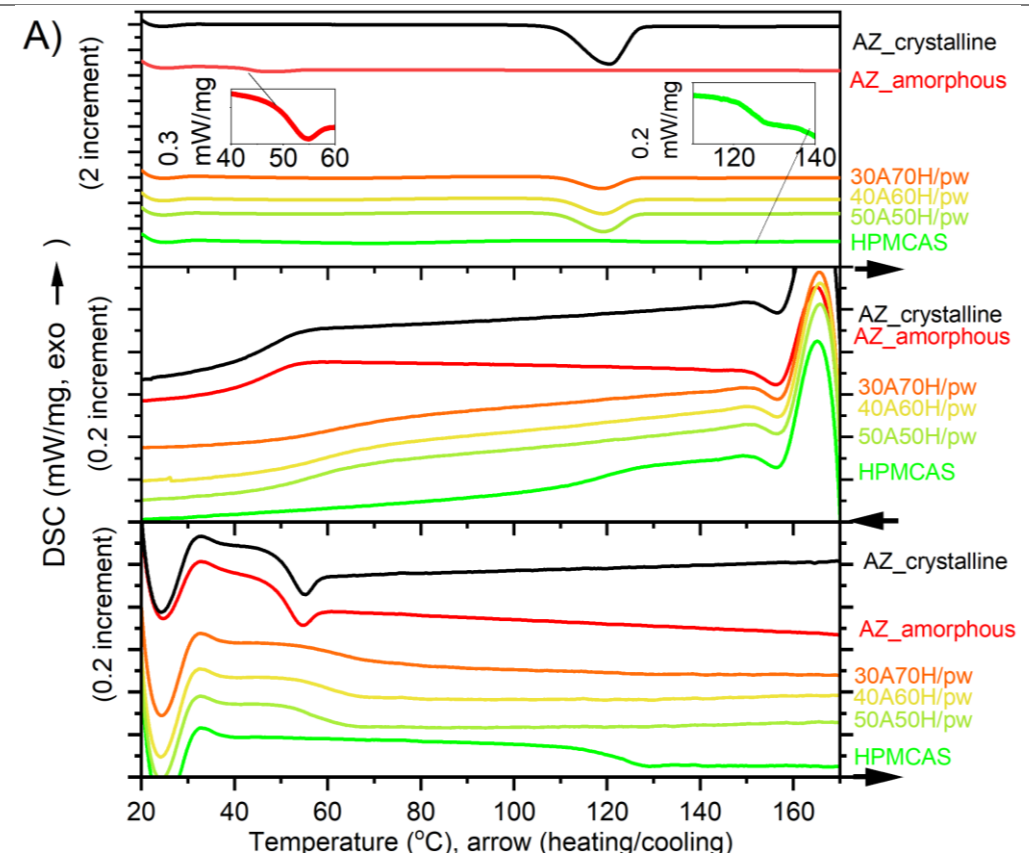

B)

	1st heating		1st cooling	2nd heating
	Tg * (°C)	Tm(°C)/enthalpy (Jm)	Tg (°C)	Tg (°C)
AZ-crystalline	-	120.5/470	55	48.9
AZ-amorphous	41.6	-	54	46.5
30A70H/pw	-	119.2/136.4	73.4	54
40A60H/pw	-	119.2/182.7	69.6	49.7
50A50H/pw	-	119/232	66.9	50.3
HPMCAS	119**	-	126.8	116.7
*onset, **126 inflection				

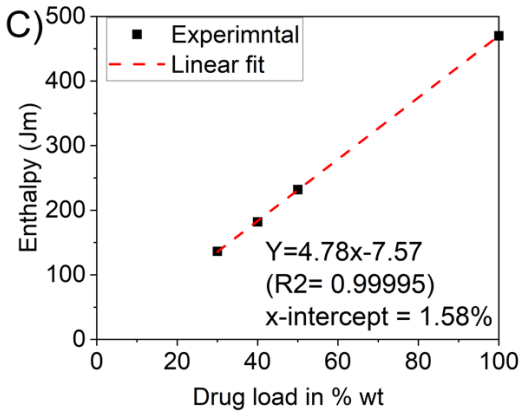

Figure 5-5. DSC traces of AZ, HPMCAS and AZ-MPMCAS physical mixtures (A), glass transitions and melting values (B) and linear fitting of the melting enthalpy to estimate the drug solubility level in HPMCAS (C).

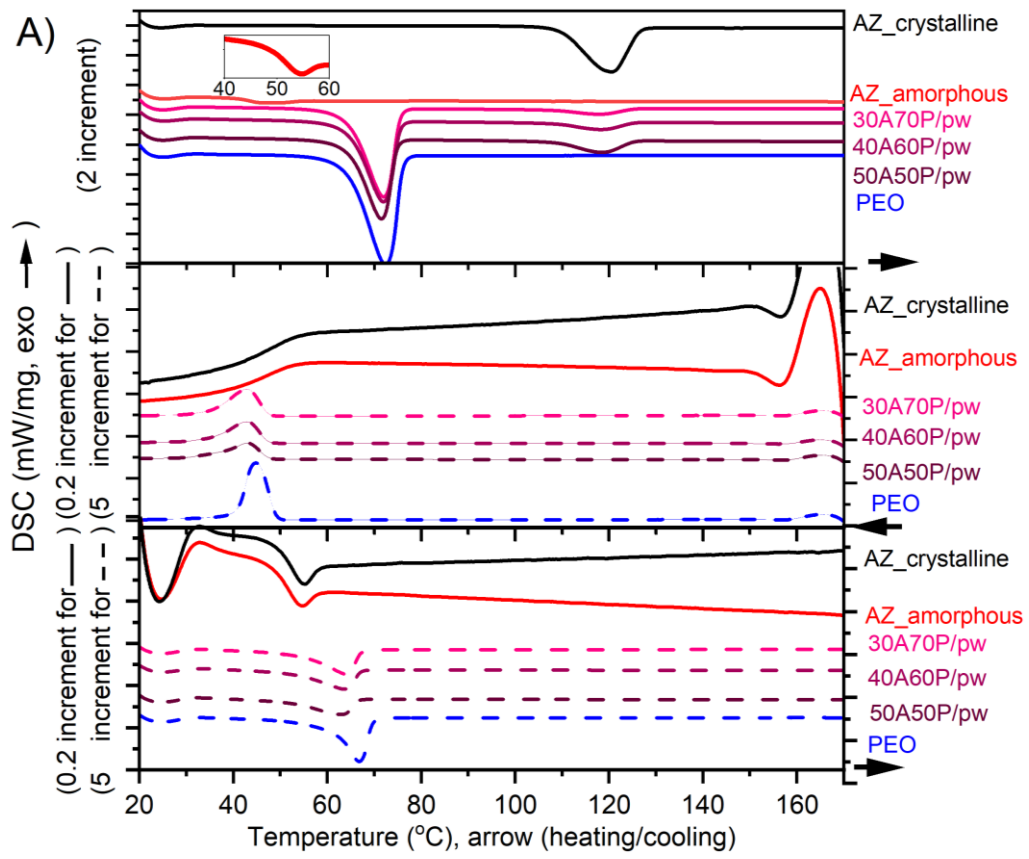

B)

	Tm(°C)/enthalpy (J/g)			
	1st heating		1st cooling	2nd heating
	Melting	Melting	Crystallisation	Melting
AZ-crystalline	-	120.5/94.9	Tg = 55	Tg = 49
30A70P/pw	72/132	117.5/10.5	41/71.3	63/78.3
40A60P/pw	71.8/113	118.4/18	41/59	63.9/84.17
50A50P/pw	71.5/111.1	118.6/26.6	429.47.4	63/64.25
PEO	72.4/172.5	-	43.8/115	66.8/124.9

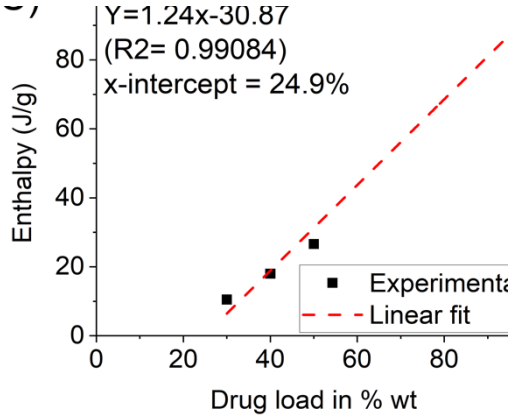

Figure 5-6. DSC traces of AZ, PEO and AZ-PEO physical mixtures (A), glass transitions and melting values (B) and linea fitting of the melting enthalpy to estimate the drug solubility level in PEO (C).

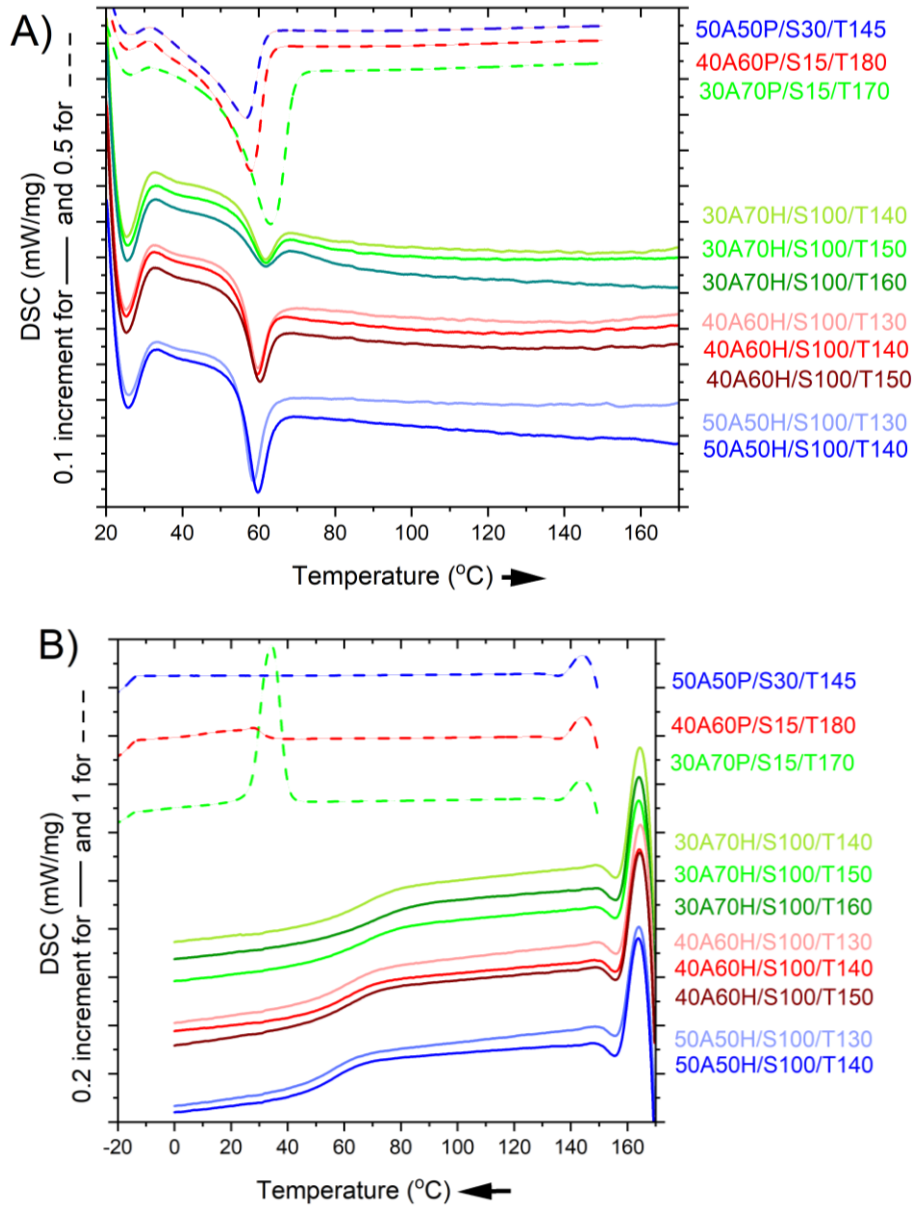

C)

	Heating	Cooling
	Tm (°C)/enthalpy (J/g)	Tg (°C)/ Tm (°C)
50A50P/S30/T145	56.8/52	-18.3/-
40A60P/S15/T170	58/66.7	-18.8/27.4
30A70P/S15/T180	63.7/90.1	-18.5/33.5
	Tg (°C) - onset	Tg (°C) – onset
30A70H/S100/T140	53.2	80.4
30A70H/S100/T150	52.9	88.6
30A70H/S100/T160	53.0	87.8
40A60H/S100/T130	54.4	72.1
40A60H/S100/T140	50.0	72.7
40A60H/S100/T150	54.2	73.3
50A50H/S100/T130	53.8	66.6
50A50H/S100/T140	54.5	65.6

D)

	PEO crystallinity
50A50P/S30/T145	50.7%
40A60P/S15/T170	54.2%
30A70P/S15/T180	62.8%
PEO	86.9%

Figure 5-7. DSC traces during heating (A) and cooling (B) of the AZ-HPMCAS and AZ-PEO formulae, both Tm and Tg assigned (C) and PEO crystallinity calculated from the enthalpy (D).

5.3.1.2.2. X-ray diffraction:

Offline x-ray diffraction was used to study the physical state of the extrudates (Figure 5-8 and 5-9). All AZ crystalline peaks disappeared in the HPMCAS-based extrudates regardless of the drug load and process temperature in the HME. While PEO-based extrudates showed two broad peaks. The peaks were not consistent between the extrudates, the first peak ranged between 18.3° to 19.5° and the second ranged between 22.5° to 23.5°. These peaks were associated with the semi-crystalline nature of the PEO, which exhibited inconsistency with the peak position based on sample processing conditions (Figure 5-9-bottom). The dependence of PEO crystallinity on time and process temperature might have affected the prolonged rubber-like state after extrusion. The peak of 30A70P/S15/T170 at 18.3° increased by 0.5° on the x-axis and 15% in intensity after 10 days of extrusion.

Zhu et al [216] studied the x-ray diffraction of PEG 3350 molecular weight with six different drugs cooled down at 25°C and 40°C. The diffraction patterns were sensitive to the thermal history and the added drug.

Based on the X-ray scattering patterns, all produced samples were amorphous solid dispersion (Figure 5-10).

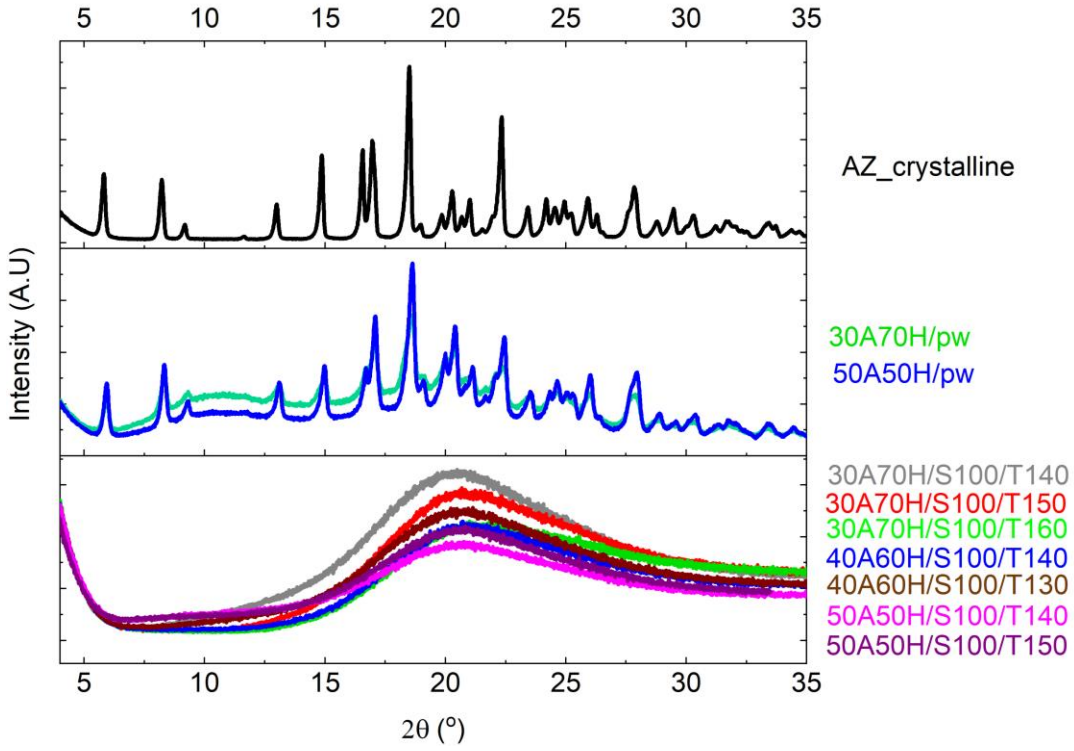

Figure 5-8. X-ray diffraction patterns of the drug and HPMCAS-based formulae.

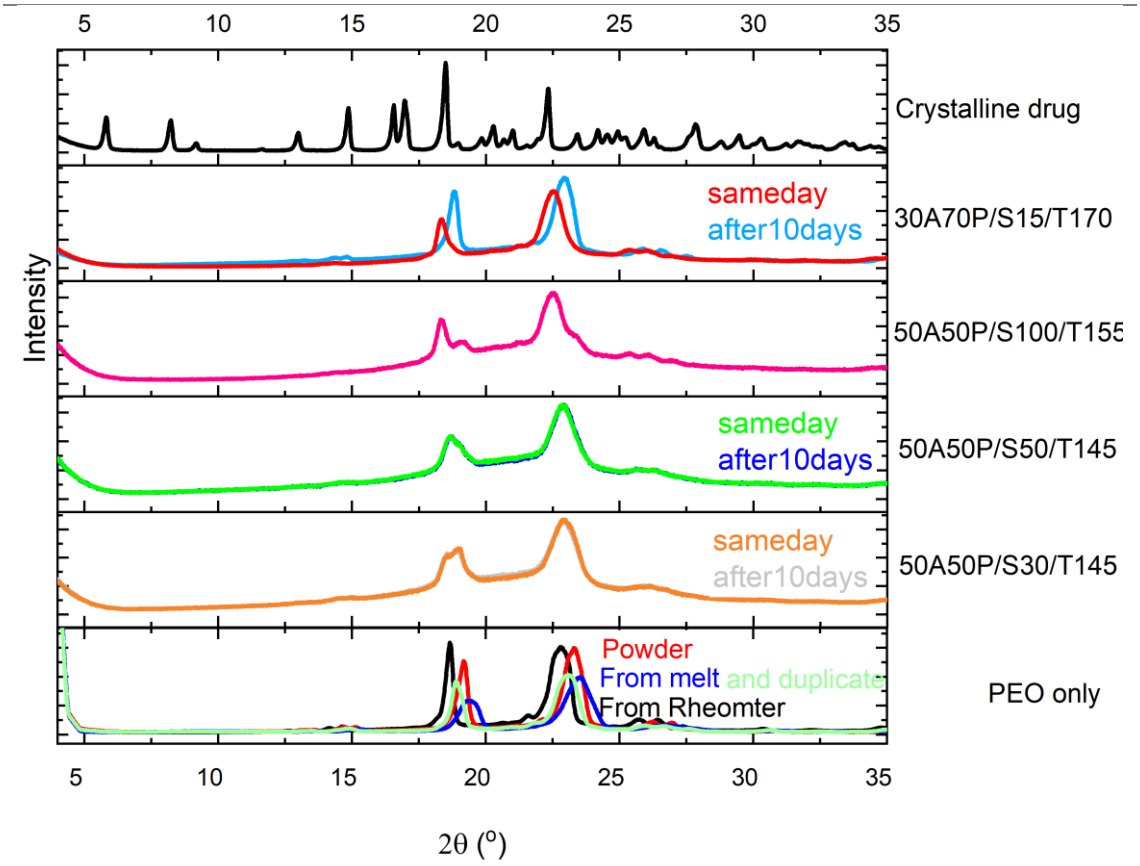

Figure 5-9. X-ray diffraction patterns of the drug (top), PEO-based formulae on the same day of the extrusion and after 10 days of the extrusion (middle), and PEO samples (bottom) as received and from the melt.

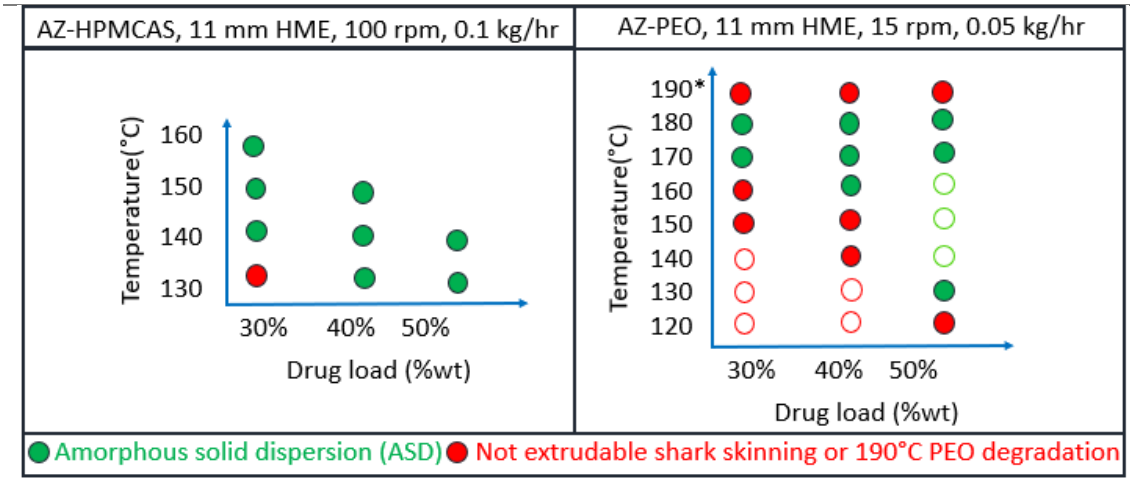

Figure 5-10. Regional phase diagram of AZ-PEO and AZ-HPMCAS formulae on 11 HME, Circles with no fill indicate process settings that were not tested, but outcomes can be inferred based on surrounding data.

5.3.1.2.3. Low frequency Raman Spectroscopy (Raman THz)

Low frequency Raman spectra were collected inline from the HME die for all the formulae (Figure 5-11). The spectra of all AZ-HPMCAS and AZ-PEO formulae showed only one peak at about 11 cm^{-1}. This peak was assigned to the AZ amorphous. While the rest of the peaks disappeared or were not detectable at the process temperature. The reason was that all the process temperatures were above the melting point of AZ and PEO. Low-frequency Raman was used for paracetamol-affinisol (Bordos et al [127]). At temperatures above the melting point of paracetamol, only one peak at low frequency appeared while all drug peaks disappeared.

Low-frequency Raman was used to collect the spectra of AZ-PEO formulae after extrusion since it was faster than the x-ray diffraction method (Figure 5-12). Solid dispersion filaments (30A70P, 40A60P and 50A50P) showed peaks similar to both PEO and AZ amorphous. For example, peaks at 12 cm^{-1}, 999 cm^{-1} and 1616 cm^{-1} presented in solid dispersion filaments and AZ amorphous. While peak at 38 cm^{-1}, 363 cm^{-1}, 844 cm^{-1}, 861 cm^{-1}, 1063 cm^{-1}, 1446 cm^{-1} came from PEO. However, some peaks appeared in one or a few systems for example at 1126 cm^{-1} for pure PEO (a black arrow), 621 cm^{-1} and 1605 cm^{-1} in solid dispersion (pink arrows). The biggest difference was in the 50A50P system which showed new peaks at 1087 cm^{-1}, 1156 cm^{-1} and 1182 cm^{-1} (blue arrow). Moreover, few peaks present in other systems disappeared in 50A50P for example 363 cm^{-1}, 844 cm^{-1}, 1063 cm^{-1}, 1143 cm^{-1}, 1233 cm^{-1}, 1280 cm^{-1}, 1397 cm^{-1}, 1472 cm^{-1} and 1481 cm^{-1} (red arrow). The difference in spectra between cooled PEO from melt versus solid dispersion filaments especially 50A50P suggested a difference in the solid state during cooling. This was aligned with the different Bragg patterns captured in the x-ray diffractometers and might cause the rubbery-like behaviour after extrusion, especially in the 50A50P filament.

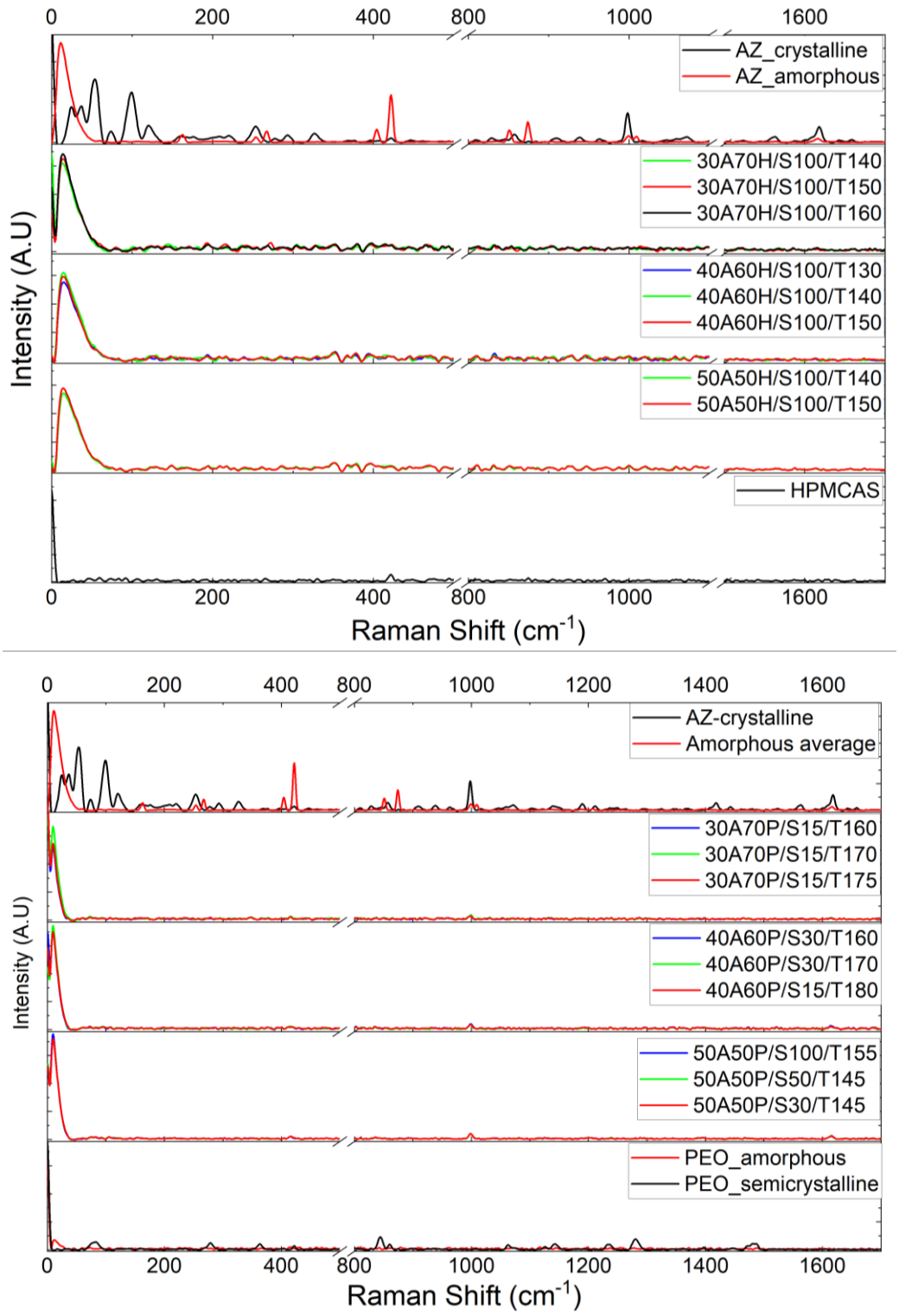

Figure 5-11. Inline low-frequency Raman spectra from the HME die for both AZ-HPMCAS based formulae (top) and AZ-PEO formulae (bottom).

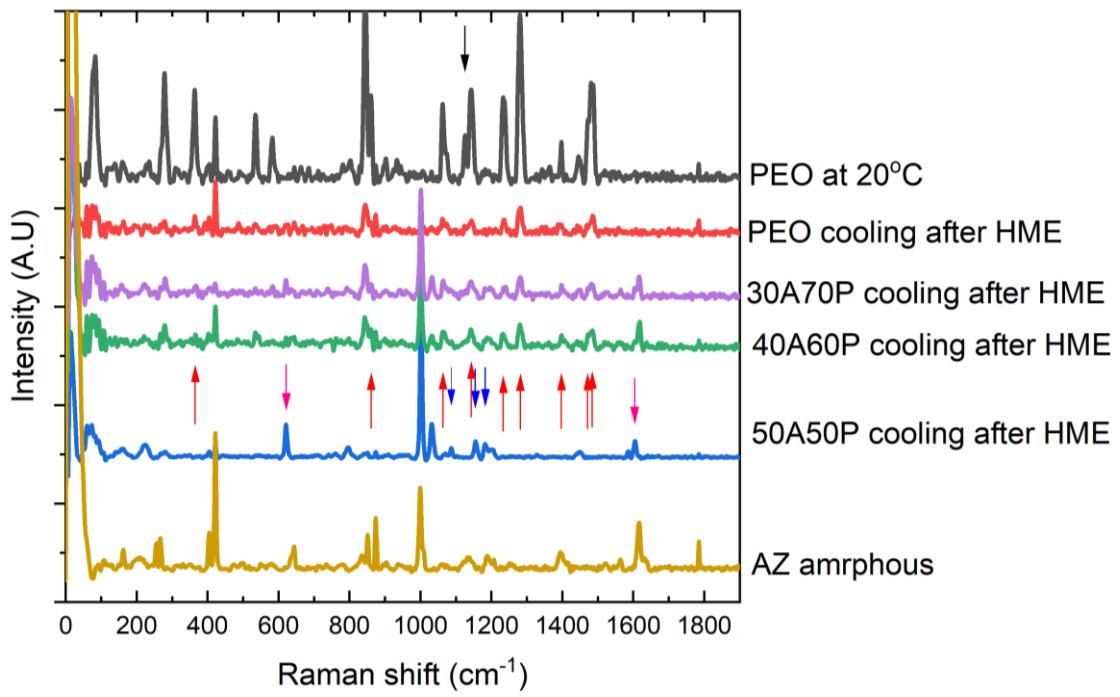

Figure 5-12. Low-frequency Raman spectra during cooling of PEO and AZ-PEO formulae filaments immediately after HME extrusion at 180°C, arrows indicated peaks presented only in PEO (black), only in solid dispersion systems (pink), only in 50A50P (blue) or in both PEO cooling and solid dispersion systems but not in 50A50P (red).

5.3.1.3. Physical properties

5.3.1.3.1. Mechanical properties (3-point bend test)

The mechanical properties of the AZ-HPMCAS and AZ-PEO filaments were evaluated using a 3-point bend test on the texture analyser. All AZ-HPMCAS formulae were brittle (break at low strain <8%) and stiff (elastic modulus >10 MPa/%). Strain at break and elastic modulus showed no significant or small differences (Figure 5-13). Increasing drug load (from 30%wt – 40%wt - 50%wt) reduced both maximum stress and strain at break. However, the differences were small (85 MPa to 71 MPa and 7% to 5.7%, respectively). For elastic modulus, the impact was not consistent as it increased from 30A70H to 40A60H (11.5 MPa/% to 12.3 MPa/%) and decreased from 40A60H to 50A50H (12.3 MPa/% to 11.5 MPa/%). While process temperature did not show an important impact on the mechanical properties except in 40A60P processed at 140°C versus 150°C. The 40A60P/S100/T140 was stiffer and had higher maximum stress and

strain at break than the 40A60P/S100/T150. Again, the differences were small (0.4 MPa/%, 14.6 MPa and 0.8%. respectively).

On the other hand, AZ-PEO formulae were soft i.e. low elastic modulus and, maximum stress and high strain at break, <0.8 MPa/%, <8 MPa and >70%, respectively. They showed greater differences with increasing drug load (Figure 5-14). The elastic modulus and maximum stress decreased as the drug load increased. The 50A50P/S30/T145 was the softest filament (0.1 MPa/% and 2.1 MPa). All AZ-PEO formulae were flexible and reached the maximum strain at break value for the 3-point bend test (>70%).

The difference in the AZ impact on each polymer might be attributed to drug-polymer and polymer-polymer interactions. AZ-HPMCAS did not show a strong increase in molecular interaction with increasing the drug load. Thus, the mechanical properties were very similar (about 6.5% increase in elastic modulus from 30A70H to 40A60H). This was in agreement with the finding using other techniques like spectra and X-ray diffraction, which were identical regardless of drug load. While DSC showed no clear difference in the Tgs between 30A70H, 40A60H and 50A50H except when it was measured from extrudates during the cooling cycle. PEO showed a stronger impact (about 100% decrease in elastic modulus from 30A70P to 40A60P) as increasing the drug load reduced the PEO crystallinity making the filament more ductile. Henry et al [186] noticed an increase in the ductility of PEO N10 with increasing Ibuprofen concentration.

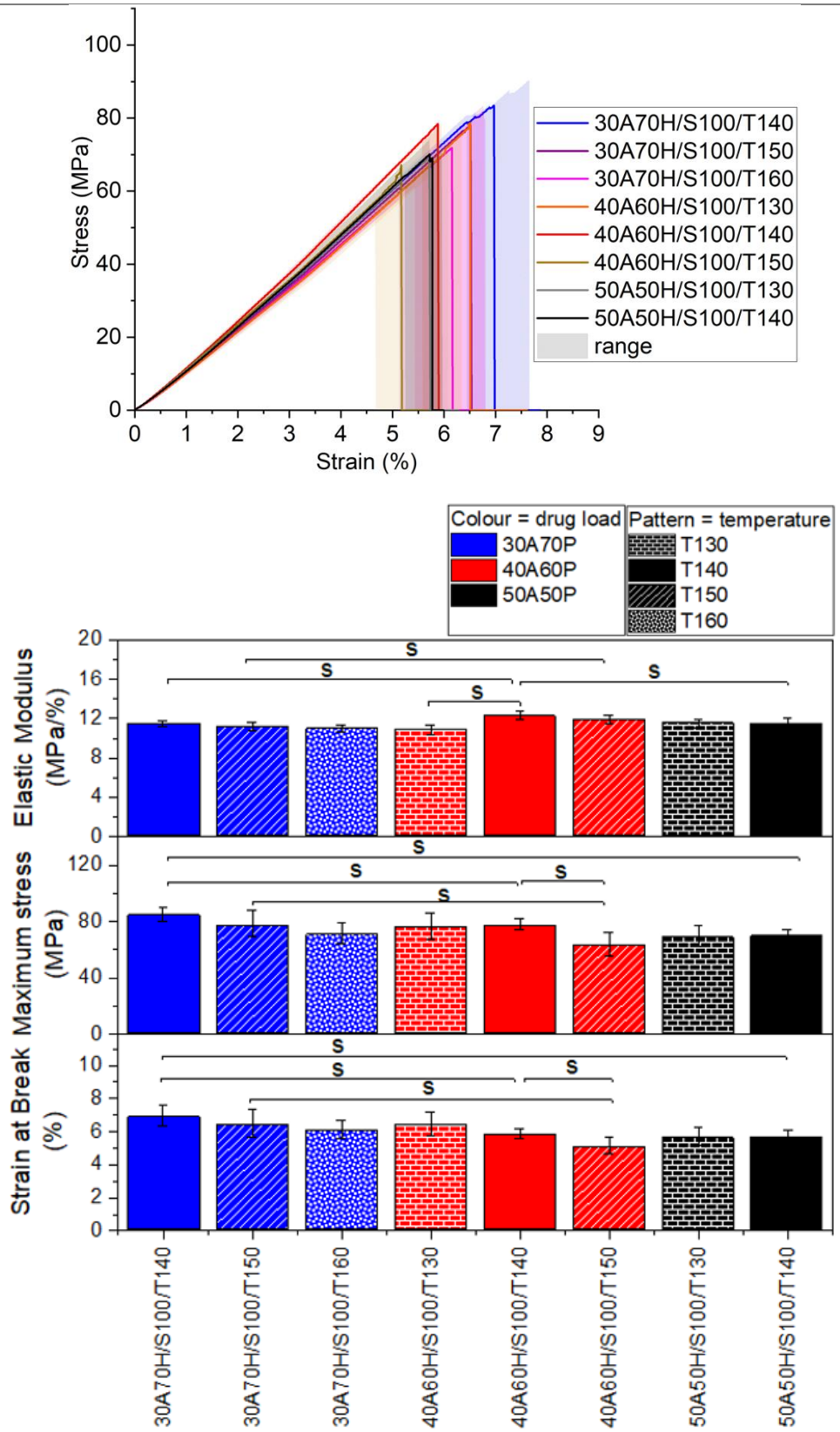

Figure 5-13. Mechanical properties of AZ-HPMCAS formulae (line plot) and extracted values (bar charts), namely elastic modulus, maximum stress and strain at break, average values recorded (n=5, error bar = SD), t-test only significant difference (s, P<0.05) added to the graph i.e. all the rest are non-significant.

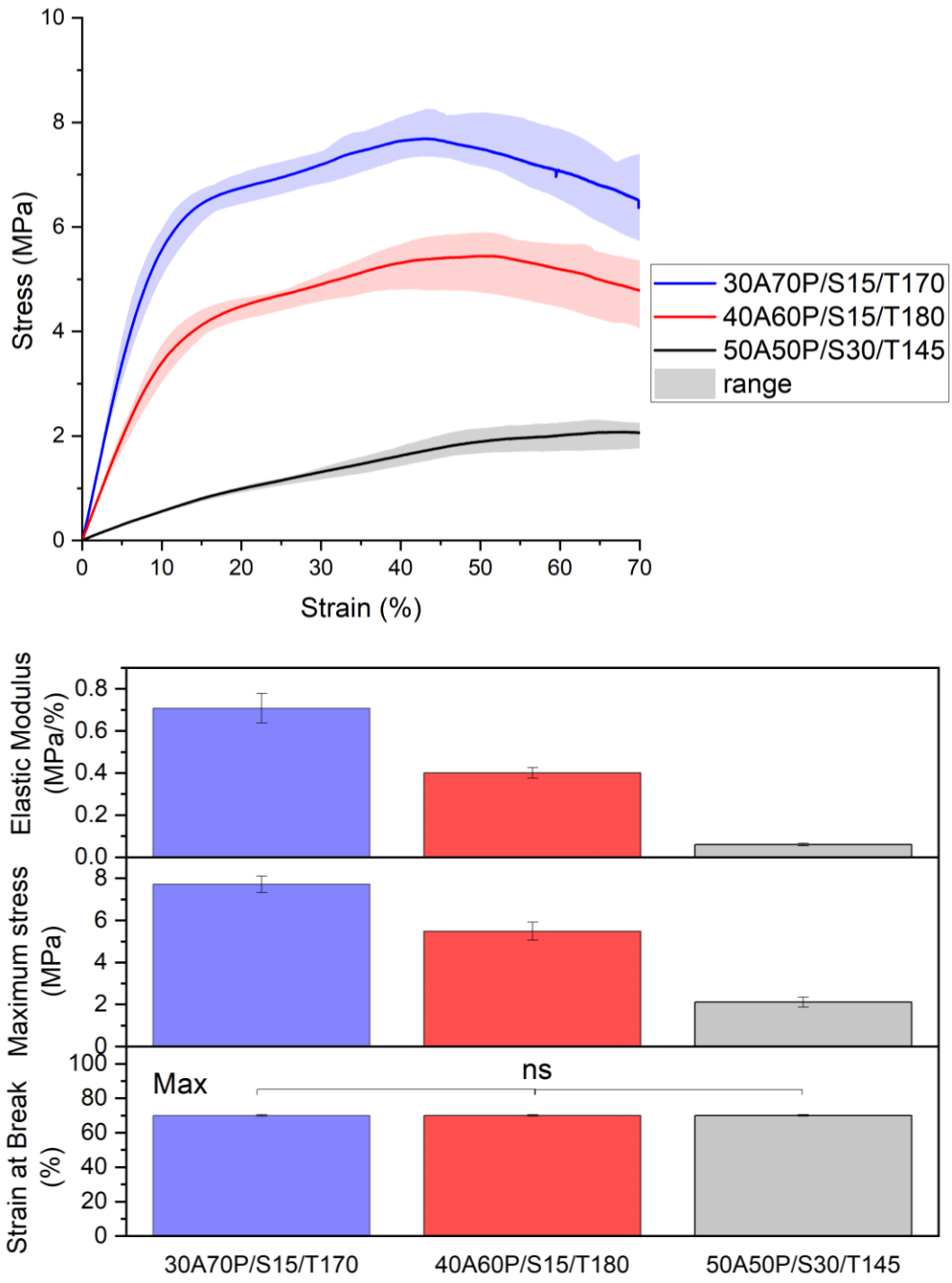

Figure 5-14. Mechanical properties of AZ-PEO formulae (line plot) and extracted values (bar charts), namely elastic modulus, maximum stress and strain at break, average values recorded (n=5, error bar = SD), t-test only non-significant difference (ns, P>0.05) added to the graph i.e. all the rest are significant.

5.3.1.3.2. Rheology

Figure 5-15 shows amplitude sweep tests of samples from both AZ-HPMCAS and AZ-PEO based filaments. All loss (G") and storage (G') moduli, except 50A50H/S100/T140 at 170°C, had linear patterns parallel to the x-axis and deviated by less than 5% (limit of the linear viscoelastic region, LVR, based on Thermal Analysis Instruments documentation [217]) below the oscillation strain of 0.5%. Moduli of 40A60H and 50A50H were increased slightly at about 0.2% strain suggesting complex behaviour. But only 50A50H/S100/T140 at 170°C increased by more than 5% making its LVR smaller than other samples. This complex behaviour might be caused by the high drug load of the drug. In the case of separation, two liquids (polymer and drug) would behave differently under the shear stress in the amplitude test [120]. This was clearer at a high test temperature (170°C). The following temperature sweep tests were conducted within the LVR region.

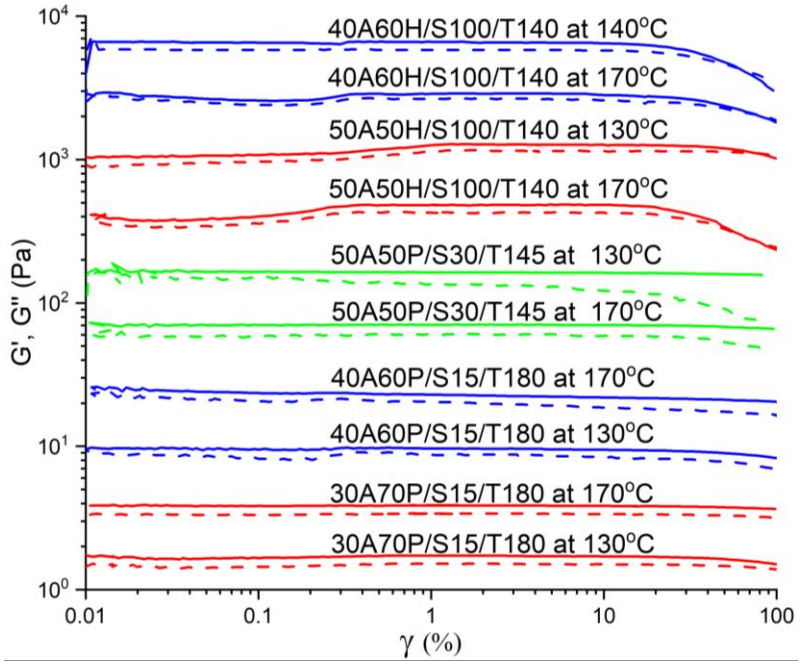

Figure 5-15. Storage (G', solid line) and loss (G", dashed line) moduli of AZ-HPMCAS and AZ-PEO filaments from the amplitude sweep test showing linear viscoelastic region.

Figure 5-16 is the temperature sweep test of the AZ-PEO and AZ-HPMCAS formulae. At low temperatures, the formulae did not maintain good adhesion to the rheometer disk except for 50A50H/S100/T140. Thus, the differences below 90°C between HPMCAS-based formulae and below 50°C between PEO-based formulae were neglected. For

PEO-based formulae, the viscosity of 30A70P/S15/T180 was the lowest below 70°C. At 82°C the same formula was the most viscous followed by 40A60P/S15/T180 then 50A50P/S30/T145. The viscosity drop was assigned to both the plasticization effect of the drug on the polymer chains (24.9% wt% MFA in PEO was miscible, Figure 5-6) and to the molten drug, especially above the drug melting point. For HPMCAS-based formulae, the viscosity decreased by increasing the drug load. Which, was also assigned to the melting of the drug. There is no clear evidence of the AZ-HPMCAS interaction detected by other techniques like DSC and texture analyser, thus it was not clear if the interaction affected the blends' viscosity or if the decrease was caused by the molten drug.

Tan(δ) showed the opposite order of the viscosity across most of the temperature range from 120°C to 170°C for AZ-HPMCAS formulae and 50°C to 170°C for AZ-PEO formulae. A higher drug load resulted in a greater tan(δ). Liquid-like behaviour (tan(δ)>1) was above 86.2°C, 113°C, 137°C and 158°C for 50A50P, 30A70P, 50A50H and 30A70H, respectively (Table 5-4 and Table 5-5). Tan(δ) peak (Tg_{Rhe}) was detected in HPMCAS-based formulae (Table 5-5). $Tg_{Rheometer}$ of 50A50H was the lowest followed by 40A60H and then 30A70H, similar to Tg_{DSC} (Figure 5-7-C Tg onset from cooling).

Ketoprofen (Tm = 94°C) with PEO WSR N-10 NF (100 kg/mol) was studied in the rheometer for HME process [218]. Similar to AZ drug, Ketoprofen plasticized PEO and reduced viscosity with increasing drug load from 0% (wt%) to 40% (wt%) with a 10% (wt%) increment. The decrease in the viscosity was stronger with Ketoprofen, which might be due to the drug-polymer molecular interactions and PEO lower molecular weight.

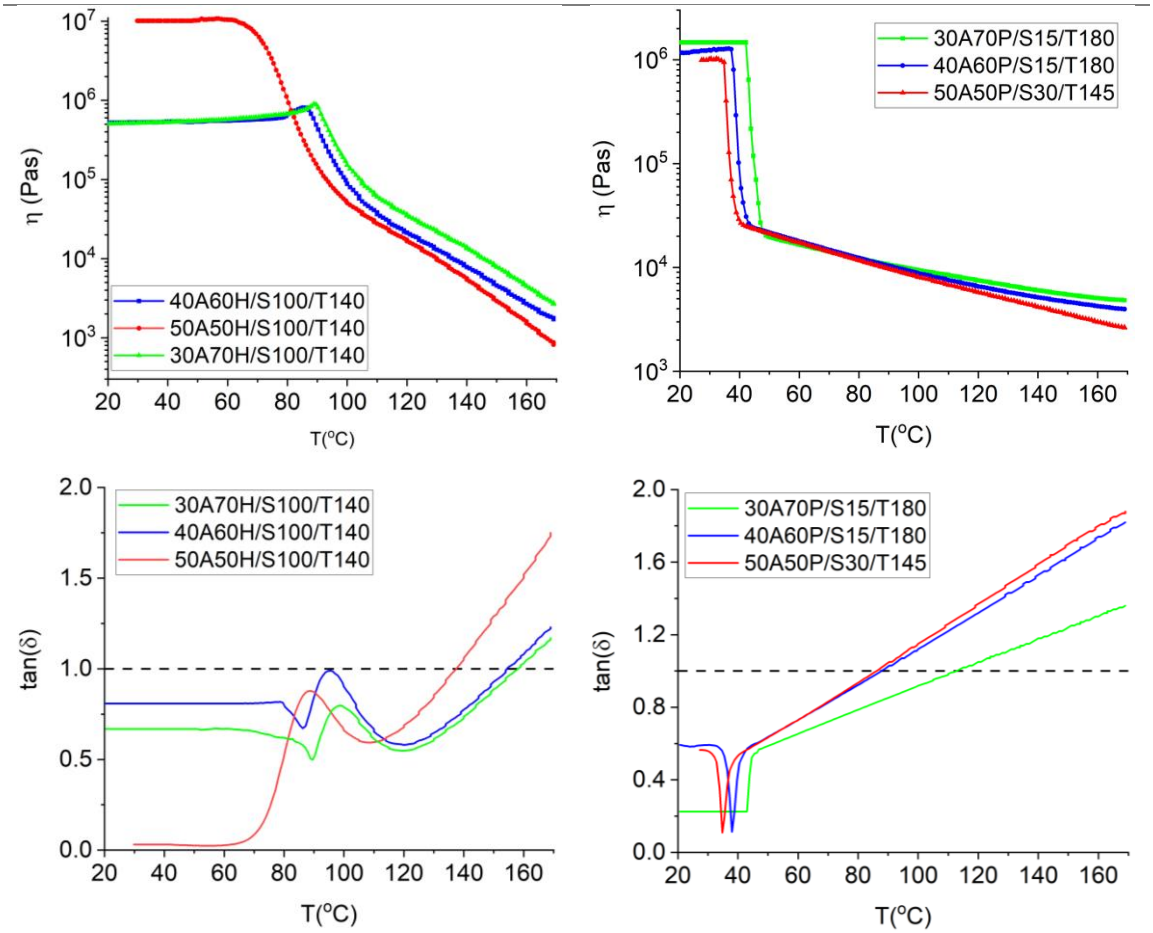

Figure 5-16. Viscosity (top) and tan(δ) (bottom) of AZ-HPMCAS (left) and AZ-PEO (right) based formulae.

5.3.1.4. 3D printing

5.3.1.4.1. 3DP- extrudability prediction

E/η ratios for both AZ-HPMCAS and AZ-PEO-based formulae were evaluated for 3D-printing extrudability prediction. Figure 5-17 shows the E/η ratios of all formulae and tables 5-4 and 5-5 are numerical values at temperatures of interest. All AZ-PEO formulae were below the E/η threshold identified in the previous chapter (0.8 $\times 10^{-3}$ MPa/%Pas). This means that the mechanical properties of AZ-PEO formulae were poor to provide enough support to push the molten material out (section 1.5.2) [70]. While AZ-HPMCAS formulae were higher than the threshold at 130°C and above. Increasing the temperature and/or the drug load decreased reduced viscosity and thus increased the E/η ratio (table 5-5).

Zhang et al [199] compared hydroxypropyl methylcellulose (HPMC), HPMCAS and Hydroxypropyl cellulose (HPC) for printability. Both mechanical properties and

viscosity were evaluated. HPMCAS was tough and had relatively low viscosity which made it extrudable with a fine texture on the Prusa i3 3D printer.

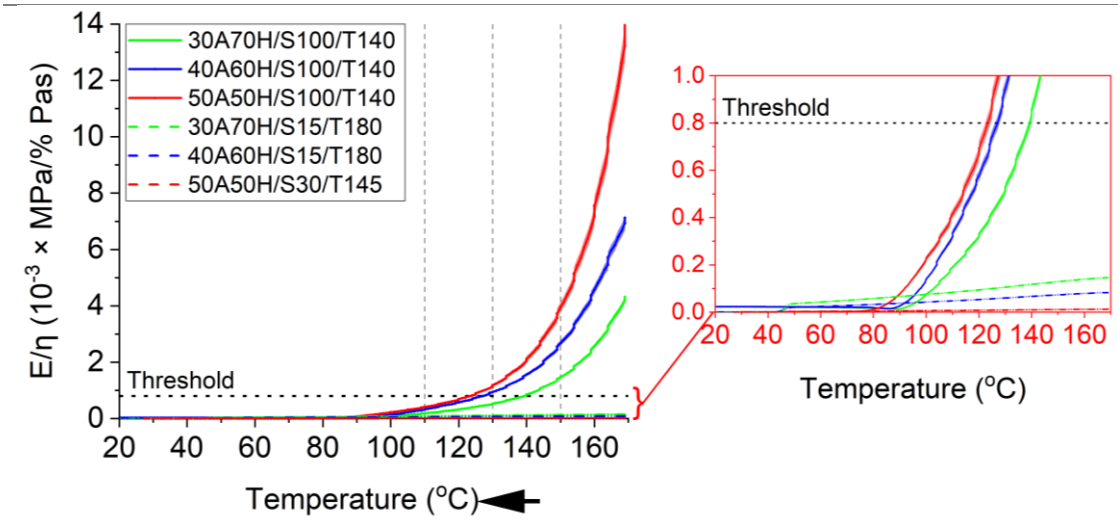

Figure 5-17. E/η ratios across a range of temperatures for AZ-HPMCAS formulae (solid lines) and AZ-PEO formulae (dashed lines, close to the x-axis). The black dotted line represents the E/η threshold (0.8 ×10^{-3} MPa/%Pas) found in the previous chapter.

Table 5-4. Crossover temperature and E/η ratio at 170°C of AZ-PEO formulae:

	Crossover point (°C)	**E/η$_{170°C, 6.28rad/s}$ (10^{-3} × MPa/%.Pas)**
30A70P/S15/T180	113	0.1461
40A60P/S15/T180	87.7	0.0829
50A50P/S30/T145	86.2	0.0124

Table 5-5. Crossover temperature, tan(δ) peak and E/η ratio at 110°C, 130°C and 150°C of AZ-HPMCAS formulae:

	Crossover point (°C)	**Peak (°C) (Tg $_{Rhe}$)**	**E/η$_{T°C, 6.28rad/s}$ (10^{-3} × MPa/%.Pas)**		
			T=110°C	**T=130°C**	**T=150°C**
30A70H/S100/T140	158	98.6	0.190	0.529	1.473
40A60H/S100/T140	154	95.5	0.337	0.943	2.683
50A50H/S100/T140	137	88.8	0.416	1.187	3.962

5.3.1.4.2. 3DP- extrudability test

To test the prediction made in the previous paragraph, 3D printing extrudability tests were performed. Table 5-6 shows the test results for the AZ-HPMCAS formulae at 110°C, 130°C, 150°C and 170°C nozzle temperatures and 3 mm/s speed. At 110°C, all AZ-HPMCAS formulae were not printable due to high viscosity in the printer nozzle. At 130°C, the 3DP-extrusion was improved for the three ratios. However, the 30A70H/S100/T140 was just 3DP-extrudable and broke often. At 150°C, all formulae were 3DP extrudable with consistent filament. At 170°C, the formulae were 3DP-extrudable, but outgassing was observed that caused disturbance of the filament consistency. These results agree with the 3DP-extrudability prediction. The outgassing was thought to be free acetic acid and succinate acid, which can be produced in processes that include high temperatures and shearing like HME [219] and 3DP.

Table 5-6. 3DP-extrudability test of the AZ-HPMCAS formulae at four nozzle temperatures and a printing speed of 3 mm/s:

Temperature (°C)	**170**	**150**	**130**	**110**
30A70H/S100/T140	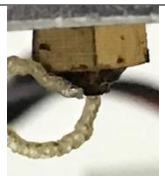			[Not available]
	Inconsistent/ outgassing	Consistent flow	Poor	Does not flow
40A60H/S100/T140		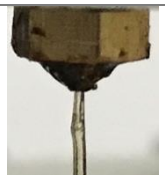		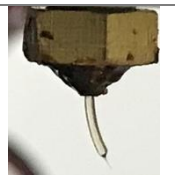
	Inconsistent/ outgassing	Consistent flow	Flow but broke	Does not flow
50A50H/S100/T140		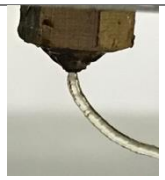		
	Inconsistent/ outgassing	Consistent flow	Flow but broke	Does not flow

All AZ-PEO formulae failed to extrude at 3 mm/s at 180°C (Table 5-7). The mechanical properties of these formulae were insufficient to be able to push the molten material out (Figure 5-18). To facilitate the process a slower printing speed was tested. At 0.5 mm/s, only 30A70P/S15/T180 was sometimes extrudable. At 0.25 mm/s, 30A70P/S15/T180 and 40A60P/S15/T180 were extrudable with good reproducibility, but 50A50P/S30/T145 was not 3DP-extrudable at any printing speed. These findings were in agreement with the 3DP-extrudability prediction i.e. all formulae were not 3DP-extrudable and showed a similar order of E/η ratios from the best to the worst; 30A70P/S15/T180, 40A60P/S15/T180 then 50A50P/S30/T145.

Table 5-7. 3DP-extrudability test of the AZ-HPMCAS formulae at 180°C nozzle temperatures and different printing speeds:

Printing speed	30A70P/S15/T180	40A60P/S15/T180	50A50P/S30/T145
3 mm/s	✗	✗	✗
2 mm/s	✗	✗	✗
1 mm/s	✗	✗	✗
0.5 mm/s	☐ ✓	✗	✗
0.25 mm/s	✓	✓	✗

✗ = fail, ✓ = success, ☐ = inconsistent (symbol combination indicates likelihood).

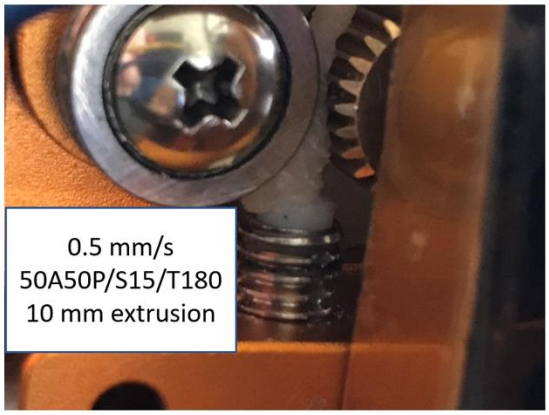

Figure 5-18. Buckling of 50A50P/15S/T180 in the 3D printer extruder head from the 3DP-extrudability test at 180°C and 0.5 mm/s.

5.3.1.4.3. 3D printing test

Although the AZ-HPMCAS filaments did not coil, 3D printing tests were conducted on rod-like filaments. All formulae failed to print the F-design caplet (Table 5-8). When slippage occurred, the gears were tightened and tests were repeated. The reason for the failure was breakage at the extruder gear for the three filaments. From the zoomed-in pictures, the breakage occurred due to the stress on the filaments. Although all three filaments had maximum stresses between 75 and 85 MPa (above the threshold of 22.9 MPa, from the previous chapter), the filaments did not show any plastic deformation until the break. Therefore, the stress from the gear's teeth was focused on one point. When low stress was applied, the gears did not have a good grip on the filament and slippage occurred and the extrusion was not consistent. By tightening the grip high tension was applied at one point of the brittle filament causing breakage. Although these filaments were 3DP-extrudable, the printing process presented more complexity due to the stop-start nature of 3DP-extrusion.

Zhang et al [199] printed HPMCAS on a Prusa i3 3D printer. However, the brittleness of the HPMCAS filaments was clear and caused breakage in the hot end by the feeding gears. The print failure occurred often during printing process up to six per ten attempts.

Table 5-8. 3D printing attempts of AZ-HPMCAS filaments at 150°C nozzle temperature and 3 mm/s speed:

30A70H/S100/T140	40A60H/S100/T140	50A50H/S100/T140
		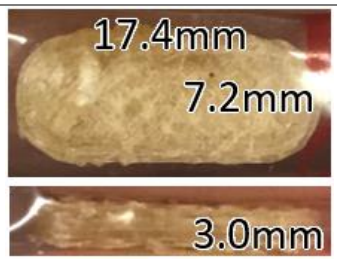
	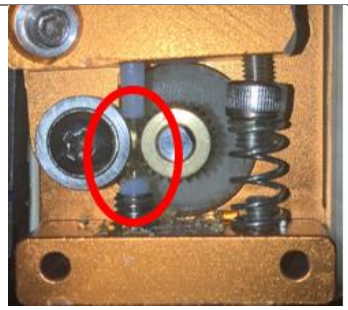	Missing Figure (was not captured)
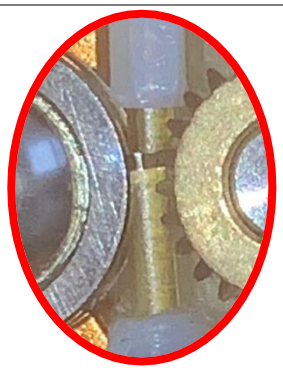		Missing Figure (was not captured)
F-design, Printing = 150°C, Bed = 25°C, Speed = 3mm/s (180mm/min)		

Due to the poor 3DP-extrudability of AZ-PEO filaments, 30A70P/S15/T180 was tested using an F-design caplet at 180°C nozzle temperature, 25°C bed temperature and 0.25 mm/s speed (the successful speed from the 3DP-extrudability test). In addition to the poor 3DP-extrudability, the filament showed other issues during printing (Figure 5-19) such as the solidification of the printed lines/layers (Figure 5-19-A). Additionally, the soft material was dragged by the nozzle causing gaps in the structure in some areas and accumulation in others. Another observed problem was skipping lines during printing mostly short lines like the one that forms the curves at the ends of the caplet. It was not clear if the motor step size facilitated this deformity. According to the motor specification, the smallest movement was half a step, which was 0.9°. This is equivalent to 0.079 to 0.086 mm (calculated based on a 10-11 mm gear diameter), which was

bigger than most of the small lines that formed the curve (Figure 5-19-B). On the other hand, the execution of the g-code accumulates the extrusion amount meaning if a step was smaller than half a step to be executed, the addition of two consequent lines was executed together (the sum is bigger than half a step). To avoid this problem, the number of walls was reduced. The caplet that has fewer curved lines was better (Figure 5-19-C and E). However, all attempts failed to produce a caplet similar to the intended design even by reducing the wall number and giving more time for solidification (Figure 5-19-D). The best attempt can be seen in Figure 5-19-E.

Henry et al [186] noted that PEO N10 was printable in some studies [81], [179] and not printable in others [220]. They printed the PEO N10 at 80°C. However, PEO-Ibuprofen at 20% (wt) and 40% (wt) were not printable using the 0.4 mm nozzle. Furthermore, printing a tablet of pure PEO N10 was very sensitive to the fan speed as the structure deformed and collapsed without turning on the fan due to the poor crystallisation and solidification of the polymer. This was also inhibited by the drug's presence. The results in the current study agreed with the cited paper findings, although the polymer was not printable because a different grade was used.

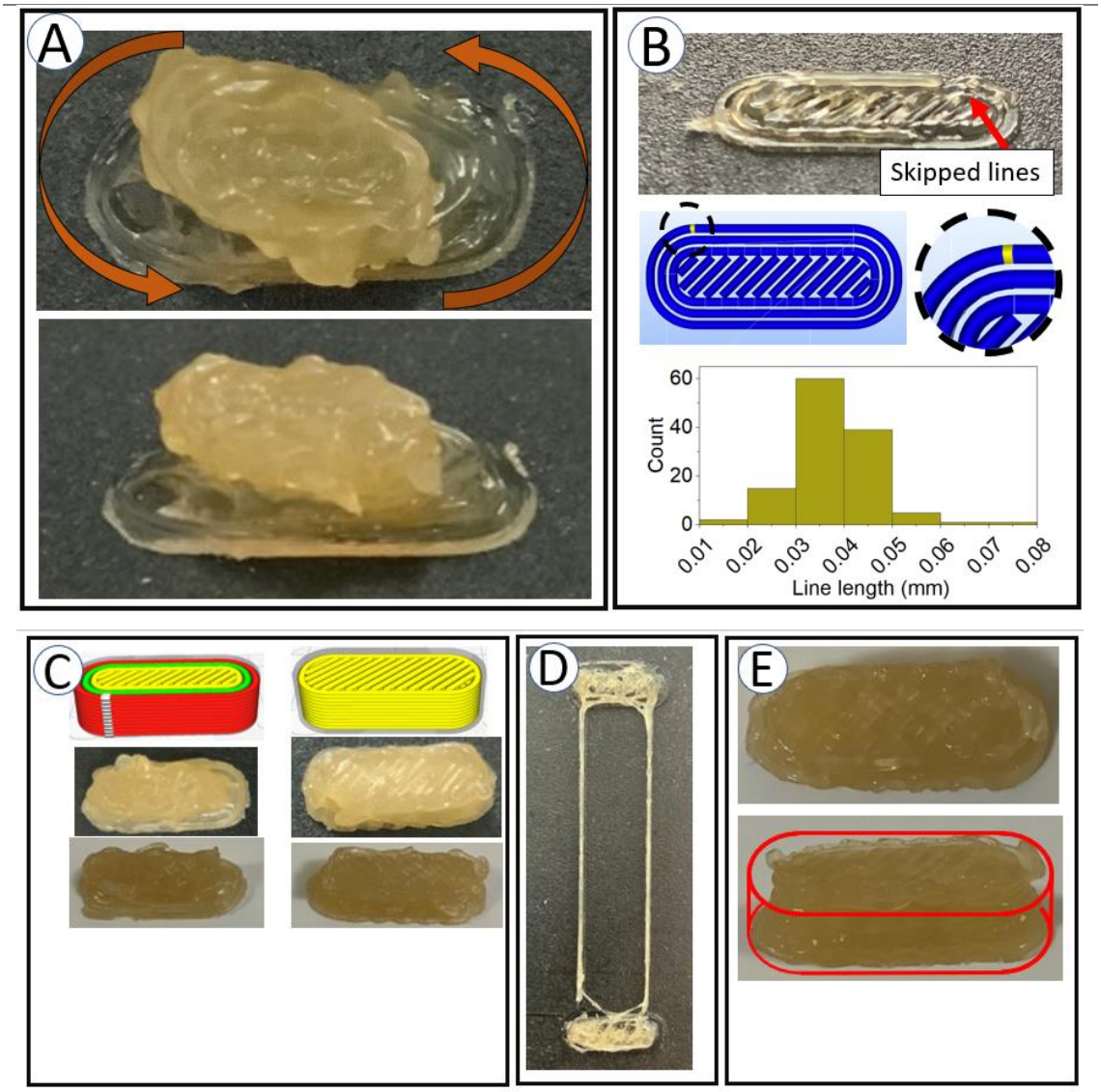

Figure 5-19. 3D printing failure of 30A70P/S15/T180 filament at 180°C nozzle temperature and 0.25 mm/s due to the lack of structural support of the prints, poor solidification and material dragging with nozzle movement (A) Skipped steps on both of the print sides and the histogram of the mini-steps that form the curves per layer (B) An attempt to reduce the mini-steps in the g-code by reducing the number of walls and increasing the number of long lines (C) An attempt to improve layer solidification by printing two caplets and increasing the time between consequential layers (D) best attempt – no walls (E).

5.3.2. Ternary mixtures

5.3.2.1. Ternary systems extrusion

Since all AZ-HPMCAS and AZ-PEO binary systems were not printable, additives were needed. In the case of AZ-HPMCAS filaments, the extrudability was good, but they

lacked the ductility (strain at break) to be fed into the printer head. While AZ-PEO filaments were the opposite as they had good flexibility but struggled to be 3DP-extruded at 3 mm/s speed. Since the properties of these two formulae were complementary a mixture of them might balance their properties. PEO:HPMCAS polymer mixtures with a fixed drug load at 30% (wt% of total weight) were used for further study. This drug load was used since 30A70P (wt%) showed the best ratio between the AZ-PEO formulae and 30A:70H (wt%) showed good mechanical properties. The 70% (wt% of the total weight) polymer mixtures consisted of different ratios of PEO:HPMCAS, 25:75, 50:50 and 75:25 (wt% of the polymer mixture). Filaments from the previous section 30A70P and 30A70H were the same as 30A(100P0H) and 30A(0P100H), respectively.

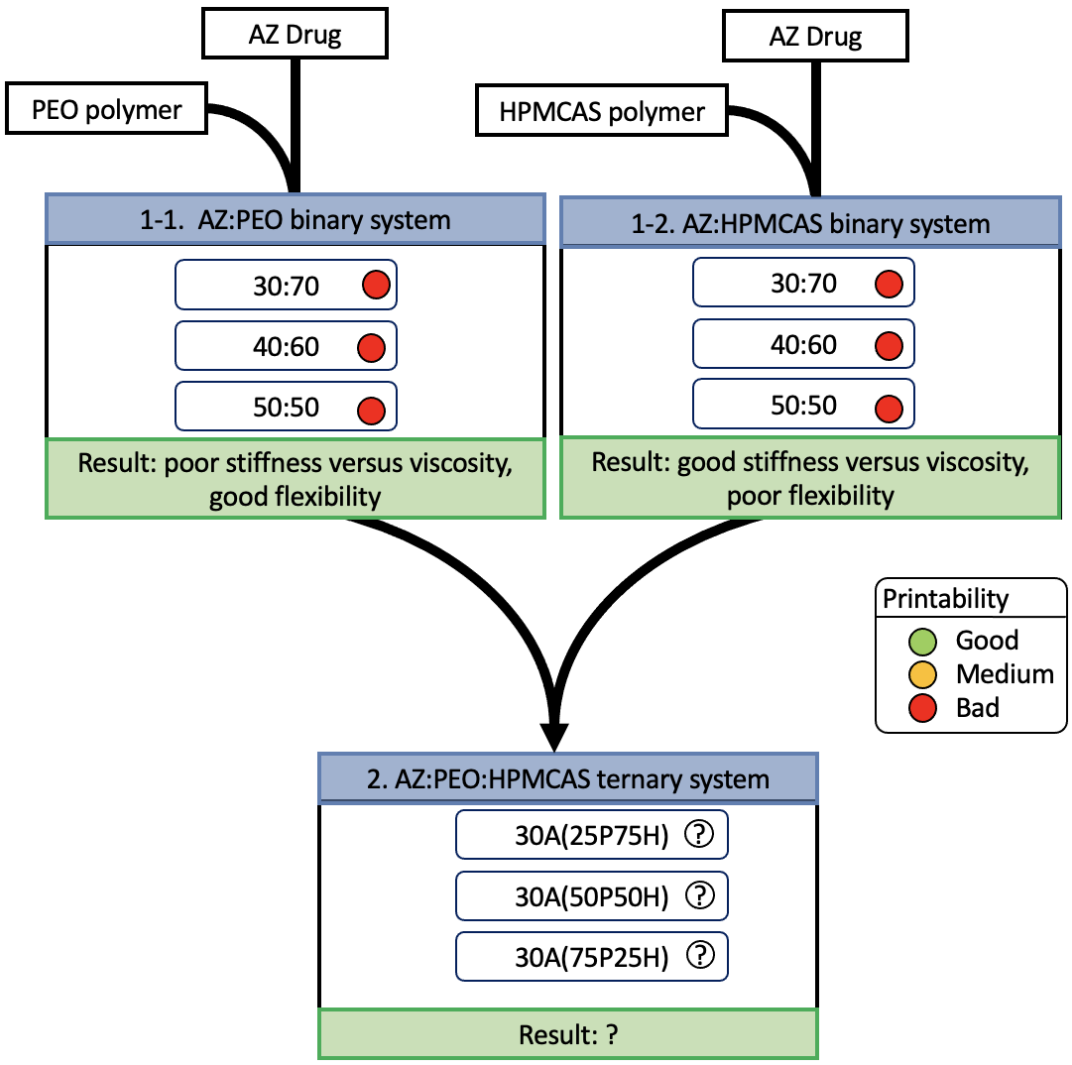

Figure 5-20. Second stage workflow for exploring the 3D printing formulation space of AZ-PEO and AZ-HPMCAS formulae.

All ternary formulae were extruded at 11 mm HME with a nozzle size of 1.7 mm, the die pressures were plotted versus the process temperature in Figure 5-21. At a high PEO ratio 30A(75P25H), the formula was not extrudable at 100 rpm screw speed due to the high-pressure alarm. Therefore, the screw speed was gradually reduced until the formula could be extruded at a screw speed of 15 rpm and a process temperature of 180°C. This process window is similar to the 30A70P formula. The other two formulae, 30A(50P50H) and 30(25P75H), were extrudable at a higher screw speed namely 100 rpm and at lower process temperatures up to 120°C and 100°C, respectively. The die pressure for the 30(25P75H) in general was lower. The reduction in the die pressure was attributed to improvements in the flow behaviour of the mixture after HPMCAS addition. It was noticed that the die pressure of 30A(25P75H) was lower than that of 30A70H (Table 5-2). PEO might have plasticized the HPMCAS.

Mixtures of HPMSAS and PEG were studied for making capsule shells using injection moulding [221]. Three molecular weights of PEG were used 1500, 8000 and 20000 MWt, and three ratios of PEG 1500 MWt were further tested at 15% 25% and 35% (wt%). PEG plasticized the HPMCAS with a higher ratio found to be more effective. The findings demonstrated that although the HPMCAS was successfully plasticized by the addition of PEG, the influence of PEG molecular weight on the properties of the material was minor in comparison to the impact of the PEG ratio.

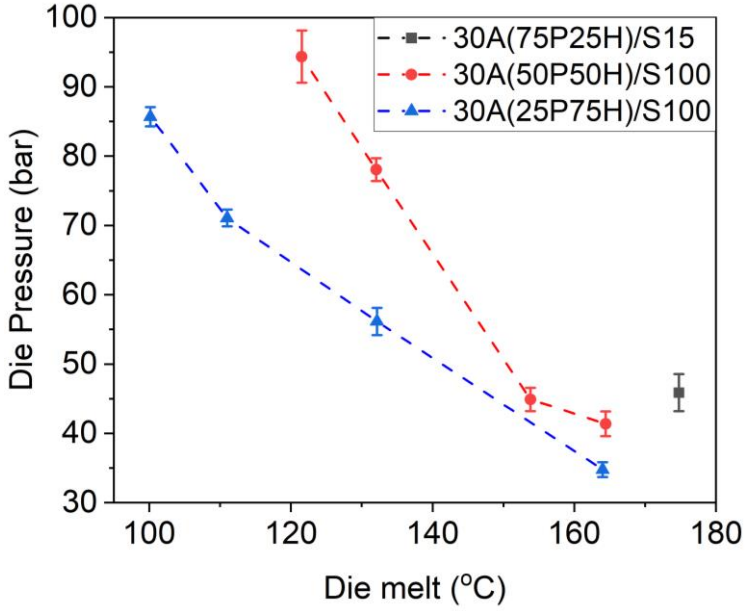

Figure 5-21. Die pressure of the 30% (wt%) AZ with 70% (wt%) polymer mixture in the HME at different HME process temperatures.

5.3.2.2. Ternary systems' solid state

Solid states of the formulae in the HME die and solid filaments were studied using low-frequency Raman spectroscopy (Figure 5-22) and XRPD (Figure 5-23), respectively. In both techniques, peaks of the crystalline AZ were absent (the small peaks at 100 cm^{-1} and 280 cm^{-1} belongs to PEO) indicating they were all amorphous solid dispersions. 30AZ(25P75H) was amorphous even when it was extruded at 100°C and 110°C below the melting point of AZ (120°C, DSC result Figure 5-6). Shear stress and polymer mixture might have helped in the amorphization of the AZ drug.

XRPD patterns (Figure 5-22) showed some peaks at around 18° and 22°. These peaks were not consistent in their position across the x-axis between different filaments and different process temperatures. PEO crystallinity showed sensitivity to process temperature (Figure 5-9), and to the presence of the HPMCAS and AZ. Zhu et al [216] studied the crystallisation of PEG during cooling with six drugs processed at different temperature profiles. PEG-drug interaction, drug ratio and temperature profile were found to affect the microstructure of the PEG.

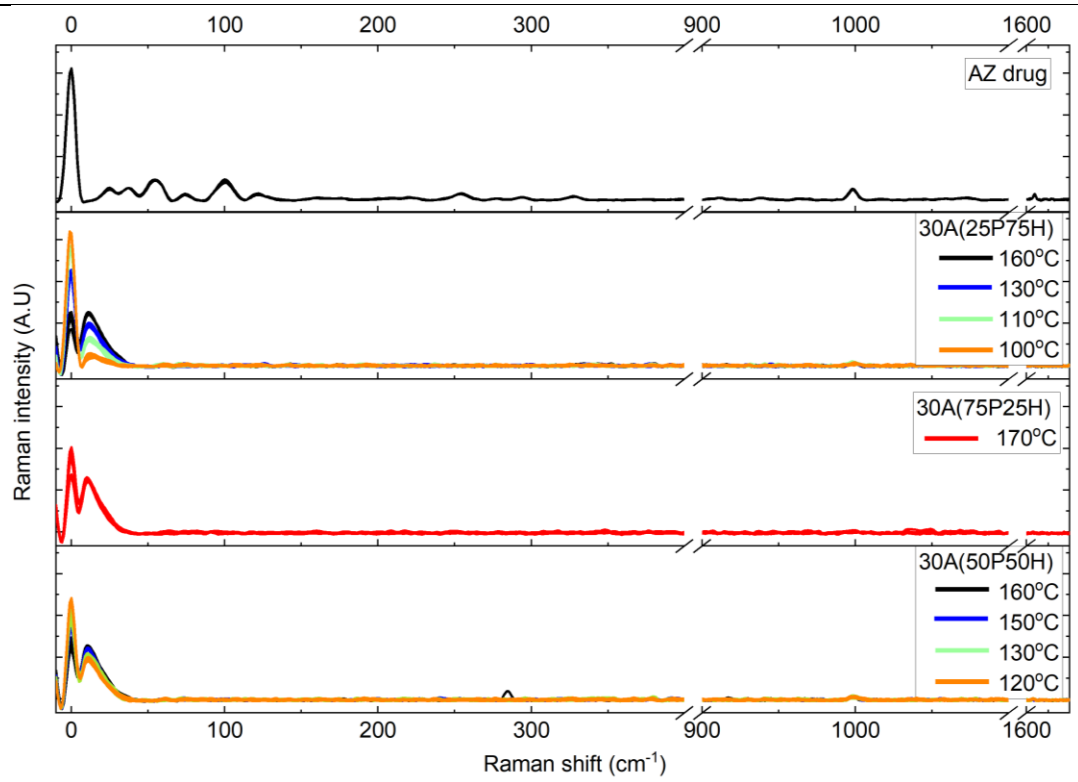

Figure 5-22. In-line low-frequency Raman spectroscopy of different AZ-PEO-HPMCAS ternary formulae compared with AZ drug spectra.

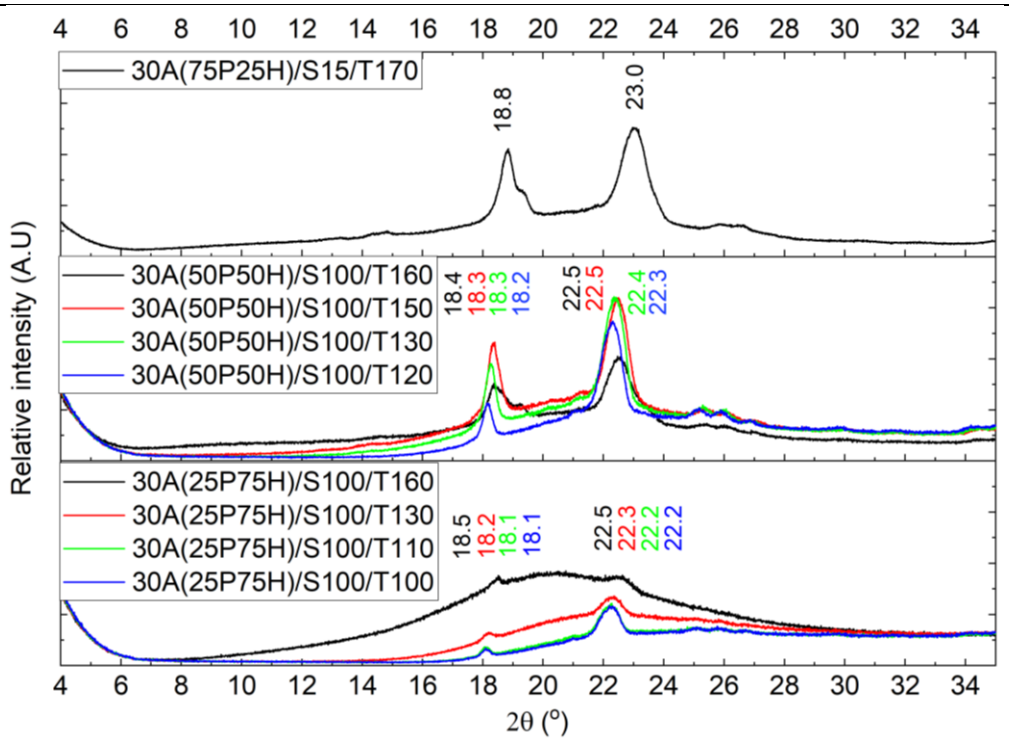

Figure 5-23. Off-line XRPD patterns of the different AZ-PEO-HPMCAS ternary formulae.

The solid state was further investigated using DSC (Figure 5-24). All DSC traces showed the absence of an AZ melting peak which agrees with the findings from low Raman frequency and XRPD. Similar to the XRPD, only peaks from the PEO were shown. The melting peak of 30AZ(75P25H)/S15/T180 was 61.4°C (71.55 J/g) only few degrees different from the 30A70P/S15/T170 melting point (63.7°C/90.1 J/g, Figure 5-7). PEO crystallinities were 66.5% and 62.8%, respectively. The presence of HPMCAS increased the PEO crystallinity slightly (3.7%).

At a lower PEO ratio i.e. 30A(50P50H), DSC curves were similar for different process temperatures. The melting peaks, melting enthalpy and PEO crystallinity were around 56°C and 43.7 J/g and 60.9%, respectively. The ranges of these values for different process temperatures were 1.2°C, 2.7 J/g and 3.72%. 30A(25P75H) showed more sensitivity to the process temperature as the enthalpy ranged from 11.9% for the filament extruded at 160°C to 55.3% for the one processed at 100°C.

The impact of the temperature on the mixing can be seen in 30A(25P75H). At a low temperature, 100°C mixing was not effective to separate and distribute PEO molecules in the matrix and PEO crystallinity was similar to crystallinity at higher PEO ratios. By

increasing the temperature to 160°C, PEO distribution was improved and crystallinity was reduced to 11.9%. Paladino et al [222] used Time-of-Flight Secondary Ion Mass Spectrometry (ToF-SIMS) and image analysis to define a rich drug region and rich polymer one in each of the paracetamol-HPMC and indomethacin-polyvinylpyrrolidone matrixes.

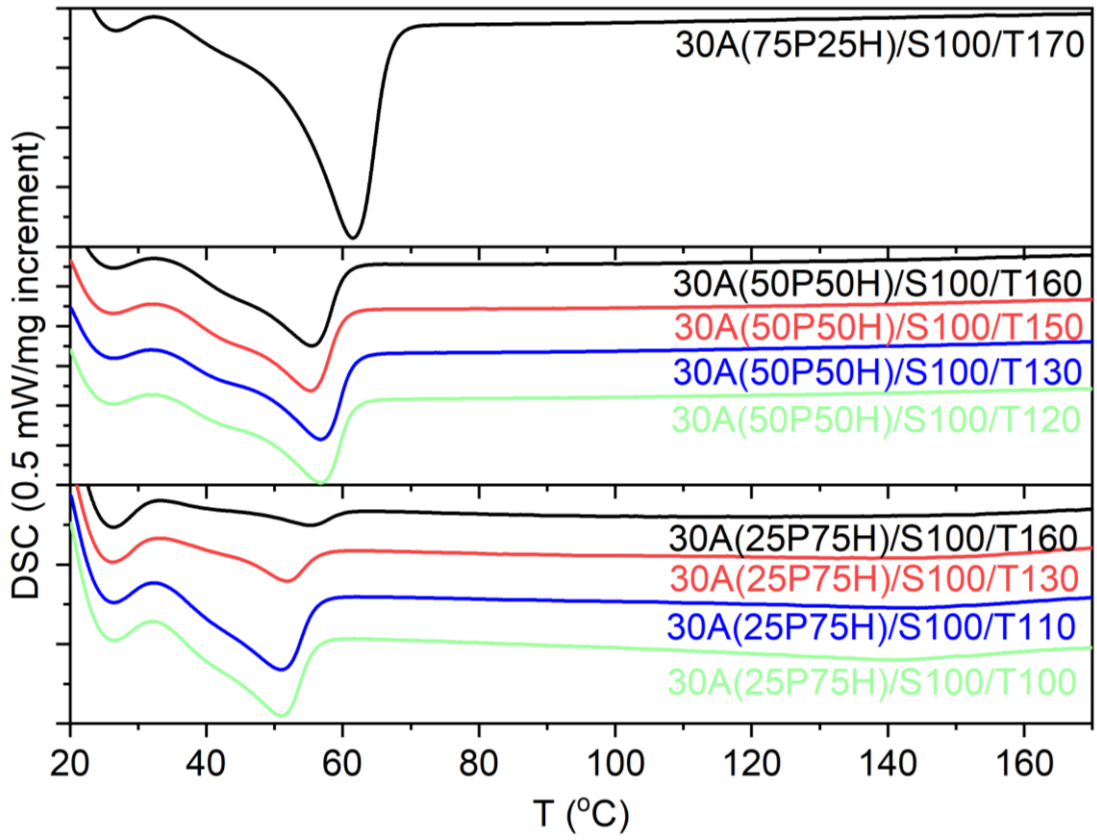

Sample	Peak (°C)	Enthalpy (J/g)	Crystalinity (% of PEO)
30A(75P25H)/S15/T170	61.4	-71.55	66.5%
30A(50P50H)/S100/T160	55.4	-42.42	59.1%
30A(50P50H)/S100/T150	55.5	-42.34	59.0%
30A(50P50H)/S100/T130	56.5	-45.01	62.7%
30A(50P50H)/S100/T120	56.6	-43.1	60.1%
30A(25P75H)/S100/T160	55.6	-4.28	11.9%
30A(25P75H)/S100/T130	52.1	-7.15	19.9%
30A(25P75H)/S100/T110	51.1	-18.85	52.5%
30A(25P75H)/S100/T100	51.1	-19.85	55.3%

Figure 5-24. DSC traces of AZ-PEO-HPMCAS based formulae during the first heating cycle.

Table 5-9 shows the processability of AZ-PEO-HPMCAS formulae at different process temperatures and screw speeds and the solid state of the produced filaments based on

inline and offline analytical techniques. Moving from 30A70P to 30A(75P25H), the process space did not improve markedly since both formulae were not extrudable at 100 rpm and possible process temperatures were still the same. Additionally, sharkskining was only observed with 30A70P to 30A(75P25H). At 30A(50P50H), a high screw speed of 100 rpm and a low process temperature down to 120°C were achieved. 30A(25P75H) showed the biggest process space with HME-extrudability at 110°C and 100°C, it was bigger than 30A70H process space (lowest process temperature of 140°C). Polymers with good processability, like the fluoropolymer family, were used to reduce sharskinning and improve process space in the HME [215].

Table 5-9. AZ-PEO-HPMCAS based formulae processability on the HME and the solid-state result at different process temperatures and screw speed:

AZ (%wt)	PEO:HPMCAS	T(°C) / rpm	180	170	160	150	140	130	120	110	100
30	100-0	100	○	○	NA	NA	NA	NA	NA	NA	NA
30	100-0	15	●	●	○	○	NA	NA	NA	NA	NA
30	75-25	100	○	○	NA	NA	NA	NA	NA	NA	NA
30	75-25	15	NA	●	○	○	NA	NA	NA	NA	NA
30	50-50	100	NA	NA	●	●	NA	●	●	NA	NA
30	25-75	100	NA	NA	●	NA	NA	●	NA	●	●
30	0-100	100	NA	NA	●	●	●	○	NA	NA	NA

● Smooth filament & ASD(Thz & XRPD)
● Pressure fail or sharkskin
NA = Not analysed (Concluded from higher or lower temperatures)

5.3.2.3. Ternary systems mechanical properties

Figures 5-25 and 5-26 show the three-point bend mechanical test results. The mixture of flexible polymer (PEO) and stiff one (HPMCAS) provided a wide range of mechanical properties. At a low PEO ratio, 30A(75P25H)/S15/T170 had the flexibility of the PEO but was stiffer due to the presence of HPMCAS.

30A(50P50H) showed small or nonsignificant differences between two consecutive process temperatures 120°C vs 130°C or 130°C vs 150°C. However, the difference became significant when comparing 120°C and 150°C. Across different process temperatures, elastic modulus ranged between 2.3 and 3.2 MPa/% and maximum stress between 32.4 to 46.3 MPa, while strain at break reached maximum strain in the test always.

Mechanical properties of 30A(25P75H) filaments were more sensitive to changes in the process temperature except between 100°C and 110°C. Filaments processed at low temperatures broke at around 25%, while those processed at higher temperatures were very ductile and reached their maximum strain value. Stiffness and maximum stress were reduced by increasing the HME process temperature. These filaments were significantly more ductile than 30A70H/S100/T140 but less stiff.

The mechanical properties of the ternary mixtures were a result of the mechanical properties of both polymers and their interactions with each other. At a high PEO ratio i.e. 30A(75P25H), PEO properties were dominant. The small difference in the mechanical properties of 30A(50P50H) was attributed to the difference in the microstructure of the PEO, which was detected on the XRPD. While 30A(25P75H) properties were assigned mainly to changes in the crystalline content of the PEO as higher crystalline content resulted in a stiffer and more brittle filament. Oladeji et al [223] used a polymer mixture of HPMCAS and 15% (wt%) PEG 600 to increase the ductility of HPMCAS for 3D printing applications.

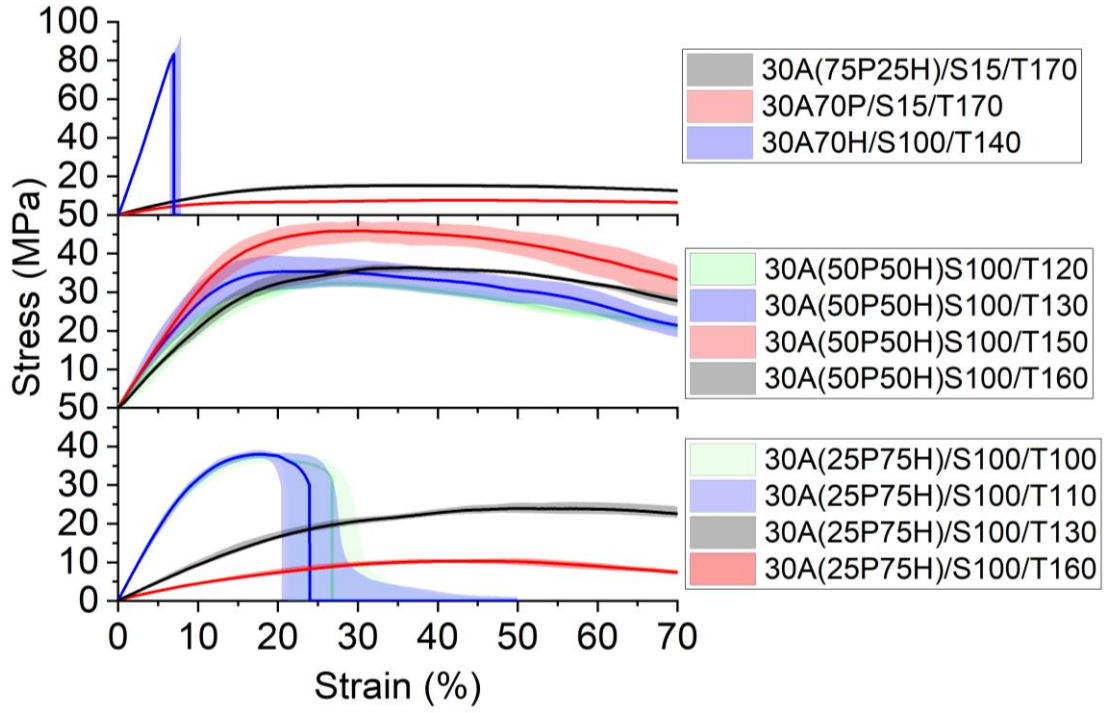

Figure 5-25. Stress-strain curve from the three-point bend test of the AZ-PEO-HPMCAS based filaments where solid lines represent the average and the shaded areas are the intervals (n=5), extracted values are shown in Figure 5-25.

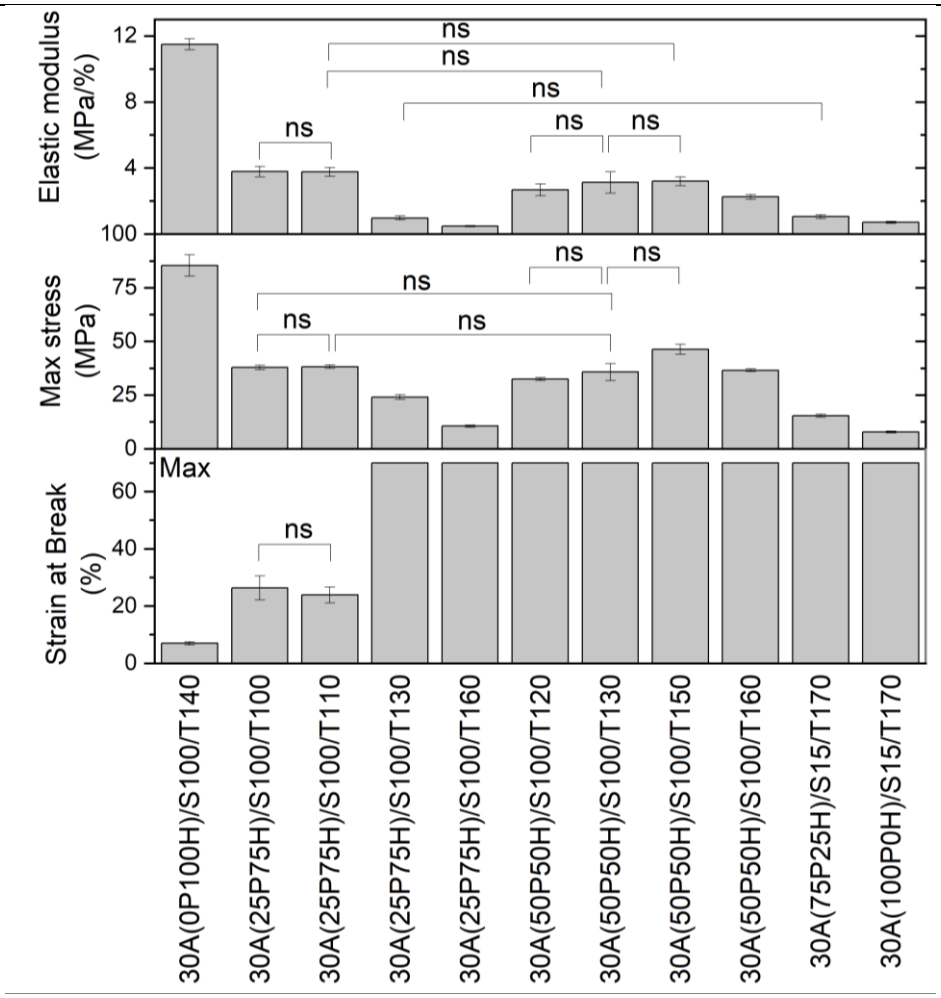

Figure 5-26. Extracted values namely elastic modulus, maximum stress and strain at break from the three-point bend test (Figure 5-24) of the AZ-PEO-HPMCAS based filaments. Values were averaged (n=5, error bar = SD), ANOVA test only non-significant difference (ns, P>0.05) added to the graph i.e. all the rest are significant.

5.3.2.4. Ternary systems optimal formula

30A(25P75H)/S100/T110 and 30A(50P50H)/S100/T150 were the best two formulae based on the mechanical test. 30A(50P50H)/S100/T150 was more ductile (higher strain at break). While 30A(25P75H)/S100/T110 was slightly stiffer (higher elastic modulus) and stronger (higher maximum stress). Because the 30A(25P75H)/S100/T110 showed lower die pressure in the HME (Figure 5-21), this filament was chosen for further investigation. The chosen formula were extruded with good diameter consistency at 1.71 ± 0.02 mm (Figure 5-27).

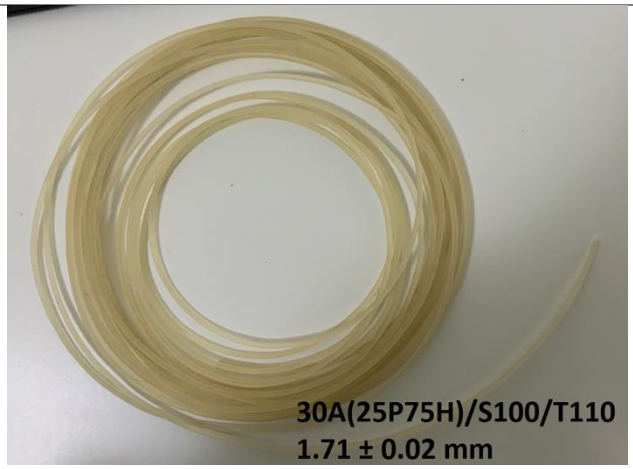

Figure 5-27. 30A(25P75H)/S100/T110 filament fresh extruded and coiled with a diameter of 1.71 ± 0.02 mm.

5.3.3. Caplets production

5.3.3.1. Printing temperature and printing test

The mass loss for the pure components was studied on the TGA (Figure 5-28). Each AZ and PEO showed mass loss of less than 0.081% at 180°C and below. HPMCAS mass loss at 170°C was -0.21%. Thus, printing at 170°C might cause degradation in the printer. At 150°C, HPMCAS was more stable with only 0.04% mass loss. Therefore, 150°C was chosen as the targeted printing temperature.

In Figure 5-28 the moisture and trapped solvent content of the HPMCAS MP grade was 2.45%. Sarode et al [224] studied the degradation of LF, MF and LF grades of HPMCAS at three temperatures 160°C, 180°C and 200°C and three screw speeds 100 rpm, 200 rpm and 300 rpm. Moisture content ranged between 1.5-1.7% depending on the grade. Although moisture content was evaluated by holding at 105°C, loss on drying (LOD) equipment was used. The different HPMCAS grade (MP) or analytical technique (TGA) in the current study might have caused the detection of higher moisture and trapped solvent content. Moreover, Sarode et al [224] found that higher temperature or screw speed increased the HPMCAS degradation and the release of free acids.

The chosen filament 30A(25P75H)/S100/T110 was tested on the 3D printer at 150°C nozzle temperature, 3 mm/s printing speed, 25°C bed temperature and using 0.8 mm nozzle (Table 5-10). The filament was successfully fed, 3DP-extruded and printed.

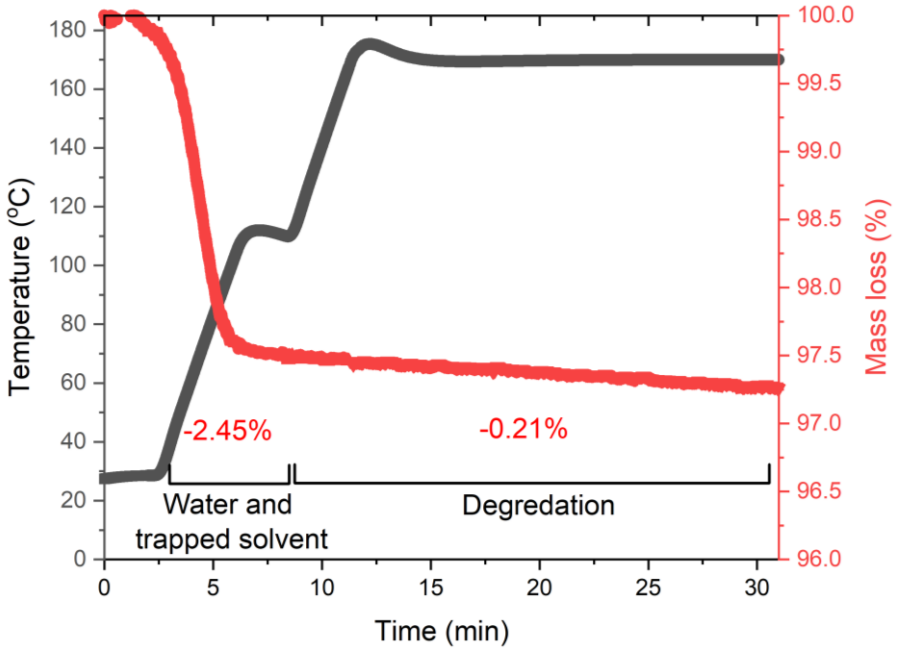

	150°C	170°C	180°C
AZ	/	/	0.01%
PEO	-0.05%	-0.06%	-0.08%
HPMCAS	-0.04%	-0.21%	/

Figure 5-28. Example of HPMCAS mass loss trace from the thermogravimetric analysis at 170°C (graph) and results for pure materials degradation.

Table 5-10. 3D-printing test for the chosen filament 30A(25P75H)/S100/T110 at 3 mm/s printing speed, 150°C nozzle temperature and using 0.8 mm nozzle:

	Feed-ability	3DP-Extrudability	Printability
30A(25P75H)/S100/T110	✓	✓ 100 mm	

5.3.3.2. Accuracy and precision evaluation

The optimum formula 30A(25P75H)/S100/T110 were tested on the 3D printer using 0.4 mm and 0.8 mm nozzle (Table 5-11). First, the slippage test was done by 3DP-extruding 100 mm of the filament without stopping. Using the 0.8 mm nozzle the flow was consistent and the 100 mm (no slippage) were all extruded without failure. Using a smaller nozzle of 0.4 mm, the 3D printer managed only to 3DP-extrude less than 25

mm. The difficulties in printing using a smaller nozzle were assigned to the increase in the required pressure to push the molten material out from the nozzle.

Although the slippage and failure were detected using a 0.4 mm nozzle, the F-caplet design was printed successfully. The caplet printed using a 0.8 mm nozzle was 669.60 mg slightly higher than the caplet printed using a 0.4 mm nozzle (666.48 mg). For the 0.4 mm nozzle, the slippage was not crucial to cause a printing failure or a massive weight difference. Moreover, the weight difference might be assigned to the higher porosity noticed by visual inspection in the 0.4 mm – caplet. Dimensional precision and accuracy were evaluated for the length, width and height (x, y and z axis, respectively). All dimensions were precise (Coefficient of variation less than 0.6%). Printing with a 0.4 mm nozzle was more accurate than a 0.8 mm nozzle, with the highest levels of inaccuracy being 2.9% and 8.9%, respectively.

The critical pressure to 3DP-extrude the molten material out of the nozzle was found to be inversely proportional to the nozzle diameter to the power of four [69]. Henry et al [186] described the relationship to be more complex and could be material sensitive. For example, the minimum printing temperature for hydroxypropyl cellulose EF grade was 160°C for 0.4 mm nozzles and 140°C for 0.6 mm and 0.8 mm nozzles. While PEO's minimal printing temperature was 80°C regardless of the nozzle size. Slippage could be evaluated in-line using a stepper motor pulse or filament encode pulse [207]. The deviation of the actual weight from the intended weight can be compensated for by increasing the caplet volume (Sadia et al [181]) or modifying the printing parameters (Henry et al [66]). The weight verification of each batch was below 0.78% (wt%) with a 95% confidence level (±2SD) and appeared to be within the acceptable limit (≤5% of the total tablet weight for tablets weighing more than 250 mg, as per the British Pharmacopoeia [225]).

Table 5-11. 3D printing of 30A(25P75H)/S100/T110 at 3 mm/s and 150°C using a 0.4 mm nozzle and a 0.8 mm nozzle:

Nozzle	**0.8 mm (n=5)**	**0.4 mm (n=4)**
Consistent flow without stopping	>100 mm	<25 mm*
Top view (F-design)		
Side view (F-design)		
Weight average (mg)	669.60 (SD = 2.5)	666.48 (SD = 2.59)
Precision, Coefficient of variation (Ideally closer to 0%)		
Width (Top-Bottom)	0.29%-0.5%	0.15%-0.54%
Length (Top-Bottom)	0.18-0.21%	0.12%-0.33%
Height	0.44%	0.24%
Accuracy (Ideally closer to 100%)		
Width (Top-Bottom)	101.8-108.5%	97.9-101.1%
Length (Top-Bottom)	99.7-103.7%	98.8-99.3%
Height	91.1%	97.1%

- Fail due to the lack of the torque from the motor not due to filament properties, 0.6 mm nozzle =50 mm.
- Precision, Coefficient of variation $= (\frac{\boldsymbol{SD}}{\boldsymbol{Ave}})/\mathbf{100}\%$
- Accuracy $= (\frac{\textbf{measurement}}{\textbf{design theoretical value}})/\mathbf{100}\%$. Accuracy describes the deviation from design.

5.3.3.3. Injection moulding equivalent caplets

Injection moulding caplets from the optimum formula (IM) were produced at 150°C (Figure 5-29-left). The IM caplet was designed on the CAD software to be 3D printed, but the Cura Slicer showed strong curvature in the structure without support (Figure 5-29-middle, in red). Since the problem in this design was structural, it was excluded from further work. Alternatively, an equivalent design with a flat bottom (IME-design) was

printed (Figure 5-29-right). The IME-caplet showed printing imperfection (elephant foot effect). Because the imperfection is from the printing process not from the design, the IME-design was used for further work.

Elephant foot is a common phenomenon in FFF-prints. R Parhi [226] assigned it to the accumulated weight of the rest layers on the first layer before solidification. A balance between bed temperature and fan speed should be achieved to reduce the phenomenon. The fan was turned off and the bed temperature was set at 25°C. Thus, most of the heat was from the nozzle especially in the first few layers where a small gap between the bed and the nozzle might cause difficulties in heating first-layer solidification. The printing was not optimised as it is beyond the scope of this work. IME-design was printed using 0.8 mm and 0.4 mm nozzles. These prints will be referred to as 3DP 0.8 mm caplets and 3DP 0.4 mm caplets, respectively.

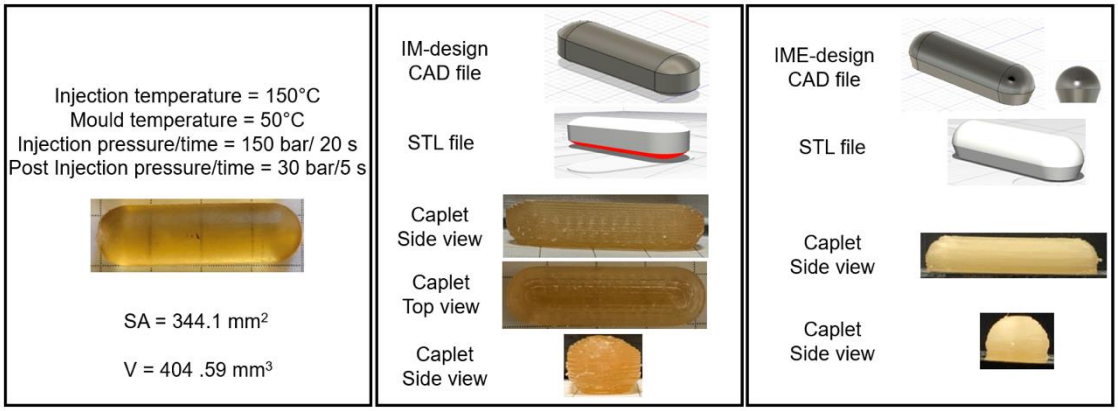

Figure 5-29. IM-caplets (IM, left) and 3D printing ones (middle and right) with the same volume and surface area. The surface area (SA) and volume (V) for all the caplets are the same.

The optical coherence tomography scans (Figures 5-30 and 5-31) show low-density areas in the IM caplet, 3DP 0.4 mm caplet and 3DP 0.8 mm caplet. In the IM caplet, only small spots appeared which might be voids or pores in the caplet generated during the injection. While 3DP 0.4 mm caplet and 3DP 0.8 mm caplet had a lot of low-density spaces generated from the lines between the printing lines. Hence, the 3DP 0.4 mm caplet was the least dense caplet. The low density can be noticed by comparing the caplets' weights (Table 5-12). 3DP 0.4 mm caplets and 3DP 0.8 mm caplets were 80% and 85% of the IM caplet, respectively. Smith et al [227] increased layer-layer overlap by increasing the nozzle diameter from 0.35 mm to 0.5 mm. It was noticed that the higher

nozzle size reduced the variation in the break force of the single wall shell. From table 5-12, the standard deviation of the 3DP 0.8 mm caplet weight was smaller than the 3DP 0.4 mm caplet one.

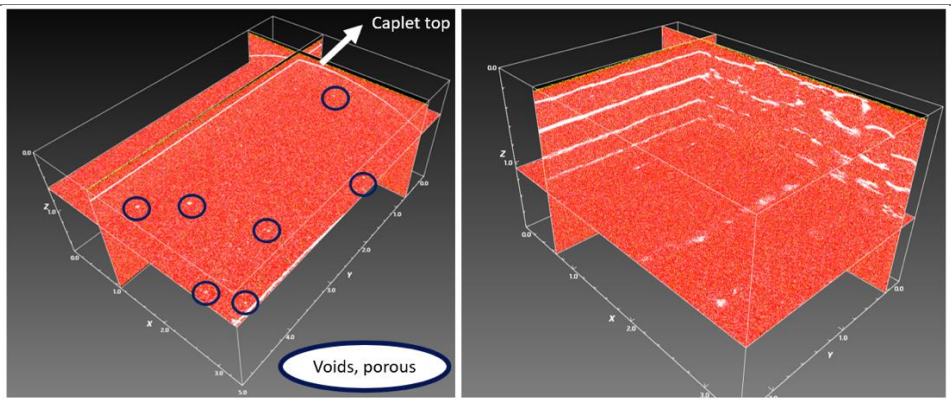

Figure 5-30. Optical coherence tomography 3D scan for IM caplet (left) and 3DP 0.4 mm caplet (right).

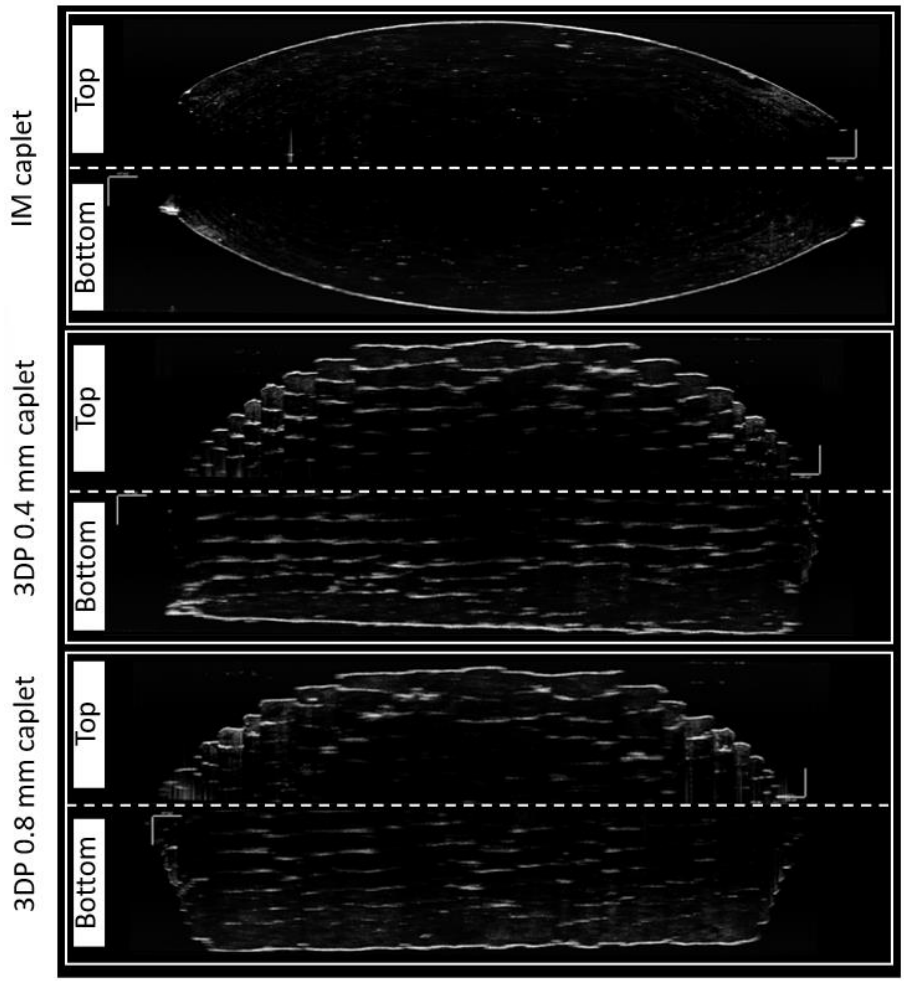

Figure 5-31. 2D optical coherence tomography scan for top and bottom for IM caplet, 3DP 0.4 mm caplet and 3DP 0.8 mm caplet.

Table 5-12. Weight of IM caplet, 3DP 0.4 mm caplet and 3DP 0.8 mm caplet:

	IM caplet (n=5)	**3DP 0.4 mm caplet (n=10)**	**3DP 0.8 mm caplet (n=10)**
Average weight (SD) in mg	513.64 (2.5)	434.21 (3.79)	413.31 (11.2)

5.3.4. Dissolution test

The 24-hour drug release curves from the IM caplet, 3DP 0.4 mm caplet and 3DP 0.8 mm caplet were plotted in Figure 5-32. The IM caplet showed the fastest release to reach a plateau after 12 hours. The 3DP 0.8 mm caplet reached it around 23 hours, while the 3DP 0.4 mm caplet did not reach the plateau at the 24-h test. The result was

surprising as the caplet with the lowest density, the 3DP 0.4 mm caplet, had the slowest release. And the densest one, the IM caplet, was the fastest. Fuenmayor et al [228] compared three tablets of a formula consisting of Kollidon VA64, PEO, Polycaprolactone and caffeine produced by injection moulding, 3D printing and direct compression. The direct compression tablet was the fastest followed by the 3D printing tablet and then the injection moulding one. Sadia et al [31] increased the drug release of a 3D printed caplet by increasing the channel opening size that went through the caplet. The bigger channel size caused a higher surface area to volume ratio, which was associated with faster drug release. The release mechanism from the Eudragit E matrix in these caplets was mainly an erosion and diffusion mechanism. However, Silke et al [229] noticed no difference between channelled and non-channelled 3D printing caplets consisting of EPO, PEO and zolpidem hemitartrate. Walsh et al [230] found that the sensitivity of channel number was different between different polymer matrixes. For example, the Affinisol matrix was less sensitive than the polyvinyl alcohol one, due to the swelling behaviour of Affinisol.

The cross-section of the IM caplet and 3DP 0.4 mm caplet took out from the dissolution test showed a yellowish core (not hydrated yet) surrounded by a whitish swollen shell (hydrated matrix). The shell assigned to the PEO, which noticed to produce a similar jelly layer at the surface of a tablet [231]. Thus, the swollen matrix limited the role of the porosities to affect drug release. The OCT scan showed a slightly denser shell (stronger red colour) in the IM caplet than the 3DP 0.4 mm caplet. This might be due to stronger penetration in the IM caplet causing the faster release.

Since the white colour of the shell could be assigned to the recrystallisation of the AZ drug. Raman spectra were collected from the shell of the caplets (Figure 5-33). All the spectra were identical and did have AZ crystal peaks. Thus, the AZ drug was considered stable in its amorphous state after dissolution.

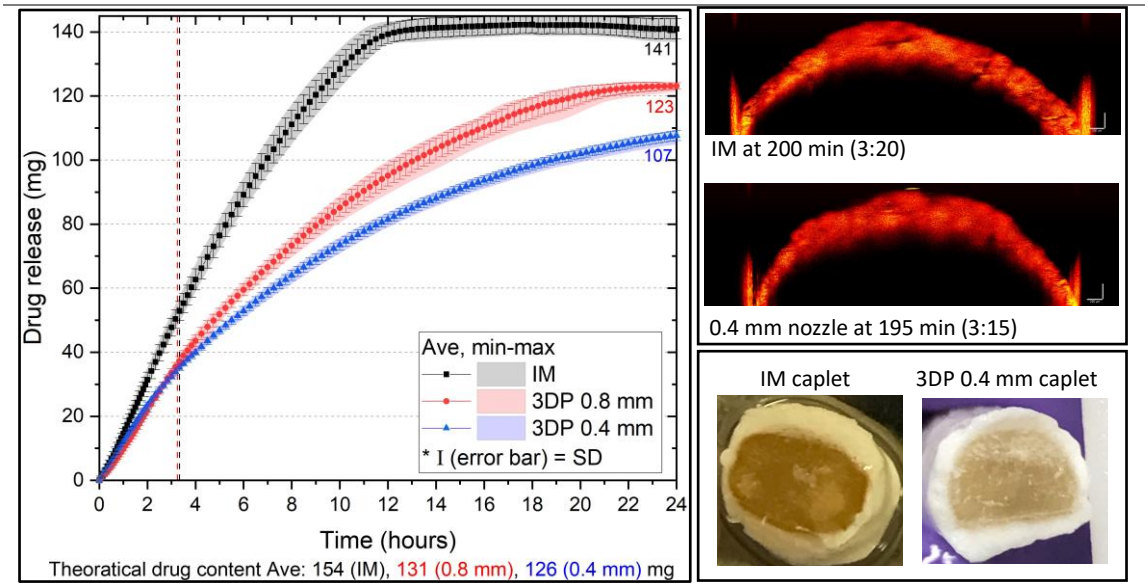

Figure 5-32. Dissolution profiles of the IM caplet, 3DP 0.4 mm caplet and 3DP 0.8 mm caplet, five repetation were averaged with error bars representing the standard deviation and the shaded area represents the range (left), optical coherence tomography scan (right top) and cross-section of IM caplet and 3DP 0.4 mm caplet after being soaked.

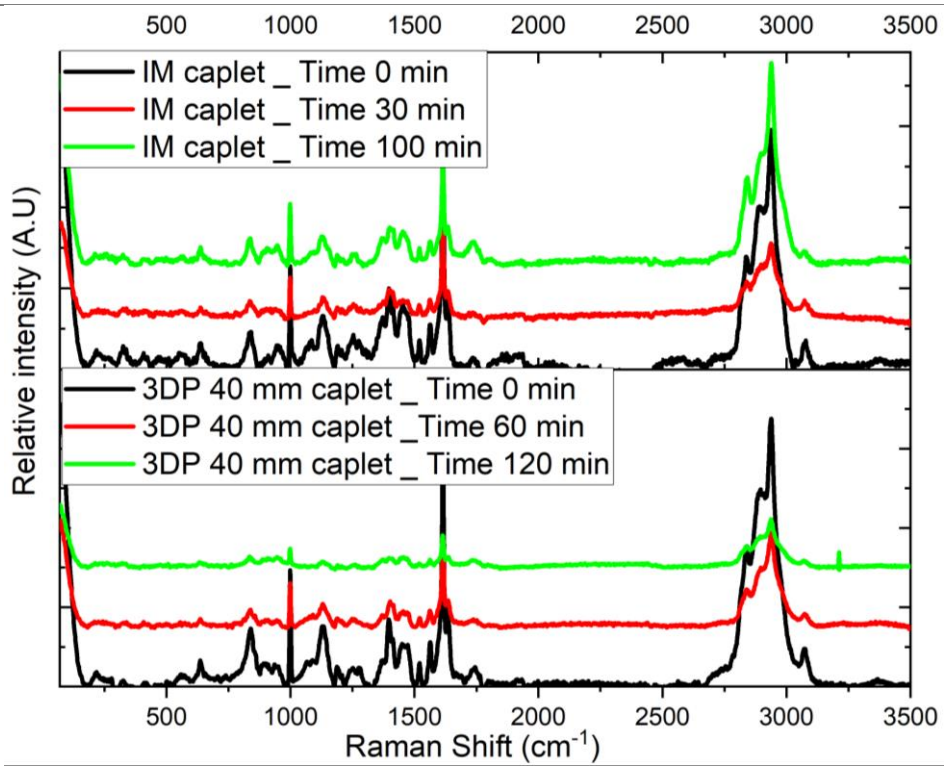

Figure 5-33. Raman spectra of the outer white surface of the IM caplet and 3DP 0.4 mm caplet after being soaked for different time.

Thus far, the unexpected order of the dissolution rate has not been fully explained. The swollen behaviour of PEO limited the effect of the porosity on the dissolution rate and theoretically, all caplets had the same SA/V (designed). The only difference noticed was in the OCT scans.

XRPD pattern was collected from both dried cut/divided caplets and soaked ones (Figure 5-34). The soaked ones showed similar patterns but different relative intensities. While the dry one did not overlap especially the peaks 18°, which was previously assigned to the PEO. To investigate this further, the caplets were tested on the DSC (Figure 5-35). The IM caplet showed the lowest PEO enthalpy (50.9 mJ). While the 3D printed caplets were 129 mJ. The higher enthalpy was assigned to the higher PEO crystalline content due to higher shear stress in the smaller nozzles (IM nozzle > 0.8 mm nozzle > 0.4 mm nozzle). The shear stress during extrusion macromolecular arrangement increases the crystallinity [135]. Therefore, the IM caplet had a more amorphous nature which might have required less energy to dissolve and as a result a faster dissolution rate [72]. This agrees with the OCT image.

Between 3DP 0.4 mm caplet and 3DP 0.8 mm caplet, the difference between their traces was small. In the 3DP 0.4 mm caplet trace, there was a broad peak from 20°C to 100°C. These microstructural differences might have caused the small change in the dissolution rate (in the first 3 hours the lines overlapped).

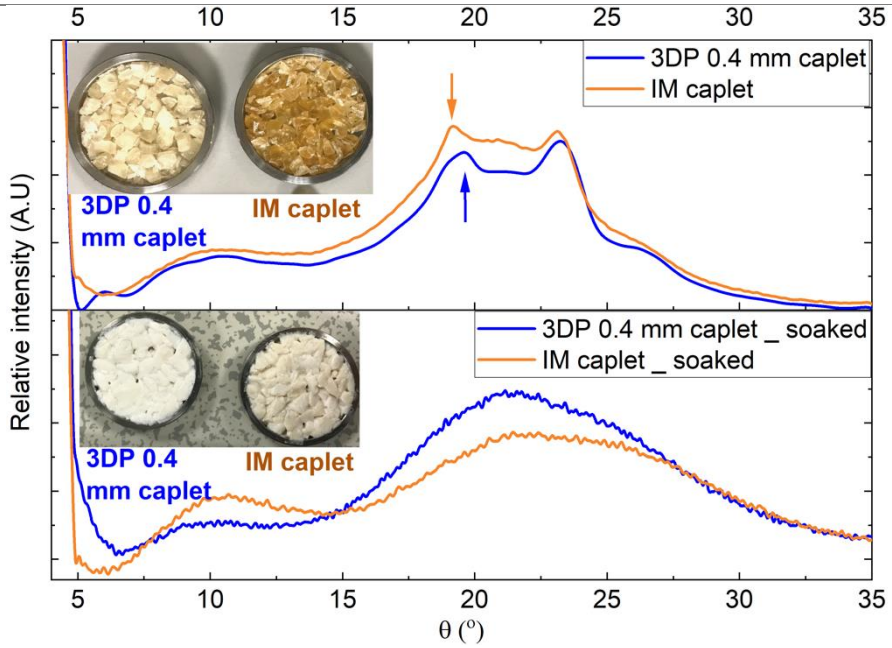

Figure 5-34. X-ray diffraction patterns of the IM caplet and 3DP 0.4 mm caplet crushed and dry (top) and after being soaked (bottom).

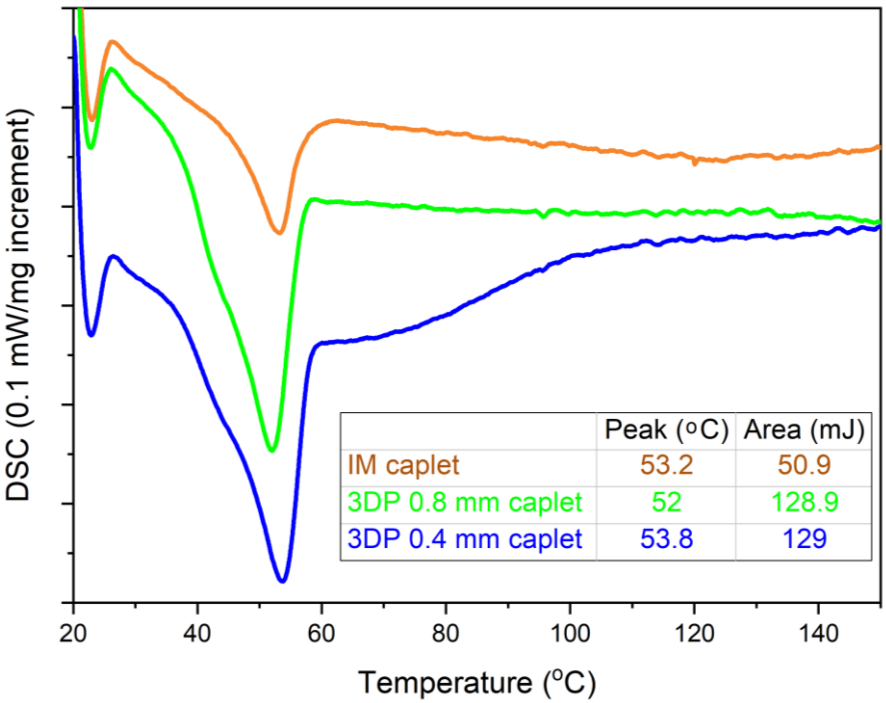

Figure 5-35. DSC traces of the IM caplet, 3DP 0.4 mm caplet and 3DP 0.8 mm caplet.

Although the DSC results explained most of the difference in dissolution rates, the impact of the actual SA / V (not the theoretical or designed) ratio could not be ruled out.

SA and V can be measured using X-Ray micro-/nano-CT [93], liquid displacement [232] paraffin wax coating [233] and 3D scanning. At the point of the study, these techniques were not accessible, expensive or required verification. Thus, the problem was circumvented by printing a simpler shape with easy to measure SA and V (C-design, Figure 5-2).

Figure 5-36 shows two dissolution profiles of cylinder-like tablets printed using 0.4 mm and 0.8 mm nozzle diameters. The dissolution rate of the one printed at 0.4 mm was slower although the SA/V difference was very small 0.003 mm^{-1}. Therefore, the difference in the dissolution rate was assigned to the microstructural difference and not to the SA/V ratios.

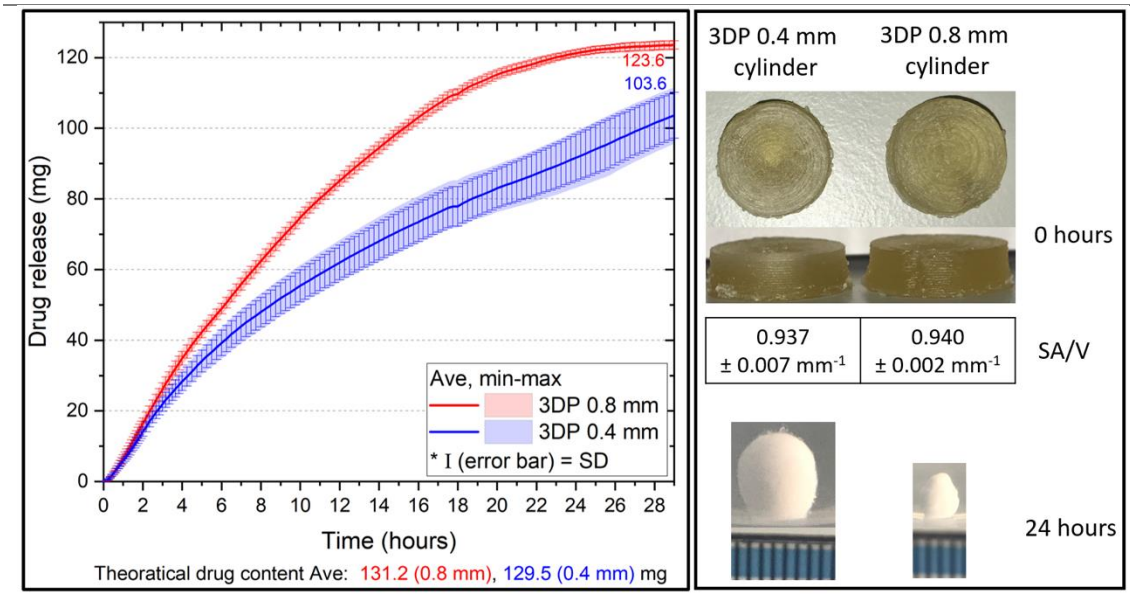

Figure 5-36. Dissolution profiles of cylinder shape tablets printed using 0.4 mm nozzle diameter (blue) and 0.8 mm nozzle diameter (red). Lines averaged from three repetitions.

5.3.5. Filament stability

After a month of the HME experiment, a change in the filament feedability in the 3D printer was noticed (Table 5-13). The filament was breaking inside the feeding tube. Thus, a new physical mixture was prepared and extruded (fresh filament, on 30/11/2021) to be compared with the old one (old filament, extruded on 24/10/2021).

Table 5-13. Feedability of an old and fresh filament:

	HME-extruding date	Feedability
Old filament	24/10/2021 (36 days old)	No
Fresh filament	30/11/2021 (fresh)	Yes

The filaments were stored in sealed high-density polyethylene bags. When the old filament bag was opened, a strong acidic odour was noticed. As a result, the mass residuals of moisture and trapped solvents were investigated using the moisture analyser. Filaments were cut into small pieces (pellets) and cryo-milled then analysed (Table 5-14). The sum of pure material mass loss multiplied by their ratio was 1.91% (%wt), which was close to the mass loss of the physical mixture (1.94% and 1.81% for old and fresh physical mixtures, respectively). The uncertainty amount for the moisture analyser was up to 0.3% for 200 mg of sample [234]. Pellets of old filament and fresh one showed also close values (1.26% and 1.46%, respectively). Since the surface area might affect the measurement, the samples were cryo-milled and then analysed. However, both samples had the same mass loss (2.46%). The cryo-milled samples showed higher mass loss than the physical mixture. This was assigned to the release of succinic acid and acetic acid from the HPMCAS during the HME process or moisture uptake during the cryo-milling process. The acid release from pure HPMCAS at 130°C and 400 rpm was 0.638% [219].

Table 5-14. Mass loss of the pure components, pelletised filament and cryo-milled filament:

Material		**Weight (g)**	**Mass loss (%wt)**	**Time (min:sec)**
HPMCAS	Powder	1.5	3.07%	02:24
PEO	Powder	1.5	0.80%	03:12
AZ drug	Powder	1.5	0.53%	02:24
Old physical mixture	Powder	1.5	1.94%	02:24
Old filament	Pellets	1.5	1.26%	04:00
Old filament	Powder *	1.5	2.46%	03:12
Fresh physical mixture	Powder	1.5	1.81%	02:24
Fresh filament	Pellets	1.5	1.46%	04:48

Fresh filament	Powder *	1.5	2.46%	03:12

*Produced using cryo-milling.

Although the moisture analyser did not explain the change during filament ageing, it was noticed that old filament pellets after cooling down to room temperature (25°C) gained back some flexibility. Thus, old and fresh filaments were heated in the oven at 40°C for 15 min and then tested on the texture analyser (Figure 5-37). The old filament was brittle and broke easily, but after heating its stiffness reduced and its ductility increased. The new filament was already ductile, thus relatively smaller change after heating was noticed for example both maximum stress and stiffness were reduced. The fresh filament was more transparent than the old one, and the heated ones were more transparent than the original ones.

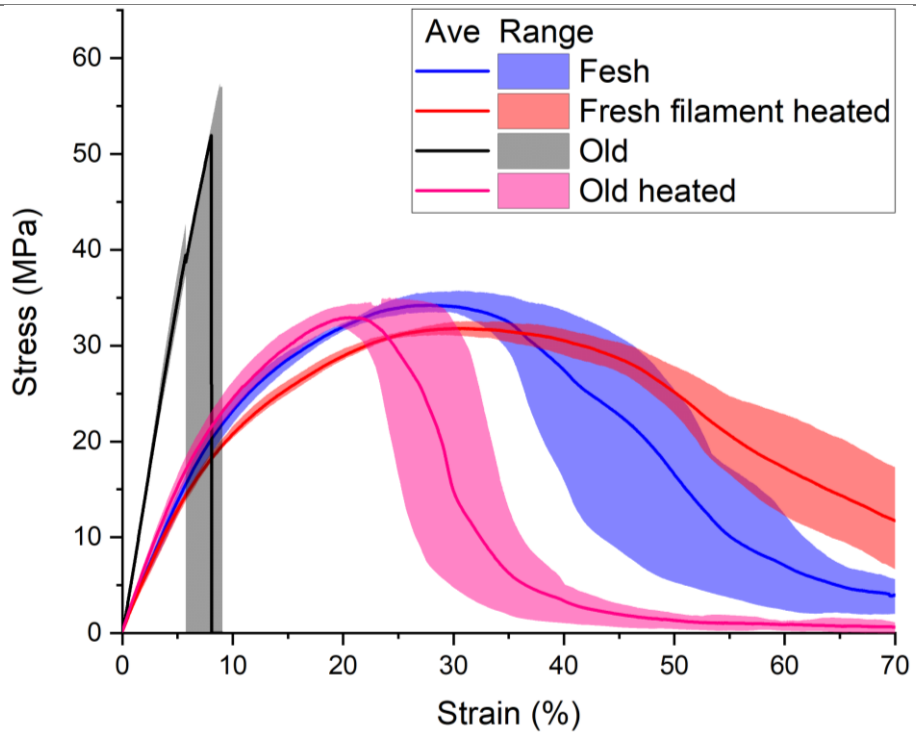

Figure 5-37. Mechanical properties from three-point bend test of old and fresh filaments and heated ones (n= 5, line reresponts the average and shaded area the range).

X-ray diffraction patterns (Figure 5-38) were collected to investigate the changes caused by ageing and heating. The x-ray pattern showed some differences in the PEO peak between old and fresh filaments and between heated and unheated ones. Therefore, the

change in the mechanical properties could be assigned to the sensitivity of PEO crystallinity to thermal treatment. Zhu et al [216] showed different x-ray patterns of PEG when it was crystallised out at 25°C and 40°C.

Filaments were also analysed on the DSC (Figure 5-39). Unheated filaments showed a thermal peak at about 40°C which overlapped with the melting peak. This event was absent in the heated filaments. Because the separation of both peaks was not possible, the enthalpies of both peaks were compared. Because of heating, the enthalpy dropped from 156.5 mJ to 122 mJ for old filament and from 108.2 mJ to 106.2 mJ for fresh filament. Moreover, the old filament's enthalpy was higher than the fresh one. This agrees with the finding from the XRPD, the change in the mechanical properties was due to the sensitivity of PEO crystallinity.

These findings in the current study were in agreement with the literature. Briatico-Vangosa et al [221] produced an injection moulding capsule shell using HPMCAS and various concentrations and molecular weights of PEG as a plasticizer. A change in the appearance was visually inspected after storing the shells at two temperatures; room temperature (referred to as either 20°C or 25°C) and 40°C. The shells stored at room temperature were the first to change from transparent to translucent. The change in appearance was assigned to the PEG, as the ageing started from the external layer of the shell while the core was transparent. The DSC of the outer layer showed a melting peak of PEG while the peak was absent in each of the fresh shells and the core. In the current study, low-frequency Raman was used to detecting the change on the outer layer of the AZ-PEO extrudates.

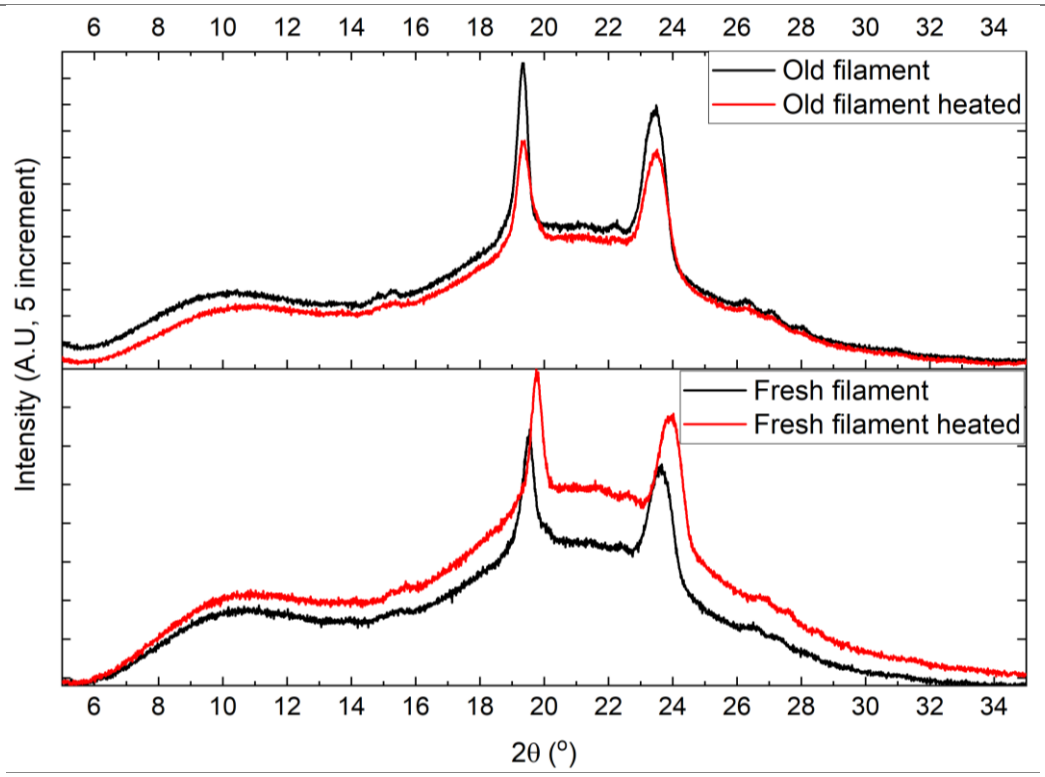

Figure 5-38. X-ray diffraction patterns of old and fresh filaments and heated ones.

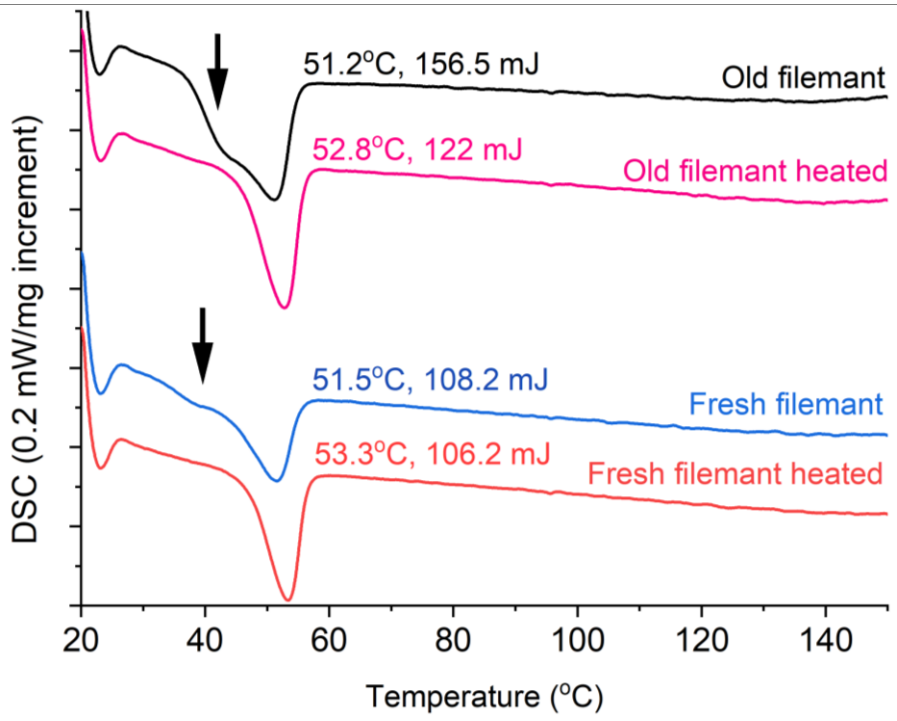

Figure 5-39. DSC traces of old and fresh filaments and heated ones.

5.4. Conclusion

Poor powder flowability of AZ-PEO formulae was caused by the drug and can be overcome by using spiral screws instead of concave ones and/or reducing the feeding rate (to 0.05 kg/hr). Moreover, the PEO-based formulae were challenging in the HME process due to the sharkskinning effect because of the linear polymer, and it was associated with high die pressure. To make the filament suitable for 3D printing, both the amplitude and the length of the wave-like (sharkskin) were evaluated and found to be reduced by reducing HME screw speed (to 15 rpm) and increasing process temperature (to 180°C). After extruding the AZ-PEO formulae, rubber-like properties were observed especially at high drug load, this phenomenon was caused by the amorphous region of PEO i.e. change according to the PEO crystallinity content. Therefore, it was sensitive to the drug content, extrusion parameters and thermal history and ageing. Regardless of drug content the drug became amorphous and stayed during the study (according to DSC, XRPD and inline low-frequency Raman), although the AZ solubility in the PEO was only 24.9% (wt). All AZ-PEO filaments showed poor 3DP-extrudability value (E/η ratio) due to formulae' low stiffness. Only 30A70P/S15/T180 was printable at 180C nozzle temperature and very slow printing speed (0.25 mm/s). However, the printing process was not successful because of poor solidification of the PEO and lack of structural support.

AZ-HPMCAS formulae were less problematic in the HME and were extrudable at a screw speed of 100 rpm ad low process temperature (down to 130°C). Although all produced extrudates were amorphous solid dispersion (according to the DSC, XRPD and the low-frequency Raman), it was unclear the amount of AZ dissolved in the HPMCAS matrix. Despite the good 3DP-extrudability of all AZ-HPMCAS based formulae, they were very brittle and were not feedable into the printer.

Since the properties of AZ-HPMCAS formulae (good 3DP extrudability but poor feed ability) and AZ-PEO formulae (good feed ability but poor 3DP extrudability) were complementary, mixtures of both were promising. A wide range of mechanical properties was obtained from the mix, which was governed by the ratio of each polymer and the amount of crystallinity of the PEO. At low PEO content, the HME process temperature affected the PEO mixing in the formula and as a result its mechanical properties. 30A(25P75H)/S100/T110 were a printable filament at 150°C and achieved a good coefficient of variation (precision) below 0.6% and high accuracy above 91%. The optimum formula was used to produce three types of caplets with the same surface area

to volume ratio: injection moulding caplets, 3D printed caplets using 0.4 mm nozzle and 3D printed caplets using 0.8 mm nozzle. Although the porosity in the caplets was the highest in the 0.4 mm caplets then 0.8 mm caplets then injection moulding caplets, the dissolution rate followed the opposite order (i.e. fastest dissolution rate was for the injection moulding caplet). The swelling behaviour of the PEO limited the impact of the porous in increasing the dissolution rate. Moreover, the higher rate of PEO crystallinity in the 3D printing caplets induced by the shear rate in the 3D printing process hindered the dissolution rate. The optimum formula was found to be unstable and exhibited crystallisation of PEO causing an increase in the brittleness and problem in the 3D printing feedability.

Chapter 6: Conclusions, Challenges and Future Work

The current research studied different drug-polymer combinations for producing FFF-3D printing filament for pharmaceutical applications. The study focused on the bottleneck in the formulation process namely obtaining the correct mechanical and rheological properties for a printable filament. It provides understanding of the material requirement for successful print by studying 'bad' and 'good' filaments on various analytical techniques including (for molecular interactions) HSPs, Raman spectroscopy, (for physical state) DSC, XRPD, Raman low frequency, (for mechanical and flow behaviour) texture analyser, rotary rheometer, (for stability) TGA, (for behaviour), dissolution tests. Both single polymer and polymer mixture approaches were discussed and explored to address the challenges in both and understand their formulation space. Printer limitations are addressed and linked with filament attributes. This work aims to keep the formula as simple as possible. Thus, this chapter will follow the same pattern starting from the simplest system to the most complex one.

6.1. Thesis achievements:

6.1.1. Essential ingredients (drug and carrier):

Three binary systems were studied MFA-EPO, AZ-HPMCAS and AZ-PEO at different drug loads and process temperatures. All these systems were not printable due to poor flexibility for EPO and HPMCAS based formulae and poor stiffness for PEO based formulae. The plasticizing effect of the drug did not help to reduce the brittleness of EPO not HPMCAS. While the main increase in the PEO ductility was due to the reduction of PEO crystallinity content with the presence of the drug.

Understanding the phase diagram using XRPD, DSC, and spectroscopic techniques was helpful to study the physical state of the filaments and link that with the material behaviour. However, each of the techniques showed limitations. For example, the spectroscopic technique showed issue in penetrating the sample providing limited information about the bulk of the material. DSC failed to provide an interpretable graph for MFA-EPO due to the complexity of the system's thermal events above 160°C. Also, it was not useful for AZ-HPMCAS system as the melting of the drug was below the liquefication of the polymer. XRPD penetrated well in the samples, but the detection limit was low. The physical state of the system affected the filament property in terms of mechanical properties as discussed earlier, fraction progression and dissolution rate.

For example, crystalline solid dispersions showed a lower dissolution rate and stronger fraction progression than amorphous solid dispersions.

Although developing a printable filament is a very challenging task two printable filaments were developed using two methods single polymer approach starting from MFA-EPO system and a polymer mixture approach starting from AZ-HPMCAS and AZ-PEO systems.

6.1.2. Single polymer approach:

As the drug-polymer (MFA-EPO) was brittle increasing ductility using a plasticizer was considered. PEG4h, PEG4k, TWN, StA and TEC were tested. Although all of them except PEG4k were good plasticizers for EPO, TWN and TEC showed a reduction in the MFA solubility in EPO. It is found that plasticizer is preferable to locate between the drug and the polymer in HSPs' Teas plot. Then, the experimental approach confirmed the finding where Tg reduction due to the plasticization effect is higher for MFA-EPO-TEC and MFA-EPO-TWN than their associated binary systems (i.e. less plasticization effect). While StA and PEG ternary systems showed lower Tgs (check the next section for further work). The best ternary formula was found to be MFA-StA-EPO system which was not printable due to the low tolerance of the gears pressure. This ductile formula was toughened by adding fillers like talc, silica and silk powder. Silica showed the most increase in the mechanical properties hence chosen for DoE to optimise the ratio.

DoE of two levels three full factorial design is used to define the 3D printer limit and choose the best formula. Both silica and MFA increase the elastic modulus and reduce the strain at break value. MFA and StA reduced η, G' and G" while Silica increased them. For 3D printing increasing in the mechanical properties and reducing rheological properties are preferable in general. Hence, the prediction aimed to find a balance between the ratios and find a printable formula. The optimum printable filament consists of 5.1% StA and 13.2% MFA (wt% of EPO) and 14.5% silica (of the total weight).

6.1.3. Polymer blend approach:

PEO-based formula and HPMCAS based formula showed complementary properties, where HPMCAS improves filament stiffness, and the PEO improves filament ductility.

Different ratios of polymer combinations were explored and a wide range of mechanical properties was obtained. The polymer blend properties were not proportional to each polymer ratio. This was due to the difficulty of two big molecules mixing. A higher temperature increases mixing efficacy and reduces PEO crystallinity content making a ductile filament. From different ratios and process temperatures 30A(25P75H)/S100/T110 was found to be the best formula and was printable successfully. The caplet batches produced using this filament achieve high precision (variation < 0.6%) and accuracy (>91%).

IM moulding and a 3D printer with 0.4 mm and 0.8 mm nozzles were used to produce caplets. The porosity of the caplets was as expected from lower to higher, IM-caplet > 0.8 mm caplet > 0.4 mm caplet. However, the dissolution followed the opposite order, which was found to be related to the lower PEO crystallinity content. A smaller nozzle causes higher shear stress and as a result higher PEO crystallinity. Although the porosity is expected to affect the dissolution in this case, the swelling behaviour of the PEO changed the caplet morphology and reduced the impact of the porosity.

6.2 Beyond findings and future work:

6.2.1. Polymer screening:

Although the focus in pharmaceutical application is the drug, the 3D printing formulation depends mainly on polymer properties including the mechanical and rheological ones as they give the filament the plastic behaviour, which are crucial for successful print. Moreover, polymer is usually the highest weight ratio (dominant) ingredient. For example, EPO and HPMCAS are brittle polymers and PEO (fresh extruded) is flexible. Thus, it is easier to start with polymers that already has good mechanical (high mechanical values) and rheological (relatively low viscosity) properties.

Loading small molecules that dissolve in the polymer matrix like drugs might alter the mechanical properties but not necessarily. In both MFA with EPO and AZ with HPMCAS, the dominant behaviour was still attributed to the polymer. However, improve in ductility (the mechanical properties) observed when the additional material changes the interaction between molecules of the matrix. When the additional molecules interact with the polymer chains by strong bonds on more than one point, they will work as lock and reduce the freedom of the polymer to move inside the matrix

similar to the MFA-EPO system (Figure 6-1-first stage). This means a reduction plastic deformation and increase in the elastic modulus. While if the additional molecule has a weak interaction on one side it would increase the molecular movement increasing ductility and reducing elastic modulus similar to StA-EPO example. It is worth to note that in PEO-AZ system, the AZ reduced the crystallinity of the PEO causing reduction in the polymer-polymer interaction and increases the ductility.

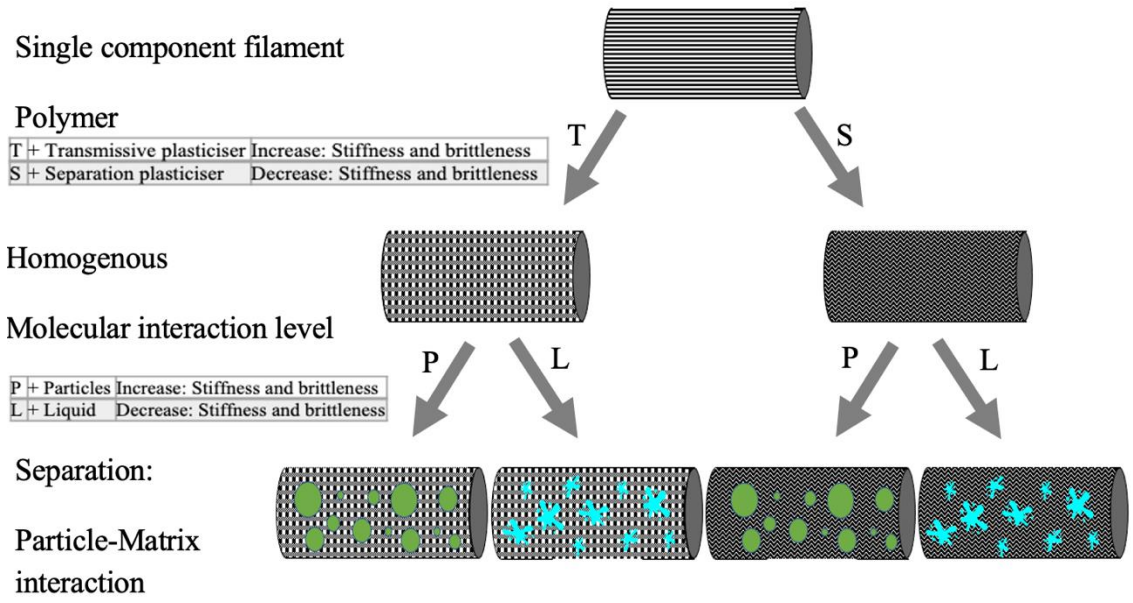

Figure 6-1. Formulation diagram starting from single polymer and the potential outcomes with additive interaction on molecular level (first stage) and on particle-matrix level (second stage).

Understanding the molecular interaction might help us to speed up the formulation development process during the screening study. We could choose flexible polymer that becomes stiffer with drug addition or brittle polymer that becomes flexible with drug addition. Computational chemistry like molecular dynamic might provide a prediction tool for choosing the appropriate polymer and reduce time and material waste. Mechanical properties were already explored for different polymer systems using molecular dynamic [235]. Figure 6.2 illustrate potential hypothesis for investigation where the left graph represent a physical interaction between two masses. At the lowest potential energy, the system is in the most stable distance. It can be argued that the stronger the interaction i.e. lower potential energy cause stiffer material (higher elastic modulus) as it will resist the big energy change. Moreover, it could be that the wider potential energy well the more forgiving moving between different distances. This

might be associated with ductile behaviour of the material. The first part of the hypothesis is mentioned in previous reviews [236], it is important to investigate the impact of these interaction differences on the filament printability as this oversimplified explanation does not take into account finding new stable position and complex interactions from multiple molecules and atoms.

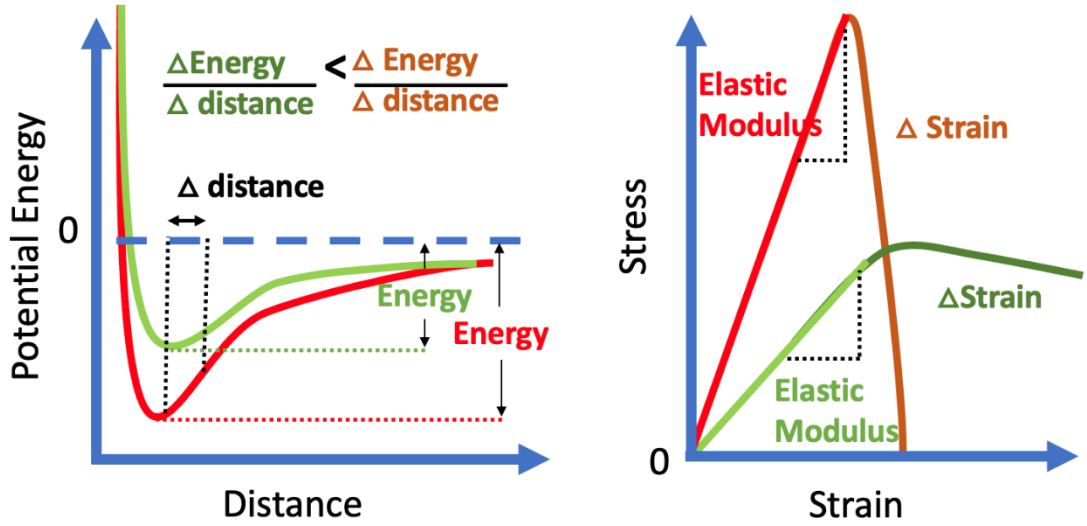

Figure 6-2. Hypothesis and future work to relate molecular interactions with mechanical properties and printability.

6.2.2. Plasticizer screening:

The HSPs was useful tool to predict a suitable plasticizer. However, a clear numerical correlation between Tgs and plasticizer properties were not fully explored. A bigger set of experiment using three drugs (one with high polar force, one with high hydrogen bonding and one with high dispersion force) and collection of plasticizers can be used to find a potential correlation between HSPs values, molecular volume and Tgs (and potentially mechanical properties). The hypothesis here is "Is there a specific type of interaction or combination of molecular volume and HSPs distances associated with strong reduction of Tg or mechanical property values? Moreover, is there a limit or numerical indication to choose the plasticizer?"

6.2.3. Define printer limitation and filament quality attributes:

DoE showed that E/η, maximum stress from 3-point bend test, strain at break from tensile strength test and Tg and Tan(δ) from the rheometer tests are important parameters to evaluate filament printability. These values are associated with 3D printing sub-processes and linked with printer specifications and parameters like the length of the liquefier and the shape, pressure of the gears, the steepest curvature in the filament path, printing temperature and printing speed (Figure 6-3). These specifications and parameters are not fully understood yet. Finding the correlation between the filament property and these specification and parameters could help us to evaluate how a 3D printing filament behave at different printers and set standard for the 3D printing manufacturer to ensure reproducibility in pharmaceutical manufacturing. Researchers should detail their printer specifications to reduce subjective evaluation.

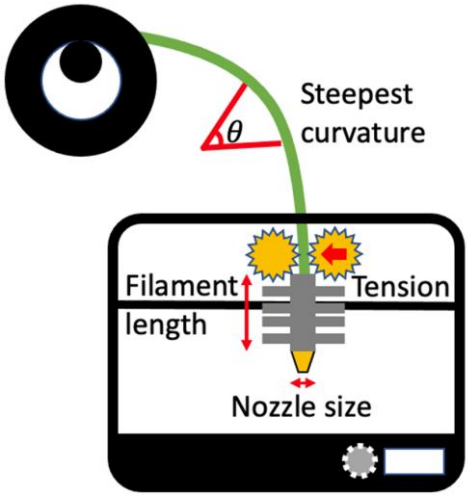

Figure 6-3. Schematic of some of the printer specification that affect variation in the filament performance between different printers.

Reference

[1] D. Zhou, W. R. Porter, and G. G. Z. Zhang, “Drug stability and degradation studies,” in *Developing Solid Oral Dosage Forms: Pharmaceutical Theory and Practice: Second Edition*, 2017. doi: 10.1016/B978-0-12-802447-8.00005-4.

[2] George A. Bender and Robert A. Thom, *Great Moments in Pharmacy: The Stories and Paintings in the Series, A History of Pharmacy in Pictures*. Northwood Institute Press, 1966.

[3] Olutayo A. Adeleye, Mbang N. Femi-Oyewo, and Michael A. Odeniyi, “Effect of compression pressure on mechanical and release properties of tramadol matrix tablets ,” *Curr. Issues Pharm. Med. Sci*, vol. 28, no. 2, pp. 120–125, 2015, doi: 10.1515/cipms-2015-0057.

[4] F. Malerba and L. Orsenigo, “The evolution of the pharmaceutical industry,” *https://doi.org/10.1080/00076791.2014.975119*, vol. 57, no. 5, pp. 664–687, Jul. 2015, doi: 10.1080/00076791.2014.975119.

[5] G. B. Hatton, C. M. Madla, S. C. Rabbie, and A. W. Basit, “All disease begins in the gut: Influence of gastrointestinal disorders and surgery on oral drug performance,” *Int. J. Pharm.*, vol. 548, no. 1, pp. 408–422, Sep. 2018, doi: 10.1016/J.IJPHARM.2018.06.054.

[6] NHS England, “Improving Outcomes Through Personalised,” 2016.

[7] J. Breitkreutz and J. Boos, “Paediatric and geriatric drug delivery,” *http://dx.doi.org/10.1517/17425247.4.1.37*, vol. 4, no. 1, pp. 37–45, Jan. 2006, doi: 10.1517/17425247.4.1.37.

[8] A. C. Freire, A. W. Basit, R. Choudhary, C. W. Piong, and H. A. Merchant, “Does sex matter? The influence of gender on gastrointestinal physiology and drug delivery,” *Int. J. Pharm.*, vol. 415, no. 1–2, pp. 15–28, Aug. 2011, doi: 10.1016/J.IJPHARM.2011.04.069.

[9] H. A. Merchant, F. Liu, M. Orlu Gul, and A. W. Basit, “Age-mediated changes in the gastrointestinal tract,” *Int. J. Pharm.*, vol. 512, no. 2, pp. 382–395, Oct. 2016, doi: 10.1016/J.IJPHARM.2016.04.024.

[10] Margaret A. Hamburg, “Paving the Way for Personalized Medicine: FDA’s Role

in a New Era of Medical Product Development," Oct. 2013.

[11] K. Alexander, "Dosage Forms and Their Routes of Administration," *Pharmacology*, pp. 9–29, Jan. 2009, doi: 10.1016/B978-0-12-369521-5.00002-6.

[12] Y. Kawabata, K. Wada, M. Nakatani, S. Yamada, and S. Onoue, "Formulation design for poorly water-soluble drugs based on biopharmaceutics classification system: Basic approaches and practical applications," Nov. 2011, *Elsevier B.V.* doi: 10.1016/j.ijpharm.2011.08.032.

[13] Y. Gao, C. Gesenberg, and W. Zheng, "Oral Formulations for Preclinical Studies: Principle, Design, and Development Considerations," *Dev. Solid Oral Dos. Forms Pharm. Theory Pract. Second Ed.*, pp. 455–495, Jan. 2017, doi: 10.1016/B978-0-12-802447-8.00017-0.

[14] M. Gupta and R. Brijesh, "A Review on: Sustained Release Technology," *Int. J. Ther. Appl.*, vol. 8, pp. 18–23, 2012.

[15] R. Talukder and R. Fassihi, "Gastroretentive Delivery Systems: A Mini Review," *http://dx.doi.org/10.1081/DDC-200040239*, vol. 30, no. 10, pp. 1019–1028, 2004, doi: 10.1081/DDC-200040239.

[16] A. Goyanes, P. Robles Martinez, and A. W. Basit, "Effect of geometry on drug release from 3D printed tablets," *Int. J. Pharm.*, vol. 494, no. 2, pp. 657–663, Oct. 2015, doi: 10.1016/J.IJPHARM.2015.04.069.

[17] L. Zema, A. Melocchi, A. Maroni, and A. Gazzaniga, "Three-Dimensional Printing of Medicinal Products and the Challenge of Personalized Therapy," *J. Pharm. Sci.*, vol. 106, no. 7, pp. 1697–1705, Jul. 2017, doi: 10.1016/J.XPHS.2017.03.021.

[18] F. Fina *et al.*, "3D printing of drug-loaded gyroid lattices using selective laser sintering," *Int. J. Pharm.*, vol. 547, no. 1–2, pp. 44–52, Aug. 2018, doi: 10.1016/J.IJPHARM.2018.05.044.

[19] M. A. Alhnan, T. C. Okwuosa, M. Sadia, K.-W. Wan, W. Ahmed, and B. Arafat, "Emergence of 3D Printed Dosage Forms: Opportunities and Challenges," *Pharm. Res.*, vol. 33, no. 8, pp. 1817–1832, Aug. 2016, doi: 10.1007/s11095-016-1933-1.

[20] S. J. Trenfield *et al.*, “The Shape of Things to Come: Emerging Applications of 3D Printing in Healthcare,” *AAPS Adv. Pharm. Sci. Ser.*, vol. 31, pp. 1–19, 2018, doi: 10.1007/978-3-319-90755-0_1.

[21] Joint Formulary Committee UK, *British National Formulary (BNF) 81*, vol. 81. Pharmaceutical Press, 2021.

[22] M. Y. Munar and H. Singh, “Drug Dosing Adjustments in Patients with Chronic Kidney Disease,” *Am. Fam. Physician*, vol. 89, no. 3, pp. 649–687, 2007, doi: 10.1016/j.mcna.2004.11.007.

[23] L. P. Párraga, I. Martínez-López, P. V. Bosch, F. P. Latorre, and O. D. Sánchez, “Drug dosage recommendations in patients with chronic liver disease,” *Rev. Española Enfermedades Dig.*, vol. 104, no. 4, pp. 165–184, 2012, doi: 10.4321/S1130-01082012000400002.

[24] P. R. Martinez, A. Goyanes, A. W. Basit, and S. Gaisford, “Influence of Geometry on the Drug Release Profiles of Stereolithographic (SLA) 3D-Printed Tablets,” *AAPS PharmSciTech*, vol. 19, no. 8, pp. 3355–3361, Nov. 2018, doi: 10.1208/S12249-018-1075-3/FIGURES/8.

[25] S. A. Khaled, J. C. Burley, M. R. Alexander, J. Yang, and C. J. Roberts, “3D printing of five-in-one dose combination polypill with defined immediate and sustained release profiles,” *J. Control. Release*, vol. 217, pp. 308–314, Nov. 2015, doi: 10.1016/J.JCONREL.2015.09.028.

[26] A. Goyanes *et al.*, “3D Printing of Medicines: Engineering Novel Oral Devices with Unique Design and Drug Release Characteristics,” *Mol. Pharm.*, vol. 12, no. 11, pp. 4077–4084, Oct. 2015, doi: 10.1021/ACS.MOLPHARMACEUT.5B00510/ASSET/IMAGES/MEDIUM/MP-2015-005109_0009.GIF.

[27] A. Maroni, A. Melocchi, F. Parietti, A. Foppoli, L. Zema, and A. Gazzaniga, “3D printed multi-compartment capsular devices for two-pulse oral drug delivery,” *J. Control. Release*, vol. 268, pp. 10–18, Dec. 2017, doi: 10.1016/J.JCONREL.2017.10.008.

[28] A. Goyanes, M. Scarpa, M. Kamlow, S. Gaisford, A. W. Basit, and M. Orlu,

"Patient acceptability of 3D printed medicines," *Int. J. Pharm.*, vol. 530, no. 1–2, pp. 71–78, Sep. 2017, doi: 10.1016/J.IJPHARM.2017.07.064.

[29] B. C. Pereira *et al.*, "'Temporary Plasticiser': A novel solution to fabricate 3D printed patient-centred cardiovascular 'Polypill' architectures," *Eur. J. Pharm. Biopharm.*, vol. 135, pp. 94–103, Feb. 2019, doi: 10.1016/J.EJPB.2018.12.009.

[30] N. Scoutaris, S. A. Ross, and D. Douroumis, "3D Printed 'Starmix' Drug Loaded Dosage Forms for Paediatric Applications," *Pharm. Res.*, vol. 35, no. 2, pp. 1–11, Feb. 2018, doi: 10.1007/S11095-017-2284-2/FIGURES/10.

[31] M. Sadia, B. Arafat, W. Ahmed, R. T. Forbes, and M. A. Alhnan, "Channelled tablets: An innovative approach to accelerating drug release from 3D printed tablets," *J. Control. Release*, vol. 269, pp. 355–363, Jan. 2018, doi: 10.1016/J.JCONREL.2017.11.022.

[32] S. Mohapatra, R. K. Kar, P. K. Biswal, and S. Bindhani, "Approaches of 3D printing in current drug delivery," *Sensors Int.*, vol. 3, p. 100146, Jan. 2022, doi: 10.1016/J.SINTL.2021.100146.

[33] P. Robles Martinez, A. W. Basit, and S. Gaisford, "The history, developments and opportunities of stereolithography," *AAPS Adv. Pharm. Sci. Ser.*, vol. 31, pp. 55–79, 2018, doi: 10.1007/978-3-319-90755-0_4/FIGURES/16.

[34] "ISO/ASTM 52900: Additive manufacturing — General principles — Fundamentals and vocabulary (second edition)," 2021.

[35] C. M. Madla, S. J. Trenfield, A. Goyanes, S. Gaisford, and A. W. Basit, "3D Printing Technologies, Implementation and Regulation: An Overview," *AAPS Adv. Pharm. Sci. Ser.*, vol. 31, pp. 21–40, 2018, doi: 10.1007/978-3-319-90755-0_2.

[36] S. A. Khaled, J. C. Burley, M. R. Alexander, and C. J. Roberts, "Desktop 3D printing of controlled release pharmaceutical bilayer tablets," *Int. J. Pharm.*, vol. 461, no. 1–2, pp. 105–111, Jan. 2014, doi: 10.1016/J.IJPHARM.2013.11.021.

[37] B. Muñiz Castro *et al.*, "Machine learning predicts 3D printing performance of over 900 drug delivery systems," *J. Control. Release*, vol. 337, pp. 530–545, Sep. 2021, doi: 10.1016/J.JCONREL.2021.07.046.

[38] F. Wang *et al.*, “Precision extruding deposition and characterization of cellular poly-ε-caprolactone tissue scaffolds,” *Rapid Prototyp. J.*, vol. 10, no. 1, pp. 42–49, 2004, doi: 10.1108/13552540410512525/FULL/PDF.

[39] J. Firth, A. W. Basit, and S. Gaisford, “The role of semi-solid extrusion printing in clinical practice,” *AAPS Adv. Pharm. Sci. Ser.*, vol. 31, pp. 133–151, 2018, doi: 10.1007/978-3-319-90755-0_7/FIGURES/10.

[40] J. Goole and K. Amighi, “3D printing in pharmaceutics: A new tool for designing customized drug delivery systems,” *Int. J. Pharm.*, vol. 499, no. 1–2, pp. 376–394, Feb. 2016, doi: 10.1016/J.IJPHARM.2015.12.071.

[41] B. K. Lee, Y. H. Yun, J. S. Choi, Y. C. Choi, J. D. Kim, and Y. W. Cho, “Fabrication of drug-loaded polymer microparticles with arbitrary geometries using a piezoelectric inkjet printing system,” *Int. J. Pharm.*, vol. 427, no. 2, pp. 305–310, May 2012, doi: 10.1016/J.IJPHARM.2012.02.011.

[42] J. Gardan, “Additive manufacturing technologies : State of the art and trends,” *Addit. Manuf. Handb.*, pp. 149–168, May 2017, doi: 10.1201/9781315119106-10.

[43] S. J. Trenfield, C. M. Madla, A. W. Basit, and S. Gaisford, “Binder jet printing in pharmaceutical manufacturing,” *AAPS Adv. Pharm. Sci. Ser.*, vol. 31, pp. 41–54, 2018, doi: 10.1007/978-3-319-90755-0_3/FIGURES/7.

[44] G. Y. Deng, L. Y. Xiang, D. H. Wei, J. Liu, G. W. Yun, and H. Xu, “Tablets with material gradients fabricated by three-dimensional printing,” *J. Pharm. Sci.*, vol. 96, no. 9, pp. 2446–2456, Sep. 2007, doi: 10.1002/jps.20864.

[45] A. Goyanes, U. Det-Amornrat, J. Wang, A. W. Basit, and S. Gaisford, “3D scanning and 3D printing as innovative technologies for fabricating personalized topical drug delivery systems,” *J. Control. Release*, vol. 234, pp. 41–48, Jul. 2016, doi: 10.1016/J.JCONREL.2016.05.034.

[46] C. G. Williams, A. N. Malik, T. K. Kim, P. N. Manson, and J. H. Elisseeff, “Variable cytocompatibility of six cell lines with photoinitiators used for polymerizing hydrogels and cell encapsulation,” *Biomaterials*, vol. 26, no. 11, pp. 1211–1218, Apr. 2005, doi: 10.1016/J.BIOMATERIALS.2004.04.024.

[47] F. Fina, S. Gaisford, and A. W. Basit, “Powder bed fusion: The working process, current applications and opportunities,” *AAPS Adv. Pharm. Sci. Ser.*, vol. 31, pp. 81–105, Jan. 2018, doi: 10.1007/978-3-319-90755-0_5/FIGURES/21.

[48] A. Awad *et al.*, “3D Printed Pellets (Miniprintlets): A Novel, Multi-Drug, Controlled Release Platform Technology,” *Pharm. 2019, Vol. 11, Page 148*, vol. 11, no. 4, p. 148, Mar. 2019, doi: 10.3390/PHARMACEUTICS11040148.

[49] J. Norman, R. D. Madurawe, C. M. V. Moore, M. A. Khan, and A. Khairuzzaman, “A new chapter in pharmaceutical manufacturing: 3D-printed drug products,” *Adv. Drug Deliv. Rev.*, vol. 108, pp. 39–50, Jan. 2017, doi: 10.1016/J.ADDR.2016.03.001.

[50] A. Mohammed, A. Elshaer, P. Sareh, M. Elsayed, and H. Hassanin, “Additive Manufacturing Technologies for Drug Delivery Applications,” *Int. J. Pharm.*, vol. 580, p. 119245, Apr. 2020, doi: 10.1016/J.IJPHARM.2020.119245.

[51] A. Awad, S. Gaisford, and A. W. Basit, “Fused deposition modelling: Advances in engineering and medicine,” *AAPS Adv. Pharm. Sci. Ser.*, vol. 31, pp. 107–132, 2018, doi: 10.1007/978-3-319-90755-0_6/FIGURES/24.

[52] A. Melocchi *et al.*, “Quality considerations on the pharmaceutical applications of fused deposition modeling 3D printing,” *Int. J. Pharm.*, vol. 592, p. 119901, Jan. 2021, doi: 10.1016/J.IJPHARM.2020.119901.

[53] D. T. Pham and R. S. Gault, “A comparison of rapid prototyping technologies,” *Int. J. Mach. Tools Manuf.*, vol. 38, no. 10–11, pp. 1257–1287, Oct. 1998, doi: 10.1016/S0890-6955(97)00137-5.

[54] A. Awad, S. J. Trenfield, A. Goyanes, S. Gaisford, and A. W. Basit, “Reshaping drug development using 3D printing,” *Drug Discov. Today*, vol. 23, no. 8, pp. 1547–1555, Aug. 2018, doi: 10.1016/J.DRUDIS.2018.05.025.

[55] L. X. Yu *et al.*, “Understanding Pharmaceutical Quality by Design,” *AAPS J.*, vol. 16, no. 4, p. 771, 2014, doi: 10.1208/S12248-014-9598-3.

[56] M. A. Staples, “The Concept of Quality-by-Design,” *Pharm. Stab. Test. to Support Glob. Mark.*, pp. 101–106, 2010, doi: 10.1007/978-1-4419-0889-6_14.

[57] Wolfgang Schmitt, “FDA: QbD becomes mandatory for Generics ,” *gmp-*

compliance.org, Feb. 2012.

[58] K. Jagtap, B. Chaudhari, and V. Redasani, “Quality by Design (QbD) concept Review in Pharmaceuticals,” *Asian J. Res. Chem*, vol. 15, no. 4, doi: 10.52711/0974-4150.2022.00054.

[59] S. Beg, M. S. Hasnain, M. Rahman, and S. Swain, “Introduction to Quality by Design (QbD): Fundamentals, Principles, and Applications,” *Pharm. Qual. by Des. Princ. Appl.*, pp. 1–17, Jan. 2019, doi: 10.1016/B978-0-12-815799-2.00001-0.

[60] A. Khairuzzaman, “Regulatory perspectives on 3D printing in pharmaceuticals,” *AAPS Adv. Pharm. Sci. Ser.*, vol. 31, pp. 215–236, 2018, doi: 10.1007/978-3-319-90755-0_11/TABLES/2.

[61] A. G. Crișan *et al.*, “QbD guided development of immediate release FDM-3D printed tablets with customizable API doses,” *Int. J. Pharm.*, vol. 613, p. 121411, Feb. 2022, doi: 10.1016/J.IJPHARM.2021.121411.

[62] Y. M. Than and V. Titapiwatanakun, “Statistical design of experiment-based formulation development and optimization of 3D printed oral controlled release drug delivery with multi target product profile,” *J. Pharm. Investig.*, vol. 51, no. 6, pp. 715–734, Nov. 2021, doi: 10.1007/S40005-021-00542-Y/FIGURES/1.

[63] J. dos Santos, M. Deon, G. S. da Silva, and R. C. R. Beck, “Multiple variable effects in the customisation of fused deposition modelling 3D-printed medicines: A design of experiments (DoE) approach,” *Int. J. Pharm.*, vol. 597, p. 120331, Mar. 2021, doi: 10.1016/J.IJPHARM.2021.120331.

[64] F. Q. Pires *et al.*, “Predictive models of FDM 3D printing using experimental design based on pharmaceutical requirements for tablet production,” *Int. J. Pharm.*, vol. 588, p. 119728, Oct. 2020, doi: 10.1016/J.IJPHARM.2020.119728.

[65] S. Palekar, P. K. Nukala, S. M. Mishra, T. Kipping, and K. Patel, “Application of 3D printing technology and quality by design approach for development of age-appropriate pediatric formulation of baclofen,” *Int. J. Pharm.*, vol. 556, pp. 106–116, Feb. 2019, doi: 10.1016/J.IJPHARM.2018.11.062.

[66] S. Henry, L. De Wever, V. Vanhoorne, T. De Beer, and C. Vervaet, “Influence of

Print Settings on the Critical Quality Attributes of Extrusion-Based 3D-Printed Caplets: A Quality-by-Design Approach," *Pharm. 2021, Vol. 13, Page 2068*, vol. 13, no. 12, p. 2068, Dec. 2021, doi: 10.3390/PHARMACEUTICS13122068.

[67] RepRap contributors, "RepRap project."

[68] N. Gottschalk, M. Bogdahn, M. Harms, and J. Quodbach, "Brittle polymers in Fused Deposition Modeling: An improved feeding approach to enable the printing of highly drug loaded filament," *Int. J. Pharm.*, vol. 597, p. 120216, Mar. 2021, doi: 10.1016/j.ijpharm.2021.120216.

[69] B. N. Turner, R. Strong, and S. A. Gold, "A review of melt extrusion additive manufacturing processes: I. Process design and modeling," *Rapid Prototyp. J.*, vol. 20, no. 3, pp. 192–204, 2014, doi: 10.1108/RPJ-01-2013-0012/FULL/XML.

[70] N. Venkataraman *et al.*, "Feedstock material property ± process relationships in fused deposition of ceramics (FDC)".

[71] B. N. Turner and S. A. Gold, "A review of melt extrusion additive manufacturing processes: II. Materials, dimensional accuracy, and surface roughness," *Rapid Prototyp. J.*, vol. 21, no. 3, pp. 250–261, Apr. 2015, doi: 10.1108/RPJ-02-2013-0017/FULL/PDF.

[72] C. Leuner and J. Dressman, "Improving drug solubility for oral delivery using solid dispersions," Jul. 2000, *Elsevier*. doi: 10.1016/S0939-6411(00)00076-X.

[73] T. Vasconcelos, B. Sarmento, and P. Costa, "Solid dispersions as strategy to improve oral bioavailability of poor water soluble drugs," Dec. 2007, *Elsevier Current Trends*. doi: 10.1016/j.drudis.2007.09.005.

[74] S. Baghel, H. Cathcart, and N. J. O'Reilly, "Polymeric Amorphous Solid Dispersions: A Review of Amorphization, Crystallization, Stabilization, Solid-State Characterization, and Aqueous Solubilization of Biopharmaceutical Classification System Class II Drugs," Sep. 2016, *Elsevier B.V.* doi: 10.1016/j.xphs.2015.10.008.

[75] M. F. Simões, R. M. A. Pinto, and S. Simões, "Hot-melt extrusion in the pharmaceutical industry: toward filing a new drug application," *Drug Discov. Today*, vol. 24, no. 9, pp. 1749–1768, Sep. 2019, doi:

10.1016/J.DRUDIS.2019.05.013.

[76] M. M. Crowley *et al.*, “Pharmaceutical Applications of Hot-Melt Extrusion: Part I,” *Drug Dev. Ind. Pharm.*, vol. 33, no. 9, pp. 909–926, Jan. 2007, doi: 10.1080/03639040701498759.

[77] A. L. Sarode, H. Sandhu, N. Shah, W. Malick, and H. Zia, “Hot melt extrusion (HME) for amorphous solid dispersions: Predictive tools for processing and impact of drug-polymer interactions on supersaturation,” *Eur. J. Pharm. Sci.*, vol. 48, no. 3, pp. 371–384, Feb. 2013, doi: 10.1016/j.ejps.2012.12.012.

[78] A. Goyanes, A. B. M. Buanz, A. W. Basit, and S. Gaisford, “Fused-filament 3D printing (3DP) for fabrication of tablets,” *Int. J. Pharm.*, vol. 476, no. 1–2, pp. 88–92, Dec. 2014, doi: 10.1016/J.IJPHARM.2014.09.044.

[79] A. Goyanes, A. B. M. Buanz, G. B. Hatton, S. Gaisford, and A. W. Basit, “3D printing of modified-release aminosalicylate (4-ASA and 5-ASA) tablets,” *Eur. J. Pharm. Biopharm.*, vol. 89, pp. 157–162, Jan. 2015, doi: 10.1016/J.EJPB.2014.12.003.

[80] J. Skowyra, K. Pietrzak, and M. A. Alhnan, “Fabrication of extended-release patient-tailored prednisolone tablets via fused deposition modelling (FDM) 3D printing,” *Eur. J. Pharm. Sci.*, vol. 68, pp. 11–17, Feb. 2015, doi: 10.1016/J.EJPS.2014.11.009.

[81] A. Melocchi, F. Parietti, A. Maroni, A. Foppoli, A. Gazzaniga, and L. Zema, “Hot-melt extruded filaments based on pharmaceutical grade polymers for 3D printing by fused deposition modeling,” *Int. J. Pharm.*, vol. 509, no. 1–2, pp. 255–263, Jul. 2016, doi: 10.1016/j.ijpharm.2016.05.036.

[82] W. Jamróz *et al.*, “3D printed orodispersible films with Aripiprazole,” *Int. J. Pharm.*, vol. 533, no. 2, pp. 413–420, Nov. 2017, doi: 10.1016/J.IJPHARM.2017.05.052.

[83] W. Kempin *et al.*, “Immediate Release 3D-Printed Tablets Produced Via Fused Deposition Modeling of a Thermo-Sensitive Drug,” *Pharm. Res.*, vol. 35, no. 6, p. 124, Jun. 2018, doi: 10.1007/s11095-018-2405-6.

[84] J. Zhang, X. Feng, H. Patil, R. V. Tiwari, and M. A. Repka, “Coupling 3D

printing with hot-melt extrusion to produce controlled-release tablets," *Int. J. Pharm.*, vol. 519, no. 1–2, pp. 186–197, Mar. 2017, doi: 10.1016/j.ijpharm.2016.12.049.

[85] M. Alhijjaj, P. Belton, and S. Qi, "An investigation into the use of polymer blends to improve the printability of and regulate drug release from pharmaceutical solid dispersions prepared via fused deposition modeling (FDM) 3D printing," *Eur. J. Pharm. Biopharm.*, vol. 108, pp. 111–125, Nov. 2016, doi: 10.1016/J.EJPB.2016.08.016.

[86] A. Samaro *et al.*, "Can filaments, pellets and powder be used as feedstock to produce highly drug-loaded ethylene-vinyl acetate 3D printed tablets using extrusion-based additive manufacturing?," *Int. J. Pharm.*, vol. 607, p. 120922, 2021, doi: 10.1016/J.IJPHARM.2021.120922.

[87] M. Elbadawi *et al.*, "M3DISEEN: A novel machine learning approach for predicting the 3D printability of medicines," *Int. J. Pharm.*, vol. 590, p. 119837, Nov. 2020, doi: 10.1016/J.IJPHARM.2020.119837.

[88] R. C. R. Beck *et al.*, "3D printed tablets loaded with polymeric nanocapsules: An innovative approach to produce customized drug delivery systems," *Int. J. Pharm.*, vol. 528, no. 1–2, pp. 268–279, Aug. 2017, doi: 10.1016/J.IJPHARM.2017.05.074.

[89] G. Kollamaram, D. M. Croker, G. M. Walker, A. Goyanes, A. W. Basit, and S. Gaisford, "Low temperature fused deposition modeling (FDM) 3D printing of thermolabile drugs," *Int. J. Pharm.*, vol. 545, no. 1–2, pp. 144–152, Jul. 2018, doi: 10.1016/J.IJPHARM.2018.04.055.

[90] A. Goyanes *et al.*, "Fabrication of controlled-release budesonide tablets via desktop (FDM) 3D printing," *Int. J. Pharm.*, vol. 496, no. 2, pp. 414–420, Dec. 2015, doi: 10.1016/J.IJPHARM.2015.10.039.

[91] T. C. Okwuosa, D. Stefaniak, B. Arafat, A. Isreb, K. W. Wan, and M. A. Alhnan, "A Lower Temperature FDM 3D Printing for the Manufacture of Patient-Specific Immediate Release Tablets," *Pharm. Res.*, vol. 33, no. 11, pp. 2704–2712, Nov. 2016, doi: 10.1007/S11095-016-1995-0/TABLES/1.

[92] M. Sadia *et al.*, “Adaptation of pharmaceutical excipients to FDM 3D printing for the fabrication of patient-tailored immediate release tablets,” *Int. J. Pharm.*, vol. 513, no. 1–2, pp. 659–668, Nov. 2016, doi: 10.1016/j.ijpharm.2016.09.050.

[93] A. Goyanes, F. Fina, A. Martorana, D. Sedough, S. Gaisford, and A. W. Basit, “Development of modified release 3D printed tablets (printlets) with pharmaceutical excipients using additive manufacturing,” *Int. J. Pharm.*, vol. 527, no. 1–2, pp. 21–30, Jul. 2017, doi: 10.1016/J.IJPHARM.2017.05.021.

[94] G. Verstraete *et al.*, “3D printing of high drug loaded dosage forms using thermoplastic polyurethanes,” *Int. J. Pharm.*, vol. 536, no. 1, pp. 318–325, Jan. 2018, doi: 10.1016/j.ijpharm.2017.12.002.

[95] C. Korte and J. Quodbach, “Formulation development and process analysis of drug-loaded filaments manufactured via hot-melt extrusion for 3D-printing of medicines,” *https://doi.org/10.1080/10837450.2018.1433208*, vol. 23, no. 10, pp. 1117–1127, Nov. 2018, doi: 10.1080/10837450.2018.1433208.

[96] K. Pietrzak, A. Isreb, and M. A. Alhnan, “A flexible-dose dispenser for immediate and extended release 3D printed tablets,” *Eur. J. Pharm. Biopharm.*, vol. 96, pp. 380–387, Oct. 2015, doi: 10.1016/J.EJPB.2015.07.027.

[97] A. Melocchi, F. Parietti, G. Loreti, A. Maroni, A. Gazzaniga, and L. Zema, “3D printing by fused deposition modeling (FDM) of a swellable/erodible capsular device for oral pulsatile release of drugs,” *J. Drug Deliv. Sci. Technol.*, vol. 30, pp. 360–367, Dec. 2015, doi: 10.1016/J.JDDST.2015.07.016.

[98] N. G. Solanki, M. Tahsin, A. V. Shah, and A. T. M. Serajuddin, “Formulation of 3D Printed Tablet for Rapid Drug Release by Fused Deposition Modeling: Screening Polymers for Drug Release, Drug-Polymer Miscibility and Printability,” *J. Pharm. Sci.*, vol. 107, no. 1, pp. 390–401, Jan. 2018, doi: 10.1016/j.xphs.2017.10.021.

[99] A. Goyanes *et al.*, “PET/CT imaging of 3D printed devices in the gastrointestinal tract of rodents,” *Int. J. Pharm.*, vol. 536, no. 1, pp. 158–164, Jan. 2018, doi: 10.1016/J.IJPHARM.2017.11.055.

[100] W. Kempin *et al.*, “Assessment of different polymers and drug loads for fused

deposition modeling of drug loaded implants," *Eur. J. Pharm. Biopharm.*, vol. 115, pp. 84–93, Jun. 2017, doi: 10.1016/J.EJPB.2017.02.014.

[101] A. Goyanes, N. Allahham, S. J. Trenfield, E. Stoyanov, S. Gaisford, and A. W. Basit, "Direct powder extrusion 3D printing: Fabrication of drug products using a novel single-step process," *Int. J. Pharm.*, vol. 567, p. 118471, Aug. 2019, doi: 10.1016/J.IJPHARM.2019.118471.

[102] T. Tracy, L. Wu, X. Liu, S. Cheng, and X. Li, "3D printing: Innovative solutions for patients and pharmaceutical industry," *Int. J. Pharm.*, vol. 631, p. 122480, Jan. 2023, doi: 10.1016/J.IJPHARM.2022.122480.

[103] E. Prasad, J. Robertson, and G. W. Halbert, "Mefenamic acid solid dispersions: Impact of formulation composition on processing parameters, product properties and performance," *Int. J. Pharm.*, vol. 616, p. 121505, Mar. 2022, doi: 10.1016/J.IJPHARM.2022.121505.

[104] T. Kojima, K. Higashi, T. Suzuki, K. Tomono, K. Moribe, and K. Yamamoto, "Stabilization of a Supersaturated Solution of Mefenamic Acid from a Solid Dispersion with EUDRAGIT® EPO," *Pharm. Res.*, vol. 29, no. 10, pp. 2777–2791, Oct. 2012, doi: 10.1007/s11095-011-0655-7.

[105] J. Dos Santos, G. S. da Silva, M. C. Velho, and R. C. R. Beck, "Eudragit®: A Versatile Family of Polymers for Hot Melt Extrusion and 3D Printing Processes in Pharmaceutics," *Pharm. 2021, Vol. 13, Page 1424*, vol. 13, no. 9, p. 1424, Sep. 2021, doi: 10.3390/PHARMACEUTICS13091424.

[106] S. Deshmukh *et al.*, "Injection moulded controlled release amorphous solid dispersions: Synchronized drug and polymer release for robust performance," 2019, doi: 10.1016/j.ijpharm.2019.118908.

[107] D. K. Jha, D. S. Shah, and P. D. Amin, "Effect of Hypromellose Acetate Succinate Substituents on Miscibility Behavior of Spray-dried Amorphous Solid Dispersions: Flory–Huggins Parameter Prediction and Validation," *Carbohydr. Polym. Technol. Appl.*, vol. 2, p. 100137, Dec. 2021, doi: 10.1016/J.CARPTA.2021.100137.

[108] Shin-Etsu Chemical Co., "Shin-Etsu AQOAT® (Hypromellose Acetate

Succinate)."

[109] A. A. D'souza and R. Shegokar, "Polyethylene glycol (PEG): a versatile polymer for pharmaceutical applications," *http://dx.doi.org/10.1080/17425247.2016.1182485*, vol. 13, no. 9, pp. 1257–1275, Sep. 2016, doi: 10.1080/17425247.2016.1182485.

[110] L. LastNameSumitomo Seika Co., "PEO(Polyethylene Oxide), product description."

[111] P. Zarrintaj, M. R. Saeb, S. H. Jafari, and M. Mozafari, "Application of compatibilized polymer blends in biomedical fields," *Compat. Polym. Blends Micro Nano Scale Phase Morphol. Interphase Charact. Prop.*, pp. 511–537, Jan. 2020, doi: 10.1016/B978-0-12-816006-0.00018-9.

[112] N. K. Thakral, R. L. Zanon, R. C. Kelly, and S. Thakral, "Applications of Powder X-Ray Diffraction in Small Molecule Pharmaceuticals: Achievements and Aspirations," *J. Pharm. Sci.*, vol. 107, no. 12, pp. 2969–2982, Dec. 2018, doi: 10.1016/J.XPHS.2018.08.010.

[113] I. Ivanisevic, "Physical Stability Studies of Miscible Amorphous Solid Dispersions," *J. Pharm. Sci.*, vol. 99, no. 9, pp. 4005–4012, Sep. 2010, doi: 10.1002/jps.22247.

[114] B. Plazzotta, J. S. Diget, K. Zhu, B. Nyström, and J. S. Pedersen, "Small-angle X-ray scattering as a useful supplementary technique to determine molecular masses of polyelectrolytes in solution," *J. Polym. Sci. Part B Polym. Phys.*, vol. 54, no. 19, pp. 1913–1917, Oct. 2016, doi: 10.1002/polb.24107.

[115] E. A. Nagul, C. F. Croft, R. W. Cattrall, and S. D. Kolev, "Nanostructural characterisation of polymer inclusion membranes using X-ray scattering," *J. Memb. Sci.*, vol. 588, Oct. 2019, doi: 10.1016/j.memsci.2019.117208.

[116] P. Gill, T. T. Moghadam, and B. Ranjbar, "Differential Scanning Calorimetry Techniques: Applications in Biology and Nanoscience," *J. Biomol. Tech.*, vol. 21, no. 4, p. 167, Dec. 2010.

[117] S. Niu *et al.*, "Apparent kinetic and thermodynamic calculation for thermal degradation of stearic acid and its esterification derivants through

thermogravimetric analysis," *Renew. Energy*, vol. 133, pp. 373–381, Apr. 2019, doi: 10.1016/J.RENENE.2018.10.045.

[118] A. Tai, R. Bianchini, and J. Jachowicz, "Texture analysis of cosmetic/pharmaceutical raw materials and formulations," *Int. J. Cosmet. Sci.*, vol. 36, no. 4, pp. 291–304, Aug. 2014, doi: 10.1111/ICS.12125.

[119] Y. X. Liu, M. J. Cao, and G. M. Liu, "Texture analyzers for food quality evaluation," *Eval. Technol. Food Qual.*, pp. 441–463, Jan. 2019, doi: 10.1016/B978-0-12-814217-2.00017-2.

[120] T. G. Mezger, *The Rheology Handbook: For Users of Rotational and Oscillatory Rheometers*, 4th Editio. Hanover, Germany: Vincentz Network - European coating, 2014.

[121] A. G. Podoleanu, "Optical coherence tomography," *J. Microsc.*, vol. 247, no. 3, pp. 209–219, Sep. 2012, doi: 10.1111/J.1365-2818.2012.03619.X.

[122] Hamamatsu Photonics, "Optical coherence tomography."

[123] T. Vankeirsbilck *et al.*, "Applications of Raman spectroscopy in pharmaceutical analysis," *TrAC Trends Anal. Chem.*, vol. 21, no. 12, pp. 869–877, Dec. 2002, doi: 10.1016/S0165-9936(02)01208-6.

[124] HORIBA, "What is Raman Spectroscopy?"

[125] E. Prasad, J. Robertson, and G. W. Halbert, "Improving Consistency for a Mefenamic Acid Immediate Release Formulation," *J. Pharm. Sci.*, vol. 109, no. 11, pp. 3462–3470, Nov. 2020, doi: 10.1016/J.XPHS.2020.08.012.

[126] R. K. Gilpin and W. Zhou, "Infrared studies of the thermal conversion of mefenamic acid between polymorphic states," 2004, doi: 10.1016/j.vibspec.2004.06.001.

[127] E. Bordos, M. T. Islam, A. J. Florence, G. W. Halbert, and J. Robertson, "Use of Terahertz-Raman Spectroscopy to Determine Solubility of the Crystalline Active Pharmaceutical Ingredient in Polymeric Matrices during Hot Melt Extrusion," *Mol. Pharm.*, vol. 16, no. 10, pp. 4361–4371, Aug. 2019, doi: 10.1021/acs.molpharmaceut.9b00703.

[128] J. Midelet, A. H. El-Sagheer, T. Brown, A. G. Kanaras, A. Débarre, and M. H. V. Werts, “Spectroscopic and Hydrodynamic Characterisation of DNA-Linked Gold Nanoparticle Dimers in Solution using Two-Photon Photoluminescence,” *ChemPhysChem*, vol. 19, no. 7, pp. 827–836, Apr. 2018, doi: 10.1002/cphc.201701228.

[129] A. O. Surov, I. V Terekhova, A. Bauer-Brandl, and G. L. Perlovich, “Thermodynamic and Structural Aspects of Some Fenamate Molecular Crystals”, doi: 10.1021/cg900002q.

[130] E. Prasad *et al.*, “Development of a hot-melt extrusion (HME) process to produce drug loaded Affinisol^{TM} 15LV filaments for fused filament fabrication (FFF) 3D printing,” *Addit. Manuf.*, vol. 29, p. 100776, Oct. 2019, doi: 10.1016/J.ADDMA.2019.06.027.

[131] Moulham Alsuleman, “Screening Study for Mefenamic Acid Solid Dispersion Systems for Hot Melt Extrusion Applications,” University of Strathclyde, 2018.

[132] A. Forster, J. Hempenstall, I. Tucker, and T. Rades, “Selection of excipients for melt extrusion with two poorly water-soluble drugs by solubility parameter calculation and thermal analysis,” *Int. J. Pharm.*, vol. 226, no. 1–2, pp. 147–161, Sep. 2001, doi: 10.1016/S0378-5173(01)00801-8.

[133] G. W. (Gottfried W. Ehrenstein and R. P. (Richard P. . Theriault, “Thermomechanical properties,” in *Polymeric materials : structure, properties, applications*, Hanser, 2001, ch. Chapter Fi, pp. 143–165.

[134] T. Parikh, S. S. Gupta, A. Meena, and A. T. M. Serajuddin, “Investigation of thermal and viscoelastic properties of polymers relevant to hot melt extrusion - III: Polymethacrylates and polymethacrylic acid based polymers,” *AAPS PharmSciTech*, vol. 5, no. 1, pp. 56–64, 2014, doi: 10.1208/s12249-015-0426-6.

[135] G. W. (Gottfried W. Ehrenstein and R. P. (Richard P. . Theriault, “Structure of polymeric materials,” in *Polymeric materials : structure, properties, applications*, Hanser, 2001, ch. Chapter Fo, pp. 61–139.

[136] G. W. (Gottfried W. Ehrenstein and R. P. (Richard P. . Theriault, “Molecular Stracutre and Synthesis of Polymers,” in *Polymeric materials : structure,*

properties, applications, Hanser, 2001, p. 277.

[137] Y. Li *et al.*, “Interactions between drugs and polymers influencing hot melt extrusion,” *J. Pharm. Pharmacol.*, vol. 66, no. 2, pp. 148–166, Feb. 2014, doi: 10.1111/jphp.12183.

[138] S. SeethaLekshmi and T. N. Guru Row, “Conformational Polymorphism in a Non-steroidal Anti-inflammatory Drug, Mefenamic Acid,” *Cryst. Growth & Des.*, vol. 12, no. 8, pp. 4283–4289, Jul. 2012, doi: 10.1021/cg300812v.

[139] V. R. R. Cunha *et al.*, “Mefenamic Acid Anti-Inflammatory Drug: Probing Its Polymorphs by Vibrational (IR and Raman) and Solid-State NMR Spectroscopies,” *J. Phys. Chem. B*, vol. 118, no. 16, pp. 4333–4344, Apr. 2014, doi: 10.1021/jp500988k.

[140] S. Roy, B. Chamberlin, and A. J. Matzger, “Polymorph Discrimination Using Low Wavenumber Raman Spectroscopy,” *Org. Process Res*, vol. 17, no. 7, pp. 976–98, 2013, doi: 10.1021/op400102e.

[141] C. R. Groom, I. J. Bruno, M. P. Lightfoot, and S. C. Ward, “The Cambridge Structural Database,” *urn:issn:2052-5206*, vol. 72, no. 2, pp. 171–179, Apr. 2016, doi: 10.1107/S2052520616003954.

[142] K. Higashi *et al.*, “Insights into atomic-level interaction between mefenamic acid and Eudragit EPO in a supersaturated solution by high-resolution magic-angle spinning NMR spectroscopy,” *Mol. Pharm.*, vol. 11, no. 1, pp. 351–357, Jan. 2014, doi: 10.1021/mp4005723.

[143] E. H. Lee, S. R. Byrn, and M. T. Carvajal, “Additive-induced metastable single crystal of mefenamic acid,” *Pharm. Res.*, vol. 23, no. 10, pp. 2375–2380, Oct. 2006, doi: 10.1007/s11095-006-9045-y.

[144] D. Bertoldo Menezes, A. Reyer, A. Yüksel, B. Bertoldo Oliveira, and M. Musso, “Introduction to Terahertz Raman spectroscopy,” *Spectrosc. Lett.*, vol. 51, no. 8, pp. 438–445, Sep. 2018, doi: 10.1080/00387010.2018.1501704.

[145] I. Fix and K. J. Steffens, “Quantifying Low Amorphous or Crystalline Amounts of Alpha-Lactose-Monohydrate Using X-Ray Powder Diffraction, Near-Infrared Spectroscopy, and Differential Scanning Calorimetry,”

http://dx.doi.org/10.1081/DDC-120037482, vol. 30, no. 5, pp. 513–523, 2004, doi: 10.1081/DDC-120037482.

[146] P. Matousek and A. W. Parker, "Bulk Raman Analysis of Pharmaceutical Tablets," *Appl. Spectrosc.*, vol. 60, no. 12, pp. 1353–1357, Dec. 2006, doi: 10.1366/000370206779321463.

[147] T. Daimay Lin-Vien (Shell Development Company, Houston, C. Norman B. Colthup (Stamford, K. William G. Fateley (Kansas State University, Manhattan, and O. Jeanette G. Grasselli (Ohio University, Athens, *The Handbook of Infrared and Raman Characteristic Frequencies of Organic Molecules*. Elsevier Inc., 1991.

[148] P. Larkin, *Infrared and Raman Spectroscopy: Principles and Spectral Interpretation*. Elsevier, 2017.

[149] M. De Veij, P. Vandenabeele, T. De Beer, J. P. Remon, and L. Moens, "Reference database of Raman spectra of pharmaceutical excipients," *J. Raman Spectrosc.*, vol. 40, no. 3, pp. 297–307, Mar. 2009, doi: 10.1002/jrs.2125.

[150] Y. Pang *et al.*, "A simultaneous X-ray diffraction–differential scanning calorimetry study into the phase transitions of mefenamic acid," *urn:issn:1600-5767*, vol. 52, no. 6, 2019, doi: 10.1107/S1600576719012500.

[151] K. Wlodarski *et al.*, "The influence of amorphization methods on the apparent solubility and dissolution rate of tadalafil," *Eur. J. Pharm. Sci.*, vol. 62, pp. 132–140, Oct. 2014, doi: 10.1016/J.EJPS.2014.05.026.

[152] S. M. Alshehri *et al.*, "Mefenamic acid taste-masked oral disintegrating tablets with enhanced solubility via molecular interaction produced by hot melt extrusion technology," *J. Drug Deliv. Sci. Technol.*, vol. 27, pp. 18–27, Jun. 2015, doi: 10.1016/J.JDDST.2015.03.003.

[153] J. R. Hughey *et al.*, "Dissolution enhancement of a drug exhibiting thermal and acidic decomposition characteristics by fusion processing: A comparative study of hot melt extrusion and KinetiSol® Dispersing," *AAPS PharmSciTech*, vol. 11, no. 2, pp. 760–774, Jun. 2010, doi: 10.1208/S12249-010-9431-Y/TABLES/5.

[154] H. S. Yang, H. J. Kim, J. Son, H. J. Park, B. J. Lee, and T. S. Hwang, "Rice-husk

flour filled polypropylene composites; mechanical and morphological study," *Compos. Struct.*, vol. 63, no. 3–4, pp. 305–312, Feb. 2004, doi: 10.1016/S0263-8223(03)00179-X.

[155] A. Rabinovitch, G. Belizovsky, and D. Bahat, "Origin of mist and hackle patterns in brittle fracture," *Phys. Rev. B*, vol. 61, no. 22, p. 14968, Jun. 2000, doi: 10.1103/PhysRevB.61.14968.

[156] D. R. Bortz, M. Weisenberger, B. Marrs, and R. Andrews, "Fatigue Performance of Multiwall Carbon Nanotube Composite PMMA and ABS," *ASME Int. Mech. Eng. Congr. Expo. Proc.*, vol. 13, no. PART A, pp. 235–242, Aug. 2009, doi: 10.1115/IMECE2008-67578.

[157] K. Matsushige, Y. Sakurada, and K. Takahashi, "X-ray microanalysis and acoustic emission studies on the formation mechanism of secondary cracks in PMMA," *J. Mater. Sci. 1984 195*, vol. 19, no. 5, pp. 1548–1555, May 1984, doi: 10.1007/BF00563052.

[158] S. Saboo, N. A. Mugheirbi, D. Y. Zemlyanov, U. S. Kestur, and L. S. Taylor, "Congruent release of drug and polymer: A 'sweet spot' in the dissolution of amorphous solid dispersions," *J. Control. Release*, vol. 298, pp. 68–82, Mar. 2019, doi: 10.1016/j.jconrel.2019.01.039.

[159] D. Ouyang, "Investigating the molecular structures of solid dispersions by the simulated annealing method," *Chem. Phys. Lett.*, vol. 554, pp. 177–184, Dec. 2012, doi: 10.1016/j.cplett.2012.10.056.

[160] S. Abbott, C. Hansen, H. Yamamoto, and R. S. Valpey III, "Hansen Solubility Parameters in Practice Complete with eBook, software and data 5th Edition The HSPiP team," in *Progress in Polymer Science*, vol. 33, no. 8, Hansen-Solubility.com, 2008, ch. 30, pp. 820–852.

[161] C. M. Hansen, "Solubility Parameters - An introduction," in *Hansen Solubility Parameters: A User's Handbook*, Second Edi., CRC Press, 2007, ch. Chapter 1, pp. 26–51.

[162] C. M. Hansen, "Applications — Coatings and Other Filled Polymer," in *Hansen Solubility Parameters: A User's Handbook*, Second Edi., CRC Press, 2007, ch.

Chapter 8, pp. 137–150.

[163] M. Fanous *et al.*, “Development of immediate release 3D-printed dosage forms for a poorly water-soluble drug by fused deposition modeling: Study of morphology, solid state and dissolution,” *Int. J. Pharm.*, vol. 599, p. 120417, Apr. 2021, doi: 10.1016/J.IJPHARM.2021.120417.

[164] D. J. Greenhalgh, A. C. Williams, P. Timmins, and P. York, “Solubility parameters as predictors of miscibility in solid dispersions,” *J. Pharm. Sci.*, vol. 88, no. 11, pp. 1182–1190, Nov. 1999, doi: 10.1021/JS9900856.

[165] S. Y. Lin, K. S. Chen, and L. Run-Chu, “Organic esters of plasticizers affecting the water absorption, adhesive property, glass transition temperature and plasticizer permanence of Eudragit acrylic films,” *J. Control. Release*, vol. 68, no. 3, pp. 343–350, Sep. 2000, doi: 10.1016/S0168-3659(00)00259-5.

[166] C. Gabriel, H. Muè, C. Gabriel, and H. Muè, “Creep recovery behavior of metallocene linear low-density polyethylenes,” *Rheol. Acta 1999 385*, vol. 38, no. 5, pp. 393–403, 1999, doi: 10.1007/S003970050190.

[167] S. Honary and H. Orafai, “The Effect of Different Plasticizer Molecular Weights and Concentrations on Mechanical and Thermomechanical Properties of Free Films,” *https://doi.org/10.1081/DDC-120003863*, vol. 28, no. 6, pp. 711–715, 2002, doi: 10.1081/DDC-120003863.

[168] N. S. Vrandečić, M. Erceg, M. Jakić, and I. Klarić, “Kinetic analysis of thermal degradation of poly(ethylene glycol) and poly(ethylene oxide)s of different molecular weight,” *Thermochim. Acta*, vol. 498, no. 1–2, pp. 71–80, Jan. 2010, doi: 10.1016/J.TCA.2009.10.005.

[169] M. Monshizadeh, S. Seifi, I. Hejazi, J. Seyfi, and H. A. Khonakdar, “Enhanced properties of poly(lactic acid) by concurrent addition of organo-modified Mg-Al layered double hydroxide (LDH) and triethyl citrate:,” *https://doi.org/10.1177/0892705719868272*, vol. 34, no. 10, pp. 1334–1349, Aug. 2019, doi: 10.1177/0892705719868272.

[170] G. Roudaut, D. Simatos, D. Champion, E. Contreras-Lopez, and M. Le Meste, “Molecular mobility around the glass transition temperature: a mini review,”

Innov. Food Sci. Emerg. Technol., vol. 5, no. 2, pp. 127–134, Jun. 2004, doi: 10.1016/J.IFSET.2003.12.003.

[171] A. Engel *et al.*, "Quality attributes of EUDRAGIT® polymer filaments for 3D-printing processes," in *European Conference on Pharmaceutics*, Bolog, Italy, p. Poster 162.

[172] S. P. Chaudhari and R. P. Dugar, "Application of surfactants in solid dispersion technology for improving solubility of poorly water soluble drugs," *J. Drug Deliv. Sci. Technol.*, vol. 41, pp. 68–77, Oct. 2017, doi: 10.1016/J.JDDST.2017.06.010.

[173] J. J. Moes, S. L. W. Koolen, A. D. R. Huitema, J. H. M. Schellens, J. H. Beijnen, and B. Nuijen, "Pharmaceutical development and preliminary clinical testing of an oral solid dispersion formulation of docetaxel (ModraDoc001)," *Int. J. Pharm.*, vol. 420, no. 2, pp. 244–250, Nov. 2011, doi: 10.1016/J.IJPHARM.2011.08.041.

[174] C. M. Hansen, "Methods of Characterization — Polymers," in *Hansen Solubility Parameters: A User's Handbook*, Second Edi., CRC Press, 2007, ch. Chapter 5, pp. 95–112.

[175] M. E. Lauer *et al.*, "A Miniaturized Extruder to Prototype Amorphous Solid Dispersions: Selection of Plasticizers for Hot Melt Extrusion," *Pharm. 2018, Vol. 10, Page 58*, vol. 10, no. 2, p. 58, May 2018, doi: 10.3390/PHARMACEUTICS10020058.

[176] A. N. Ghebremeskel, C. Vemavarapu, and M. Lodaya, "Use of surfactants as plasticizers in preparing solid dispersions of poorly soluble API: Selection of polymer–surfactant combinations using solubility parameters and testing the processability," *Int. J. Pharm.*, vol. 328, no. 2, pp. 119–129, Jan. 2007, doi: 10.1016/J.IJPHARM.2006.08.010.

[177] M. Chandola and S. Marathe, "A QSPR for the plasticization efficiency of polyvinylchloride plasticizers," *J. Mol. Graph. Model.*, vol. 26, no. 5, pp. 824–828, Jan. 2008, doi: 10.1016/J.JMGM.2007.04.008.

[178] A. Engel *et al.*, "Characterization of Pharmaceutical Polymer Filaments for 3D

Printing Processes," in *AAPS PharmSci 360 conference*, Washington, DC, 2018, pp. W130-06–046.

[179] J. M. Nasereddin, N. Wellner, M. Alhijjaj, P. Belton, and S. Qi, "Development of a Simple Mechanical Screening Method for Predicting the Feedability of a Pharmaceutical FDM 3D Printing Filament," *Pharm. Res.*, vol. 35, no. 8, pp. 1–13, Aug. 2018, doi: 10.1007/S11095-018-2432-3/FIGURES/7.

[180] B. Arafat, N. Qinna, M. Cieszynska, R. T. Forbes, and M. A. Alhnan, "Tailored on demand anti-coagulant dosing: An in vitro and in vivo evaluation of 3D printed purpose-designed oral dosage forms," *Eur. J. Pharm. Biopharm.*, vol. 128, pp. 282–289, Jul. 2018, doi: 10.1016/J.EJPB.2018.04.010.

[181] M. Sadia *et al.*, "From 'fixed dose combinations' to 'a dynamic dose combiner': 3D printed bi-layer antihypertensive tablets," *Eur. J. Pharm. Sci.*, vol. 123, pp. 484–494, Oct. 2018, doi: 10.1016/J.EJPS.2018.07.045.

[182] T. C. Okwuosa, C. Soares, V. Gollwitzer, R. Habashy, P. Timmins, and M. A. Alhnan, "On demand manufacturing of patient-specific liquid capsules via co-ordinated 3D printing and liquid dispensing," *Eur. J. Pharm. Sci.*, vol. 118, pp. 134–143, Jun. 2018, doi: 10.1016/J.EJPS.2018.03.010.

[183] M. Heppenstall-Butler and M. F. Butler, "Nonequilibrium Behavior in the Three-Component System Stearic Acid - Sodium Stearate - Water," *Langmuir*, vol. 19, no. 24, pp. 10061–10072, Nov. 2003, doi: 10.1021/LA034833P/ASSET/IMAGES/LARGE/LA034833PF00027.JPEG.

[184] Daniel Burkat (Dburkat), "Development of a time temperature superposition program (Master-curve-project)," 2018, *Github, McGill University*: MATLAB.

[185] G. Toth, D. Nagy, A. Bata, and K. Belina, "Determination of polymer melts flow-activation energy a function of wide range shear rate," *J. Phys. Conf. Ser.*, vol. 1045, no. 1, p. 012040, Jun. 2018, doi: 10.1088/1742-6596/1045/1/012040.

[186] S. Henry *et al.*, "Extrusion-based 3D printing of oral solid dosage forms: Material requirements and equipment dependencies," *Int. J. Pharm.*, vol. 598, p. 120361, 2021, doi: 10.1016/J.IJPHARM.2021.120361.

[187] L. Liu *et al.*, "Comparative study on the water uptake kinetics and

dehumidification performance of silica gel and aluminophosphate zeolites coatings," *Energy*, vol. 242, p. 122957, Mar. 2022, doi: 10.1016/J.ENERGY.2021.122957.

[188] H. Zhang, J. Magoshi, M. Becker, J. Y. Chen, and R. Matsunaga, "Thermal properties of Bombyx mori silk fibers," *J. Appl. Polym. Sci.*, vol. 86, no. 8, pp. 1817–1820, Nov. 2002, doi: 10.1002/APP.11089.

[189] S. Boufi, H. Kaddami, and A. Dufresne, "Mechanical Performance and Transparency of Nanocellulose Reinforced Polymer Nanocomposites," *Macromol. Mater. Eng.*, vol. 299, no. 5, pp. 560–568, May 2014, doi: 10.1002/MAME.201300232.

[190] L. A. Castillo, S. E. Barbosa, and N. J. Capiati, "Influence of talc morphology on the mechanical properties of talc filled polypropylene," *J. Polym. Res.*, vol. 20, no. 5, pp. 1–9, May 2013, doi: 10.1007/S10965-013-0152-2/FIGURES/9.

[191] H. Alter, "Filler particle size and mechanical properties of polymers," *J. Appl. Polym. Sci.*, vol. 9, no. 4, pp. 1525–1531, Apr. 1965, doi: 10.1002/APP.1965.070090427.

[192] D. Zhao, S. Ge, E. Senses, P. Akcora, J. Jestin, and S. K. Kumar, "Role of Filler Shape and Connectivity on the Viscoelastic Behavior in Polymer Nanocomposites," *Macromolecules*, vol. 48, no. 15, pp. 5433–5438, Aug. 2015, doi: 10.1021/ACS.MACROMOL.5B00962/SUPPL_FILE/MA5B00962_SI_001.PDF.

[193] S. Sahin and P. Yayla, "Effects of testing parameters on the mechanical properties of polypropylene random copolymer," *Polym. Test.*, vol. 24, no. 5, pp. 613–619, Aug. 2005, doi: 10.1016/j.polymertesting.2005.03.002.

[194] A. G. Tabriz, N. Scoutaris, Y. Gong, H. W. Hui, S. Kumar, and D. Douroumis, "Investigation on hot melt extrusion and prediction on 3D printability of pharmaceutical grade polymers," *Int. J. Pharm.*, vol. 604, p. 120755, Jul. 2021, doi: 10.1016/J.IJPHARM.2021.120755.

[195] Y. Yang, H. Wang, X. Xu, and G. Yang, "Strategies and mechanisms to improve the printability of pharmaceutical polymers Eudragit® EPO and Soluplus®," *Int.*

J. Pharm., vol. 599, p. 120410, 2021, doi: 10.1016/J.IJPHARM.2021.120410.

[196] Y. Ding, J. Wang, and S. Song, "Development and Optimisation of Novel Polymeric Compositions for Sustained Release Theophylline Caplets (PrintCap) via FDM 3D Printing," *Polym. 2020, Vol. 12, Page 27*, vol. 12, no. 1, p. 27, Dec. 2019, doi: 10.3390/POLYM12010027.

[197] A. Melocchi *et al.*, "The Chronotopic™ System for Pulsatile and Colonic Delivery of Active Molecules in the Era of Precision Medicine: Feasibility by 3D Printing via Fused Deposition Modeling (FDM)," *Pharm. 2021, Vol. 13, Page 759*, vol. 13, no. 5, p. 759, May 2021, doi: 10.3390/PHARMACEUTICS13050759.

[198] C. I. Gioumouxouzis *et al.*, "A 3D printed bilayer oral solid dosage form combining metformin for prolonged and glimepiride for immediate drug delivery," *Eur. J. Pharm. Sci.*, vol. 120, pp. 40–52, 2018, doi: 10.1016/J.EJPS.2018.04.020.

[199] J. Zhang *et al.*, "Development and evaluation of pharmaceutical 3D printability for hot melt extruded cellulose-based filaments," *J. Drug Deliv. Sci. Technol.*, vol. 52, p. 292, Aug. 2019, doi: 10.1016/J.JDDST.2019.04.043.

[200] P. Xu *et al.*, "Development of a quantitative method to evaluate the printability of filaments for fused deposition modeling 3D printing," *Int. J. Pharm.*, vol. 588, p. 119760, Oct. 2020, doi: 10.1016/J.IJPHARM.2020.119760.

[201] S. S. Gupta, A. Meena, T. Parikh, and A. T. M. Serajuddin, "Investigation of thermal and viscoelastic properties of polymers relevant to hot melt extrusion - I: Polyvinylpyrrolidone and related polymers," *J. Excipients Food Chem.*, vol. 5, no. 1, pp. 32–45, 2014.

[202] S. S. Gupta, T. Parikh, A. K. Meena, N. Mahajan, I. Vitez, and A. T. M. Serajuddin, "Effect of carbamazepine on viscoelastic properties and hot melt extrudability of Soluplus®," *Int. J. Pharm.*, vol. 478, no. 1, pp. 232–239, Jan. 2015, doi: 10.1016/J.IJPHARM.2014.11.025.

[203] G. Kimbell and M. A. Azad, "3D printing: Bioinspired materials for drug delivery," *Bioinspired Biomim. Mater. Drug Deliv.*, pp. 295–318, Jan. 2021, doi:

10.1016/B978-0-12-821352-0.00011-3.

[204] D. G. Papageorgiou, M. Liu, Z. Li, C. Vallés, R. J. Young, and I. A. Kinloch, “Hybrid poly(ether ether ketone) composites reinforced with a combination of carbon fibres and graphene nanoplatelets,” *Compos. Sci. Technol.*, vol. 175, pp. 60–68, May 2019, doi: 10.1016/J.COMPSCITECH.2019.03.006.

[205] M. Kumar, N. Shanmuga Priya, S. Kanagaraj, and G. Pugazhenthi, “Melt rheological behavior of PMMA nanocomposites reinforced with modified nanoclay,” *http://dx.doi.org/10.1080/20550324.2016.1221876*, vol. 2, no. 3, pp. 109–116, Jul. 2016, doi: 10.1080/20550324.2016.1221876.

[206] S. S. Gupta, N. Solanki, and A. T. M. Serajuddin, “Investigation of Thermal and Viscoelastic Properties of Polymers Relevant to Hot Melt Extrusion, IV: Affinisol™ HPMC HME Polymers,” *AAPS PharmSciTech*, vol. 17, no. 1, pp. 148–157, Feb. 2016, doi: 10.1208/S12249-015-0426-6/TABLES/3.

[207] T. J. Coogan and D. O. Kazmer, “In-line rheological monitoring of fused deposition modeling,” *Cit. J. Rheol.*, vol. 63, no. 1, p. 141, Dec. 2019, doi: 10.1122/1.5054648.

[208] E. Prasad, J. Robertson, and G. W. Halbert, “Enabling future manufacture of dose forms: screening tools for an HME-3D printing process - Strathprints,” Glasgow, UK: CMAC UK Showcase, University of Strathclyde, 2019, p. 1.

[209] B. C. Hancock and G. Zografi, “Characteristics and significance of the amorphous state in pharmaceutical systems,” *J. Pharm. Sci.*, vol. 86, no. 1, pp. 1–12, Jan. 1997, doi: 10.1021/JS9601896.

[210] Y. Zhang, X. Li, Y. Dai, and B.-H. Sun, “On the Number of Fractured Segments of Spaghetti Breaking Dynamics,” *Theor. Appl. Mech. Lett.*, p. 100347, Jun. 2022, doi: 10.1016/J.TAML.2022.100347.

[211] N. Gottschalk, J. Quodbach, A. G. Elia, F. Hess, and M. Bogdahn, “Determination of feed forces to improve process understanding of Fused Deposition Modeling 3D printing and to ensure mass conformity of printed solid oral dosage forms,” *Int. J. Pharm.*, vol. 614, p. 121416, Feb. 2022, doi: 10.1016/J.IJPHARM.2021.121416.

[212] D. McKechnie, J. Cree, D. Wadkin-Snaith, and K. Johnston, “Glass transition temperature of a polymer thin film: Statistical and fitting uncertainties,” *Polymer (Guildf).*, vol. 195, p. 122433, May 2020, doi: 10.1016/j.polymer.2020.122433.

[213] Sartorius Stedim Data Analytics, *User Guide to MODDE - Version 12*, V12 ed. Sweden: Sartorius LtD, 2017. doi: ID #2068.

[214] L. Zhao, W. Kai, Y. He, B. Zhu, and Y. Inoue, “Effect of aging on fractional crystallization of poly(ethylene oxide) component in poly(ethylene oxide)/poly(3-hydroxybutyrate) blends,” *J. Polym. Sci. Part B Polym. Phys.*, vol. 43, no. 19, pp. 2665–2676, Oct. 2005, doi: 10.1002/POLB.20552.

[215] J.-F. Agassant *et al.*, “Polymer Processing Extrusion Instabilities and Methods for their Elimination or Minimisation,” 2006.

[216] Q. Zhu, M. T. Harris, and L. S. Taylor, “Time-Resolved SAXS/WAXS Study of the Phase Behavior and Microstructural Evolution of Drug/PEG Solid Dispersions,” *Mol. Pharm.*, vol. 8, 2011, doi: 10.1021/mp200041j.

[217] Kevin Whitcomb, “RH107: Determining the Linear Viscoelastic Region in Oscillatory Measurements,” 2021. doi: RH107.

[218] J. Van Renterghem, C. Vervaet, and T. De Beer, “Rheological Characterization of Molten Polymer-Drug Dispersions as a Predictive Tool for Pharmaceutical Hot-Melt Extrusion Processability,” *Pharm. Res.*, vol. 34, no. 11, pp. 2312–2321, Nov. 2017, doi: 10.1007/s11095-017-2239-7.

[219] J. Lu, S. Obara, N. Ioannidis, J. Suwardie, C. Gogos, and S. Kikuchi, “Understanding the Processing Window of Hypromellose Acetate Succinate for Hot-Melt Extrusion, Part I: Polymer Characterization and Hot-Melt Extrusion,” *Adv. Polym. Technol.*, vol. 37, no. 1, pp. 154–166, Feb. 2018, doi: 10.1002/ADV.21652.

[220] A. Isreb, K. Baj, M. Wojsz, M. Isreb, M. Peak, and M. A. Alhnan, “3D printed oral theophylline doses with innovative ‘radiator-like’ design: Impact of polyethylene oxide (PEO) molecular weight,” *Int. J. Pharm.*, vol. 564, pp. 98–105, Jun. 2019, doi: 10.1016/J.IJPHARM.2019.04.017.

[221] F. Briatico-Vangosa, A. Melocchi, M. Uboldi, A. Gazzaniga, L. Zema, and A.

Maroni, “Effect of Polyethylene Glycol Content and Molar Mass on Injection Molding of Hydroxypropyl Methylcellulose Acetate Succinate-Based Gastroresistant Capsular Devices for Oral Drug Delivery,” *Polym. 2019, Vol. 11, Page 517*, vol. 11, no. 3, p. 517, Mar. 2019, doi: 10.3390/POLYM11030517.

[222] E. Paladino *et al.*, “High spatial resolution ToF-SIMS imaging and image analysis strategies to monitor and quantify early phase separation in amorphous solid dispersions,” *Int. J. Pharm.*, vol. 628, p. 122191, Nov. 2022, doi: 10.1016/J.IJPHARM.2022.122191.

[223] S. Oladeji, V. Mohylyuk, D. S. Jones, and G. P. Andrews, “3D printing of pharmaceutical oral solid dosage forms by fused deposition: The enhancement of printability using plasticised HPMCAS,” *Int. J. Pharm.*, vol. 616, p. 121553, Mar. 2022, doi: 10.1016/J.IJPHARM.2022.121553.

[224] A. L. Sarode, S. Obara, F. K. Tanno, H. Sandhu, R. Iyer, and N. Shah, “Stability assessment of hypromellose acetate succinate (HPMCAS) NF for application in hot melt extrusion (HME),” *Carbohydr. Polym.*, vol. 101, no. 1, pp. 146–153, Jan. 2014, doi: 10.1016/J.CARBPOL.2013.09.017.

[225] B. P. COMMISSION., “British Pharmacopoeia,” vol. III, no. 2021, Stationery Office, Ed., Stationery Office, 2021, ch. Levomeprom.

[226] R. Parhi, “A review of three-dimensional printing for pharmaceutical applications: Quality control, risk assessment and future perspectives,” *J. Drug Deliv. Sci. Technol.*, vol. 64, p. 102571, Aug. 2021, doi: 10.1016/J.JDDST.2021.102571.

[227] D. M. Smith, Y. Kapoor, G. R. Klinzing, and A. T. Procopio, “Pharmaceutical 3D printing: Design and qualification of a single step print and fill capsule,” *Int. J. Pharm.*, vol. 544, no. 1, pp. 21–30, Jun. 2018, doi: 10.1016/j.ijpharm.2018.03.056.

[228] E. Fuenmayor *et al.*, “Comparison of fused-filament fabrication to direct compression and injection molding in the manufacture of oral tablets,” *Int. J. Pharm.*, vol. 558, pp. 328–340, Mar. 2019, doi: 10.1016/J.IJPHARM.2019.01.013.

[229] S. Henry *et al.*, “Development of a 3D-printed dosing platform to aid in zolpidem withdrawal therapy,” *Pharmaceutics*, vol. 13, no. 10, p. 1684, Oct. 2021, doi: 10.3390/PHARMACEUTICS13101684/S1.

[230] E. Walsh *et al.*, “Manufacture of tablets with structurally-controlled drug release using rapid tooling injection moulding,” *Int. J. Pharm.*, vol. 624, p. 121956, Aug. 2022, doi: 10.1016/J.IJPHARM.2022.121956.

[231] F. Zhang and J. W. McGinity, “Properties of Sustained-Release Tablets Prepared by Hot-Melt Extrusion,” *https://doi.org/10.1081/PDT-100101358*, vol. 4, no. 2, pp. 241–250, 1999, doi: 10.1081/PDT-100101358.

[232] L. C. Hwa, S. Rajoo, A. M. Noor, N. Ahmad, and M. B. Uday, “Recent advances in 3D printing of porous ceramics: A review,” *Curr. Opin. Solid State Mater. Sci.*, vol. 21, no. 6, pp. 323–347, Dec. 2017, doi: 10.1016/J.COSSMS.2017.08.002.

[233] C. Fischer and R. Gaupp, “Multi-scale rock surface area quantification—a systematic method to evaluate the reactive surface area of rocks,” *Geochemistry*, vol. 64, no. 3, pp. 241–256, Sep. 2004, doi: 10.1016/J.CHEMER.2003.12.002.

[234] M. Krachler, “Critical assessment of the performance of electronic moisture analyzers for small amounts of environmental samples and biological reference materials,” *Anal. Bioanal. Chem.*, vol. 371, no. 7, pp. 944–950, 2001, doi: 10.1007/S002160101058/METRICS.

[235] L. Shi, X. Fu, Y. Li, S. Wu, S. Meng, and J. Wang, “Molecular Dynamic Simulations and Experiments Study on the Mechanical Properties of HTPE Binders,” *Polym. 2022, Vol. 14, Page 5491*, vol. 14, no. 24, p. 5491, Dec. 2022, doi: 10.3390/POLYM14245491.

[236] D. A. Padmavathi, “Potential Energy Curves & Material Properties,” *Mater. Sci. Appl.*, vol. 02, no. 02, pp. 97–104, Feb. 2011, doi: 10.4236/MSA.2011.22013.

Appendix 1: Chapter 2 supporting information

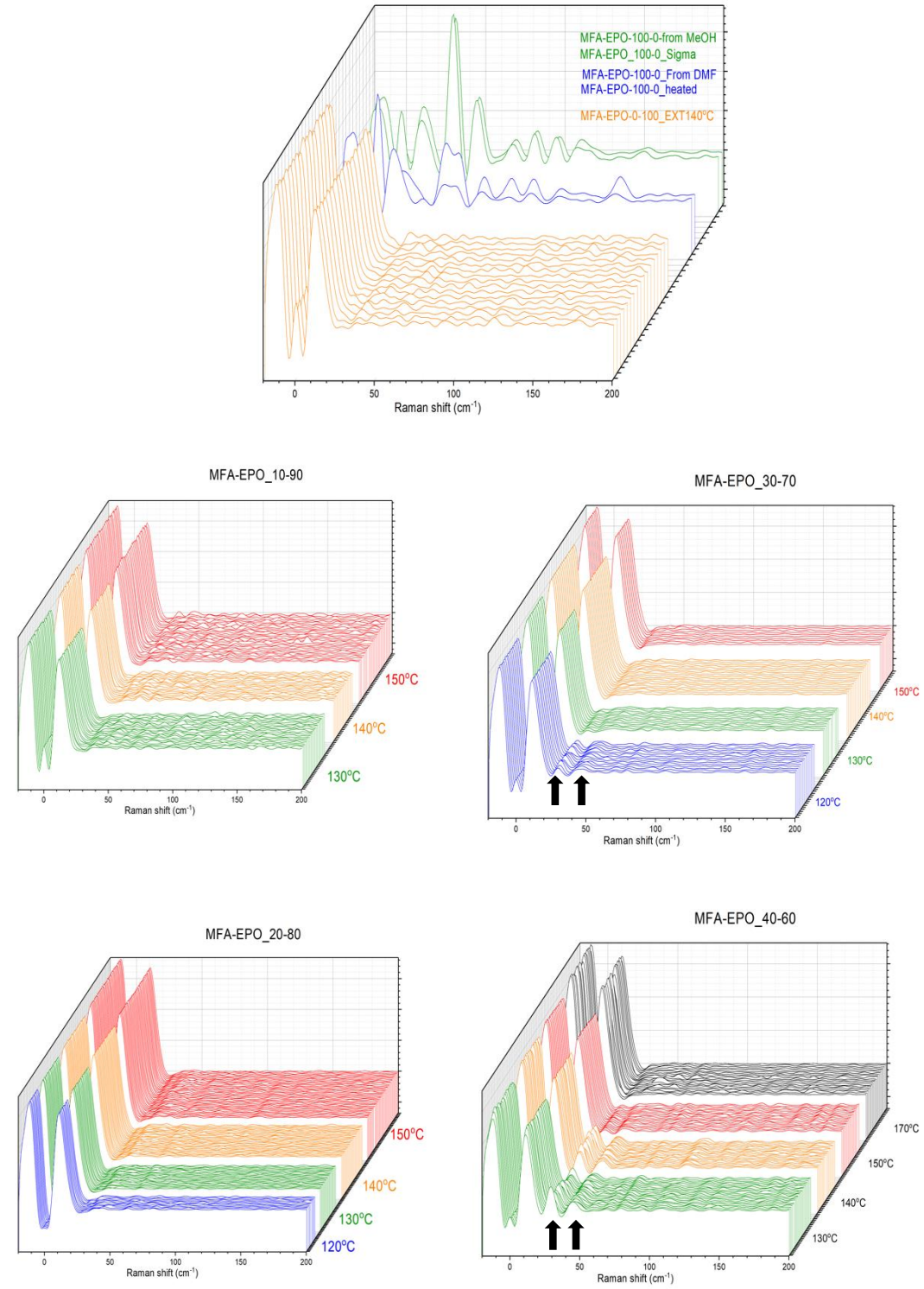

Figure Appendix 1-1. Inline Raman low frequency spectra from the HME experiment of binary system MFA-EPO at concentration range 10-40% drug load and different process temperature.

In-line THz-Raman raw data

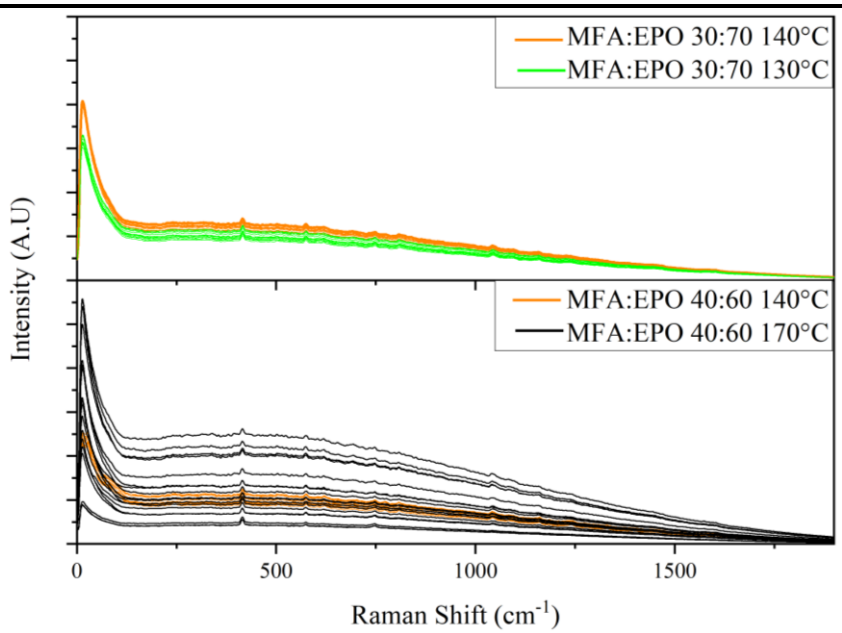

Appendix Figure 1-2. Raw inline-THz-Raman data from the HME experiment showing the increase in the backscattering due to the increase in the temperature as well as the intensity fluctuation in at the 170°C process temperature.

XRPD of some of the extrudates:

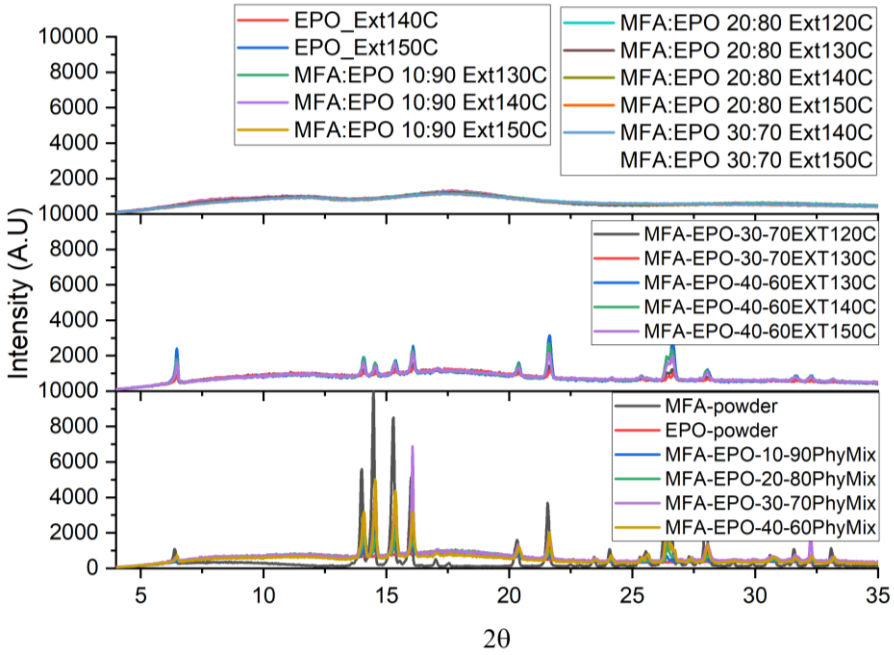

Appendix Figure 1-3. XRPD patterns of the pure components and MFA:EPO physical mixtures and extrudates at different drug loads and extruded at different temperatures.

Raman spectra of the pure components:

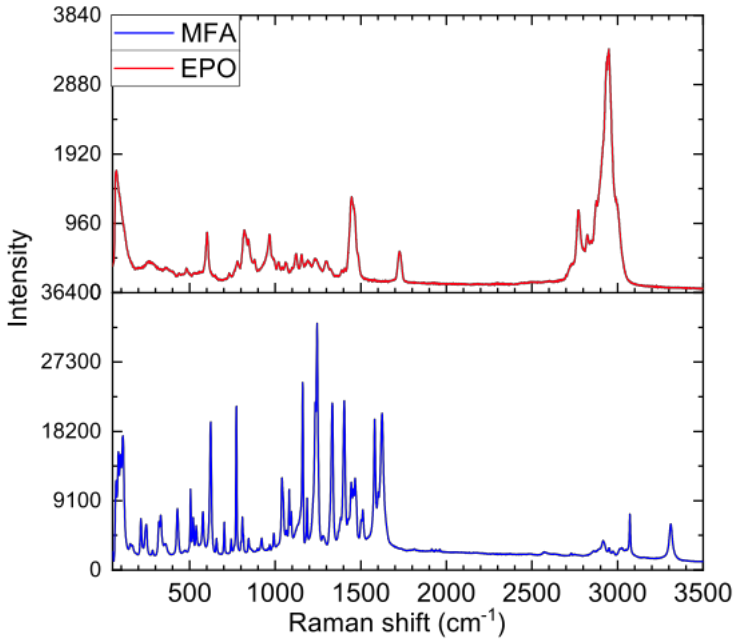

Figure Appendix 1-4. Experimental Raman Spectra of MFA form I powder (Blue) and Eudragit EPO powder (Red), Raman shift range (50-3500cm-1).

Table Appendix 1-1. Raman wavenumbers (in cm-1) of solid state Eudragit EPO peaks:

Raman shift (cm^{-1})	Bond vibration in Eudragit EPO
76.7	CH3-CH2 & CH2-CH2 torsion or/and CCC deformation (1)
263.4	[R] C-C skl. deformation (1)
365.9	Zig-zag bend (2) or/and [R-NR2] CNC deformation (1)
483.9	[R] C-C skl. deformation (1)
534.9	Not assigned
601.6	CN stretching vibration (3)
733.6	C-C4 symmetric stretching (1)
779.5	[R] C-C-C symmetric stretching (1)
821.9	[R] -(CC) stretching vibration (2) , [R] C-C-C stretching (1)
878	[N-C3] in plane stretching (2) or/and [R] -(CC) stretching vibration (3)
966.3	[-CH2-] rocking-twisting or/and [-CH2-] terminal rocking (1)

1019.1	[R-NR2] C-N stretching or/and [-CH2-] rocking-twisting (1)
1062.9	[-CH2-] trans chain out plane stretching (2) or/and [-COO-] v C-O (1) or/and [R-NR2] C-N stretching (1)
1122.8	[C-N] C-N-C out plane stretching (2)
1156.8	C-C skel. stretching or/and [R-NR2] C-N stretching (1)
1194.1	[R-NR2] C-N stretching or/and [-CH2-] rocking-twisting (1)
1236.6	[-COO-] vC-O stretching or/and [R-NR2] C-N stretching or/and [-CH2-] wagging or/and [-CH2-] twisting-rocking (1)
1300.4	[-CH2-] in phase twist (1,2)
1366.5	[-CH2-] O-CH2 wag or/and [CH3-] (R-CH3)3 (2) or/and [-COO-R] due to the O-CH2, CH2 symmetric deformation (1)
1393.9	[-CH2-] O-CH2 wag [-CH2-] R-CH2-R bend (2)
1449.6	[-CH2-] and [-CH3) deformations (3) or/and [CH3-] in-phase deformation O-CH3 and C-CH3 (2) or/and [CH3-] R-CH3 o. phase bend (2) or/and [CH3-] asymmetric bend (2) or/and [-COO-R] due to the O-CH3, CH3 asymmetric deformation (2)
1727.4	[C=O] in R-CO-O-R, C=O stretching (1,2)
2772	Not assigned
2771.4	[CH3-] R2-N-CH3 in phase stretching (2)
2824.1	[CH3] R2-N-CH3 in phase stretching (2)
2877.9	[CH3-] symmetric stretching (1)
2947.8	[CH3] R-CH3 out phase stretching or/and [CH3] (N)-CH3 in phase stretching or/and [-CH2-] R-CH2-R Fermi resonance or/and [-CH2-] R-CH2-R out phase stretching (1)
3000	[(N)-CH3] out phase stretching or/and [(O)-CH3] out phase stretching (2)

1. The handbook of infrared and Raman characteristic frequencies of organic molecules
2. Peter Larkin-Infrared and Raman Spectroscopy_ Principles and Spectral Interpretation -Elsevier (2011)
3. Reference database of Raman spectra of pharmaceutical excipients

Table Appendix 1-2 (Part 1). Raman wavenumber (in cm-1) of MFA peaks and their change in the extrudates samples:

Raman shift cm-1	Peak assignment*	Pattern** Yes/No	What type of pattern	Peak or shoulder	Pure component peak relative intensity (vs-s-m-w-vw)	Peak relative intensity (vs-s-m-w-vw)	Can be used for molecular interaction interpretation ? *** Yes/No
578.1	[Ar] C-C-C in phase bending	Yes	Disappear in 10% drug load	Peak	m	m-w	Yes
622.9	N-H bending out of plane	Yes	Appear only in crystalline solid suspension samples	Peak	s	s	Yes (with conscious)
703	[Ar] C-C-C in phase puckering and [-CH3]	Yes	Present in almost all drug loaded samples	Peak	w to m	w	No
1042.4	[C-C] str (Øb)	Yes	No change	Peak	m	m	No
1083.8	[C-H] bending in plane (Øa, Øb), [CH3] wagging	Yes	Shift in all samples except few reads.[1][2]Comment: about (+) 10 cm-1	Peak	m to w	m to w	Yes
1243.1	[O-H] bending in plane and [C-H] bending in plane in phase (Øa, Øb) and [C-COOH] str	Yes	Split in 10% and 20% drug loaded samples with a drop in the intensity. Higher dug ratio shows same pattern or no change depends on the presence of crystal in the beam path.	Peak	vs	s	No
1332.7	[O-H] bending in plane and [C-C] str (¯b)	Yes	Present in Form I crystalline solid dispersion only	Peak	s	s	No
1403.5	[N-H] bending in plane and [C-C] bending in plane (¯a and ¯b) and [O-H] bending in plane and [C=O] str and [CH3] bending	No	Shifting in all solid solution samples and reducing in the intensity while in crystalline solid suspension no shifting observed	Peak	s	s & m (change in the intensity)	No

Table Appendix 1-2 (Part 2). Raman wavenumber (in cm-1) of MFA peaks and their change in the extrudates samples:

Raman shift cm-1	Peak assignment*	Pattern** Yes/No	What type of pattern	Peak or shoulder	Pure component peak relative intensity (vs-s-m-w-vw)	Peak relative intensity (vs-s-m-w-vw)	Can be used for molecular interaction interpretation? *** Yes/No
1510.3	[C-C] str (¯b) and [N-H] str	No	Shifting and reduction in the intensity in solid solution samples, no change in the crystalline solid suspensions. Comment: about (+) 10 cm-1	Peak	m	m (crysatalline) - w (amorphous)	Yes (with conscious)
1581.5	[N-H] bending in plane and [C-C] str (¯a and ¯b)	Yes	No change	Peak	s	s	No
1624.2	[N-H] bending in plane and [C-C] str (¯b) and [O-H] bending in plane and [C=O] str	Yes	In solid solution samples, the peak disappear. A new peak appear at 1602 cm-1. In some crystalline samples both peaks were observed.	Peak	s	s - m	Yes (with conscious)
3072.7	[C-H] str in phase (¯a and ¯b))	Yes	Present in almost all drug loaded samples	Peak	m	m - w	Yes
3311.3	[N-H] str	Yes	Present in crystalline solid dispersion samples.	Peak	m	m	Yes

* peaks assignment were taken from the literature 14,20–22
** Pattern was indicated if the peak followed a change with the drug load, process temperature or amorphous state
*** The confidence level of using the peak for interpretation according to the peak intensity, presence of pattern and being assigned to one bond vibration

Table Appendix 1-3: Carboxyl to amine group ratio calculation for MFA:EPO formulae:

Calculation	
Molecular weight (EPO_{Mwt}): 47000 g/mol Chemical name: Poly[(dimethylaminoethyl methacrylate)-co-(methyl methacrylate)-co-(butyl methacrylate)] Dimethylaminoethyl methacrylate monomer ratio (DM%) = 28.92% Monomer of total EPO monomers Total Mwt of DM in each EPO (TDM_{Mwt}) = EPO_{Mwt} X DM% = 13592.4 g/mol Molecular weight (DM_{Mwt}): 157.21 g/mol Number of DM in each EPO= TDM_{Mwt} / DM_{Mwt} = 86.46 Monomer Number of amine group in each EPO (NCCC) = n umber on DM = 86.46 group	
MFA Molecular weight (MFA_{Mwt}): 241.29 g/mol Number of carboxyl groups (COOH) = number of MFA molecules	
Carboxyl to amine group ratio = (MFA ratio/ MFA_{Mwt})/(NCCC X EPO ratio/ EPO_{Mwt})	
Formula (wt)	COOH/NCCC
EPO (MFA:EPO 0:100)	0
MFA:EPO 10:90	0.25
MFA:EPO 20:80	0.56
MFA:EPO 30:70	0.97
MFA:EPO 40:60	1.50

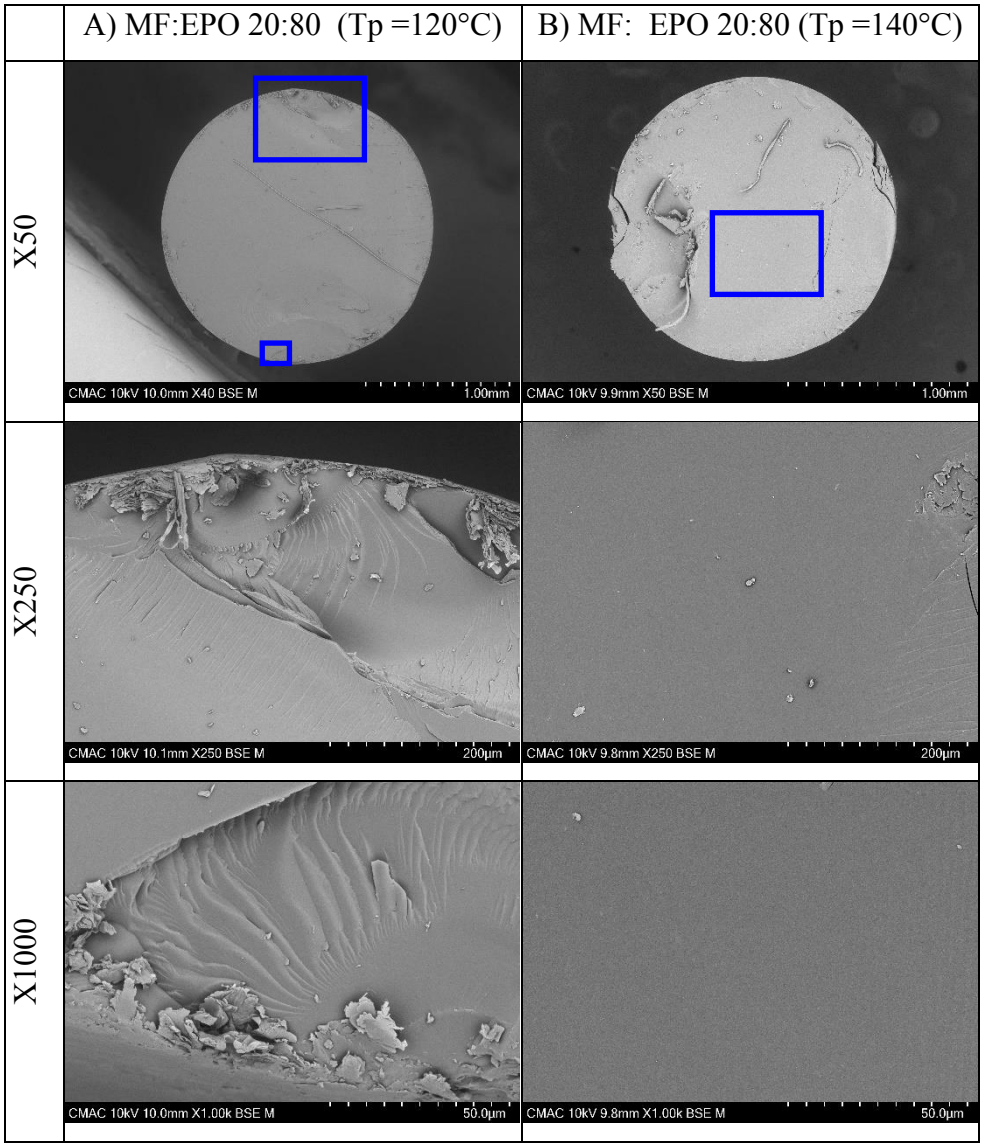

Figure Appendix 1-5. Cross section images from the SEM of the MFA:EPO 20:80 extrudates at different process temperature 120 and 140°C (A and B, repectively). Red arrows (stress direction), dashed line (separate the compresion and tension areas) and stars (toward the tesnion area).

Appendix 2: Chapter 3 supporting information

Table Appendix 2-1. Drug, polymer and plasticizers' molecular volumes (MVol in cm^3/mol) as calculated on HSPiP software:

	MVol		MVol
Eudragit-EPO *	369.3	**Triethylene Glycol**	133.4
Polyethylene Glycol *	39.4	**Propylene Glycol**	74.3
Stearic Acid	324.3	**Urea**	49.7
Triacetin	189.3	**Ethyl glycol**	56.2
Mefenamic Acid	200.6	**Glycerol**	75
Tween 80	586.7	**Xylitol**	131
Triethyl Citrate	238.9	**D-Mannitol**	161.7
Methylparaben	128.6		
* For polymer the value is calculated for the monomer/s not for the whole molecule			

Hot stage microscope of MFA:StA

The interaction between MFA and StA at two concentrations (MFA:StA 0:100, 2.5:97.5 and 5:95, wt%) was investigated using HSM. Temperature profile is presented in Table 3-1 and after cooling the samples analysed on the Raman microscope (see section 2.2.2.2.3).

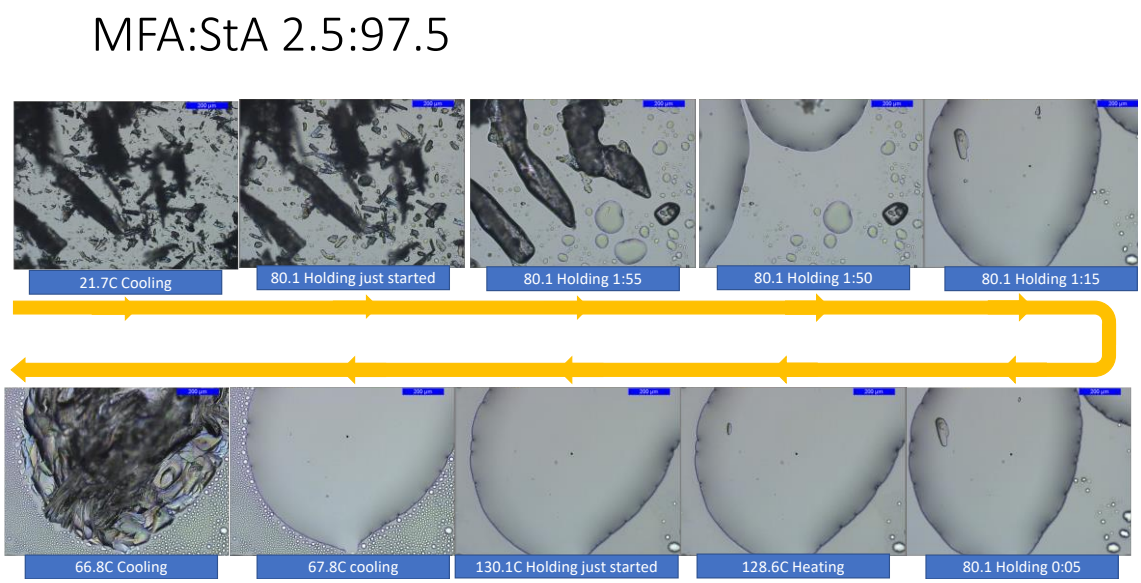

Raman spectra (2.2.2.2.3) was collected for the MFA:EPO:StA 20:76:4 extrudate.

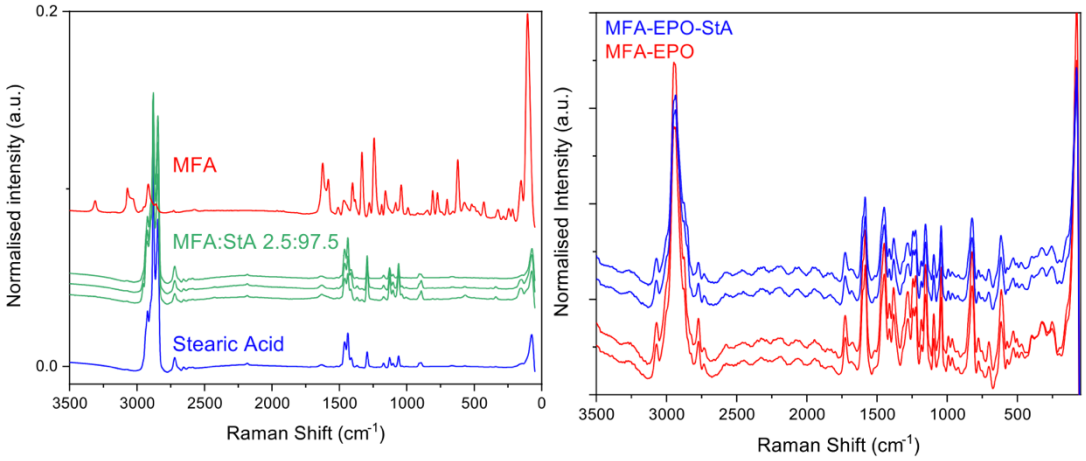

MFA – Edudragit NM

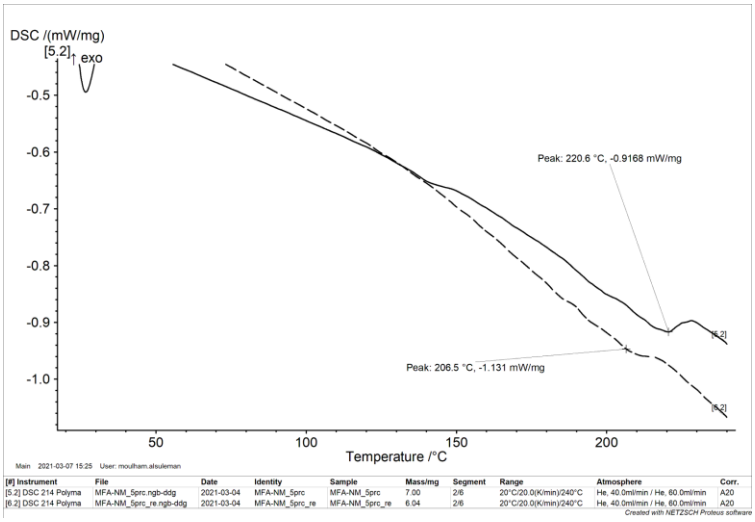

Appendix 3: Chapter 4 supporting information

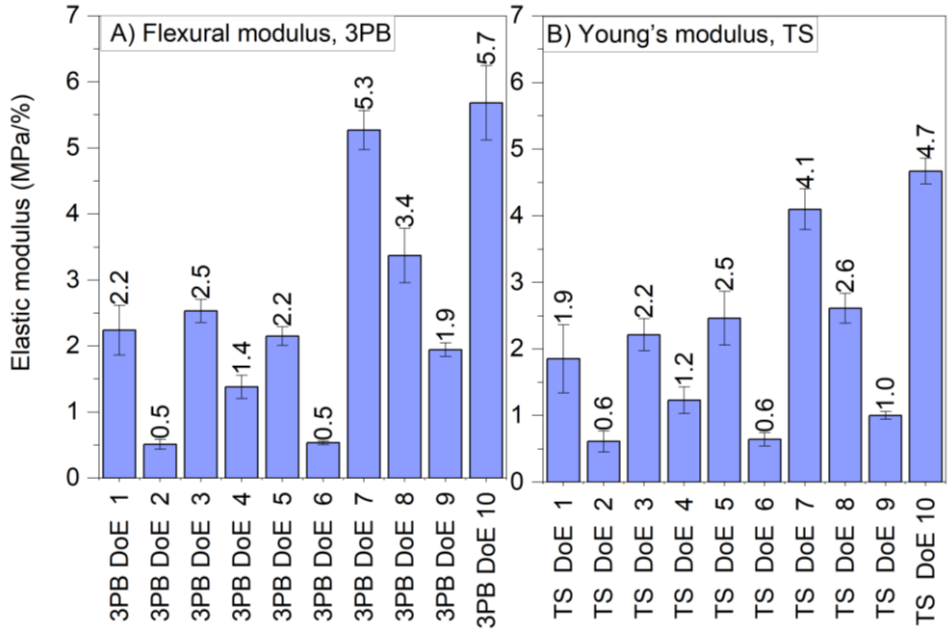

Figure Appendix 3-1. Elastic modulus from 3PB test (left) and TS test (right) fo DoE samples.

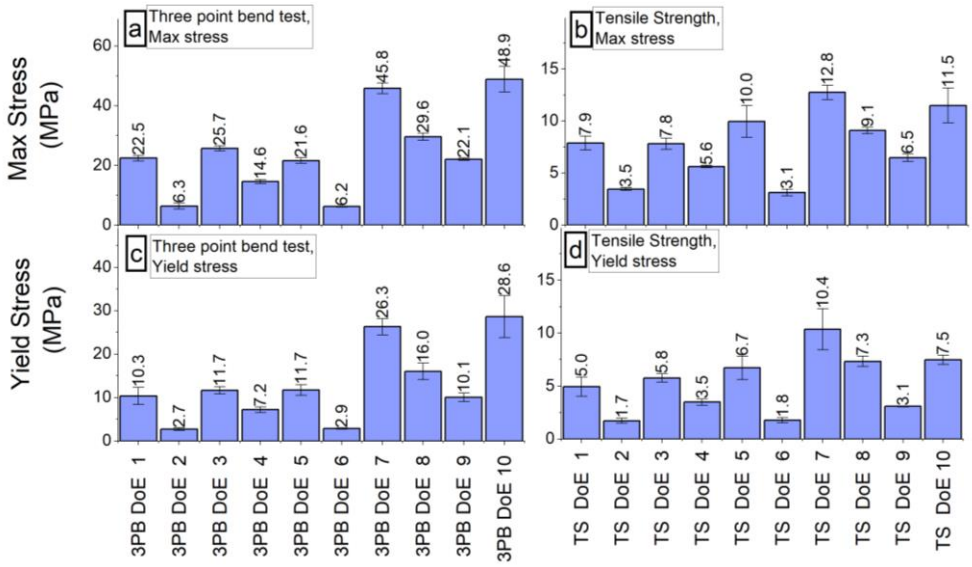

Figure Appendix 3-2. Maximum stress (top) and yeild point stress (bottom) from 3PB test (left) and TS test (right) fo DoE samples.

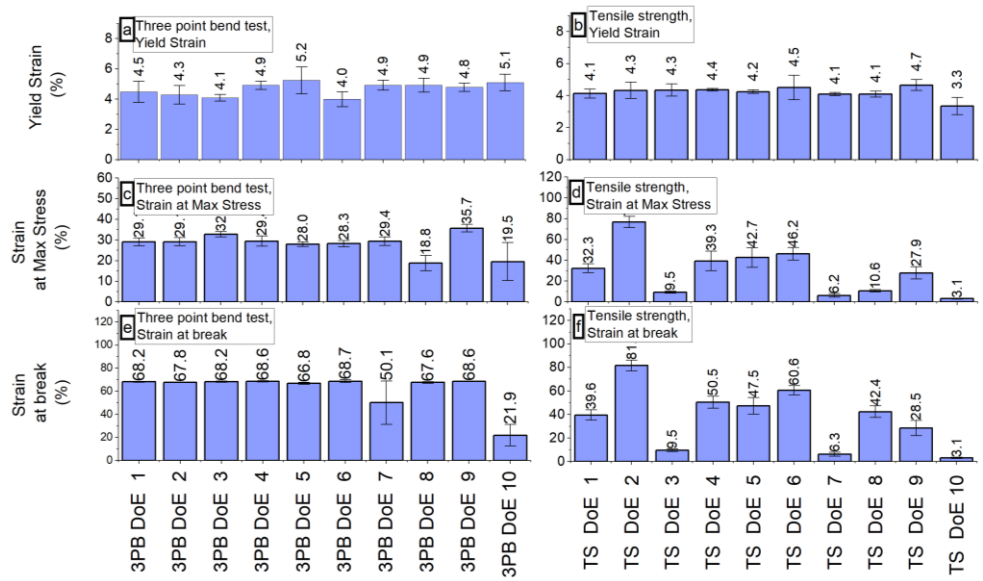

Figure Appendix 3-3. Yeild point strain (top), strain at maximum stress (middle) and strain at break (bottom) from 3PB test (left) and TS test (right) fo DoE samples.

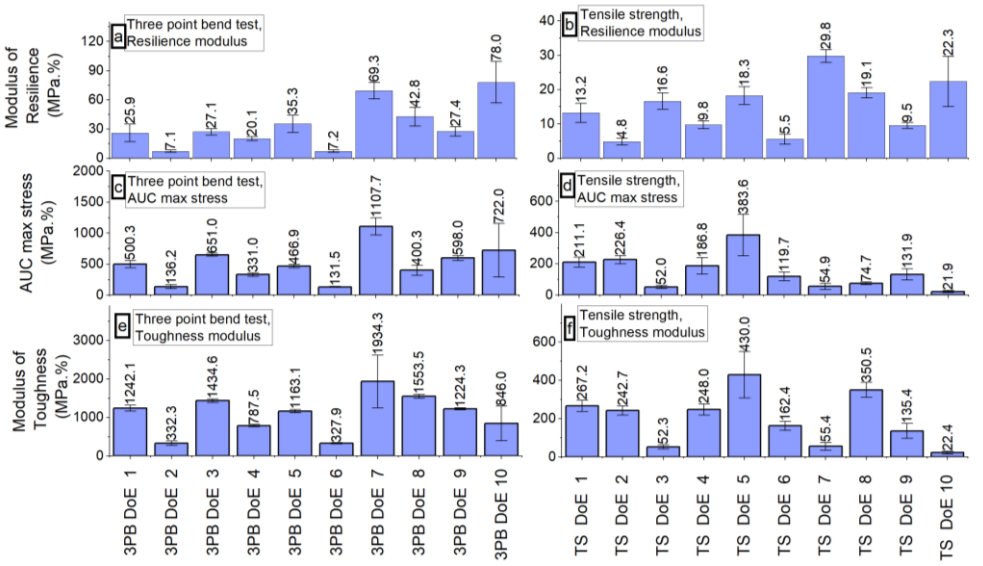

Figure Appendix 3-4. Modulus of resiliance (top), modulus of maximum stress (middle) and modulus of toughness (bottom) from 3PB test (left) and TS test (right) fo DoE samples.

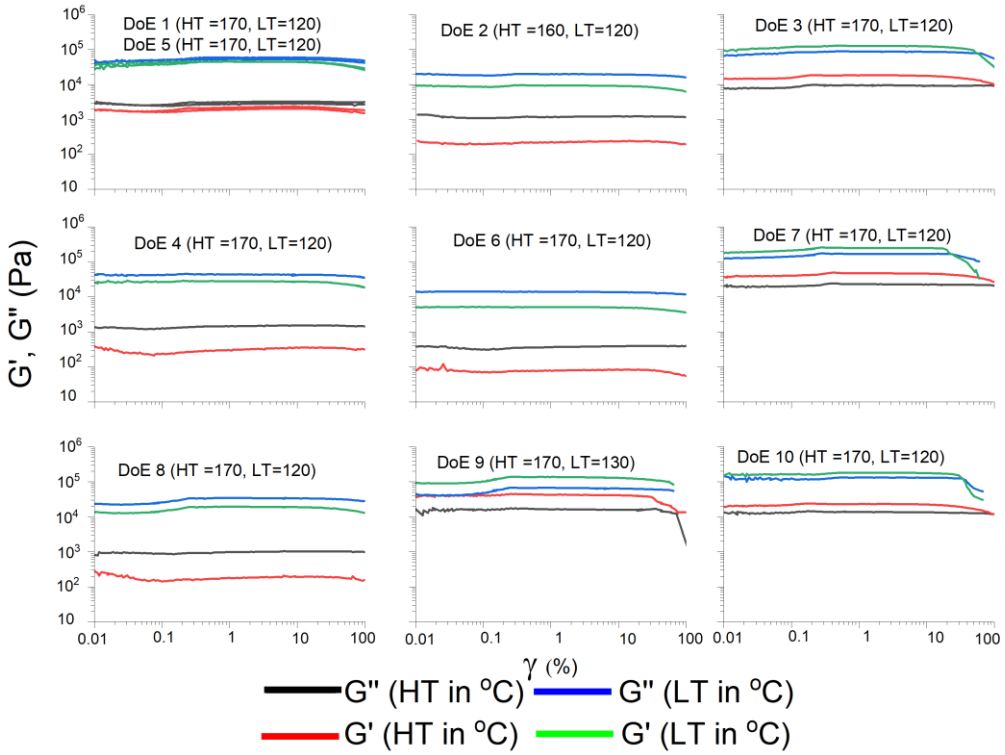

Figure Appendix 3-5 Storage (G') and loss (G") moduli of DoE filaments (1 to 10) from the amplitude sweep test.

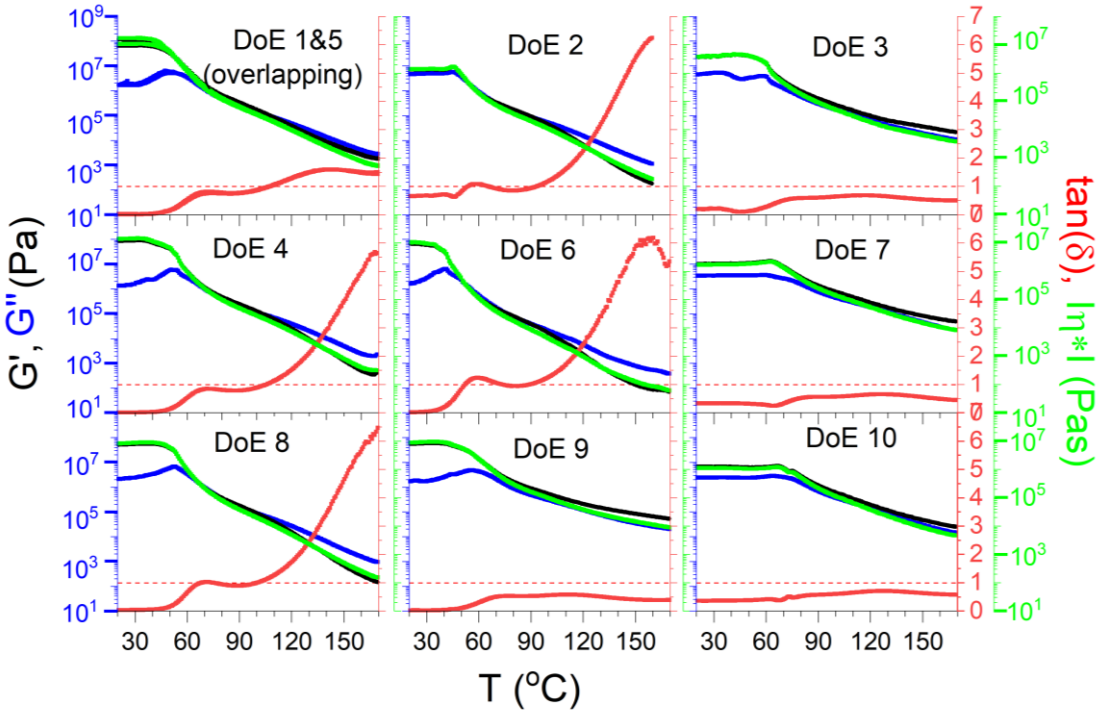

Figure Appendix 3-6 Temperature sweep test of the DoE formulae showing storage modulus (G'), loss modulus (G") viscosity (η) and dumping factor (tan(δ)).

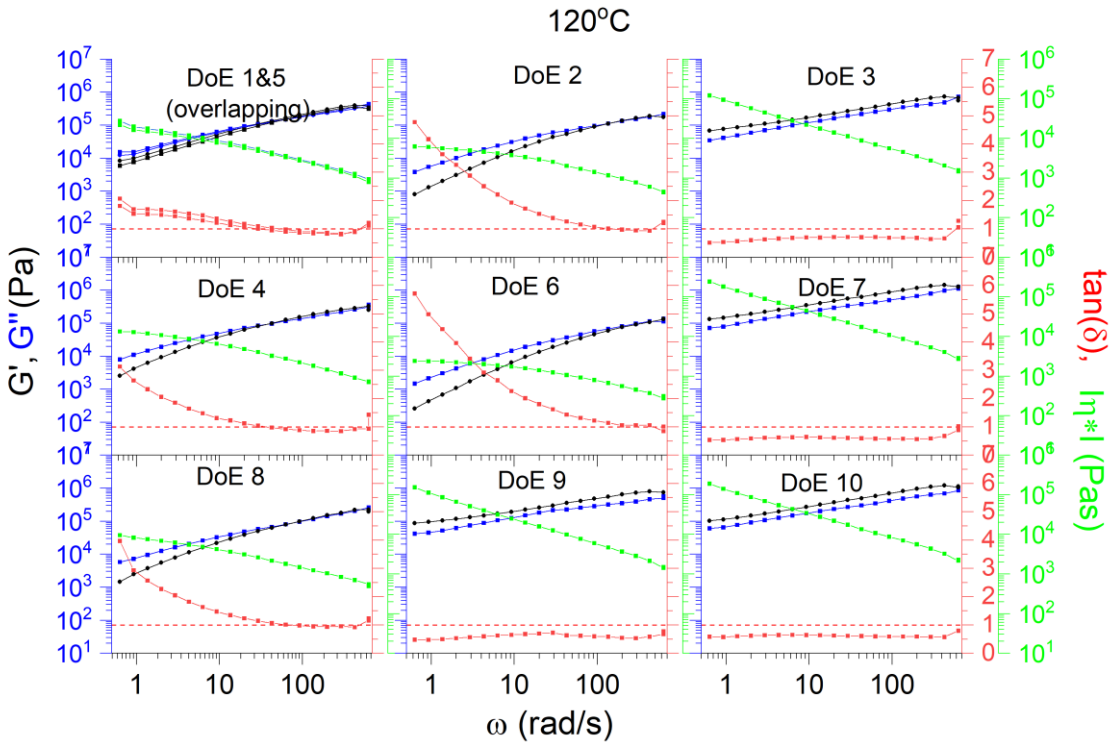

Figure Appendix 3-7 Frequency sweep test of DoE filaments at 120°C.

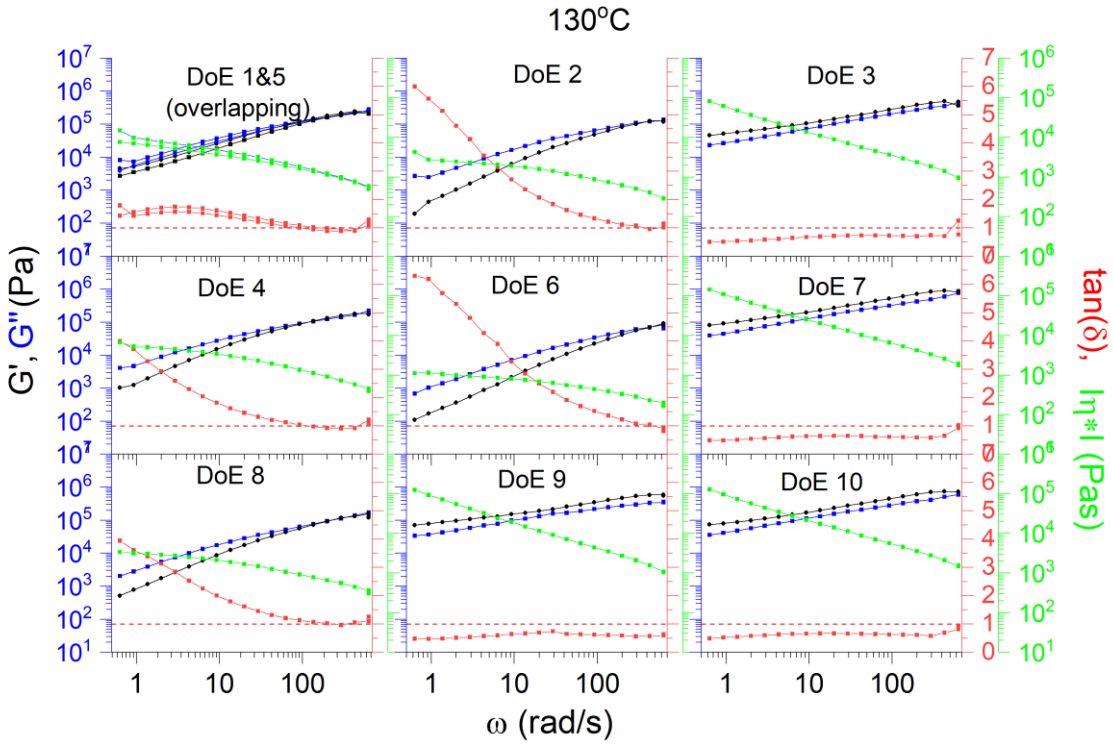

Figure Appendix 3-8 Frequency sweep test of DoE filaments at 130°C.

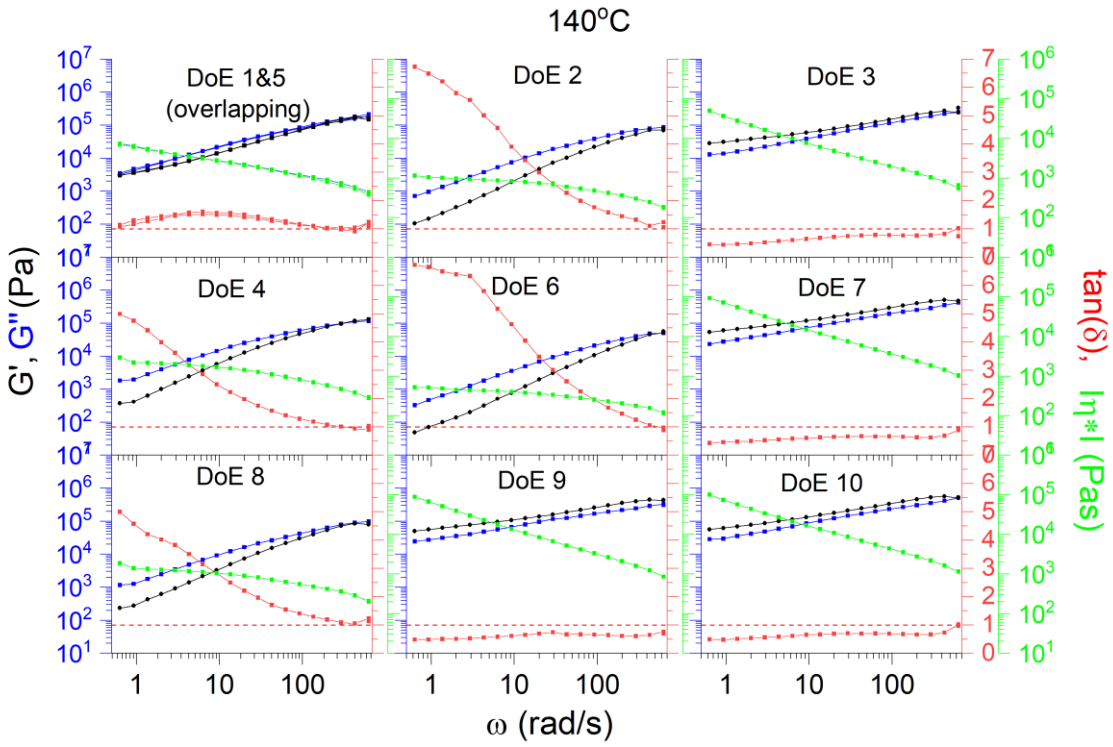

Figure Appendix 3-9 Frequency sweep test of DoE filaments at 140°C.

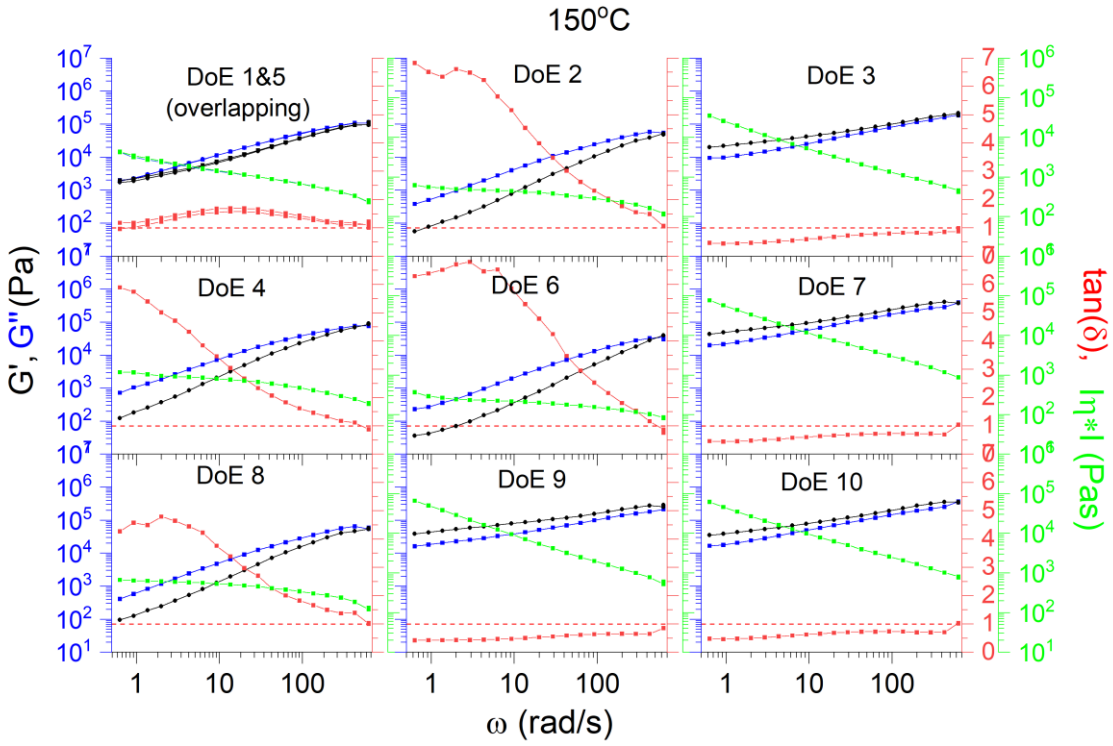

Figure Appendix 3-10 Frequency sweep test of DoE filaments at 150°C.

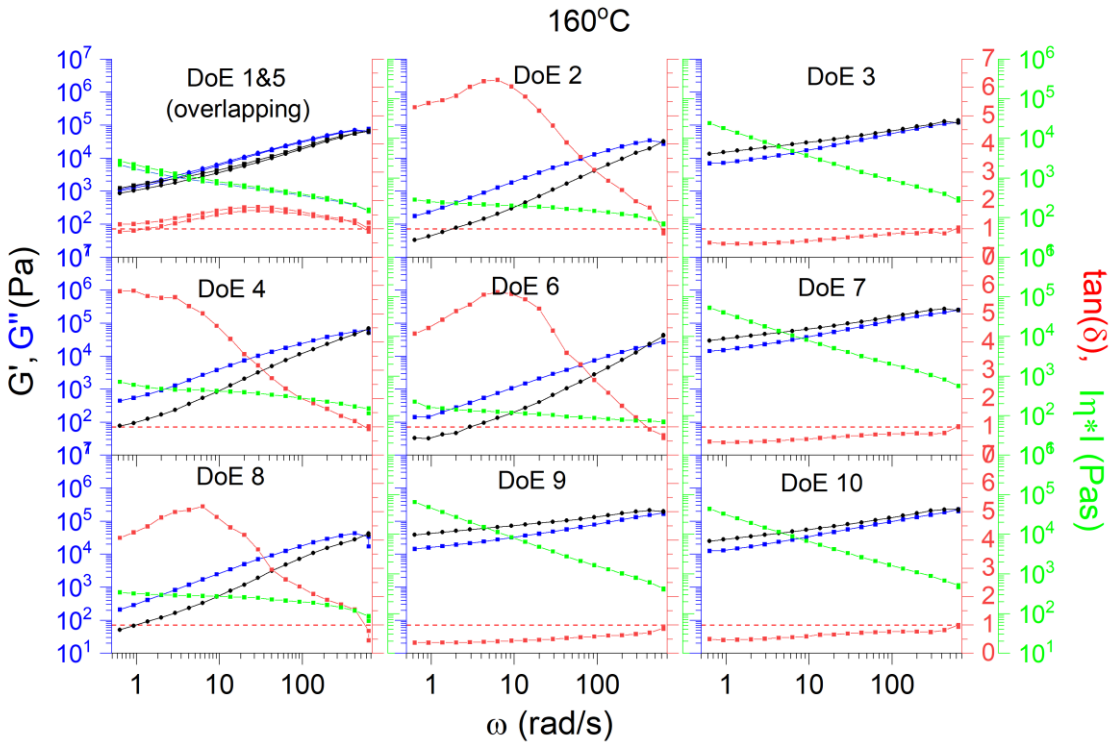

Figure Appendix 3-11 Frequency sweep test of DoE filaments at 160°C.

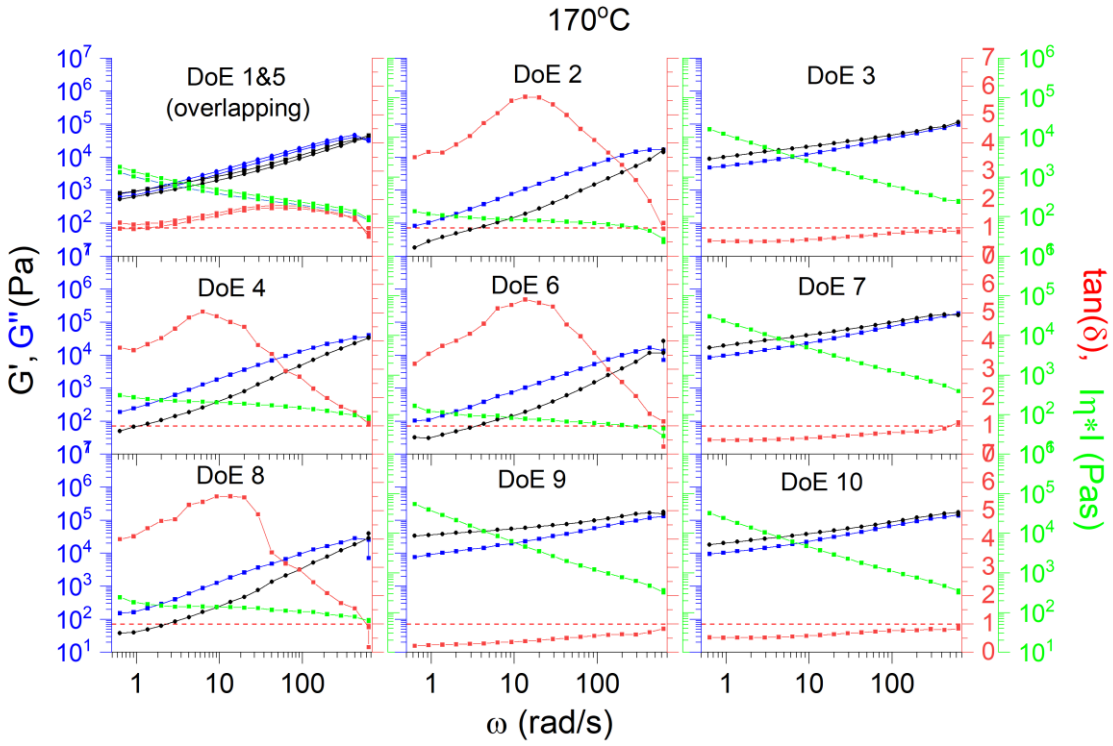

Figure Appendix 3-12 Frequency sweep test of DoE filaments at 170°C.

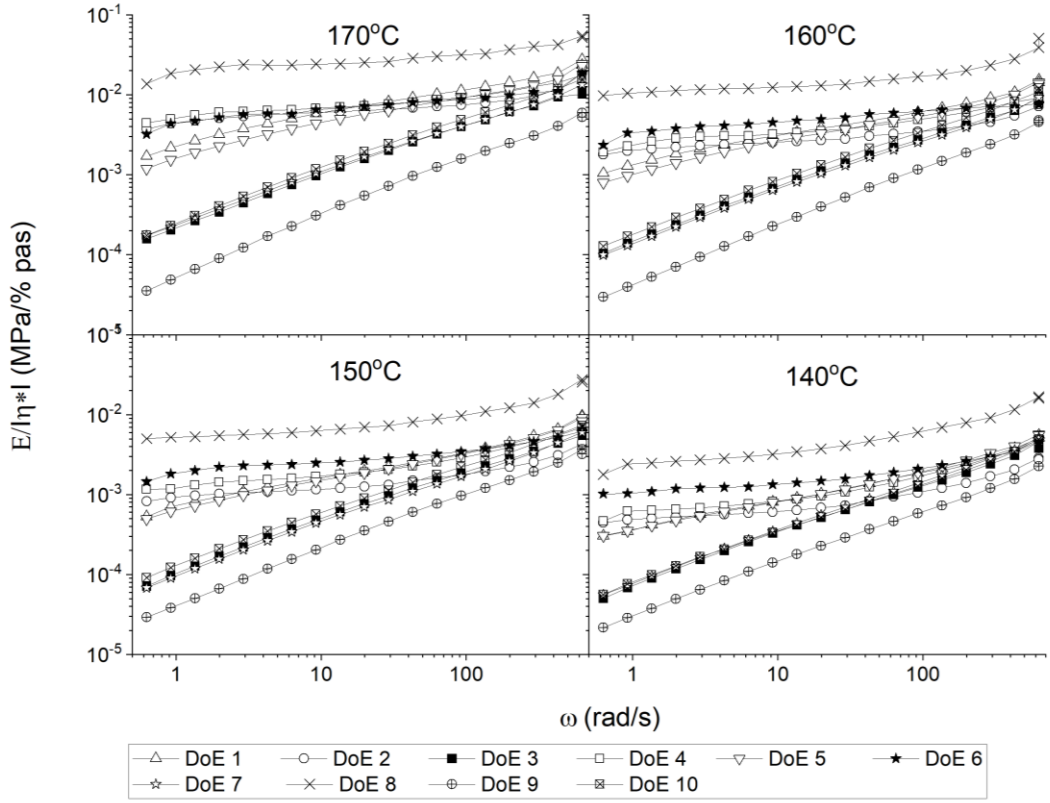

Figure Appendix 3-13 E/η in MPa/%Pas of all DoE formulae at different temperatures and range of frequencies.

Table Appendix 3-1 Coefficient of DoE responses, non-significant coefficients were removed to improve DoE model:

	E/InI		**Max stress (3BP)**		**Strain at break (TS)**		**MFA content**	
	CoEff	**SD**	**CoEff**	**SD**	**CoEff**	**SD**	**CoEff**	**SD**
Constant	0.267	0.0099	7.66	0.243	8.51	0.376	16.57	0.058
StA	-0.015	0.0049	-2.12	0.271	1.59	0.421	-0.41	0.064
MFA	0.021	0.0049	0.57	0.271	-1.05	0.421	5.95	0.064
Silica	-0.049	0.0049	2.37	0.271	-3.89	0.421	-2.54	0.064
Sil*Sil	-0.018	0.0110	-	-	-	-	-	-
MFA*Sil	-0.010	0.0049	-	-	-	-	-0.91	0.064
StA*MFA	-	-	-	-	-0.52	0.421	-	-
StA*Sil	-	-	-	-	-	-	-	-

N, DF	10, 4		10, 6		10, 5		10, 5	
Q2	0.795		0.855		0.893		0.997	
R2	0.971		0.959		0.956		1	
R2 adj.	0.935		0.939		0.92		0.999	
Cond. no.	4.266		1.118		1.118		1.118	
RSD	0.014		0.767		1.19		0.182	
Confidence	0.95		0.95		0.95		0.95	
	Yield stress (3BP)		**Elasticity**		**Strain at Max**		**Tg (Rhe)**	
	CoEff	**SD**	**CoEff**	**SD**	**CoEff**	**SD**	**CoEff**	**SD**
Constant	2.40	0.050	1.035	0.0040	8.78	0.85	74.25	0.625
StA	-0.48	0.056	-0.030	0.0045	2.07	0.42	-4.60	0.699
MFA	0.12	0.056	0.008	0.0045	-1.63	0.42	0.25	0.699
Silica	0.47	0.056	0.030	0.0045	-2.56	0.42	9.42	0.699
Sil*Sil	-	-	-	-	-2.17	0.95	-	-
MFA*Sil	-	-	-	-	-	-	-	-
StA*MFA	-	-	-	-	-	-	1.68	0.699
StA*Sil	-	-	-	-	-	-	1.65	0.699
N, DF	10, 6		10, 6		10, 5		10, 4	
Q2	0.863		0.79		0.767		0.806	
R2	0.961		0.94		0.942		0.983	
R2 adj.	0.942		0.91		0.895		0.963	
Cond. no.	1.118		1.118		4.266		1.118	
RSD	0.158		0.013		1.196		1.976	
Confidence	0.95		0.95		0.95		0.95	

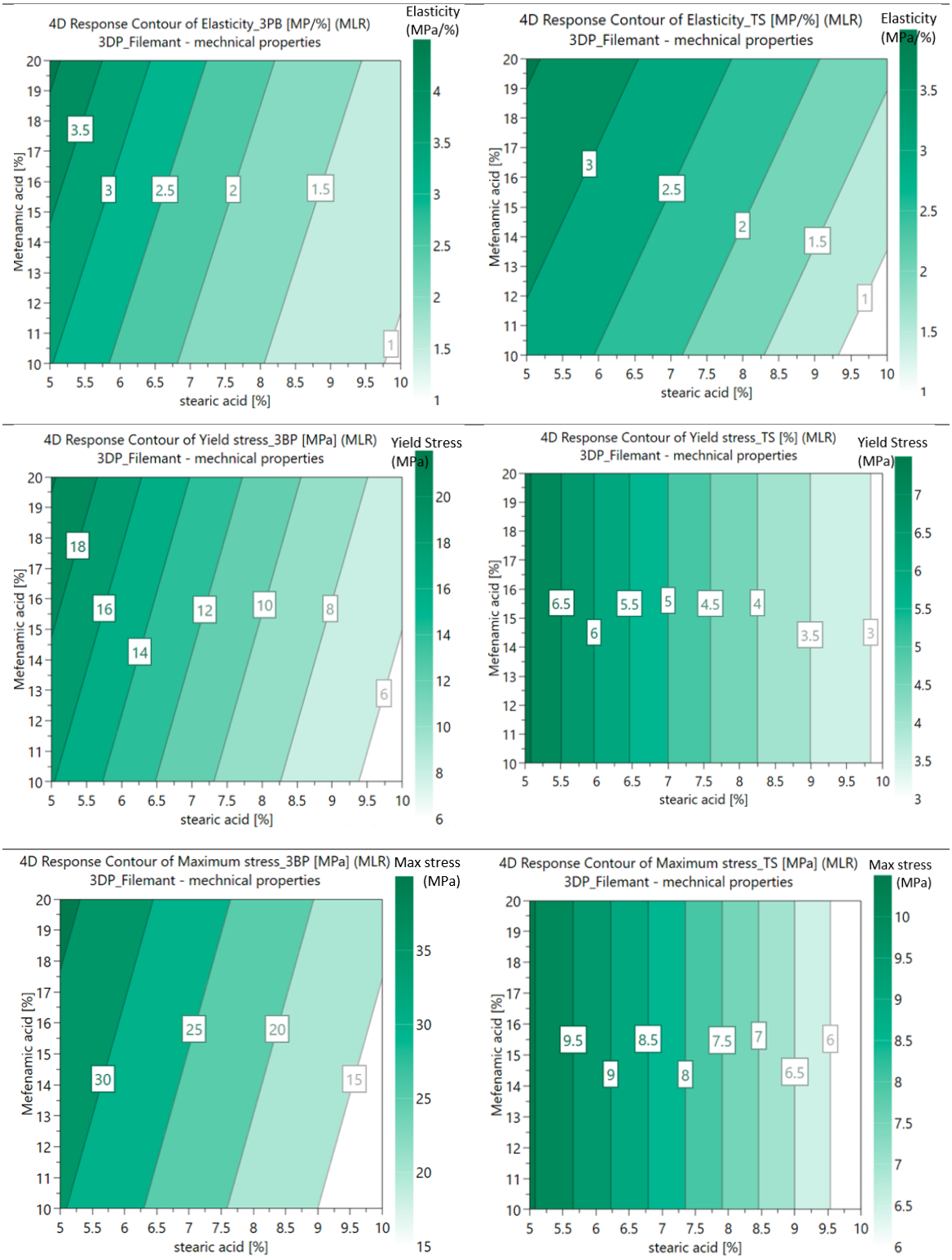

Figure Appendix 3-14 Contour plot of elastic modulus, yield stress and maximum stress from 3PB test and TS test.

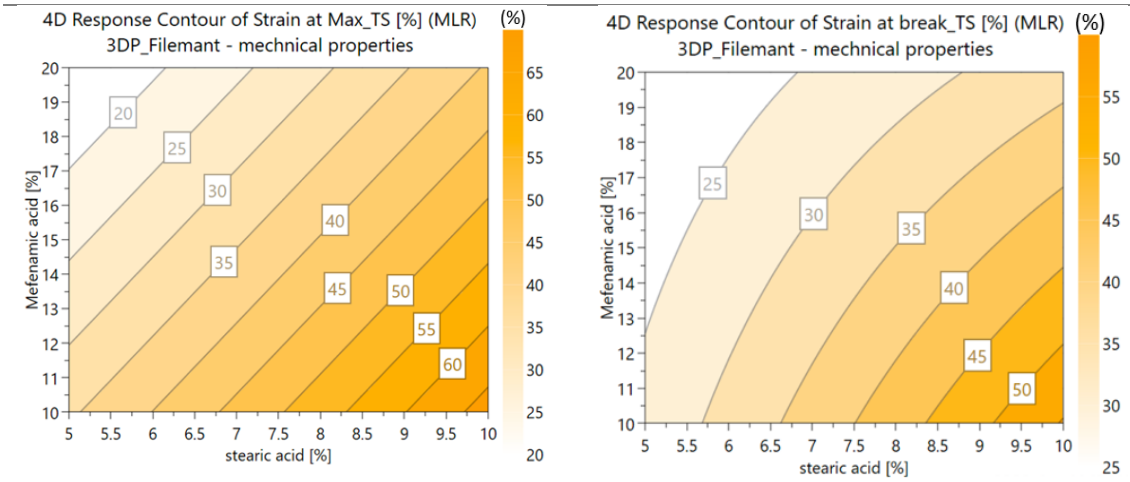

Figure Appendix 3-15 Contour plot of strain at maximum stress and strain at break.